https://doi.org/10.15388/vu.thesis.732
https://orcid.org/0000-0003-2178-3393

VILNIUS UNIVERSITY
CENTER FOR PHYSICAL SCIENCES AND TECHNOLOGY

Ernestas Nacius

Development and application of beam shaping elements fabricated by laser micro-machining in the NIR and THz wavelength ranges for material processing and imaging

DOCTORAL DISSERTATION

Technological Sciences,
Material engineering (T 008)

VILNIUS 2025

This dissertation was prepared between 2020 and 2024 in the Center for Physical Sciences and Technology.

Academic supervisor – Assoc. Prof. Dr. Vytautas Jukna (Center for Physical Sciences and Technology, Technological Sciences, Materials Engineering — T 008)
This doctoral dissertation will be defended in a public meeting of the Dissertation Defense Panel:

Chairman – Dr. Paulius Gečys (Center for Physical Sciences and Technology, Technological Sciences, Materials Engineering – T 008).

Members:
Dr. Martynas Beresna (University of Southampton, United Kingdom, Technological Sciences, Materials Engineering – T 008)
Dr. Francois Courvoisier (Femto-ST Institute, University Bourgogne-Franche-Comte, CNRS, Technological Sciences, Materials Engineering – T 008)
Dr. Mindaugas Gedvilas (Center for Physical Sciences and Technology, Technological Sciences, Materials Engineering – T 008)
Assoc. Prof. Dr. Nikolaj Višniakov (Vilnius Gediminas Technical University, Technological Sciences, Materials Engineering – T 008)

The dissertation shall be defended at a public meeting of the Dissertation Defense Panel at 14:00 on 19th of March 2025 in Room D401 of the Center for Physical Sciences and Technology. Address: Saulėtekis av. 3, FTMC, Room D401, Vilnius, Lithuania. Tel. +370 5 264 9211; email: office@ftmc.lt.

The text of this dissertation can be accessed at the libraries of the Center for Physical Sciences and Technology and Vilnius University, as well as on the website of Vilnius University: www.vu.lt/lt/naujienos/ivykiu-kalendorius

https://doi.org/10.15388/vu.thesis.732
https://orcid.org/0000-0003-2178-3393

VILNIAUS UNIVERSITETAS
FIZINIŲ IR TECHNOLOGIJOS MOKSLŲ CENTRAS

Ernestas Nacius

Lazerinio mikroapdirbimo būdu pagamintų pluoštus formuojančių elementų NIR ir THz bangų ruože kūrimas ir pritaikymas medžiagų apdirbime bei vaizdinime

DAKTARO DISERTACIJA

Technologijos mokslai,
Medžiagų inžinerija (T 008)

VILNIUS 2025

Disertacija rengta 2020–2024 metais Fizinių ir technologijos mokslų centre.

Mokslinis vadovas – doc. dr. Vytautas Jukna (Fizinių ir technologijos mokslų centras, technologijos mokslai, medžiagų inžinerija – T 008).

Gynimo taryba:

Pirmininkas – dr. Paulius Gečys (Fizinių ir technologijos mokslų centras, technologijos mokslai, medžiagų inžinerija – T 008).

Nariai:
dr. Martynas Beresna (University of Southampton, Jungtinė Karalystė, technologijos mokslai, medžiagų inžinerija – T 008).
dr. Francois Courvoisier (Femto-ST Institute, University Bourgogne-Franche-Comte, CNRS, Prancūzija, technologijos mokslai, medžiagų inžinerija – T 008).
dr. Mindaugas Gedvilas (Fizinių ir technologijos mokslų centras, technologijos mokslai, medžiagų inžinerija – T 008).
doc. dr. Nikolaj Višniakov (Vilniaus Gedimino technikos universitetas, technologijos mokslai, medžiagų inžinerija – T 008).

Disertacija ginama viešame Gynimo tarybos posėdyje 2025 m. kovo mėn. 19 d. 14 val. Fizinių ir technologijos mokslų centro D401 auditorijoje.
Adresas: Saulėtekio al. 3, FTMC, D401 aud., Vilnius, Lietuva.
Tel. +370 5 264 9211; el. paštas: office@ftmc.lt.

Disertaciją galima peržiūrėti Fizinių ir technologijos mokslų centro bei Vilniaus universiteto bibliotekose ir VU interneto svetainėje adresu: www.vu.lt/lt/naujienos/ivykiu-kalendorius

LIST OF ABBREVIATIONS

a.u.	Arbitrary Units
CCD	Charge-coupled device
CMOS	Complementary metal-oxide semiconductor
CSRR	Complementary split ring resonator
CW	Continuous wave
DOE	Diffractive optical element
GPE	Geometric phase element
HAZ	Heat affected zone
FFT	Fast Fourier transform
FTDT	Finite-difference time-domain
FWHM	Full width at half maximum
NIR	Near-infrared
NA	Numerical aperture
OAM	Orbital angular momentum
PBP	Pancharatnam-Berry phase
RMS	Root mean square
SEM	Scanning electron microscopy
SLM	Spatial light modulator
SRR	Split ring resonator
SOP	State of polarization
TEM	Transverse Electromagnetic (mode)
USP	Ultra short pulse
UVFS	Ultraviolet grade fused silica

CONTENTS

1. INTRODUCTION

Since the invention of pulsed laser sources, the application of non-contact precise micromachining has become a substantial part of the ever-growing photonics industry and scientific research field. Lasers have emerged as indispensable tools, transforming the landscape of various industries with their precision and versatility. As the lasers are continuously under development, having higher average power and repetition rates, the need for optimizing their performance and energy delivery to the material has become increasingly evident. In some cases, having a standard Gaussian beam has become a bottleneck for various micromachining tasks: cutting, drilling, as well as more complex structuring of various materials on the surface or in the bulk. The bell-shaped spatial intensity distribution of such beam has a negative impact on various materials due to increased heat affected zone (HAZ) which is even more problematic for fluences much higher than the material's optical damage threshold [1]. The Rayleigh length is another limiting factor, especially in transparent material processing where longer focal zones are desired. One of the key advantages that beam shaping brings to micromachining is the more efficient utilization of power deposition in the material. By customizing the laser beam profile to match the requirements of the task at hand, it becomes possible to concentrate energy precisely where it is needed, minimizing waste and maximizing the effectiveness of the laser [2]. This targeted energy deposition not only enhances the accuracy of material removal but also contributes to the overall cost-effectiveness of the process. General knowledge from light engineering can be applied not only in the enhancement of laser processing but also in imaging, microscopy, and other various fields of optics, not limited to the visible or infrared wavelength range [3].

This research focuses on the development of beam-shaping elements designed to modify laser light into a more complex field. The first and major part of the thesis is about the employment of geometric phase elements in application for high-power laser beam shaping to enhance specific material laser micromachining tasks: generation of complex field Bessel-type beams; employment of elongated focal line Bessel-like beams for rapid stealth dicing; and transforming the initial

Gaussian beam to a more complex intensity field in the transverse plane at the focal zone having additional unique polarization properties. In the second part of this thesis, beam shaping knowledge is applied in the terahertz spectral range, where experiments are conducted to find the optimal manufacturing process of diffractive and metasurface elements. The manufactured elements are later used to construct structured THz beams, which are tested in the imaging.

To fully elucidate the field of interest of the thesis, the work material is structured in such a way as first to cover the foundation knowledge in the field of interest needed to understand the subject of the dissertation. The **second chapter** of this work is dedicated to the theoretical background of light properties, essential for understanding laser optics and material micromachining. Topics such as light diffraction in free space, nonlinear high-intensity pulsed light interaction with material, and beam shaping importance are presented. The **third chapter** describes methods used to numerically simulate beam propagation, as well as ultrashort pulsed laser systems that were used in experimental verifications. The **fourth chapter** covers the results of the investigation on non-diffracting Bessel-type beams and their customized versions in applications for complex focal zone engineering and utilization in fast laser dicing of transparent materials. The **fifth chapter** is dedicated to the research of vector beam shaping, where the state of the polarization plays an important role in structuring the beam's intensity profile. A special case of flat-top intensity distribution (Super-Gaussian) beam generation is investigated. The final **sixth chapter** is devoted to exploring laser manufacturing of beam-shaping elements for the terahertz frequency range, showing possible uses of optical imaging utilizing diffractive and metaoptics made using ultrashort laser micromachining technology.

1.1. The aim of the dissertation

This thesis focuses on beam shaping of laser light, altering it to a more complex structured field. The aim of this dissertation is to be split into two parts.

Firstly, it was set to explore and investigate near-infrared laser beam shaping capabilities using the geometric phase elements, applying them for the enhancement of various material micromachining cases.

Secondly, the aim of the research was expanded by transferring the knowledge of beam shaping and material micromachining to produce structured terahertz radiation beams by manufacturing different shaping elements with potential application in imaging.

1.2. Dissertation tasks

To achieve the aim, several tasks were set:

1. To employ and develop numerical modeling of laser beam diffraction by using geometric phase optical elements. Conduct beam shaping simulations in free space utilizing diffraction paraxial approximation in combination with Jones matrix formalism.

2. To investigate the Bessel beam shaping technique for creating new and unique invariant beams utilizing spatial phase mask displacement – a division into halves with controllable spatial shifts. Characterize obtained beam intensity patterns numerically and experimentally employing a spatial light modulator and high-power ultrashort laser systems. Inspect induced material modifications on the surface and in the bulk of transparent material made by the created Bessel-type beams.

3. To create elliptic Bessel beam using modified axicon phase-split mask of two opposite zones in pair. Numerically investigate and find optimal parameters of the phase splitting defined by opening angle and phase difference between the zones. Experimentally test manufactured geometric phase element having selected parameters set for inducing controlled micro-cracks in transparent material.

4. To investigate the superposition of orthogonal polarization state beams utilizing customized spatially variable waveplate made as geometric phase element. Numerically explore intensity and polarization state distributions in the focal zone of the beams. Conduct experimental beam inspection, create and investigate modifications in bulk of transparent material and on the surface of semiconductor and thin metallic film.

5. To explore manufacturing of terahertz beam shaping elements based on the ultrashort laser ablation technique using laser system of $\lambda = 1030$ nm wavelength. Find optimal laser processing parameters for creating diffractive optical elements from silicon and distributed C-shaped metasurfaces from thin stainless-steel foil.

1.3. Scientific novelty and relevance

1. A novel design of geometric phase elements having spatially transposed axicon phase patterns was proposed to generate new custom Bessel-like beams. These types of modifications led to superposition of many multi-order Bessel beams with different amplitude coefficients, resulting in multi-peak, ring-shaped, or elongated central peak intensity distributions. The latter case was successfully applied in the directional fracturing of thin glass.

2. It was demonstrated that the optimization of the axicon phase pattern by dividing it into two relatively shifted pairs leads to a case when an elliptical central peak of a Bessel-like beam can be created. This optimized phase distribution realized in geometric phase elements was used to replace conventional glass axicons in high-power rapid glass dicing applications.

3. For the first time, the concept of spatially variable waveplates with a hollow center was demonstrated. Utilization of such elements in the laser microfabrication system led to a generation of flattop beams in the focal zone of an optical system at the highest intensity plane by using standard focusing lenses. Variation of beam intensity cross-section is achieved by changing input beam size without needing to replace beam shaping elements: from Gaussian-like to ring-shaped patterns can be created.

4. It was experimentally demonstrated that the use of hollow center space variant waveplates enables the creation of vector flat-top beams of hyper-lemon polarization singularities, having topological charges of $I_c = \frac{1}{2} * N$, where N is the winding (slow axis modulation) number. This novel implementation employing geometric phase elements is suitable for high-power applications under

various numerical aperture focusing conditions.

5. It was demonstrated that the near-infrared beam shaping technique can be transferred to a different electromagnetic wave spectrum of terahertz irradiance. The conducted micromachining experiments of silicon reveal possible manufacturing of diffractive elements suitable for up to 6 THz frequency. The production of flexible beam shaping elements over the large aperture (> 50 mm) made from stainless steel foil was employed to create metasurface-based zone plates, with potential application frequency ranging from as low as 90 GHz to 2.5 THz. The demonstrated production of complex beam shaping elements paves the way for creating more compact imaging systems.

1.4. Statements to be defended

1. The induced asymmetry in axicon phase masks can generate an elliptical Bessel-beam central core to produce directional material cracking, which is important in stealth dicing applications. The investigated spatial shifting of axicon halves produces ellipticity of the central core of 1.05 when spatial shift is equal to 0.25 phase period, sufficient for directional cracking in the bulk of a glass.

2. The parametric study of azimuthal phase modulation produces a range of values suitable to achieve directional material cracking. The splitting angle of $\gamma = 17°$ and the phase difference of $\Delta\varphi = 5\pi/4$, a Bessel-type beam with the ellipticity of 1.19 can be created which can be efficiently used in stealth cracking applications.

3. The hollow center spatially variable waveplates can be utilized to efficiently create vector flat-top beams having hyper-lemon polarization singularities with topological charges of $I_c = \frac{1}{2} * N$, where N is the modulation number of the slow axis.

4. By adjusting the beam diameter and hollow center of S-waveplate ratio, the beam intensity distribution at the lens focus can be continuously changed from Gaussian to flat-top or ring-shaped. A small ratio results in minimal beam alteration, creating a bell-shaped intensity distribution at the focal point. The increase of

this ratio flattens the intensity peak, and further increases will lead to the ring intensity distribution. The specific ratio 1.45 for the ideal geometric phase element of order $N = 2$ can generate a flat-top beam with <5% peak-to-valley intensity variation. The proposed optical scheme utilized a single geometric phase element to achieve a continuous change of intensity distribution.

5. Ultrashort pulse laser ablation using a $\lambda = 1030$ nm wavelength and galvanometer scanner can be used for precise and rapid fabrication of terahertz diffractive elements from silicon and optical elements based on metaelements from stainless steel foil. The applicable frequencies are up to 2.5 THz for metaelements and up to 6 THz for silicon-based elements, with the achievable ablated surface quality of $\approx \lambda/40$.

1.5. Approbation

The main results were published in 7 scientific peer-reviewed papers [A1–A7] and 12 conference proceedings [B1–B12]. Other 3 publications that were not directly related to the dissertation [C1–C3]. Results were presented by the author at 12 international and national conferences [D1–D12]. Conference presentations by the co-authors are excluded.

Scientific peer-reviewed papers on the dissertation topic

[A1] **E. Nacius**, L. Tauraitė, O. Ulčinas, S. Orlov, V. Jukna, Asymmetric phase-split axicon masks for an improved Bessel beam-based glass stealth dicing, Optics & Laser Technology, **118**, 112008 (2025). DOI: 10.1016/j.optlastec.2024.112008

[A2] **E. Nacius**, O. Ulčinas, S. Orlov, V. Jukna, Polarization singularities for shaping of vector flat-top beams in utilization for high-power laser micromachining of various materials, Optics & Laser Technology, **177**, 111133 (2024). DOI: 10.1016/j.optlastec.2024.111133

[A3] S. Orlov, R. Ivaškevičiūtė-Povilauskienė, K. Mundrys, P. Kizevičius, **E. Nacius**, D. Jokubauskis, K. Ikamas, A. Lisauskas, L. Minkevičius, G. Valušis, Light engineering and silicon diffractive optics assisted nonparaxial terahertz imaging, Laser & Photonics Reviews **18**(5) (2024). DOI: 10.1002/lpor.202301197

[A4] R. Ivaškevičiūtė-Povilauskienė, V. Čižas, **E. Nacius**, I. Grigelionis, K. Redeckas, M. Bernatonis, S. Orlov, G. Valušis, L. Minkevičius, Flexible terahertz optics: light beam profile engineering via C-shaped metallic metasurface, Frontiers in Physics, **11**, 1196726, 1–9 (2023). DOI: 10.3389/fphy.2023.1196726

[A5] R. Ivaškevičiūtė-Povilauskienė, P. Kizevičius, **E. Nacius**, D. Jokubauskis, K. Ikamas, A. Lisauskas, N. Alexeeva, I. Matulaitienė, V. Jukna, S. Orlovas, L. Minkevičius, G. Valušis, Terahertz structured light: nonparaxial Airy imaging using silicon diffractive optics, Light: Science & applications, **11**(326), 1–13 (2022). DOI: 10.1038/s41377-022-01007-z

[A6] P. Šlevas, S. Orlov, **E. Nacius**, O. Ulčinas, Azimuthally modulated axicon vortical beams for laser microprocessing, Optics communications, **505**, 127509, 1–7 (2022). DOI: 10.1016/j.optcom.2021.127509

[A7] **E. Nacius**, P. Gotovski, O. Ulčinas, S. Orlov, A. Urbas, V. Jukna, Spatially displaced and superposed Bessel beams for transparent material laser microprocessing, Journal of the Optical Society of America B, **38**(12), 127509, 3886–3895 (2021). DOI: 10.1364/JOSAB.435706

Conference proceedings

[B1] R. Ivaškevičiūtė-Povilauskienė, V. Čižas, **E. Nacius**, I. Grigelionis, K. Redeckas, K. Stanaitis, S. Orlov, G. Valušis, L. Minkevičius, Terahertz imaging using C-shaped metallic metasurface-based optics, Terahertz Photonics III, 129940G, Proc. SPIE 12994, (2024). DOI: 10.1117/12.3016992

[B2] R. Ivaškevičiūtė-Povilauskienė, V. Čižas, **E. Nacius**, I. Grigelionis, K. Redeckas, M. Bernatonis, S. Orlov, G. Valušis, L. Minkevičius, Flexible C-shaped metallic metasurface based optics for terahertz beam shaping, 48th International conference on infrared, millimeter and terahertz waves (IRMMW-THz), IEEE, (2023). DOI: 10.1109/IRMMW-THz57677.2023.10299193

[B3] R. Ivaškevičiūtė-Povilauskienė, P. Kizevičius, **E. Nacius**, D. Jokubauskis, K. Ikamas, A. Lisauskas, I. Matulaitienė, K. Mundrys, S. Orlov, L. Minkevičius, G. Valušis, Nonparaxial imaging using terahertz structured light 48th International conference on infrared, millimeter and terahertz waves (IRMMW-THz), IEEE (2023). DOI: 10.1109/IRMMW-THz57677.2023.10299005

[B4] V. Jukna, **E. Nacius**, O. Ulčinas, S. Orlov, Beam shaping of high-energy beams for laser micromachining of transparent materials, Proceedings of SPIE. Frontiers in ultrafast optics: biomedical, scientific, and industrial applications XXIII, **PC12411**, 1–2 (2023). DOI: 10.1117/12.2657417

[B5] **E. Nacius**, O. Ulčinas, S. Orlov, V. Jukna, Focal zone engineering with hollow spatially variable waveplates applicable in laser micromachining, Procedia CIRP: 12th CIRP conference on photonic technologies (LANE 2022), **111**, 609–612, (2022). DOI: 10.1016/j.procir.2022.08.161

[B6] **E. Nacius**, O. Ulčinas, S. Orlov, V. Jukna, Focal beam zone engineering for enhanced transparent material laser micro-welding process, Proceedings of SPIE. Laser-based Micro- and Nanoprocessing XVI, **11989**(1198904), 1–6, (2022). DOI: 10.1117/12.2610170.6295509205001

[B7] **E. Nacius**, P. Gotovski, B. Stanionis, O. Ulčinas, S. Orlov, V. Jukna, Thin glass processing using Bessel-type beams generated with spatially phase-shifted axicons, Proceedings of SPIE, Laser-based Micro- and Nanoprocessing XV, **11674**(116741K), 1–11, (2021). DOI: 10.1117/12.2577295

[B8] **E. Nacius**, B. Stanionis, P. Gotovski, O. Ulčinas, S. Orlov, V. Jukna, Micro-processing of transparent material by modified Bessel beams generated with spatially displaced axicons, 2021 Conference on Lasers and Electro-Optics Europe and European Quantum Electronics Conference, IEEE, (2021). DOI: 10.1109/CLEO/Europe-EQEC52157.2021.9541712

[B9] P. Gotovski, P. Šlevas, **E. Nacius**, V. Jukna, S. Orlov, J. Baltrukonis, O. Ulčinas, T. Gertus, Formation of optical needles by Pancharatnam-Berry phase element for laser-induced modifications in transparent materials, Proceedings of SPIE, Laser-based Micro- and Nanoprocessing XIV, **11268**(112681Y), 1–9, (2020). DOI: 10.1117/12.2544925

[B10] P. Gotovski, P. Šlevas, **E. Nacius**, V. Jukna, S. Orlov, O. Ulčinas, J. Baltrukonis, T. Gertus, Design of efficient Gauss to top-hat converters using geometrical phase elements inscribed in the glass by femtosecond laser pulses, Proceedings of SPIE, **11266**(112661J), 1–10, (2020). DOI: 10.1117/12.2546620

[B11] **E. Nacius**, P. Gotovski, V. Jukna, O. Ulčinas, T. Gertus, S. Orlov, Generation of Bessel type beams via phase shifted axicons encoded in geometrical phase elements, Proceedings of SPIE, **11266**(112660Z), 1–8, (2020). DOI: 10.1117/12.2546561

[B12] P. Šlevas, S. Orlov, **E. Nacius**, O. Ulčinas, P. Gotovski, J. Baltrukonis, V. Jukna, Laser induced modifications in transparent materials using azimuthally modulated axicon beams, Proceedings of SPIE, **11267**(12670B), 1–7, (2020). DOI: 10.1117/12.2546580

Publications were not directly related to the thesis

[C1] M. Vainoris, **E. Nacius**, P. Šlevas, V. Sabonis, The future of dicing is here: High-precision processing of transparent materials for various applications, Photonics Views, **20**(4), 42–45, (2023). DOI: 10.1002/phvs.v20.4

[C2] S. Orlov, A. Juršėnas, **E. Nacius**, Optical Bessel-like beams with engineered axial phase and intensity distribution, Journal of laser micro/nanoengineering, **13**(3), 244–248, (2018). DOI: 10.2961/jlmn.2018.03.0017

[C3] S. Orlov, A. Juršėnas, **E. Nacius**, J. Baltrukonis, Controllable spatial array of optical needles with independent axial intensity distributions for laser microprocessing, Procedia CIRP, 10th CIRP Conference on Photonic Technologies (LANE 2018), **74**, 589–593, (2018). DOI: 10.1016/j.procir.2018.08.081

[D1] **E. Nacius**, O. Ulčinas, S. Orlovas, V. Jukna, Vektorinių kontroliuojamo intensyvumo skirstinio pluoštų pritaikymas lazeriniam įvairių medžiagų mikroapdirbimui, Fiztech 2023, Vilnius, Lithuania, October 18–19, (2023) (oral).

[D2] **E. Nacius**, O. Ulčinas, J. Minkevičius, S. Orlov, V. Jukna, Adjustable focal zone beam shaping by using custom spatially variable waveplates aimed for laser micromachining, CLEO Europe 2023, Munchen, Germany, June 25–30 (2023) (oral).

[D3] **E. Nacius**, O. Ulčinas, S. Orlovas, V. Jukna, Lazerio pluošto židinio zonos kontrolė panaudojant tuščiavidurius S-bangininių plokštelių pagrindu įrašytus elementus“, FizTech2022, Vilnius, Lithuania, October 19–20 (2022) (oral).

[D4] **E. Nacius**, O. Ulčinas, S. Orlov, V. Jukna, Focal zone engineering with hollow spatially variable waveplates applicable in laser micromachining, LANE 2022, Furth, Germany, September 4–9 (2022) (oral).

[D5] **E. Nacius**, O. Ulčinas, S. Orlov, V. Jukna, Focal beam zone engineering for enhanced transparent material laser micro-welding process, SPIE Photonics West 2022, San Francisco, USA, January 22–27 (2022) (oral).

[D6] **E. Nacius**, P. Gotovski, O. Ulčinas, S. Orlovas, V. Jukna, Erdviškai praslinktu aksikonu generuojamų asimetrinių Beselio pluoštų panaudojimas skaidrių terpų mikroapdirbime, 44-oji Lietuvos Nacionalinė Fizikos Konferencija, October 6–8, Vilnius, Lithuania (2021) (poster).

[D7] **E. Nacius**, P. Gotovski, B. Stanionis, O. Ulčinas, S. Orlov, V. Jukna, Micro-processing of transparent material by modied Bessel beams generated with spatially displaced axicons, CLEO Europe 2021, virtual conference, June 21–25 (2021) (oral).

[D8] **E. Nacius**, P. Gotovski, B. Stanionis, O. Ulčinas, S. Orlov, V. Jukna, Transparent material laser processing with modified

Bessel beams generated by relocated phase axicons, Laser Precision Microfabrication (LPM) 2021, virtual conference, June 8–11 (2021) (oral).

[D9] **E. Nacius**, P. Gotovski, B. Stanionis, P. Ševas, O. Ulčinas, S. Orlov, V. Jukna, Laser microprocessing of thin transparent material with beams generated by spatially displaced axicon halves realized by geometric phase optical elements, E-MRS Spring Meeting 2021, virtual conference, May 31–June 3 (2021) (oral).

[D10] **E. Nacius**, P. Gotovski, B. Stanionis, O. Ulčinas, S. Orlov, V. Jukna, Laser micro-machining of transparent material with Bessel beams generated by spatially displaced axicons, Open Readings 2021, virtual conference, March 16–19 (2021) (poster).

[D11] **E. Nacius**, P. Gotovski, B. Stanionis, O. Ulčinas, S. Orlov, V. Jukna, Thin glass processing using Bessel-type beams generated with spatially phase-shifted axicons, SPIE Photonics West 2021, virtual conference, March 6–11 (2021) (oral).

[D12] **E. Nacius**, P. Gotovski, V. Jukna, S. Orlov, T. Gertus, O. Ulčinas, Generation of Bessel-type beams via phase shifted axicons encoded in geometrical phase elements, SPIE Photonics West 2020, San Francisco, USA, February 1-6 (2020) (oral).

1.6. Contribution of the author

The author conducted experimental studies on designing and assembling laser workstations used for laser beam shaping measurements, inspection, and conducted various materials micro-processing. The author has also executed some of the simulations on beam shaping and propagation and developed the numerical model program. Obtained results of experimental work and numerical modeling, analyzed, compared, and processed to be presented in final form.

In [**A1**], the author performed numerical simulations of beam propagation, established initial GPE design, helped to assemble experimental setup, processed experimental data, wrote most of the text, L. Tauraitė investigated modeling of GPE, conducted primary numerical simulations and carried out experimental work, wrote parts of the text, O. Ulčinas fabricated GPE, S. Orlov wrote theoretical analysis of beam transformation and derivations of equations, V. Jukna supervised the whole work and edited the text.

In [**A2**], the author came up with the principal idea of the work, performed numerical simulations of beam propagation, assembled experimental setup, processed experimental data, wrote most of the text, O. Ulčinas provided GPE fabrication algorithm and manufactured some of the GPEs, S. Orlov wrote theoretical analysis and derivations of equations, envisioned polarization singularities phenomenon, V. Jukna helped with numerical modeling, supervised the whole work and edited the text.

In [**A3**], [**A4**] and [**A5**], the author was responsible for setting up the laser workstation to manufacture optical elements suitable for applications in the terahertz frequency range, found optimal micro processing parameters for different materials, conducted production of various types of optical elements, wrote parts in texts about manufacturing processes. R. Ivaškevičiūtė-Povilauskienė and the rest of the team were responsible for the design, imaging, analysis, and writing parts of the papers.

In [**A6**], the author designed a GPE with 6 phase zones and conducted a laser light-material interaction experiment, P. Šlevas designed a GPE with 180 phase zones, made the samples and beam measurements, analyzed the data, and wrote most of the text, O. Ulčinas fabricated GPEs. S. Orlov wrote the theoretical background, supervised the work, and edited the text.

In [**A7**], author came up with principal idea of the work, performed numerical simulations of beam propagation, assembled experimental setup, processed experimental data, wrote most of the text, P. Gotovski developed beam propagation code, O. Ulčinas fabricated GPEs, S. Orlov wrote theoretical analysis and derivations of equations, A. Urbas consulted about beam shaping specifics, V. Jukna supervised the whole work and edited the text.

The other colleagues worth mentioning are A. Juršėnas and A. Gajauskaitė for helping with numerical simulation code development and consulting. J. Berškys helped with Stokes parameters analysis. K. Mundrys and P. Kizevičius provided with the help of analyzing and comparing fabricated THz elements to numerical modeling. The author supervised Bachelor student B. Stanionis, who assisted in setting up a laser workstation and obtaining some of the numerical and experimental results for Bessel-type beam applications in glass micromachining.

2. **THEORETICAL BACKGROUND**

2.1. Light propagation in transparent media

The understanding of light's properties has been under exploration since the early days of our era. Greek philosophers attempted to explain the physical properties of light, and later the science of optics was revived during the Renaissance period, when more scientists began to study light and derive mathematical models. One of the first advances was the formulation of Snell's law, which establishes a relationship between the angles of incidence and refraction [4]:

$$n_1 \sin(\alpha) = n_2 \sin(\beta), \tag{2.1}$$

where n_1 is the refractive index of the first medium, n_2 is the refractive index of the second medium, α is the angle of incident light ray, β is the angle of refraction. This law can be used to explain why light bends when it passes from one medium to another with different refractive indexes, and it is a fundamental law of optics and has many applications in the real world. For example, it is used in the design of lenses and mirrors, which are used in a wide variety of devices, such as telescopes, microscopes, and other more complex optical imaging systems.

The understanding of light as a wave began with C. Huygens' formulation of the wave propagation principle. This concept was further solidified by T. Young's double-slit experiment. Through the contributions of physicists like A.J. Fresnel, J. Fraunhofer, and others, mathematical expressions were developed. These expressions allowed for the precise prediction of light behavior, including how a beam would diffract after traveling a certain distance, interact with an opaque obstacle, or produce an interference pattern on a screen. The wave theory, along with later work by J.C. Maxwell, laid the foundation for the electromagnetic theory of light. This theory established light as an electromagnetic wave comprised of electric and magnetic fields oscillating perpendicular to each other and the direction of propagation [5].

The advent of quantum mechanics in the early 20-th century further expanded the understanding of light propagation. Quantum optics, pioneered by M. Planck and A. Einstein, provided insights into the particle-like nature of light, known as photons. Despite this wave-particle duality, the wave theory remains a crucial tool for explaining light behavior in transparent media at macroscopic scales. Quantum optics, on the other hand, addresses light interactions at the microscopic level. Together, these theories provide a comprehensive framework for understanding light.

Contemporary research has seen a significant expansion in the exploration of light propagation in transparent media. This has been driven by the development of coherent light sources, advanced materials, and new technologies. The invention of the laser, for instance, opened the field of photonics, leading to numerous novel applications of light manipulation and its interactions with materials.

2.1.1. Diffraction of scalar light

Spherical Waves

Light propagation can be analyzed as a spherical wave phenomenon. Huygens' principle states that any source can be considered to be made up of many point sources [6]. Each of these sources oscillates in the field according to the formula $\exp(-\mathrm{j}\omega t)$, where t is time and ω is the oscillation frequency. It takes time v/r for a wave to travel a distance r, from the source at speed v, creating a new wavefront with the same phase value as the original source at time v/t. This spherical field can be described as [5]:

$$E(t,r) = E(r)\exp[-\mathrm{j}\omega(t - r/v)] = E(r)\exp(-\mathrm{j}\omega t + \mathrm{j}kr) \tag{2.2}$$

where $k = \omega/v = 2\pi/\lambda$ is wave number, λ is wavelength - distance between two wave fronts (see Figure 2.1). In the spherical wave expression, energy from the light source radiates equally in all directions with a radius of r. The expression for a spherical wave is [5]:

$$E(t,r) = \frac{E(r)}{r}\exp[-\mathrm{j}(\omega t - kr)] \tag{2.3}$$

If the observation plane P is sufficiently far away from the source S, the spherical expression can be approximated using the Cartesian coordinate system in xyz space (depicted in Figure 2.2), expressing the

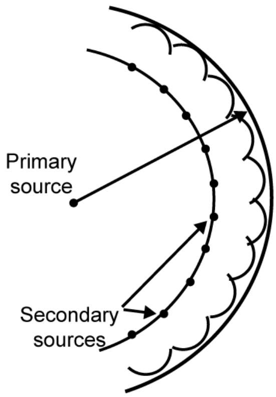

Figure 2.1: Principle sketch explaining nature of spherical wavefront from a primary source, emerging as the new fronts formed from secondary sources. Author's image.

distance as:

$$r = \sqrt{z_i^2 + (x_i - x_0)^2 + (y_i - y_0)^2} = z_i\sqrt{1 + \frac{(x_i - x_0)^2 + (y_i - y_0)^2}{z_i^2}} \tag{2.4}$$

With this expression, a spherical wave can be simplified to a plane wave when the distances z_i are relatively large and the angle $\theta = \sqrt{[(x_i - x_0)^2 + (y_i - y_0)^2]/z_i^2}$ is small.

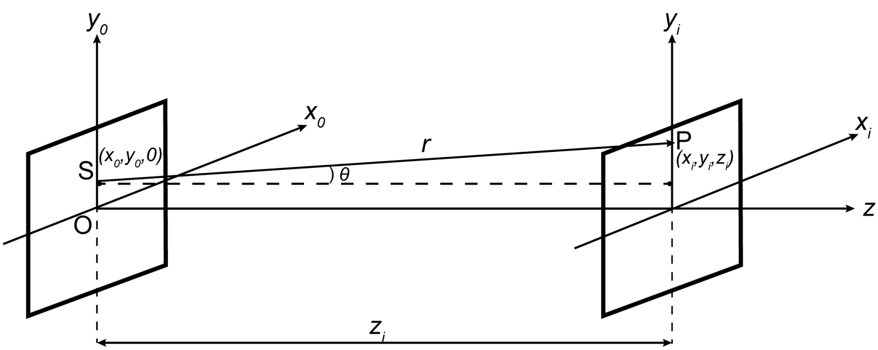

Figure 2.2: Cartesian space used to find light propagation from source plane S to observation point P on screen at distance r and small angle θ. Author's image.

When solving light propagation problems, complex expression calculations can be simplified and accelerated in numerical modeling by applying the paraxial approximation [7]. This approximation assumes that light propagates at small angles ($\sin\theta \approx \theta$). In practice, this is useful for numerically solving propagation problems, as it simplifies the mathematical calculations. However, if the angle θ is sufficiently large, the paraxial approximation can distort the results and deviate from the real ones. Therefore, when modeling and analyzing light propagation, it is necessary to evaluate whether it is possible to use the approximation.

Fourier optics

The problem of light propagation can be solved using mathematical expressions of Fourier transformation [8]. Here, we can define the concept of "spatial frequency", which means the decomposition of a set of plane waves in space (as depicted in Fig. 2.3). This concept is analogous to the "temporal frequency" concept used in the analysis of temporal signals, where the wave oscillations are important with respect to time. The concept of spatial frequencies is used in the field of Fourier optics, where light beams emitted from a source are analyzed using mathematical expressions [9]. Spatial frequencies are expressed inversely proportional to the distances between the same phase planes of waves - wavelengths, in x and y coordinates as:

$$f_x = \frac{1}{\lambda_x}, \\ f_y = \frac{1}{\lambda_y}. \tag{2.5}$$

The distance OH would be linked by the sum of the components of both expressions:

$$\lambda = \lambda_x \cos\angle HOA, \\ \lambda = \lambda_y \sin\angle HOA. \tag{2.6}$$

Then the full spatial frequency is described as:

$$f = \frac{1}{\lambda} = \sqrt{\frac{1}{\lambda_x^2} + \frac{1}{\lambda_y^2}} = \sqrt{f_x^2 + f_y^2}. \tag{2.7}$$

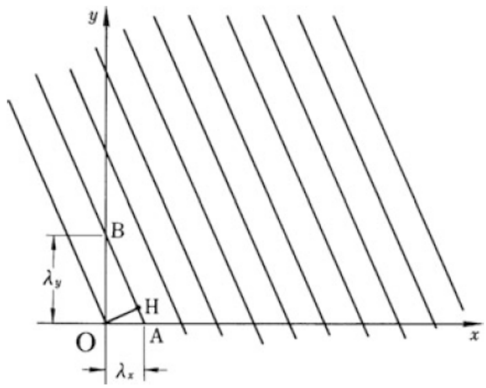

Figure 2.3: Principle sketch defining spatial frequencies λ_x and λ_y. Adapted from Ref. [5].

These spatial frequencies are important for further expressing the relationship between the light emitted by the source and the image observed on the screen. One can imagine a one-dimensional light source (slit) of length a that emits light with amplitude $E(x_0)$ in the z-axis direction. Then, from the source origin $E(x_i, 0)$ to the point on the screen $E(x_i, y_i)$, the expression for the light rays would be [5]:

$$E(x_i, y_i) = -\frac{\mathrm{j}}{\lambda z_i} \exp\left[\mathrm{j}k\left(z_i + \frac{x_i^2 + y_i^2}{2z_i}\right)\right] \times \int_{-a/2}^{a/2} E(x_o) \exp\left(-\mathrm{j}2\pi \frac{x_i}{\lambda z_i} x_0\right) dx_o, \quad (2.8)$$

where K is a constant, considering that the slit is a certain number of point sources, and considering the condition $x_0^2/\lambda z_i << 1$ [5]. By performing mathematical analysis [8], this expression can be understood as a Fourier transform, which is defined as

$$G(f) = \mathcal{F}\{g(x_0)\} = \int_{-\infty}^{\infty} g(x_0) \exp(-\mathrm{j}2\pi f x_0) dx_0 \quad (2.9)$$

and by adding

$$f = \frac{x_i}{\lambda z_i},$$
$$g(x_0) = E(x_0) \quad (2.10)$$

to the Eq. (2.8) and Eq. (2.9) the final expression can take such form [5]:

$$E(x_i, y_i) = -\frac{\mathrm{j}}{\lambda z_i} \exp\left[\mathrm{j}k\left(z_i + \frac{x_i^2 + y_i^2}{2z_i}\right)\right] \mathcal{F}\{E(x_0)\}. \tag{2.11}$$

In summary, the light amplitude distribution on the screen is the result of the Fourier transform of the source. Fourier optics is often used in the analysis and design of optical systems because it links the spatial and spectral parts of light. Knowing one of these domains, it is possible to calculate the other through the Fourier transform relationship.

Another concept of optical systems analysis is the use of impulse response (point spread) function, which is often used to evaluate light propagation [8]. This function describes the final result of a light signal passing through the system. An ideal optical system can reproduce or transfer an image from a source to an observation plane without changing (distorting) properties of it. If an infinitely small source is imaged as an infinitely small point on the screen, the impulse response function will be an infinitely narrow function - a delta function $\delta(x, y)$. However, in reality, optical systems are not perfectly ideal. Therefore, by using impulse response calculations, it is possible to find the result of light propagating through an optical system [5, 10]:

$$u(x_i, y_i) = g(x_i, y_i) * h(x_i, y_i), \tag{2.12}$$

where $g(x_i, y_i)$ is the source function, $u(x_i, y_i)$ is the resulting image, and $h(x_i, y_i)$ is the impulse response function. Mathematically, this is the convolution of the source and impulse response functions [5].

The use of the convolution property in Fourier space simplifies the mathematical evaluation. The convolution in Fourier space is just the multiplication in that domain. The Fourier transform of the impulse response function $h(x_0, y_0)$ is called the transfer function $H(f_x, f_y)$. Thus, such analysis in the spatial frequency domain is described as [5]:

$$U(f_x, f_y) = G(f_x, f_y)H(f_x, f_y). \tag{2.13}$$

In general, when analyzing the propagation of light through optical systems, the following factors are also very important: the distance between the source and plane of interest, the step size in z direction, the mesh grid size of the transverse xy space, since numerical modeling of light propagation can more effectively find the desired result and avoid numerical artifacts [11].

Diffraction models and approximations

Diffraction models are used to calculate the full propagation of light beams, allowing us to determine the light distribution on a screen at a certain distance. One of the main analytical models that fully describes light diffraction is the Rayleigh-Sommerfeld solution [10, 11]. If a light source in the plane $U_1(x_0, y_0)$ at initial coordinates x_0 and y_0, then the image on the screen $U_2(x_i, y_i)$ is expressed by the following integral:

$$U_2(x_i, y_i) = \frac{z}{\mathrm{j}\lambda} \iint\limits_{\Sigma} U_1(x_0, y_0) \frac{\exp(\mathrm{j}kr_{12})}{r_{12}^2} dx_0 dy_0 \tag{2.14}$$

r_{12} is the position between a point from the source plane to the point in the observation plane, hence it can be expressed as:

$$r_{12} = \sqrt{z^2 + (x_i - x_0)^2 + (y_i - y_0)^2}. \tag{2.15}$$

The expression from Eq. (2.14) is a general description of the Huygens-Fresnel principle, mentioned at the beginning of this chapter. In the general case, it is an integral expression of superposition, and if the source and screen planes are parallel, this expression can be written as a convolution integral [10]:

$$U_2(x_i, y_i) = \iint U_1(x_0, y_0) h(x_i - x_0, y_i - y_0) dx_0 dy_0, \tag{2.16}$$

where the impulse response function is

$$h(x_i, y_i) = \frac{z}{\mathrm{j}\lambda} \frac{\exp(\mathrm{j}kr)}{r^2}, \tag{2.17}$$

here $r = \sqrt{z^2 + x^2 + y^2}$. Using the Fourier convolution property, equation (2.16) can be transformed into a transfer function:

$$H(f_x, f_y) = \exp\left(\mathrm{j}kz\sqrt{1 - (\lambda f_x)^2 - (\lambda f_y)^2}\right) \tag{2.18}$$

The Rayleigh-Sommerfeld diffraction solution is the most accurate analytical form, provided that the distance r is much larger than the wavelength of light. The square root term in Eq. (2.15) significantly complicates the search for analytical solutions and numerical simulations, making the calculation process longer. By introducing approximations, we can simplify this part and speed up the simulation without losing the necessary information. Using the binomial expansion and choosing only the first two terms and approximating $r_{12} \approx z$, we arrive at the Fresnel diffraction formula [11]:

$$\begin{aligned} U_2(x_i, y_i) = \frac{\exp(\mathrm{j}kz)}{\mathrm{j}\lambda z} \iint U_1(x_0, y_0) \\ \times \exp\left\{\frac{\mathrm{j}k}{2z}\left[(x_i - x_0)^2 + (y_i - y_0)^2\right]\right\} dx_0 dy_0. \end{aligned} \quad (2.19)$$

Then, the impulse response function is:

$$h(x_i, y_i) = \frac{\exp(\mathrm{j}kz)}{\mathrm{j}\lambda z} \exp\left[\frac{\mathrm{j}k}{2z}\left(x^2 + y^2\right)\right] \quad (2.20)$$

and the transfer function is:

$$H(f_x, f_y) = \exp(\mathrm{j}kz) \exp\left[\mathrm{j}\pi\lambda z(f_x^2 + f_y^2)\right]. \quad (2.21)$$

The Fresnel approximation has limitations when the area of interest is close to the source, as there is a distortion of the results due to the simplification of the square root, approximating the spherical wave to a parabolic one. Often, to assess whether this approximation can be used in modeling, the Fresnel number N_F is evaluated [11]:

$$N_F = \frac{A^2}{\lambda z}, \quad (2.22)$$

where A is the characteristic size of the aperture, λ is the wavelength of light, and z is the distance from the aperture to the observation point. Fresnel number is a dimensionless quantity that characterizes the transition between the near-field and far-field diffraction regimes. If the N_F number is close to or less than 1, then the condition is considered satisfied and the area under consideration is in the Fresnel zone. However, if this indicator is higher, the results will be inaccurate.

When considering far fields, the Fraunhofer diffraction approximation can be used, which is in principle a scaled version of the Fourier transform [11]:

$$U_2(x_i, y_i) = \frac{\exp(\mathrm{j}kz)}{\mathrm{j}\lambda z} \exp\left[\frac{\mathrm{j}k}{2z}(x^2 + y^2)\right] \\ \times \iint U_1(x_0, y_0) \exp\left[\frac{-\mathrm{j}2\pi}{\lambda z}(x_i x_0 + y_i y_0)\right] dx_0 dy_0. \quad (2.23)$$

The Fraunhofer diffraction expression is convenient for quickly solving image formation behind a lens since it is in principle a far-field result. The Fresnel number condition can also be applied here, according to which the most accurate results are obtained when $N_F << 1$. The considered diffraction calculation expressions can be schematically represented in Fig. 2.4.

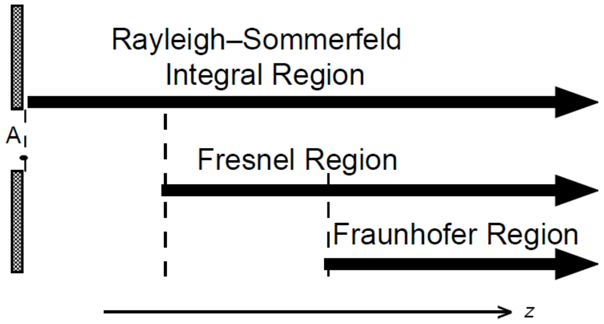

Figure 2.4: Principle sketch of the main three diffraction regions, depending on the distance z from the aperture A taken as a source. Adapted from Ref. [10].

2.1.2. Polarization properties

So far, light propagation has been considered as the propagation of a monochromatic scalar wave in an ideal isotropic medium, without taking into account the electric and magnetic vectors. However, these vectors are also very important in modeling and analyzing the properties of light. The full properties and propagation of light as an electromagnetic wave are described by Maxwell's equations [12]. In general, if the medium under consideration does not have magnetic properties and is homogeneous, only the electric field vector, $\mathbf{E}(x, y, z)$, is included in the description of the propagation of polarized (vector) light, the state of which is additionally included in the wave equation from the expression in Eq. (2.2) (the z component can also be neglected for simplicity since it becomes important only when considering light propagating at large angles [10, 13]):

$$\mathbf{E} = (E_x\mathbf{e_x} + E_y\mathbf{e_y})\exp[\mathrm{j}(kz + \omega t)] \tag{2.24}$$

here $\mathbf{e_x}, \mathbf{e_y}$ are arbitrary vectors on x and y axes. E_x and E_y field components are then expressed relative to each other as [13]

$$\begin{aligned} E_x &= E_{x0}, \\ E_y &= E_{y0}\exp(\mathrm{j}\phi), \end{aligned} \tag{2.25}$$

where E_{x0} and E_{y0} are amplitudes of electric fields in x and y axes, and ϕ is phase difference, determining the state of polarization (SOP).

Linear polarization is when the phase difference between the vectors are $\phi = 0$ or $\phi = \pi$ [13]:

$$\mathbf{E} = (E_{x0}\mathbf{e_x} \pm E_{y0}\mathbf{e_x})\cos(kz + wt) \tag{2.26}$$

Circular polarization will be when $\phi = \pm\pi/2$ and $E_0 = E_{x0} = E_{y0}$. If the difference ϕ is negative, then circular polarization is defined as the direction of rotation clockwise, if the difference is positive - counterclockwise. The state of elliptical polarization will be intermediate between linear and circular and will have a ϕ difference not equal to 0, $\pm\pi/2$ or $\pm\pi$.

$$\mathbf{E} = E_0\cos(kz + wt)\mathbf{e_x} \pm E_0\sin(kz + wt)\mathbf{e_y} \tag{2.27}$$

All the main SOPs can be visualized in three-dimensional space, as depicted in Fig. 2.5 [13]. A more complete description of polarized light is possible through Mueller matrices [14], which also cover the states of partially or depolarized light, but is not relevant in this work, as only the fully polarized coherent laser light is considered.

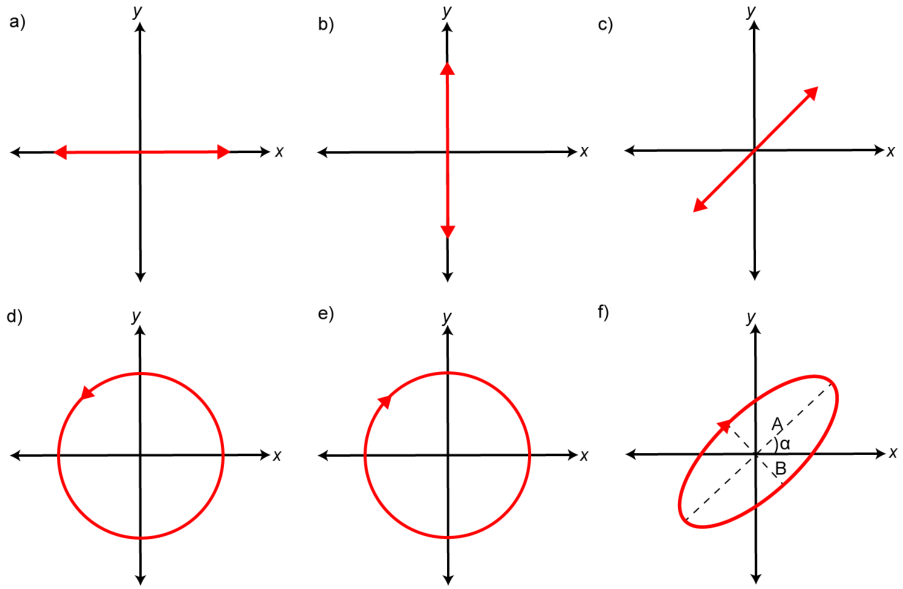

Figure 2.5: Representation of polarization states a) linear horizontal, b) linear vertical, c) linear at 45°angle, d) circular left, e) circular right, f) elliptical right with major axis A and minor axis B, with inclination angle α. Author's image.

Jones vectors

When modeling the propagation of polarized coherent light, it is sufficient to define and consider only the basic states of polarized light, which can be conveniently expressed in terms of Jones matrices [14,15]. The full polarized electric field vector is described as:

$$\mathbf{E} = \begin{pmatrix} E_x \\ E_y \end{pmatrix} = \begin{pmatrix} E_{x0} \exp(-\mathrm{j}\phi_x) \\ E_{y0} \exp(-\mathrm{j}\phi_y) \end{pmatrix} \tag{2.28}$$

here E_{x0}, E_{y0} are amplitudes, $\phi_{x,y}$ - phases with difference $\phi = \phi_y - \phi_x$. The general form of linear polarization to x axis will be

$$\mathbf{E_x} = \begin{pmatrix} 1 \\ 0 \end{pmatrix} \tag{2.29}$$

and to y axis:

$$\mathbf{E_y} = \begin{pmatrix} 0 \\ 1 \end{pmatrix}. \tag{2.30}$$

Linear polarization with an angle of 45° to x axis:

$$\mathbf{E_{xy}} = \frac{1}{\sqrt{2}} \begin{pmatrix} 1 \\ 1 \end{pmatrix}. \tag{2.31}$$

The right circular and left circular SOPs are expressed as

$$\mathbf{E_{RC}} = \frac{1}{\sqrt{2}} \begin{pmatrix} 1 \\ -\mathrm{j} \end{pmatrix},$$

$$\mathbf{E_{LC}} = \frac{1}{\sqrt{2}} \begin{pmatrix} 1 \\ \mathrm{j} \end{pmatrix}. \tag{2.32}$$

The general vector for the elliptical polarization state, for intermediate states between linear and circular polarization, when $\phi \neq n\pi$ and $\phi \neq (n + 1/2)\pi$, is described as [14]:

$$\mathbf{E} = \begin{pmatrix} E_{x0} \\ E_{y0} \exp(\mathrm{j}\phi) \end{pmatrix} \tag{2.33}$$

The inclination angle α is [see Fig. 2.5(e)-(f)]:

$$\alpha = \frac{1}{2} \tan^{-1} \left(\frac{2E_{x0}E_{y0}\cos\phi}{E_{x0}^2 - E_{y0}^2} \right). \tag{2.34}$$

These basic expressions are convenient for numerical modeling of the propagation of vector laser beams due to their simplified description of polarization states and are further useful for evaluating how the polarization can change after the beam passes through an optical element that can alter it.

Polarization transformations

Polarized light can change its SOP when passing through an anisotropic media [13]. If a transparent medium has birefringence properties, the light beam passing through it acquires a phase delay between the electric field components, which will change the polarization state. For example, a vertically linearly polarized beam can become an elliptically or horizontally linearly polarized beam. An element that can change the polarization state of light passing through it is called a phase (retardation) plate. Such an element is in principle a lossless birefringent crystal, the optic axis z of which is in the plane of the plate (see Fig. 2.6). The ordinary and extraordinary waves that make up the light propagate differently through the element, since the refractive indices n_o and n_e differ depending on the reference to the optical axis.

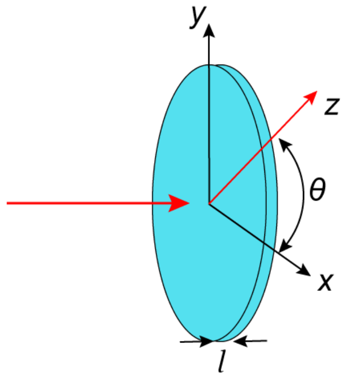

Figure 2.6: Representation of a phase plate of thickness l with the optic axis z at an angle θ to the horizontal direction. Author's image.

Then, in general, any polarization-changing element can be described as a rotation matrix $\mathbf{M}$ and the Jones vectors can be used to find the polarization state after it [14, 15]:

$$\mathbf{E_{out}} = \mathbf{M}\mathbf{E_{in}} \tag{2.35}$$

where $\mathbf{E_{in}}$ and $\mathbf{E_{out}}$ are the expressions of the incident electric field and the field after the element. The parameters describing the element $\mathbf{M}$ are the angle of the slow axis (the angle of the optical axis with respect to the incident wave) θ and the delay (retardance) φ. Then the general expression for the element is [13, 14]:

$$\mathbf{M}(\theta, \varphi) = \begin{pmatrix} \mathrm{e}^{\mathrm{j}\varphi} \cos^2\theta + \sin^2\theta & (\mathrm{e}^{\mathrm{j}\varphi} - 1) \sin\theta + \cos\theta \\ (\mathrm{e}^{\mathrm{j}\varphi} - 1) \sin\theta + \cos\theta & \mathrm{e}^{\mathrm{j}\varphi} \sin^2\theta + \cos^2\theta \end{pmatrix} \tag{2.36}$$

Usually, some of the most commonly used element examples are the half-wave and quarter-wave plates. When the retardance between the ordinary and extraordinary waves is $\varphi = \pi$ ($\varphi = \lambda/2$), and the rotation angle is θ, we will have the Jones matrix of the half-wave plate [14]:

$$\mathbf{M_{HWP}} = \mathrm{j} \begin{pmatrix} \cos(2\theta) & \sin(2\theta) \\ \sin(2\theta) & -\cos(2\theta) \end{pmatrix} \tag{2.37}$$

Using this element, the polarization of the transmitted light will remain linear, but its angle with the x axis will rotate by 2θ. The quarter-wave plate has a wave retardation of $\varphi = \pi/2$ ($\varphi = \lambda/4$) and its general expression will be [14]:

$$\mathbf{M_{QWP}} = \frac{1}{\sqrt{2}} \begin{pmatrix} 1 + \mathrm{j}\cos(2\theta) & \mathrm{j}\sin(2\theta) \\ \mathrm{j}\sin(2\theta) & 1 - \mathrm{j}\cos(2\theta) \end{pmatrix} \tag{2.38}$$

Such a plate would convert linear polarization to circular polarization and vice versa.

Stokes parameters

In practice, it is impossible to directly measure the polarization state when the electric field components oscillate in time. However, there is a way to evaluate and analyze the state of a polarized field using Stokes vector $\mathbf{S}$ [13]:

$$\mathbf{S} = \begin{pmatrix} S_0 \\ S_1 \\ S_2 \\ S_3 \end{pmatrix} \tag{2.39}$$

here the Stokes parameters are:

$$\begin{aligned} S_0 &= |E_x|^2 + |E_y|^2 \\ S_1 &= |E_x|^2 - |E_y|^2 \\ S_2 &= |E_{45}|^2 - |E_{135}|^2 \\ S_3 &= |E_{RC}|^2 - |E_{LC}|^2 \end{aligned} \tag{2.40}$$

The parameters S_1, S_2, and S_3 each describe the difference of intensities in two orthogonal polarization modes. In addition, a general definition can be given for the additional parameter S_0, which describes the intensity of the total field [13]:

$$S_0^2 = S_1^2 + S_2^2 + S_3^2 \tag{2.41}$$

The Stokes vector can be used to calculate several different parameters that describe the polarization state of light, such as the degree of polarization, the angle of polarization, and the ellipticity. The degree of polarization is described as [16]:

$$P = \frac{\sqrt{\langle S_1 \rangle^2 + \langle S_2 \rangle^2 + \langle S_3 \rangle^2}}{\langle S_0 \rangle}. \tag{2.42}$$

If $P = 1$, then the light is fully polarized and with $P = 0$ it would be completely depolarized. In intermediate values, the field would be partially polarized.

Poincare sphere

All polarization states can be represented on a sphere called the Poincaré sphere for complex vector fields [13]. This sphere helps to better understand all polarization states and how they can change as waves propagate through a retarding element. Figure 2.7 shows the Poincaré sphere with normalized Stokes vectors. The equator corresponds to the linear polarization state, when there is no phase difference between the E_x and E_y fields. Vertically and horizontally linearly polarized fields would be on opposite sides of the equator. At the poles, when the phase difference is a quarter wavelength or $\pi/2$, there are circular polarization states, which are either at the north or south pole depending on the direction. Points on the same meridian line will have the same azimuthal angle in the polarization ellipse, and points on the same latitude will have the same ellipticity in polarization.

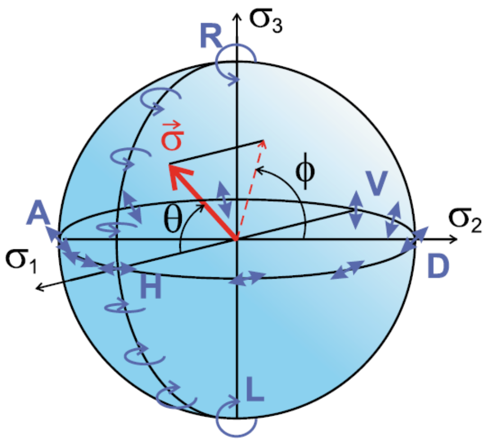

Figure 2.7: Representation of Poincaré sphere with normalized Stokes vectors $\sigma_1, \sigma_2, \sigma_3$. Adapted from Ref. [13].

2.1.3. Pancharatnam-Berry (geometric) phase

When examining the change in polarization states on the Poincaré sphere when moving from one point (A) to another point (C) through point (B) along a closed contour (see Figure 2.8), an interesting phenomenon is observed, where an additional phase change δ is observed. This phenomenon was first described by the Indian scientist S. Pancharatnam [17], and a general formulation applicable to quantum physics was formulated by M. Berry [18]: a wave (particle) moving in a system adiabatically (slowly) changes polarization (state) when going around a closed contour, it acquires an additional phase change, which depends on the half of the spatial angle $\delta = \omega/2$. This phenomenon arises only due to the change in the geometric path, and is therefore sometimes simply called the geometric phase.

One example could be the use of a half-wave plate. Since its retardance is $\lambda/2$, if a left circularly polarized wave passes through it, the polarization state will change to right circularly polarized. Depending on the rotation angle θ of the optical axis, the wave will acquire an additional phase $\Delta\phi$. Continuous optical axis rotation of birefringent material from 0 to π will result in continuous phase change from 0 to 2π [19] (see Fig. 2.9). This effect is later employed in geometric phase element beam shaping applications, presented in 2.3.4 subsection.

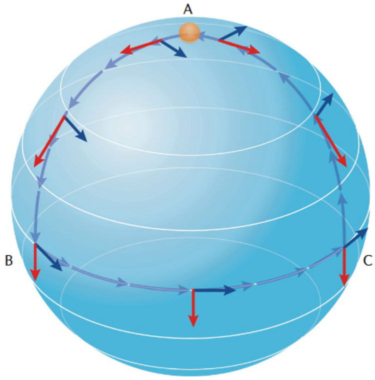

Figure 2.8: Polarization state changes, represented as red and blue arrows, when moving from point A to point C through point B illustrated on the Poincaré sphere. Adapted from Ref. [19].

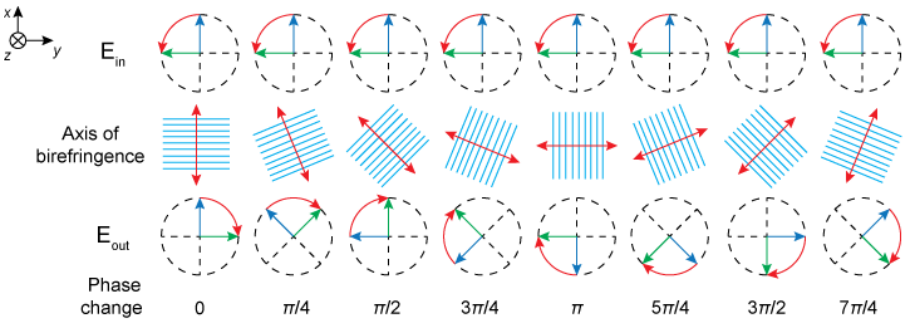

Figure 2.9: The dependence of phase delay on the rotation angle of birefringent material with respect to the incident beam, where the polarization of the incident field E_{in} is left circular and changes to the opposite polarization (right circular) E_{out}. Author's image adapted from Ref. [19].

When the first laser was invented in 1960 [20], the field of photonics began to develop rapidly, enabling faster research into linear and non-linear optics and the creation of new laser technologies for contactless material processing. Early research on the interaction of laser light with material showed that a strong light pulse on the order of 10 TW/cm^2 can damage optical elements irreversibly, forming defects on the surface or in the volume of a transparent material. This opened up a new era in photonics, which led to the development of a high-precision material processing technology for various materials: dielectrics, semiconductors, and metals [21]. Although the interaction of a material with a strong ultra-short light pulse is a complex process when considering material micromachining it can be divided into three main parts: electron plasma generation, energy absorption in the material, and structural changes in the material after energy relaxation [22].

2.2.1. Nonlinear photoionization in transparent material

Transparent media do not interact with the electromagnetic field itself in a weak field and are also called dielectrics. Most dielectrics are transparent in the visible and near-infrared spectral regions. In this region, there are also the most powerful ultrashort pulsed lasers, but the energy of their photons is not enough for electrons to be transferred from the valence band to the conduction band due to the much larger band gap E_g than the photon energy of that spectrum. For example, the band gap in fused silica glass is 9 eV. If we try to excite this material with a Yb:KGW laser source (central wavelength $\lambda = 1.03$ µm, one photon energy $E_{ph} = 1.2$ eV) [23], one would need at least several photons that would transfer their energy to force the electrons to be transferred from the valence band to the conduction band [24]. So, in order to cause an effect, it is necessary to "force" the transparent material to absorb much lower energy photons. This energy absorption is enabled by the nonlinear multiphoton photoionization process, which is expressed as a probabilistic event that depends on the radiation intensity [25]:

$$P\left(I\right) = \sigma_N I^N \tag{2.43}$$

where N is the number of photons absorbed simultaneously, I is the intensity, and σ_N is the multiphoton absorption coefficient. For example, multiphoton ionization in fused quartz requires N photons that satisfy the condition $N h\omega_{ph} > E_g$, where E_g is the band gap and ω_{ph} is the laser radiation frequency. Multiphoton absorption is the dominant mechanism when the radiation intensity is low and the frequency is high. However, at higher intensity and lower frequency, nonlinear absorption proceeds via tunneling. This phenomenon occurs when the strength of the exciting electric field is so high that the valence and conduction band levels are distorted, and the electron has a probability of tunneling to a higher energy level. The nature of the ionization mechanism can be described by the Keldysh parameter, which is expressed as following [26]:

$$\gamma_K = \frac{\omega_{ph}}{e}\sqrt{\frac{m_e c n \epsilon_0 E_g}{I}} \tag{2.44}$$

where ω_{ph} is the radiation frequency, I is the intensity, m_e is the effective electron mass, e is the electron charge, c is the speed of light, n is the material refractive index, ϵ_0 is the dielectric constant, and E_g is the band gap. The introduction of the Keldysh parameter allows one to better understand what kind of photoionization process takes place during the interaction in the material. When the parameter $\gamma_K << 1.5$, tunnel ionization dominates, when $\gamma_K >> 1.5$, multiphoton ionization determines the interaction, and when the parameter is $\gamma_K \approx 1$, both processes occur simultaneously. The photoionization schemes are shown in Fig. 2.10 [27].

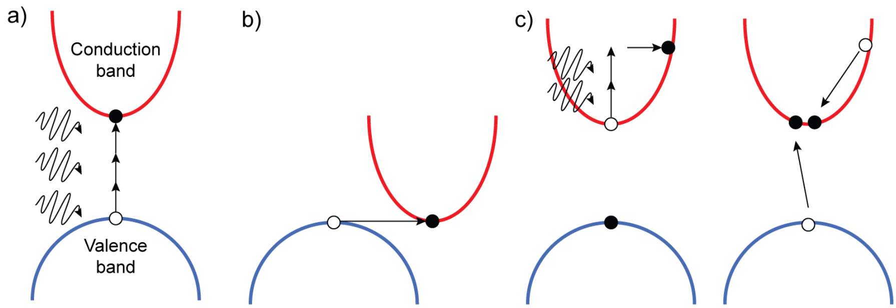

Figure 2.10: Mechanisms of nonlinear material absorption under the influence of ultrashort pulses: multiphoton ionization (a), tunneling ionization (b), avalanche ionization (c) - absorption of free carrier radiation energy followed by impact ionization. Author's image adapted from Ref. [27].

During multiphoton and tunnel ionization, the average kinetic energy of electrons increases due to the absorption of free carriers. If a hot electron that has absorbed energy and risen to the conduction band has enough energy, it can still knock out new electrons from the valence band and thus create impact ionization, resulting in two excited electrons at the conduction band minimum. These two electrons can continue to absorb energy, and this process becomes the cause of avalanche breakdown [22, 28]. As long as the electrons are excited by a strong external electric field of the laser pulse, the electron plasma density increases until it reaches the density of the laser light frequency and begins to directly absorb the incoming radiation. For 1 µm wavelength laser radiation, the plasma frequency will match the laser frequency when the free carrier frequency reaches 10^{21} cm^{-3}, this limit is known as the critical density of free electrons. It is generally said that optical breakdown in a material occurs when the number of free carriers reaches this critical limit. In a glass, optical breakdown is achieved at the intensities of 10^{13} W/cm^2 [21].

Typically, the thermal relaxation time of the material lattice is on the order of 10 ps or longer, so that the absorbed radiation energy is transferred to the surrounding molecules around the damage zone. If the pulses are much shorter - less than a few ps - they take less time to reach optical breakdown and have a higher intensity, which causes the ionization in the material to occur and end faster than the heat has time to dissipate, so there is a smaller heat affected zone (HAZ). For this reason, ultra-short pulses can be used to create a variety of damage to materials with very high precision (a few microns) and to change their properties both in volume and on the surface [21].

2.2.2. Types of induced defects in bulk of silica glass

After the nonlinear interaction process in a transparent medium (glass), different material damage results are possible, depending on the process parameters: refractive index change, anisotropic nano gratings or micro-voids can be formed [29]. Such a division into separate regimes helps to better understand each of them and to predict the window of laser parameters in which it is possible to perform micromachining and obtain the desired effect. Typical damage classification is refractive index change (type I), birefringent damage (type II) or micro-void or crack formation (type III) in silica glass (see Fig. 2.11). The properties of the formed structures will depend on the radiation parameters (wavelength, pulse duration, energy, repetition rate), material properties (bandgap, thermal properties, chemical composition), and focusing conditions (numerical aperture, focusing lens properties).

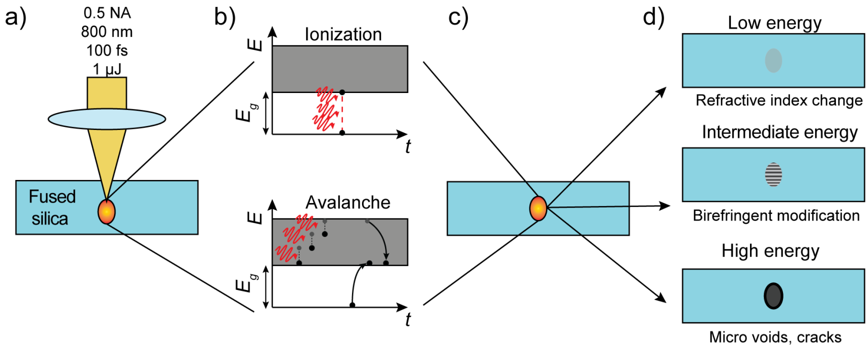

Figure 2.11: Illustration of typical bulk damage types in fused silica glass: a focused laser pulse within the material volume (a) induces nonlinear absorption and ionization, generating electron-hole pairs, with electrons gaining additional energy and triggering an avalanche process (b); in the plasma, all accumulated energy is transferred to the material's lattice (c); classification of damage based on the impact (energy density delivered) (d). E_g denotes the bandgap energy. Author's image adapted from Ref. [29].

Refractive index change

In-depth studies of material damage were initiated when the first ultrashort pulses were generated in laboratory conditions, and it was observed that intense laser radiation focused in glass can change the properties of the material - for example, isotropic refractive index change [30]. It was observed that with low pulse energies and high scanning density by near-threshold femtosecond laser irradiation, it is possible to write smooth tracks of increased refractive index [31]. Due to the fast interaction of laser pulse and excited electrons, the surrounding space in the material lattice does not have time to heat up and the irradiated region cools rapidly after the radiation ends, forming a volume of densified material. In this region, the refractive index can increase slightly up to $\Delta n \approx 0.0035$ [31] and this is sufficient for the light subsequently introduced into the written channel to propagate as a waveguide, due to total internal reflection [32]. In one case, it is possible to have all types of damage by varying only the pulse energy: when the pulse energy is $E_p = 100$ nJ with tight $NA = 0.6$ focusing $\lambda = 800$ nm wavelength,

$\tau = 100$ fs pulse duration, a uniform refractive index change can be achieved in fused silica [33]. Examples of laser written waveguides are shown in Fig. 2.12.

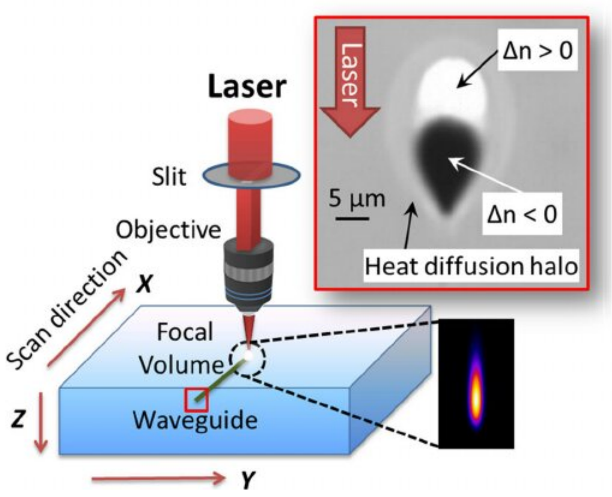

Figure 2.12: Example of direct laser writing of waveguides by inducing refractive index changes in the bulk of a glass. Adapted from Ref. [34].

Such uniform change in the refractive index is used to directly write waveguides in glass, through which light can propagate and be controlled and manipulated in various ways. This process is being rapidly improved and tested for application in the production of optical communication devices [35].

Birefringent nanogratings

Increasing the pulse energy to the range of 150-500 nJ under the same conditions mentioned above for changing the refractive index, there is a regime where irradiated space is made birefringent [33, 36, 37]. These are the so-called type II defects, caused by higher energy pulses, which are characterized by periodic nanogratings, typically formed in fused silica glass or other oxygen-rich glasses [38, 39]. These gratings are periodic self-organized rarefactions and densifications of the material and are formed perpendicular to the electric field vector of the incident pulse, their period is typically $\Lambda = \lambda/2n$, where λ is wavelength, n is refractive index [40, 41] (see Fig. 2.13). The mechanism of formation of these nanogratings is not fully agreed upon, but two primary models have been proposed for the formation of nanogratings. The first model relies on the formation of electron plasma and light field interference that modulates the electron plasma density periodically, leading to subsequent modulations within the material [42, 43]. The second model explanation tells that nanograting formation is the result of the growth of small, asymmetric nanoplasmas. These nanoplasmas are believed to amplify due to field enhancement effects with each successive laser pulse and eventually merge into planar nanoplasma structures and then evolve into nanopores [44].

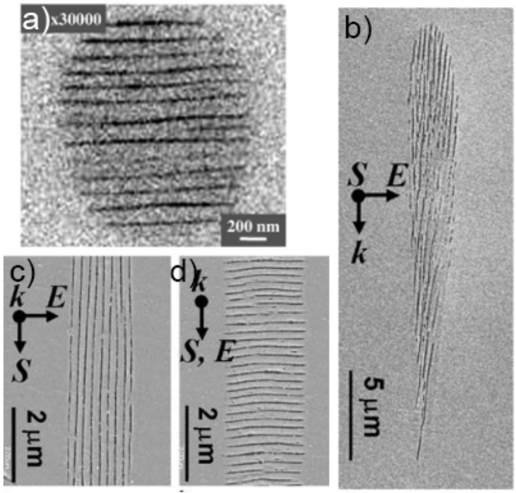

Figure 2.13: SEM images of a) cross section of formed nanogratings in bulk of fused silica. Reprinted from Ref. [40]. b) Side view of nanograting area where k is denoting direction of writing pulse, c) and d) show nanograting orientation dependence on the writing pulse polarization E along direction S. Adapted from Ref. [45].

Recently, there was reported a subtype of this nanograting regime, called type X nanogratings [44]. These nanogratings are distinguished for their low loss (scattering) compared to the ordinary type II modification, especially in shorter wavelength range, beyond visible light range, see the comparison in Fig. 2.14. For this direct writing regime, reduced fluence and pulse densities are needed. The modified glass volume consists of slightly elongated nanopores, which have smaller dimensions and therefore reduce light scattering of shorter wavelength (see Fig. 2.15).

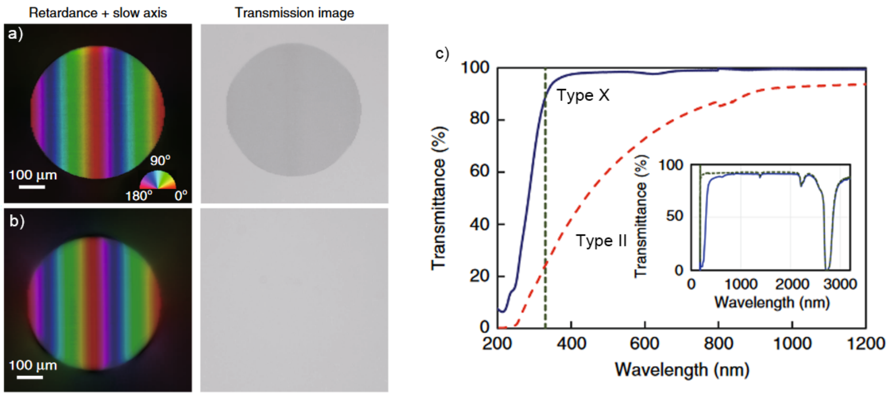

Figure 2.14: Comparison of transmission of type II (a) and type X (b) inscribed nanogratings. In (c) the type X transmission spectrum is improved in visible and near UV range compared to type II modification. Adapted from Refs. [44, 46].

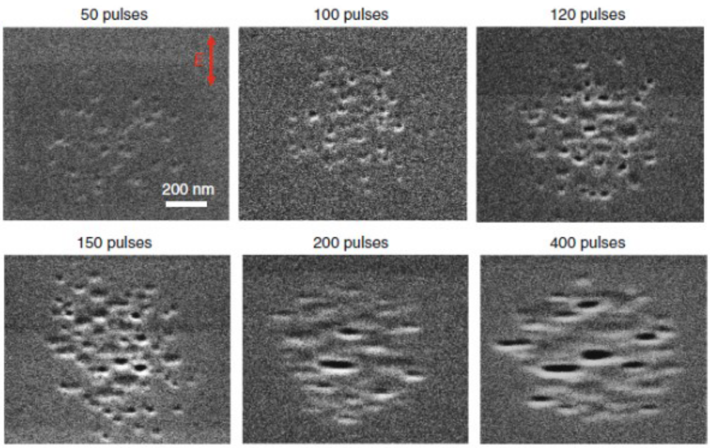

Figure 2.15: SEM images of polished fused silica sample with revealed nanopores under different numbers of writing pulses. Adapted from Ref. [44].

The formation of periodic nanogratings and nanopores is influenced by chemical changes in the material lattice. In the initial stage, approximately 250 fs after the interaction between the laser pulse and the material begins, the first defects are created [47]:

$$\equiv \mathrm{Si} - \mathrm{O} - \mathrm{Si} \equiv \longrightarrow \equiv \mathrm{Si} \cdot + \cdot \mathrm{O} - \mathrm{Si} \equiv \tag{2.45}$$

where $\equiv \mathrm{Si}\cdot$ is a defect center, and $\cdot\mathrm{O} - \mathrm{Si} \equiv$ is a non-bridging oxygen-silicon bond. Further interaction with light leads to the dissociation of oxygen into separate atoms, disrupting the original silicon lattice structure [47]:

$$\equiv \mathrm{Si}\cdot + \cdot \mathrm{O} - \mathrm{Si} \equiv \longrightarrow \equiv \mathrm{Si} \cdot^{+} \mathrm{Si} \equiv + \mathrm{O}^0 + \mathrm{e}^- \tag{2.46}$$

here, $\equiv \mathrm{Si} \cdot^{+} \mathrm{Si} \equiv$ is a defected Si bond, O^0 is a separated oxygen atom, and e^- is a free electron. The initial defects formed in random locations grow in size with each subsequent pulse, aligning perpendicularly to the polarization direction of the beam.

This nanograting formation regime is in a narrow direct writing parameter window, so any imperfections or process deviations during actual formation can affect the final result. For example, it has been observed that there is a quill effect, where the morphology of the written structures depends on the translation direction during direct laser writing due to the pulse front tilt [48]. A recent study also found that the asymmetry of the writing beam can significantly affect the properties of the formed periodic structures [49], as well as the temporal contrast of pulse train coming from a laser source will make different impact on writing the birefringent nanostructures in bulk [50]. Direct laser writing of nanogratings is an attractive technology because it allows modifying the fused silica glass with five degrees of freedom, where in addition to the spatial formation of structures in xyz coordinates, the phase delay (retardance) and fast/slow axis are additionally manipulated. The formation of these structures is applied in the manufacturing of flat optical retarders, as well as in research for development for the storage of large amounts of information in fused silica [46, 51, 52].

Micro voids

If applying ultrashort radiation under the same conditions as before from Ref. [33], but increasing the pulse energy above 500 nJ, results in stronger damage to the glass: it is possible to structurally disassemble the material lattice, breaking the bonds between molecules, thus forming, for example, microvoids or microcracks in the transparent medium. Very powerful pulses can create strong defects, thus distorting the original substrate, therefore, radiation parameters are usually used to create the necessary defects with minimal destruction of the surrounding material. Microvoids or microcracks are formed when electrons have absorbed a large amount of excess energy that is used to break the bonds between lattice atoms and an explosion wave can be formed, which distorts a certain area of space in the material. The result is an empty space area where there is no material, or it is rarefied (see Fig. 2.16) [53, 54]. The

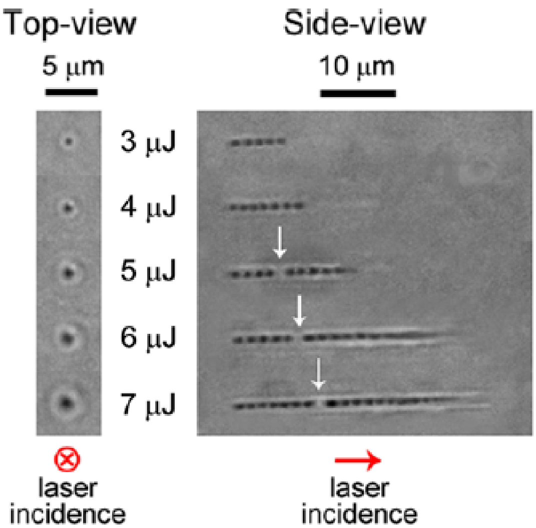

Figure 2.16: Top and side views of inscribed micro voids in fused silica glass with different pulse energies. Adapted from Ref. [54].

rarefied material spots or induced micro-fractures can be used as weak points in the separation process, i.e. in glass cutting applications [55] which will be covered more in-depth in the following subsection.

It is worth noting, that the discussed I-III type damages in glass can also be formed with other laser and optical setup parameters, when, for example, the focusing conditions are different, so the pulse energy, duration or other parameters are found and adjusted experimentally [56, 57].

2.2.3. Laser micromachining

The three types of damage studied are commonly encountered when working with glasses in their bulk. However, ultrashort laser micromachining is also possible with any other materials (metals, semiconductors, polymers, plastics) on their surface or in bulk if it is transparent for the wavelength since strong radiation can excite electrons, which, having formed a plasma region, transmit energy to lattice and inducing defects, evaporating or otherwise changing the properties of practically any material [58]. Some of the most common examples of laser micromachining processes are surface ablation, drilling and marking [59], cutting [60], welding [61]. Each process can be implemented with different irradiance parameters and focusing conditions.

Surface ablation

Laser ablation is, in principle, an evaporation of the material surface when focused intense radiation heats the material, and sudden sublimation begins [58]. When the focal zone of the focused beam is directed onto the material surface, linear or nonlinear (depending on the absorption of the material) energy absorption of the material electrons takes place, and these, having acquired a lot of energy from the electric field of the beam, form free electron plasma. After the electric field is gone, the excess energy is dissipated in the surrounding space, dissembling the material lattice with rapid evaporation [58]. After the end of the pulse impact, a crater is left on the surface of the material (see Fig. 2.17).

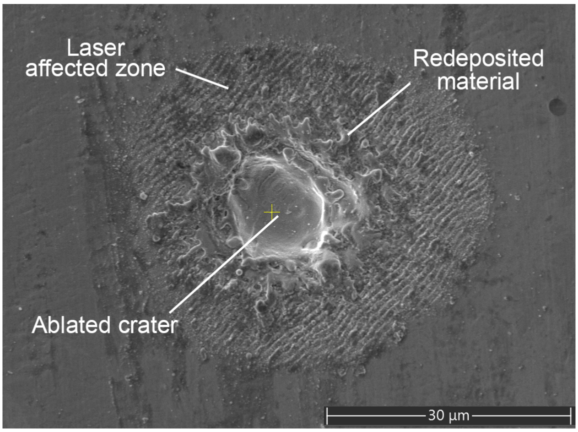

Figure 2.17: Example of laser ablated crater on silicon substrate using a single pulse of Gaussian beam at 358 fs pulse duration and 3 J/cm^2 fluence. Author's image, obtained with scanning electron microscope.

The ablation process is a widely investigated topic, the two temperature model is often employed to conduct numerical simulations of various material ablation [62]. The width of the created crater depends on the focusing conditions, material and laser irradiation properties - the size of the focused spot, wavelength, pulse duration, and energy of the pulse [63]. The fluence parameter F describes effectively absorbed energy and can be used to experimentally evaluate the optical damage threshold of any material as well as to find the optimal ablation regime [64]:

$$F = \frac{4E}{\pi D^2}, \tag{2.47}$$

where D is width of focused beam, E is pulse energy.

The affected surface area usually changes its optical properties and is visible to the naked eye. The surface at the bottom of the evaporated material area becomes rougher, more scattering light. The chemical, electrical or mechanical properties can also change, therefore, by purposefully causing changes in the initial material, it is possible to selectively and very precisely change the properties of the material. For example, selective surface ablation is one of the most suitable processes for cleaning conductive paths from a metal-coated glass substrate, thus forming channels on transparent samples [65]. The same principle can be used to perform surface marking, where laser-written structures have different reflective or transmission properties [66].

Laser cutting

Laser cutting is another application of laser micromachining that separates the initial samples into smaller ones. Material separation can be done as repetitive inline ablation, evaporating the material along a trajectory, or by evaporating a certain depth of material and thus forming weak points where the material can later be broken off along [67,68]. It is also possible to form bulk damage in the volume of transparent material under two steps: initiate cracks that cause directional stress in the material (type III defects), and if they are correctly positioned in a line, form a fracture line [55, 69] and then apply force to mechanically break it, - performing so-called stealth dicing, as depicted in sketch in Fig.2.18. Laser cutting is particularly advantageous where high precision and a small heat-affected zone around the cut line are required, compared to mechanical separation processes, and it is also non-contact [60]. An

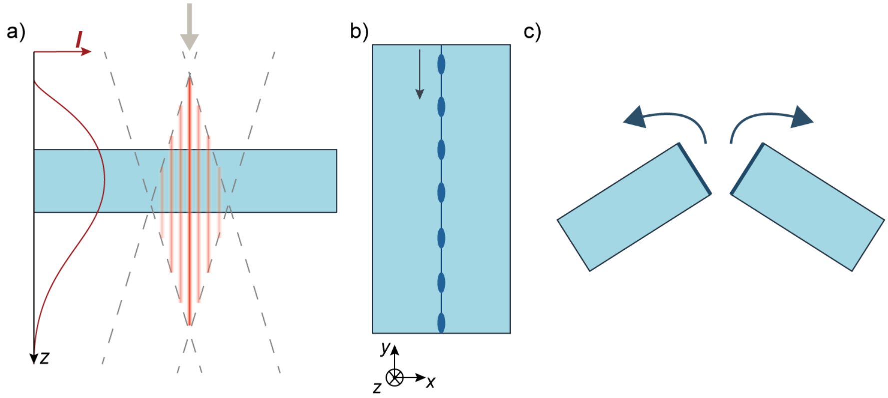

Figure 2.18: Principle sketch defining stealth laser dicing and braking in two main steps: (a) the elongated focal beam is positioned at the right height in z axis, and (b) the induced microcracks are orientated along the cutting trajectory (step one). After laser contouring, the glass sample is mechanically broken into two pieces (step two). Author's image.

example of such a process is shown in Fig. 2.19.

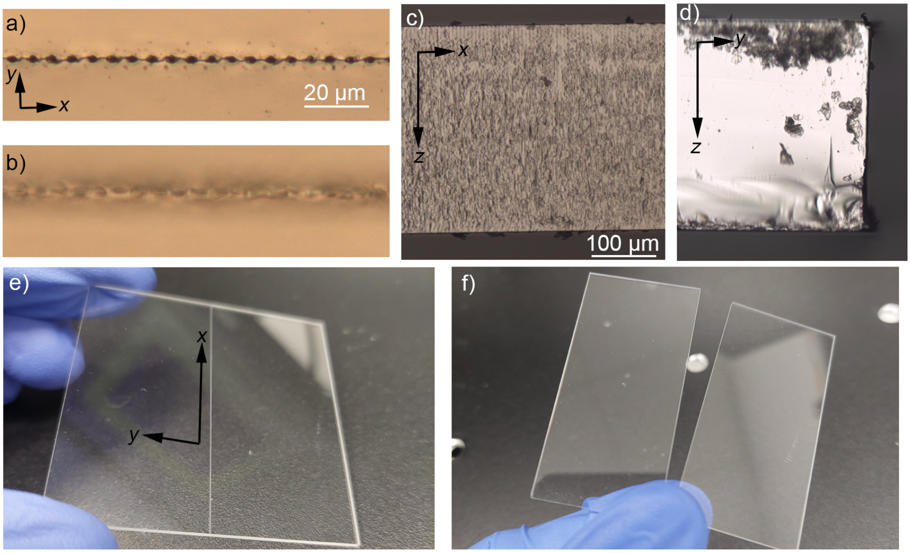

Figure 2.19: Example of transparent material cutting by inducing microfractures in bulk. (a) The laser-modified region across the whole thickness of the sample (b) creates weak points by which the substrate can be separated by mechanical force. (c) View of sidewalls after separation, (d) front view of cut edge. (e)-(f) Macro photographs of samples before and after breaking. Author's image.

Micro welding

Laser microwelding is a process that uses a laser to locally melt a region of material and join it to another sample. In this process, a tightly focused beam forms a hot plasma region in a volume of a few tens of micrometers, in which the excited electrons relax and transfer energy to the material lattice, locally reaching and exceeding the melting temperature, forming a molten zone [70, 71]. If this zone is formed at the joint of two transparent or one transparent and one opaque material, the molten material will adhere to the other sample, and the samples will bond upon rapid cooling. Figure 2.20 shows an example of laser micro welding. The successful welding can be seen visually if there are micro gaps between two glass pieces – white light interference is visible, and from the colors of interference fringes, it can be used to determine the preexisting gap [70–72]. After laser welding, this gap vanishes where tracks are created, indicating that the two glass substrates are joined together in optical contact [71]. This microwelding technique is often employed in transparent microfluidic chip manufacturing, where multiple layers of glass can be joined to make buried fluidic channels [73].

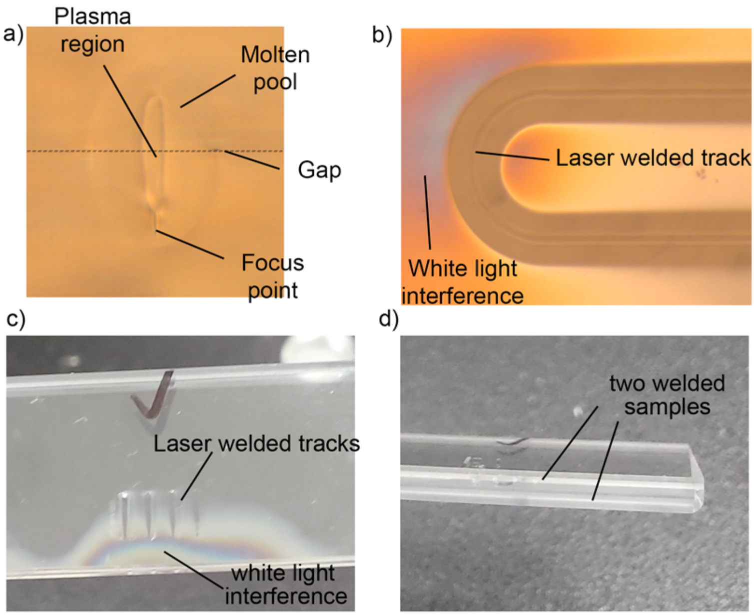

Figure 2.20: Example of transparent material laser welding, where (a) weld seam cross-section is shown and (b) top view of welded seam. Due to the gap between two surfaces, white light interference is visible, which disappears when two materials are joined. (c)-(d) Photographs of two welded glass samples. Author's image.

2.3. Laser beam shaping

The laser micromachining of various materials is essential in many industrial applications [74]. The ultrashort pulsed laser sources are evolving rapidly towards the direction of increasing average power and pulse repetition rate, and the energy of a single pulse is more than enough for the ablation of the material, the efficiency of the laser micromachining process can be greatly enhanced by distributing the energy in the spatiotemporal domain [75]. Therefore, the different laser beam shaping techniques have increased interest in the fields of laser micromachining and light-matter interaction research [76]. On the other hand, light structuring also plays an important role in other specific applications [77–79]: photonic communications [80, 81], imaging enhancements [82–84], tomography [85], light sheet microscopy [86], and microscopy across a wide range of the electromagnetic spectrum.

In general, there are many types of laser beams, generalized as $\mathrm{TEM_{mn}}$ modes, whose amplitude, phase, or polarization distributions can have a critical impact on certain processing tasks. Any real electromagnetic wave (mode) exists only if it satisfies the Helmholtz equation [87]:

$$(\nabla^2 + k^2)E(r) = 0, \tag{2.48}$$

where E is the electric field, k is the wave number, and ∇^2 is the Laplacian operator.

Different types of laser sources can emit many different modes, and the general wave equation describing m, n modes in the Cartesian coordinate system is [87]:

$$E_{mn}(x, y) = H_m\left(\frac{\sqrt{2}x}{w}\right) H_n\left(\frac{\sqrt{2}y}{w}\right) \exp\left[-\left(\frac{x^2+y^2}{w^2}\right)\right] \exp[\phi(z)], \tag{2.49}$$

here H_m and H_n are Hermite polynomials. When m and n are equal to zero, we have the $\mathrm{TEM_{00}}$ mode, also known as the Gaussian beam, which is the fundamental mode emitted by solid-state ultrafast pulsed lasers having stable resonators [88]. For the Gaussian beam, when mode numbers m and n are equal to zero, the intensity distribution is expressed as [87]:

$$I(r, z) = |E(r, z)|^2 = I_0 \left(\frac{w_0}{w(z)}\right)^2 \exp\left(-\frac{2r^2}{w^2(z)}\right) \tag{2.50}$$

where w_0 is the beam waist radius at the Rayleigh range, when z is equal to 0, and $w(z)$ is the beam radius at a distance z:

$$w(z) = w_0 \left[1 + \left(\frac{z}{z_0}\right)^2\right]^{1/2} \tag{2.51}$$

and the wavefront radius will be:

$$R(z) = z\left[1 + \left(\frac{z_0}{z}\right)^2\right]. \tag{2.52}$$

The wavefront will have one radius before the focus, the opposite sign after the focus, and will be flat in the middle of the focus. This change in phase front is described by the Gouy phase [89]. The spatial intensity distribution of a Gaussian beam at the waist is shown in Fig. 2.21.

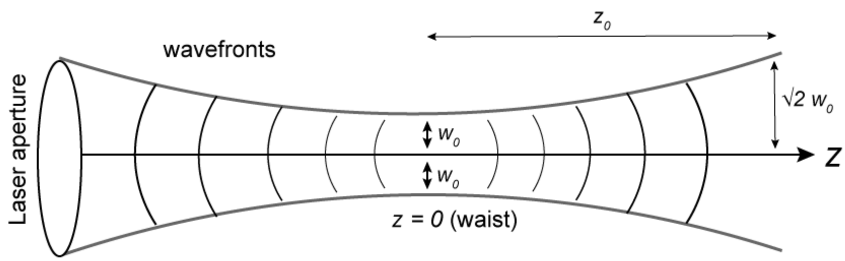

Figure 2.21: Principal sketch of a spatial intensity distribution of a Gaussian beam at the waist. Author's image adapted from Ref. [87].

A Gaussian beam emitted from a laser source has convergence (narrowing) and divergence (widening) beyond the focal zone. As the beam propagates away from the laser due to diffraction, it expands and diverges, so a parameter has been introduced to estimate the divergence angle [87]:

$$\theta_0 \approx \frac{\lambda}{\pi w_0}. \tag{2.53}$$

An ideal beam is considered to be one with zero divergence - the beam is then considered to be collimated, but in reality, this value is not zero. Lenses can be used to change the divergence, so the beam can be narrowed (focused) or expanded (defocused). In laser processing, it is usually necessary to focus the beam to achieve the required intensity and small spot size at the focus. The size of the focused Gaussian spot will depend on the focusing conditions and the wavelength of the radiation. If we consider the incoming beam to be collimated, using the thin lens formula in the paraxial approximation, we will find the spot size as [87]:

$$D = \frac{2\lambda f}{\pi w_0} \tag{2.54}$$

where f is the focal length of the lens, λ is the wavelength, and w_0 is the beam waist before the lens. The depth of field of the focused beam around the focal plane will be [87]:

$$\mathrm{DOF} = \frac{4\lambda}{\pi}\left(\frac{f}{w_0}\right)^2. \tag{2.55}$$

DOF corresponds to twice the Rayleigh range length, where the beam expands by a factor of $\sqrt{2}$. Knowing these basic beam parameters and the properties of the optical system, it is possible to estimate in advance the size of the spot that will be focused on the surface of the material.

2.3.1. Modified profile beams

With the development and increasing power of laser sources, the Gaussian beam has become a bottleneck in some processes due to its bell-shaped intensity distribution. This is because too much energy or its accumulation can negatively affect the processed materials at the center of the beam or on the sides. This is a drawback that causes more powerful energy pulses to create surrounding damage zones in the materials, thus reducing the quality and accuracy of laser processing due to uneven intensity distribution [90]. To address this, the field of beam shaping research has gradually developed, which studies the formation and propagation of various beams, with potential applications in materials processing, where the Gaussian beam is transformed into a beam of different structure, suitable for improving ablation, cutting or other processes [58].

Higher-order modes

The Gaussian beam is the lowest-order mode of a laser. Higher-order modes, which can have different values of the m and n parameters from Eq. (2.49), can be used to create beams with more complex intensity distributions [91]. In Cartesian coordinates, Hermite-Gaussian modes can be formed by independently changing the amplitudes in the x and y directions (see Fig. 2.22) [92]. By manipulating coordinate systems, parabolic or elliptic beams can be formed (see examples in Fig. 2.23) [93, 94].

In Cartesian coordinates, the full amplitude expression for a TEM_{mn}

Hermite-Gaussian beam is given by [87]:

$$E_{mn}(x,y,z) = E_0 \left(\frac{w_0}{w(z)}\right) H_m \left(\frac{\sqrt{2}x}{w(z)}\right) H_n \left(\frac{\sqrt{2}y}{w(z)}\right) \\ \times \exp\left[-\left(\frac{x^2+y^2}{w(z)^2}\right)\right] \\ \times \exp\Big[-\mathrm{j}kz - \mathrm{j}k(x^2+y^2)/2R(z) + \mathrm{j}(m+n+1))\xi(z)\Big], \quad (2.56)$$

where w is the beam waist width, R is the radius of curvature, ξ is the Guoy phase, and H_m and H_n are the m-th and n-th Hermite polynomials. Since these modes are described in a rectangular xy coordinate system, the coordinates can be separated into individual functions. A mn mode will have $m{+}1$ maxima in the x direction and $n+1$ maxima in the y direction. If the waves under consideration are in a cylindrical coordi-

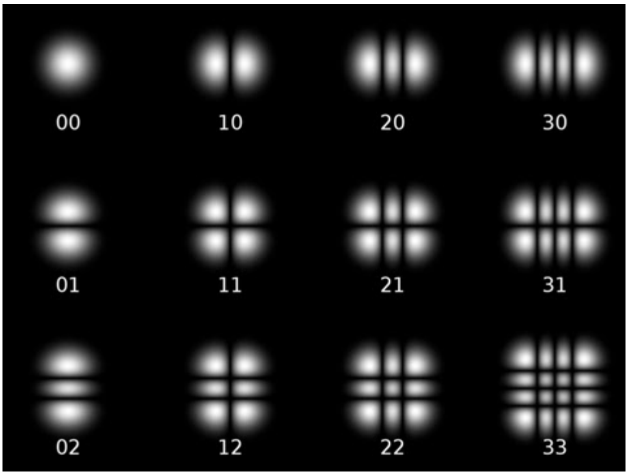

Figure 2.22: Examples of Hermite-Gaussian modes having m and n modes, respectively. Adapted from Ref. [95].

nate system, their propagating modes can be described by the Laguerre-

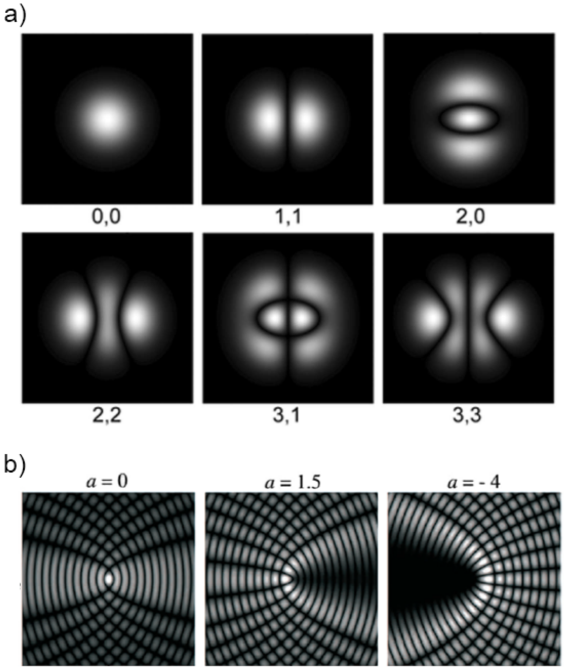

Figure 2.23: Examples of the transverse intensity distribution of (a) Ince-Gaussian beams in an elliptical coordinate system, (b) transverse cross-sections of parabolic beams. Adapted from Ref. [93].

Gaussian analytical solution (see mode examples in Fig. 2.24) [91]:

$$E_{lp}(r,z,\phi) = \left(\frac{E_0}{w(z)}\right)\left(\frac{\sqrt{2}r}{w(z)}\right)^{|l|} \exp\Big[-r^2/w^2(r)\Big] L_p^{|l|}\left(\frac{2r^2}{w^2(r)}\right)$$
$$\times \exp\Big[-\Big(-\mathrm{j}kr^2z/(2(z^2+z_R^2))\Big)\Big]$$
$$\times \exp[-\mathrm{j}l\phi + \mathrm{j}(2p+|l|+1)\arctan(z/z_R)], \quad (2.57)$$

here l is the azimuthal modulation number, p is the radial node, and L_p is the Laguerre polynomial. The azimuthal phase modulation gives the beam a topological charge - a helical twist of the wavefront as the beam propagates [96]. The topological charge here is expressed as the number of closed turns of the wavefront by l as the wave propagates a distance of λ (phase from 0 to 2π), and such beams are also called vortex beams, carrying orbital angular momentum (OAM) [97] (see Fig. 2.25). Orbital

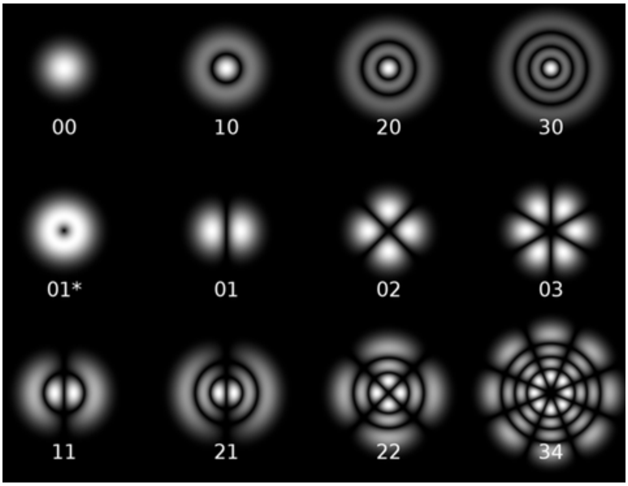

Figure 2.24: Examples of Laguerre-Gaussian modes with various l and p mode numbers. Adapted from Ref. [95].

angular momentum is a widely studied property of beams, since this momentum can be transferred by light to bodies, and has applications, for example, in microscopic particle manipulation [98].

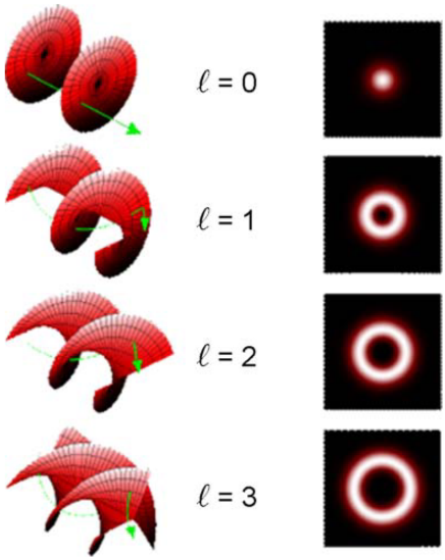

Figure 2.25: Phase front and intensity distribution examples of vortex beams carrying OAM, when $l \neq 0$. Adapted from Ref. [99].

Super-Gaussian (flat-top) beams

Another beam profile that has attracted wide interest is the Super-Gaussian beam (also known as flat-top or top hat in other similar matches) [100–102]. The main characteristic of this beam is a flat intensity distribution over a large area of the beam, which is very attractive in laser micromachining [see examples in Fig. 2.26(a)-(c)]. Since the

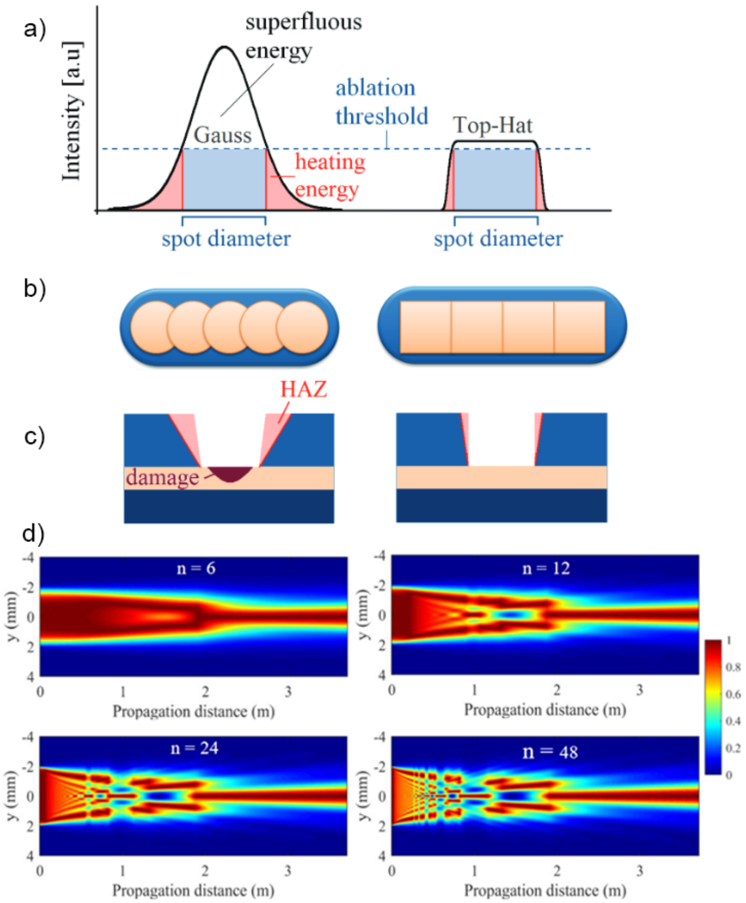

Figure 2.26: Intensity profile comparison of (a) Gaussian beam with Top-hat (flat-top, Super-Gaussian) beam. Due to different transverse distributions, the flat-top beam may improve overlapping (b) and reduce HAZ in micromachining (c). On the other side, (d) the desired spatial intensity distribution is limited due to diffraction, depending on the Super-Gaussian order N. Adapted from Refs. [90, 102].

material's response during processing depends on the beam intensity at that point, a more uniform distribution ensures a more uniform heat distribution, especially where it is necessary to form flat-bottomed craters or grooves or where selective surface ablation is required [90, 103]. The Super-Gaussian beam profile can generally be described by raising the exponent from Eq. (2.50) to the power of N [102]:

$$E(x, y) = E_0 \exp\left[-\frac{\sqrt{(x^2 + y^2)}}{w_0}\right]^N \tag{2.58}$$

The larger the order number N, the larger the flat area and steeper the walls. As the order N approaches infinity, the distribution cross-section would approach a rectangular shape. However, it is only possible to generate beams with perfectly steep walls and a flat top in a very limited propagation zone, since the spatial frequency components quickly phase out, so such a beam is not a free-space propagating mode [see Fig. 2.26(d)] [102, 104].

2.3.2. Non-diffracting (invariant) beams

Another family of beams that satisfy the wave equation is that of non-diffracting or propagation-invariant beams [105, 106]. Analogously to the case of TEM modes, different beams can be formed in different symmetry coordinate systems: Bessel beams can be formed in cylindrical coordinate systems [107], Mathieu beams in elliptical systems [108], Weber beams in parabolic systems, and self-accelerating Airy beams that vary with the z coordinate [109, 110]. All of these beams have elongated focal line and have the property of self-healing [111], since they can recover from an obstacle and maintain their transverse intensity distribution as they propagate [112], and are widely studied in optical imaging [84,113], particle manipulation [114], laser micromachining [115,116], optical communication [117].

Bessel beam

The Bessel beam is a solution to the wave equation in cylindrical coordinates, whose electric field is described as [105, 118]:

$$E(r, \phi, z) = E_0 \exp(\mathrm{j}k_z z) J_n(k_r r) \exp(\pm\mathrm{j}n\phi), \tag{2.59}$$

where, E_0 is the amplitude, J_n is the n-th order Bessel function of the first kind. The zero-order Bessel beam has an intensity maximum at the center and zones of lower-intensity concentric circles around it (see Fig. 2.27). An ideal Bessel beam has infinite energy and cannot be

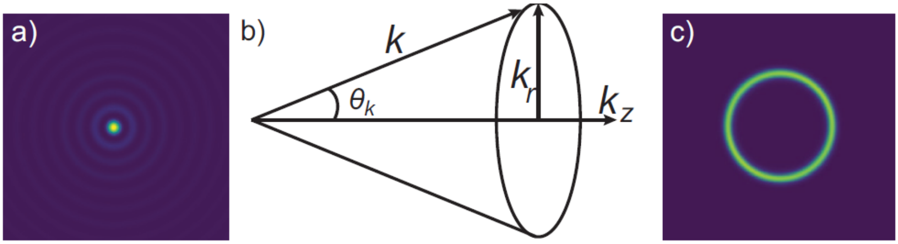

Figure 2.27: Modeled images of (a) Bessel beam intensity distribution in the near field, (b) principal sketch of plane waves traveling on the surface of a cone at angle θ_k, which result in (c) ring-shaped far field distribution. Author's image.

formed under real conditions, but a Bessel-Gauss beam can be formed in the laboratory, which is in principle a Bessel beam transformed in a limited space from an initial Gaussian beam [75]. If we superimpose many plane wave vectors on the surface of a cone in the direction of propagation, we would in principle obtain a Bessel beam, since it is the result of the interference of such waves. Under real conditions, this can be achieved by passing the wave through a ring-shaped aperture, and due to diffraction, the wave passing through it will interfere and create a Bessel distribution on the screen. Another, more effective way is to use an axicon - a conical lens that can directly transform a Gaussian beam into a Bessel-Gauss beam [106,119,120]. This transmissive optical element changes the flat phase front of the incoming beam to a cone-shaped with a tip angle of $\theta_c = (n-1)\alpha$, where n is the refractive index of the material from which the axicon is made, α is a base angle. Behind such an element, the wave propagates at an angle β, called the Bessel cone angle [87]:

$$\tan\beta = \frac{|k_r|}{k_z}. \tag{2.60}$$

Based on this angle and the radius of the incoming Gaussian beam, it is possible to estimate the length of the zone over which a Bessel-Gauss beam can be formed [87]:

$$z_{max} = \frac{R}{\tan \beta}. \tag{2.61}$$

The focal line length of a Bessel-Gauss beam behind an axicon may be several centimeters, depending on the apex angle. This may require a lot of energy to reach the required fluence levels in laser micromachining, therefore usually a spatial compression setup, consisting of a pair of convex lenses is used (see Fig. 2.28). In Eq. (2.59), the n-th order in

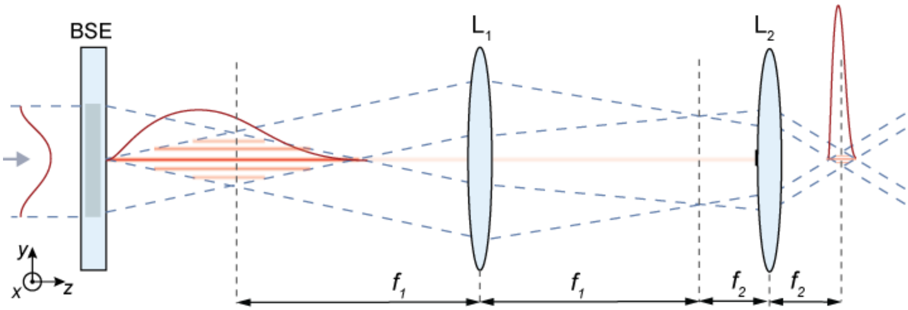

Figure 2.28: Principal optical scheme example of using $4f$ optical system to spatially compress the Bessel-Gauss beam made with any beam shaping element (BSE). The compression in longitudinal space is according to $(f_1/f_2)^2$, while in transverse space the compression depends on the ratio f_1/f_2, where f_1 and f_2 are the focal lengths of the lenses L1 and L2, respectively. Author's image.

part $\exp(\pm \mathrm{j} n\phi)$ also indicates that this beam can have OAM. When n has a non-zero value, the Bessel beam is transformed into a ring-shaped beam with helical phase front [121]. Additionally, it is possible to perform superpositions of such beams and obtain new and interesting intensity distribution beams [122, 123] (see Fig. 2.29):

$$E_{m,n}(r, \phi, z) = E_m(r, \phi, z) + E_n(r, \phi, z). \tag{2.62}$$

A few examples of superposed Bessel beams are depicted in Fig. 2.29.

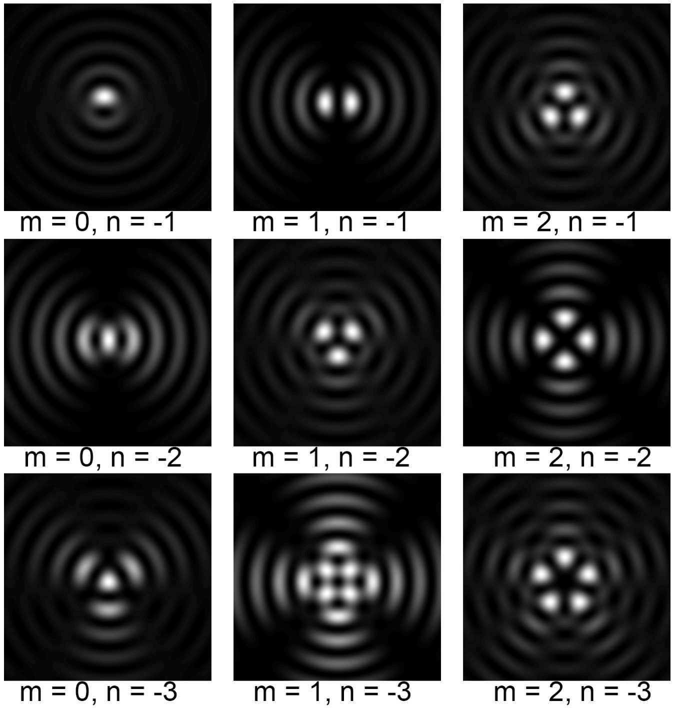

Figure 2.29: Examples of coaxial superposition of different higher-order Bessel beams, where m and n represent order number. Author's image.

Airy beam

Another member of the non-diffracting beam family that has attracted a lot of attention is the so-called Airy beam. This beam is special in that its central intensity maximum bends parabolically as the beam propagates, and the general expression for the field of such a beam is [87, 110]:

$$E(r) = \mathrm{Ai}\left(\frac{x}{x_0} - \frac{z^2}{4k^2x_0^4}\right)\exp\left(\frac{\mathrm{j}xz}{2kx_0^3} - \frac{\mathrm{j}z^3}{12k^3x_0^6}\right) \tag{2.63}$$

where Ai is the so-called Airy function, depicted in Fig. 2.30. Beams with this bending property are also called self-accelerating beams. This property is widely applied, from laser micromachining forming curved sidewall cuts [124, 125], to optical imaging or trapping [126].

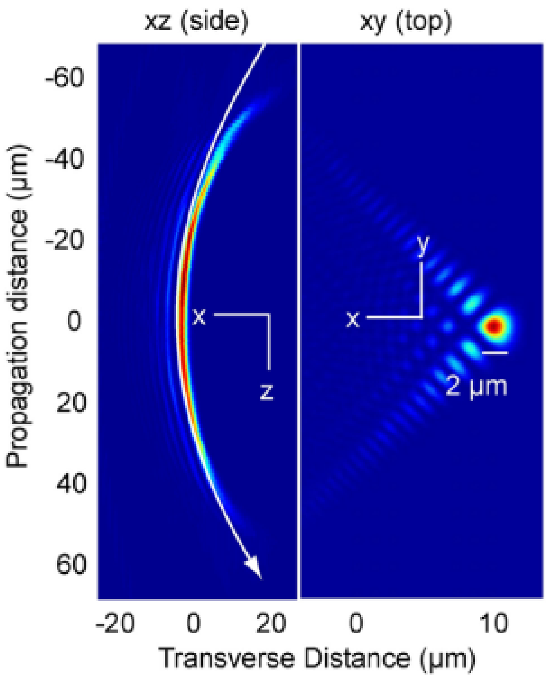

Figure 2.30: Intensity distribution of an Airy beam in longitudinal and transverse coordinates. Adapted from Ref. [124].

2.3.3. Structured vector beams

In the context of beams and their possible variants, scalar cases have been considered, but there are also beams whose distributions contain more than one polarization state or whose polarization states are different in different parts of the xyz space [127]. Such beams can be used in more complex optical communication [128], since they have an additional degree of freedom of varying polarization, and can also be used in laser micromachining, where the polarization state is different in multiple areas of the beam and the induced defect may give advantages in the process over a simple single-polarization state beam [129].

Cylindrical vector beams

In addition to the earlier discussed standard polarization states (linear, elliptical, or circular), the laser beam can be rearranged so that the SOPs would be different at each point in the field. One of the first methods to do this was to use phase plates cut at the desired angle and assembled into a single optical element - the so-called q-plate [130]. Such an element with differently oriented optical axes will rotate the beam polarization (for example, linear) at different angles. From this, azimuthally or radially polarized beams can be obtained (see Fig. 2.31). In the case of azimuthal polarization, the polarization state of the beam

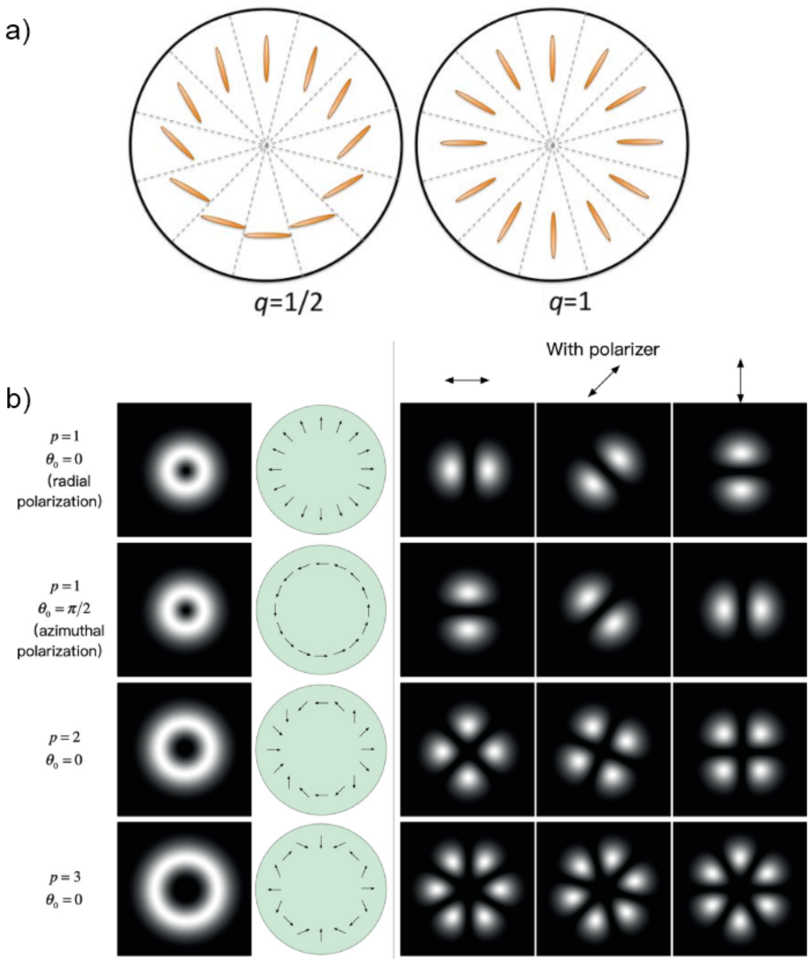

Figure 2.31: (a) Q-plates, where q describes axis winding order, and (b) obtained vector beams of first, second, and third orders. Adapted from Refs. [95, 131]

changes in azimuth relative to the center and forms a picture similar to linearly arranged states in concentric circles. In the case of radial polarization, on the other hand, the polarization vectors at different points of the beam are directed radially from the center to the outside or vice versa [132]. These states have found application in confocal microscopy [133] and laser micromachining [134], since the light focused at a large angle additionally acquires the influence of the z polarization component and changes the final beam intensity.

Complex polarization field beams

Polarized beams can be transformed not only into states with a regular arrangement but also with a more complex and intricate patterns. If the beam contains all types of polarization states, it is generally called a Poincaré beam, since when all the beam states are plotted on the already examined Poincaré sphere, the entire surface of the sphere is covered [135, 136] [see Fig. 2.32(a)]. The map of polarization states can be very diverse, some beams can have so-called polarization singularities [137, 138]. The polarization singularities are vector extension of scalar optical vortices and are similar to the phase singularities of optical vortices, as they have undefined state in the center (C-point) [139], they similarly have various topologies and charges [140, 141], which are classified into different types ("lemon", "star", "monstar", etc.), each having its own specifics [see Fig. 2.32(b)] [13, 142–147].

2.3.4. Tools for amplitude, phase and polarization control

Laser beam shaping is an integral part of micromachining, as the initial beam can be transformed to improve processing. There are many different methods for beam shaping: these can be amplitude [148, 149], phase [150], or polarization control [151]. The simplest way to change the beam structure is to place an obstacle in the propagation space. In this way, it is possible to filter out unnecessary parts of the beam and thus modulate the amplitude [68]. However, this primitive method has the drawback of energy loss and low overall throughput, which may not be sufficient to create defects in the material. Therefore, more precise and efficient beam shaping methods use phase and/or polarization manipulation.

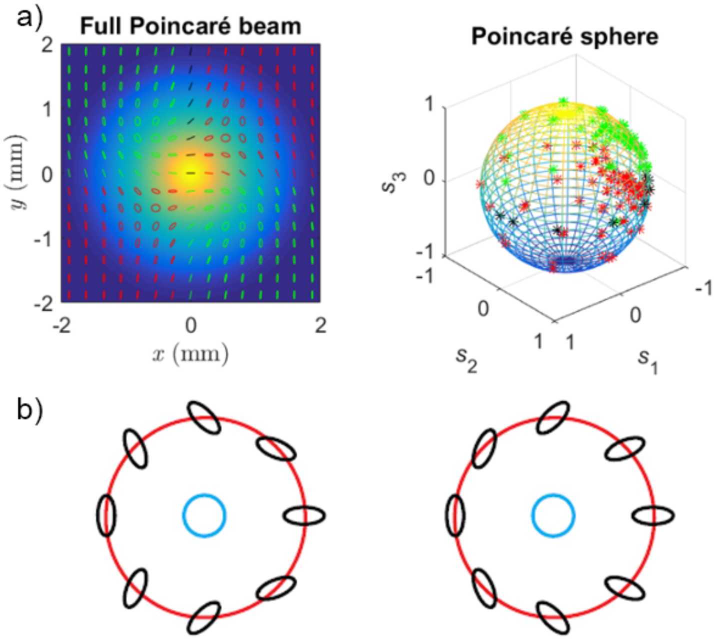

Figure 2.32: Representation of (a) a vector beam having multiple polarization states across transverse space (left) imaged on Poincare sphere (right), (b) schematic representation of beams with polarization singularities: C-point (center of the singularity) in blue circle and black polarization ellipses, where left image shows "star" shaped singularity with $-1/2$ topological index, and the right image with "lemon" shaped $+1/2$ topological index singularity. Adapted from Refs. [13, 136].

Diffractive optical elements

One of the first methods to transform a Gaussian beam into a beam with a different intensity distribution by manipulating the phase was to create diffractive optical elements [152–154]. Their operating principle is based on a difference in optical paths, as a result of which the transmitted light beam experienced a different phase delay and formed a new distribution behind the element [155]:

$$\Delta\phi = \frac{2\pi}{\lambda} nd, \tag{2.64}$$

where n is refractive index and d thickness of the material. The operating principle of diffractive elements can be understood from the example of a Fresnel lens (Fig. 2.33). Here, as the light propagates through a glass

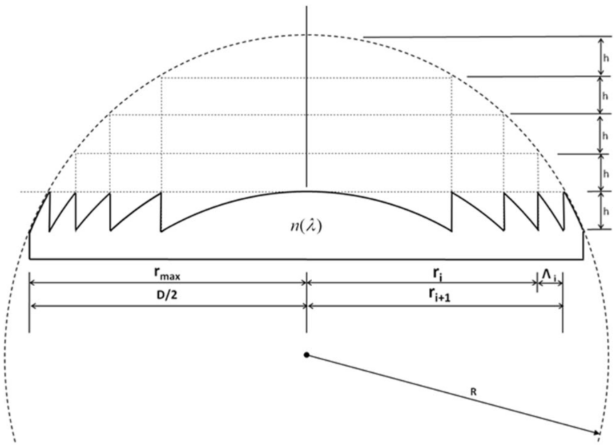

Figure 2.33: Design of a diffractive Fresnel lens with surface radius curvature R based on the principle of equal optical path difference. Adapted from Ref. [156].

of uneven thickness d, it refracts differently at different points of the element and a phase difference $\Delta\phi$ between the waves is created, and behind the element the light focuses, and thus we have an analog of a simple refractive lens. This method was later greatly improved, and it became possible to produce not only standard form diffractive elements but also unique, complex shape profiles that can generate the desired intensity distribution behind the element [154].

Spatial light modulator

Light beams can also be shaped using active elements, one of the most widely used examples being an optical light modulator. Its light control is based on the rotation of liquid crystals with respect to the incident light. Liquid crystals have birefringent properties and, upon application of an electric field, can change their angle, thereby changing the phase of the reflected light [157–160]. In this way, a matrix of liquid elements can be encoded so that individual pixels have a unique phase and, as a whole array, give the same effect as an optical element.

Spatial light modulators (SLMs) are a type of optical device that can control the amplitude, phase, or polarization of light in a spatially varying manner. They are widely used in a variety of applications, including laser beam shaping [150], optical microscopy [161], and holography [162].

There are two main types of SLMs: reflective and transmissive. Reflective SLMs use a mirror surface to reflect the incident light. The liquid crystal material is deposited on top of the mirror, and the electric field applied to the liquid crystal can change the angle of reflection of the light. This allows the SLM to modulate the phase of the reflected light (see example in Fig. 2.34).

Transmissive SLMs use a glass or plastic substrate to transmit the incident light. The liquid crystal material is deposited between the substrate and a transparent electrode. The electric field applied to the liquid crystal can change the refractive index of the liquid crystal, which in turn changes the phase of the transmitted light.

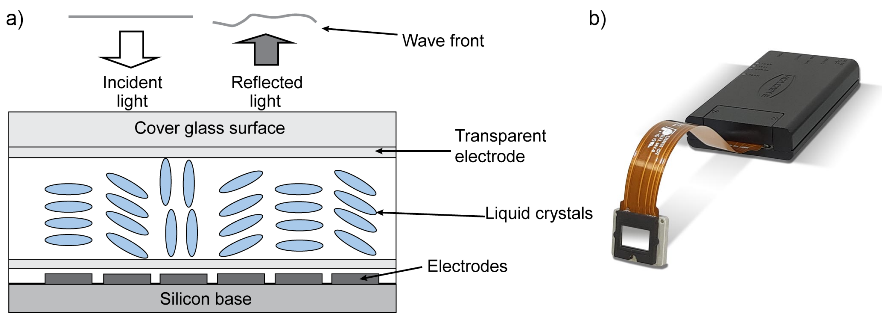

Figure 2.34: (a) Principal sketch of reflective spatial light modulator. The incident light is reflected with a modified phase front due to rotated birefringent liquid crystals. Author's image. (b) A representative image of a reflective spatial light modulator with an active pixel matrix.

Subwavelength metamaterials

Another interesting principle of beam shaping is the use of subwavelength structures to manipulate waves. Subwavelength metamaterials are a type of artificial material that is engineered to have properties that are not found in natural materials. These properties are achieved by creating structures that are smaller than the wavelength of light. The size of these structures allows them to interact with light in a way that is not possible for natural materials [163–165]. These structures of various shapes can change the properties of the passing wave due to their asymmetry [166, 167].

Metamaterials can be used to manipulate the propagation of light in a variety of ways. They can be used to control the phase, amplitude, and polarization of light [168]. They can also be used to create new types of optical phenomena, such as negative refraction and invisibility cloaking [169]. An example of a metamaterial-based optical element designed for laser beam shaping is depicted in Fig. 2.35.

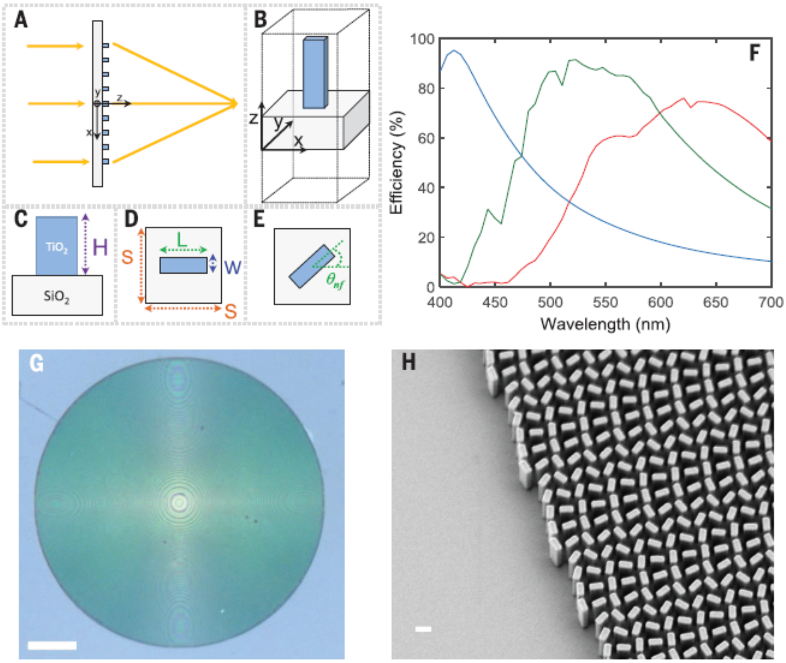

Figure 2.35: (a)-(e) Subwavelength size asymmetric structures made of TiO_2 nanofins on a glass substrate. (f) Simulated transmission spectra of designed metalens (g), scale bar is 40 µm. SEM images of the fabricated element, with a scale bar of 300 nm (h). Adapted from Ref. [167].

Geometric (PBP) phase optical elements

Light control can also be achieved using the previously discussed geometric (Pancharatnam-Berry) phase effect [170]. Birefringent nanogratings inscribed into a fused silica substrate at the desired angle in different positions can change the phase and, consequently, the polarization of the passing wave. Nanogratings are inscribed by direct laser writing and thus new optical elements can be fabricated: lenses, gratings, custom shaping elements, etc. [44, 132, 171]. The phase control through grating angles is described as [155]:

$$\Delta\phi = \frac{\pi}{\lambda}(n_e + n_o)d \pm 2\theta, \tag{2.65}$$

where θ is the grating rotation angle, n_e and n_o are the refractive indices for extraordinary and ordinary waves. The main principle of direct laser writing and examples of such elements are depicted in Fig. 2.36. These elements are unique in that the structures are inscribed only in

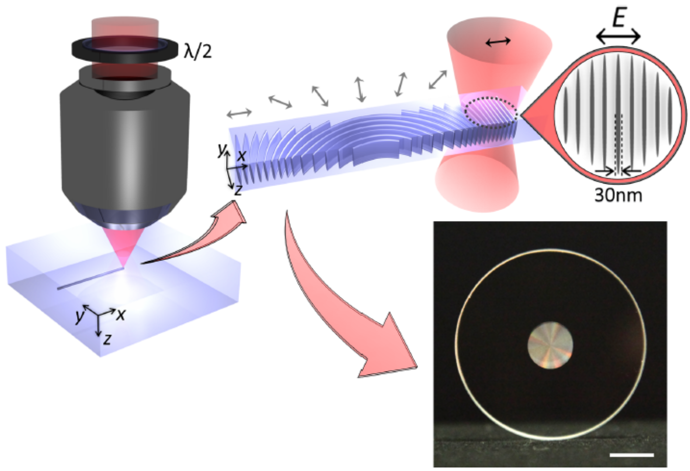

Figure 2.36: Principal illustration depicting manufacturing of geometric phase elements: type II or type X nanogratings are inscribed in the bulk of fused silica. Simultaneous control of focus in xyz space and orientation of the nanogratings by rotating linear polarization angle is demonstrated. Adapted from Ref. [172].

the glass volume, without changing the surface, and therefore have a very high optical breakdown threshold reaching 2.2 J/cm^2 at 1030 nm wavelength (212 fs regime) or 63.4 J/cm^2 at 1064 nm wavelength (10 ns regime) [173]. These values are very close to the material optical damage threshold from which they were made (in this case fused silica), thus exceeding the damage threshold of an SLM by several orders. Another advantage is a high transmission for visible and NIR spectrum, as the inscribed nanogratings under type X regime scatter light minimally and efficiently transform radiation [44, 174]. In this thesis, the geometric phase elements will be used as the main beam-shaping optical elements for applications in ultrashort laser micromachining.

3. METHODOLOGY

The results of this dissertation are based on numerical modeling and experimental work with laser systems. Initially, in the early stages of the work, numerical modeling was employed to design and simulate beam propagation in free space utilizing (geometric) phase optical elements by using propagation models presented in the literature review section. The results were analyzed, with most of the attention focused on how the intensity, phase, or polarization states of an ideal Gaussian beam are transformed. Then, various numerical simulation cases were tested using the SLM to ensure that the results of numerical simulations were replicable in the laser systems. Based on the selected numerical modeling and SLM-tested results, experimental work was conducted, during which geometric phase elements were fabricated and tested in powerful ultrashort pulse laser systems. The laser-matter interaction of the newly formed and unique ultrashort laser beams was investigated. The samples were inspected using measurement equipment. The presented numerical modeling algorithms and laser ablation of materials experiments using an ultrashort pulse laser system were also employed to develop the beam shaping elements for THz radiation.

3.1. Numerical modeling of GPEs and THz elements

Numerical beam propagation modeling was conducted using "Matlab" (*Mathworks, Inc.*) programming environment. A diffraction modeling package based on Fresnel and Rayleigh-Sommerfeld diffraction integrals was developed, refined, and commonly used in the laboratory. This numerical tool enabled us to simulate even complex phase, polarization distribution beams. The simulation results presented in the fourth and fifth chapters of the dissertation and the analysis of quantized phase masks discussed in the sixth chapter were done using this tool.

Numerical modeling of geometric phase elements

The principal diagram of numerical modeling steps is visualized in Fig. 3.1. An initial mesh grid of 512 x 512 pixels was created with a pixel size of 6 µm. Then, a Gaussian amplitude distribution beam

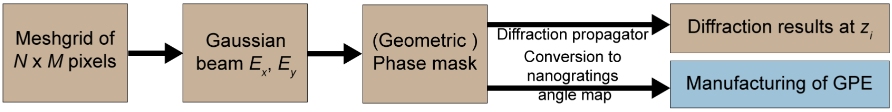

Figure 3.1: Principal diagram of numerical GPE modeling shown in steps: allocate mesh grid of $N \times M$ size; define Gaussian amplitude distribution beam with electric field components E_x and E_y; apply the (geometric) phase mask on both E_x and E_y components; the last step was either the application of diffraction propagator to observe the change in the electric field distribution after propagation of certain z_i distance, or the phase mask is converted to a map of nanogratings angles, and retardance used for manufacturing the element.

with electric field components E_x and E_y was created. The central wavelength of the ultrashort pulse laser was $\lambda = 1030$ nm; therefore, we also used this wavelength for numerical simulations. The x and y components are required to apply the change of polarization state due to the spatial distribution of birefringent material using the Jones matrix formalism [taken from Eqs. (2.29) to (2.32)]. This also allows the analysis of the beam polarization state spatial distribution. In the next step, an optical element was defined and applied to the incoming beam. This step changes the beam properties such as amplitude, phase or polarization state. For all the presented cases, the retardance was selected as $\lambda/2$, mimicking a half-wave plate with a spatially varying orientation angle. Then, by applying a diffraction propagator with the use of a Fresnel or Rayleigh-Sommerfeld diffraction integrals, the spatial distribution of electric field E_x and E_y components are retrieved at a defined position z_i on z axis. The calculation of E_z was omitted because a low numerical aperture focusing was used in the experiments.

The geometric phase element was converted to a map of linear polarization angles to be used in the nanograting inscription process with a relation:

$$\vartheta_{writing} = \frac{\Delta\phi}{4} - \frac{\pi}{2}. \tag{3.1}$$

This relation arises because the nanogratings' inscription angle follows the rotation angle of the linear polarization. Since the direction of the nanogratings is perpendicular to the linear polarization vector, it follows the relationship $\vartheta_{writing} = \theta/2 - \pi/2$, where θ represents the geometric phase. Moreover, the geometric phase depends on the relationship $\theta = \Delta\phi/2$ [from Eq. (2.65)].

Numerical modeling of silicon-based THz elements

A similar numerical modeling procedure was used for generating phase masks of THz elements from silicon. A principal diagram is depicted in Fig. 3.2. A mesh grid of 1000 x 1000 pixels was created with

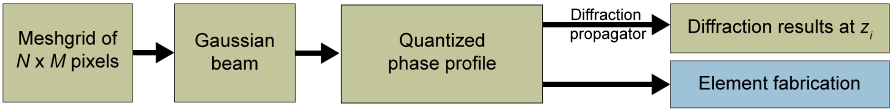

Figure 3.2: Principal diagram of numerical THz element modeling, shown in steps: allocate mesh grid of $N \times M$ size; define Gaussian amplitude distribution beam of single polarization component, apply the quantized phase profile, and apply the diffraction propagator to retrieve the resulting field at the defined distances z_i. The phase profile can be recalculated to an ablation depth distribution used for element fabrication.

a pixel size of 30 µm. The incoming beam was a scalar ideal Gaussian beam with a central wavelength of 0.5 mm, corresponding to 0.6 THz. The defined continuous profile phase mask $\Phi(r)$ was converted to a multilevel mask by quantizing to N step-like profile:

$$\Phi(r) = \frac{2\pi}{N}\left\lfloor \frac{N\Psi(x,y)}{2\pi} - N\left\lfloor \frac{\Psi(x,y)}{2\pi} \right\rfloor \right\rfloor, \tag{3.2}$$

where $\Psi(x,y)$ is a continuous phase profile of the designed element and the brackets $\lfloor\ \rfloor$ represent a rounding operation, with N being the integer number of levels in the phase mask. The resulting phase profile $\Phi(r)$ can be height encoded using the relation $\lambda\Phi(r) = 2\pi(n-1)h(r)$, where $h(r)$ are local near-wavelength variations in surface height, n is the refractive index of the material. With the applied diffraction propagator, we have retrieved the beam intensity distribution at the desired plane on the z axis. Lastly, the map of a quantized phase profile was used to encode a fabrication algorithm for silicon ablation.

The experimental work was conducted using three different laser setups utilizing three different laser sources. The main parameters of each laser are described in Table 3.1. The low-power CW diode-pumped

Model, manufacturer	MGL-III-532, *CNILaser*	Pharos SP, *Light Conversion*	Carbide, *Light Conversion*
Active medium	Nd:YAG	Yb:KGW	Yb:KGW
Emission type	continuous wave	pulsed	pulsed
Wavelength λ, nm	532	1028	1030
Mulse duration FWHM τ, ps	-	0.158 – 15	0.358 – 10
Max. average power P, W	0.1	6	4
Repetition rate f, kHz	-	4–200	60–1000
Max. pulse energy E_p, µJ	-	30 – 1500	4 - 50
Beam quality factor, M^2	< 1.4	< 1.3	< 1.2

Table 3.1: Main parameters of the laser sources used in experimental setups.

solid-state "MGL-III-532" laser was used to illuminate the spatial light modulator, which served as a dynamic tool for quick experimental verification of numerical modeling results. The SLM could not be used for high-power ultrashort laser irradiance because of its low optical damage threshold. The other two ultrashort pulse lasers, "Pharos SP" and "Carbide," were used to perform laser micromachining tests with beams produced with the help of GPE's, and were also used to manufacture THz elements.

Optical setup with spatial light modulator

The principal optical setup used in the fourth chapter employing SLM and low-power continuous wave laser is depicted in Fig. 3.3. The optical setup with SLM consists of a low-power CW laser producing a linearly polarized Gaussian beam of 3 mm width, which was used to illuminate a phase-only reflective spatial light modulator "PLUTOVIS-A" (*HOLOEYE Photonics AG*) having 1920x1080 px resolution. The beam is reflected off the SLM with a transformed phase front, and it is spatially compressed with an optical $4f$ system, consisting of a pair of lenses with focal lengths $f_1 = 300$ mm and $f_2 = 100$ mm. The compression ratio in transversal and longitudinal coordinates are $f_1/f_2 = 3$ and

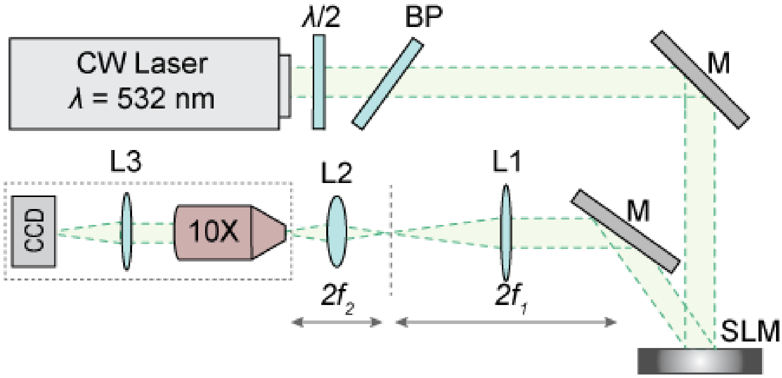

Figure 3.3: Principal optical scheme employing a low-power CW laser and spatial light modulator used as a beam shaping tool. Low power continuous wave laser of 532 nm wavelength is used as the source, BP - Brewster polarizer, M - mirrors, L1, L2 and L3 – plano-convex lenses of 300 mm, 100 mm and 200 mm focal lengths, respectively, 10X - 10 times magnifying microscope objective, CCD - imaging camera.

$(f_1/f_2)^2 = 9$, respectively. The reflected beam is then imaged onto a CCD camera ("WinCamD-LCM", *DataRay, Inc.*) with a pair of two elements: a $f_3 = 200$ mm lens and a 10X magnifying microscope objective, working as another, magnifying $4f$ system. The imaging system consisting of these components was placed on a motorized linear translation stage ("7T175-150", *Standa*) to capture the three-dimensional structure of the diffracted field by scanning along the z axis.

Ultra short pulse laser systems

Experimental GPE testing and THz element fabrication were conducted using laser systems, shown in Figure 3.4. The laser system from Fig. 3.4(a) was used to obtain experimental results presented in fourth (Bessel-type beam generation) and sixth (THz element manufacturing) chapters. The system consisted of: laser source "Pharos SP"; four linear translation stages: xy 50×50 mm travel stage "ANT90-XY" (*Aerotech Inc.*), 50 mm travel z stage "ANT90-L-Z" (*Aerotech Inc.*) and 300 mm travel additional x axis "PRO165-LM" (*Aerotech Inc.*); galvanometer scanner "IntelliScan 14" (*ScanLab*) paired with $f = 100$ mm focal length telecentric F-theta lens; fume extractor and air blower for dust removal; sample holder connected to a vacuum pump ensured that the samples

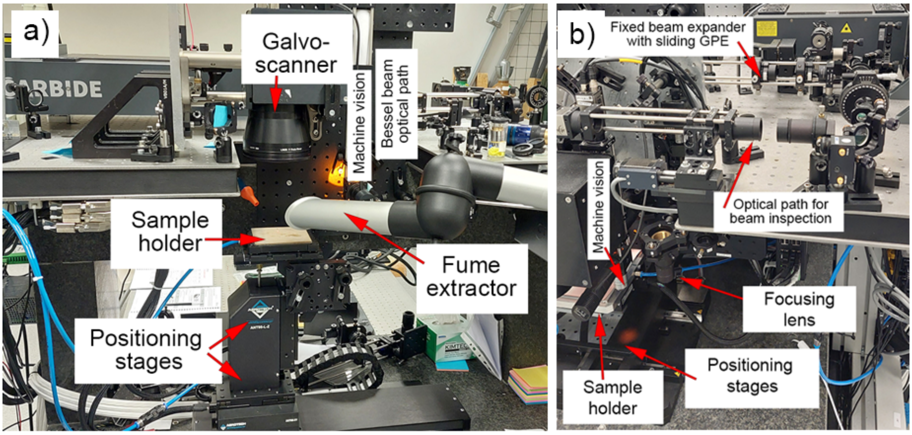

Figure 3.4: Photographs of USP laser systems: (a) setup used for Bessel-type beam experiments (fourth section) and THz element fabrications (sixth section); (b) setup used to obtain results in the fifth section. Note that the photography in (a) was made after changing the laser source.

would remain in place.

The principal optical scheme used for Bessel-type beam experiments is depicted in Fig. 3.5. The laser source was used to produce a linearly polarized Gaussian beam of 9 mm width (at the intensity level of $\exp^{-2}$, spatially compressed to 3.5 mm width using a mechanical variable beam expander from *Altechna*). The power of the laser was controlled with a $\lambda/2$ half-wave plate and a Brewster polarizer. The $\lambda/4$ quarter-wave plate converted the incoming linear polarization to circular, which illuminated GPE afterward. A pair of lenses ($f_1 = 150$ mm and $f_2 = 8$ mm) was used to construct a $4f$ imaging system, which compresses the beam 18.75 times to increase the maximal fluence for micromachining of transparent materials. The beam was imaged onto an imaging camera "UI-5240CP" (*IDS*) by a single-lens imaging system utilizing a 40X magnifying microscope lens. The micromachining of transparent samples was performed in the same setup after the spatial intensity distribution analysis of the beam was finished and the imaging system was removed.

For the manufacturing of THz elements, the same laser system was used, but for this case, the additional x axis was used to move the sample holder under the working area of the galvanometer scanner. The

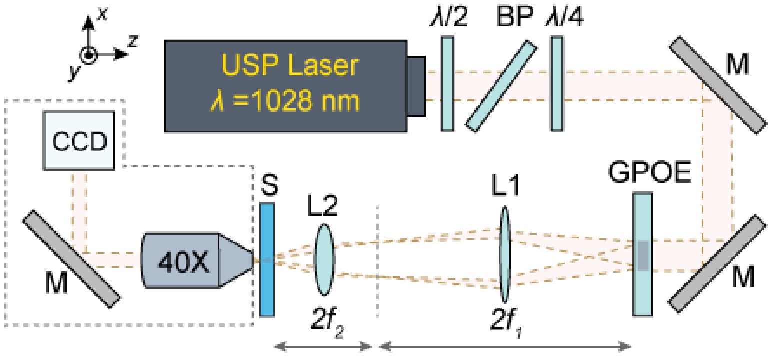

Figure 3.5: Optical scheme used for Bessel-type beam experiments consisting of an ultrashort pulse laser "Pharos SP" with central wavelength at 1028 nm, a pair of $\lambda/2$ waveplate and BP - Brewster polarizer was used as an attenuator for power control, $\lambda/4$ used for circular polarization conversion, M - dielectric mirrors, GPOE - geometric phase element, L1 and L2 - plano-convex lenses of 150 mm and 8 mm focal lengths, S - transparent glass sample, 40X - 40 times magnifying microscope objective.

optical setup depicted in Fig. 3.6 was used for rapid ablation. The most important part of this optical branch is the galvanometer scanner, which has a pair of lightweight mirrors. With the ability to rotate them, the laser beam can be scanned at high speed in x and y directions, reaching several meters per second. It can greatly reduce fabrication time compared to moving stages having larger inertia. In a pair with a telecentric F-theta lens of $f = 100$ mm focal length, the laser beam can be focused into a spot of approximately 19 µm in diameter, over 54×54 mm working field size.

The laser system shown in Fig. 3.4(b) was used to obtain experimental results presented in the fifth chapter. The system consists of linear xy stages having $200{\times}200$ mm travel "V-731" (*Physik Instrumente*) paired with 5 mm travel z stage "ANT130V" (*Aerotech Inc.*) and a sample holder on top, connected to a vacuum pump. Figure 3.7 depicts the principal optical setup used for this study. Two beam propagation paths are presented. The first path is for micro-machining of the samples, and the second one, behind flippable mirror M2, is for the imaging of the beam. The laser power was attenuated by a rotatable half-wave plate and a pair of Brewster polarizers. A quarter-wave plate was used

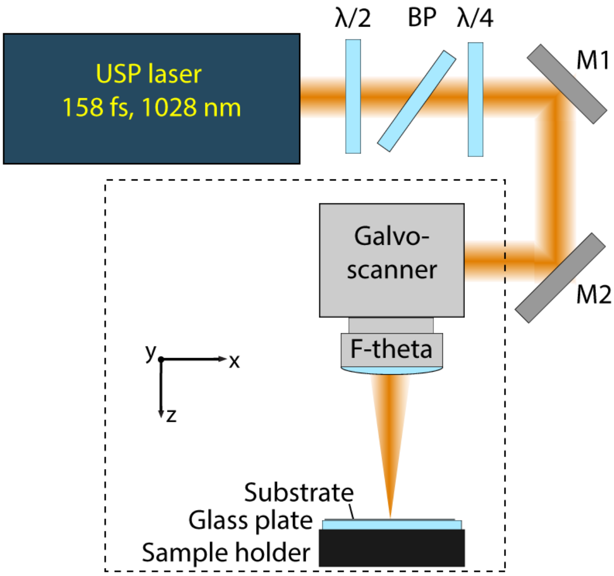

Figure 3.6: Principal optical scheme of laser ablation system: USP "Pharos SP" laser emitting 9 mm width Gaussian beam [at exp(-2) level], a pair of $\lambda/2$ waveplate and BP - Brewster polarizer was used as an attenuator for power control, $\lambda/4$ used for circular polarization conversion, M1-M2 are dielectric mirrors, the galvanometer scanner was "IntelliScan 14" (*ScanLab*), F-theta lens was with $f = 100$ mm focal length. The substrate was put on an additional perforated glass plate to protect the sample holder from laser light as the substrate would be ablated through.

to convert a linear polarization beam to circular polarization. The lens $L1$ was used to focus a laser beam for material processing. The focal length of $L1$ was $f = 8$ mm or $f = 50$ mm, depending on the material to be processed. A Glan polarizer and a rotatable quarter-wave plate were used for the Stokes parameter measurements in the beam imaging optical branch, following the technique described in [175]. Another $f = 8$ mm focal length lens $L2$ was used in combination with the microscope objective that has a magnification 50x to obtain the magnification of the focal point of the beam and the imaging on the CMOS camera "UI-5240CP" (*IDS*). This optical path was crucial for the adjustment of the laser beam size to obtain the desired beam intensity distribution at the focus.

Another important system part was a fixed magnifying telescope

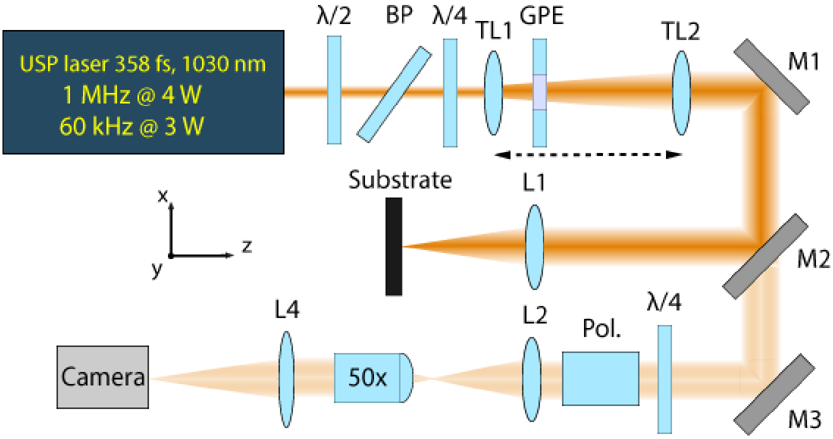

Figure 3.7: Principal optical setup used in fifth section: "Carbide" laser source, $\lambda/2$ - half-wave plate, BP - Brewster polarizer, $\lambda/4$ - quarter wave plate, $TL1$ - a plano-concave lens of $f = -50$ mm, GPE – Geometric phase element, $TL2$ - a plano-convex lens of $f = 100$ mm, $L1$ is focusing lens of $f = 8$ mm or $f = 50$ mm focal length, 50x - magnifying microscope objective in pair with $L4$ lens ($f = 200$ mm) and CMOS camera is used for beam intensity measurements, $M1 - M3$ are dielectric mirrors.

constructed out of TL1 ($f = -50$ mm) and TL2 ($f = 100$ mm) lenses. A GPE was put inside the telescope and could be slid along the optical axis as needed for the application. This solution provided easier control of the ratio between the input beam and the aperture of the element, as it will be covered in the fifth section. The slight divergence angle in the constructed telescope can be neglected (angle of incidence less than $0.2°$).

In all the presented laser systems, a system control application, "SCA" (*Workshop of Photonics*), was used. This software combines the work of the laser and translation, rotation stages, as well as other motorized optical components, and lets to program complex fabrication algorithms.

3.3. Manufacturing of geometric phase elements

The geometric phase elements investigated in this study were fabricated using a commercial laser system developed by "Workshop of Photonics" (WOP). The fabrication technology was developed by Prof.

P. Kazansky's team at the University of Southampton in collaboration with WOP and is patented [176]. The production system is based on an ultrashort-pulse laser source and a 5-axis positioning system. Three axes correspond to linear motion in the xyz coordinates, while two additional rotational axes are responsible for polarization rotation, enabling the alignment of the nanogratings orientation and the control of laser power to achieve the desired retardance value. By increasing the number of recorded layers, the retardance can be adjusted from a few nanometers up to at least 2000 nm. The standard substrate used is fused silica glass with a diameter of 1 inch or smaller. An example of a fabricated element and the production system is shown in Fig. 3.8.

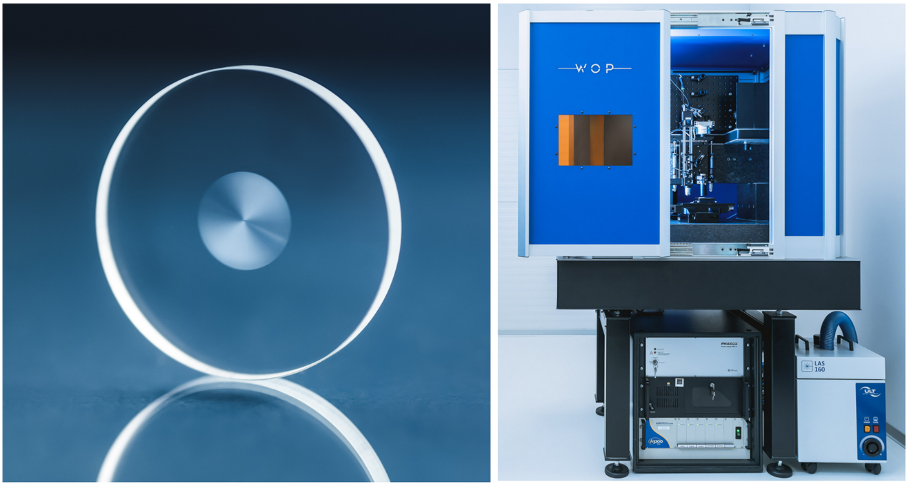

Figure 3.8: A photograph of a standard manufactured geometric phase element (on the left) and commercial laser manufacturing system produced by Workshop of Photonics (on the right).

3.4. Equipment for sample inspection

The experimentally obtained samples were inspected by using the following laboratory equipment:

- Optical microscope Olympus BX51 paired with MPlanFL objectives from 5X to 50X magnification (NA ranging from 0.15 to 0.75).
- Optical microscope Nikon Eclipse LV100ND paired with Plan

Fluor objectives from 5X to 50X magnification (NA ranging from 0.15 to 0.8).

- Birefringence microscope "Exicor MicroImager" (*Hinds Instruments*).
- Optical confocal profiler "S neox" (*Sensorfar*).
- Scanning electron microscope "Axia ChemiSEM" (*Thermo Fisher Scientific Inc*).
- Power meter for element transmission measurements "NOVA II" (*Ophir*).

4. TRANSFORMATIONS OF BESSEL-TYPE BEAMS IN AIM FOR TRANSPARENT MATERIAL MICRO PROCESSING

The Bessel-type beams and their variations are attractive choices in applications where high aspect ratio modifications in transparent materials are needed [177–179]. The elongated and narrow central part of the zeroth-order Bessel-Gauss beam perfectly fits for high width/depth ratio material modification creation in various transparent materials [116, 180–182]. These invariant beams have found many suitable applications in transparent material processing, such as Bragg grating writing [183], generation of microchannels [75] or microcracks formation [184] that can enhance glass cutting processes [55].

Yet the simplest method to experimentally produce a Bessel-Gauss beam is with the use of an axicon [120], a conical lens that has a sharp tip at the center [119]. However, to generate high-quality, modulation-free Bessel beam a precisely manufactured axicon is required, otherwise, any irregularities, especially in the tip sharpness, may critically worsen the properties of the beam. For instance, the round tip of the element will produce axial intensity modulation and central core distortions [185] that may become so severe that the produced material modification will not be homogeneous. If beam axial intensity modulation has high contrast, it may even produce separated damages along the propagation axis. Therefore, there is a need to have a beam shaping alternative which could not only shaped distortion-free beams, but also could suffer high laser power. For this reason, the employment of geometric phase elements can serve as a great Bessel beam shaping technique, in utilization for glass cutting.

4.1. Concept of spatial dislocations in axicon phase mask

The material related to this thesis chapter was published in papers ***[A1]****,* ***[A6]*** *and* ***[A7]****.*

In this first part of the research, the axicon is customized and produced as a geometric phase element, mimicking the phase mask of the concentric grating map. The ability to control nanograting orientation, therefore the phase, enables to manufacture custom axicons, for example, having distorted phase patterns. This opens up the possibility to create unique beams using a single element instead of combining a few conventional ones.

Analytical solution of beams generated by superposition of spatially displaced halves

One of the approaches to find new fanciful invariant beams is via the spatial displacement of the axicon halves. The phase profile with which the axicon alters the incoming beam is expressed by a transmission function [120, 186]:

$$T(r) = \exp\left(\frac{-2i\pi r}{r_0}\right), \tag{4.1}$$

where $r = \sqrt{x^2 + y^2}$, $r_0 = 2\pi/\left(k \sin\theta_c\right)$ is the distance at which phase jumps from 0 to 2π, it also defines the cone angle of the phase front.

By using phase masks of the axicon that are split into two halves to experimentally recreate unique non-diffracting intensity patterns that resemble the analytically obtained solutions of spatially displaced and superposed Bessel beams. Hence, the original transmission function is split into two equal parts at the center of the axicon mask, ending with one having only negative and another only positive x values. The introduced spatial shift by p of both sides in opposite directions in respect to the x axis results in the transmission function in the form:

$$T_p = \begin{cases} \exp\left[\dfrac{-2i\pi}{r_0}\sqrt{x^2 + \left(y + \frac{1}{2}pr_0\right)^2}\right], & x < 0 \\ \exp\left[\dfrac{-2i\pi}{r_0}\sqrt{x^2 + \left(y - \frac{1}{2}pr_0\right)^2}\right], & x > 0 \end{cases} \tag{4.2}$$

here x, y are coordinates of the mask, p is the parameter of the displacement between two halves of the initial phase mask. This number is measured in fractions of the circular grating period r_0. Examples of spatial phase profiles with three different p parameters (0, 0.5, and 1) are shown in Fig. 4.1.

To analytically investigate the field structure, consider finding solutions using Fresnel integral expression in cylindrical coordinates and the transmission of n-th order Bessel beam [5]. In this case, it takes

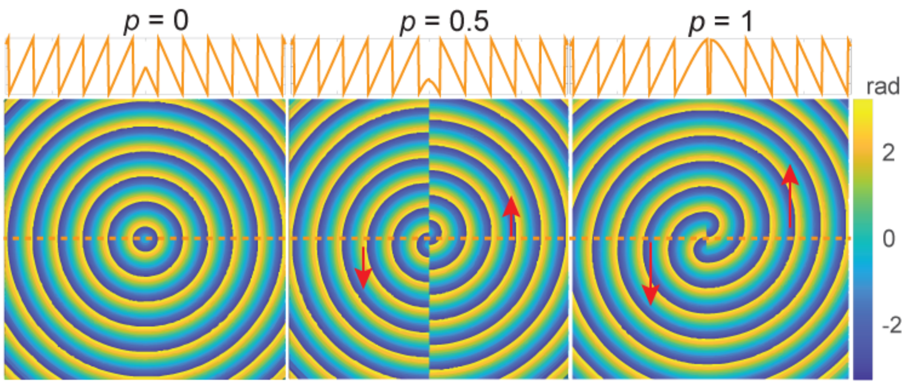

Figure 4.1: Examples of the resulting phase mask of a diffractive optical element, where p is a displacement parameter, expressed in fractions of circular grating period r_0 (distance between 0 and 2π values). The subplots on top represent the same cross-section of the phase distribution at the tip of the resulting DOE.

form [150]:

$$\begin{aligned} E(\rho, \phi, z) =& \frac{2\pi \exp\left[ik\left(z + \rho^2/2z\right)\right]}{i\lambda z} \\ &\times \sum_{n=-\infty}^{\infty} a_n(-i)^n \exp(in\phi) \\ &\times \int_0^D \rho' T(\rho') J_n\left(k\rho\rho'/z\right) \exp\left(ik\rho'^2/2z\right) \mathrm{d}\rho', \end{aligned} \tag{4.3}$$

where a_n is:

$$a_n = \frac{1}{2\pi} \int_0^{2\pi} A\left(\phi'\right) \exp\left(-in\phi'\right) \mathrm{d}\phi'. \tag{4.4}$$

Considering two parts of the transmission separately and using non-displaced cylindrical coordinates of their centers, the following expressions a_n for the left ($x < 0$) and right ($x > 0$) phase masks are derived:

$$\begin{aligned} a_n =& \frac{2 \sin\left(\frac{n\pi}{2}\right)}{n}, && x > 0, \\ a_n =& \frac{2\left(-1\right)^n \sin\left(\frac{n\pi}{2}\right)}{n}, && x < 0. \end{aligned} \tag{4.5}$$

Now, the diffraction from two parts of the mask can be calculated, however, the expressions are valid only in the shifted coordinates. To express fields in the coordinates (r, φ) of the center of the resulting mask, the so-called addition theorem for the Bessel functions is used [12]:

$$
\begin{aligned}
J_n(\lambda\rho)\exp(in\phi) = \sum_{m=-\infty}^{\infty} J_m\left(\frac{\lambda p r_0}{2}\right) J_{n+m}(\lambda r) \\
\times \exp\left[in\varphi + im(\varphi - \phi_0)\right].
\end{aligned} \tag{4.6}
$$

Here, the angle $\phi_0 = \pm\pi/2$ for the right (+) and left (−) sides correspondingly, and $\lambda = k\rho'/z$, see Eq. (4.3). Using Eq. (4.6) and rewriting Eq. (4.3) with Eqs. (4.5) as

$$
\begin{aligned}
E(r,\varphi,z) \propto \sum_{m,n=-\infty}^{\infty} \frac{4\sin\left(\frac{n\pi}{2}\right)}{n}\delta_{m+n,2\mu}(-i)^{m+n} \\
\times \exp\left[i(n+m)\varphi\right]\int_0^D \rho' T(\rho') J_m\left(\frac{k\rho' p r_0}{2z}\right) \\
\times J_{n+m}\left(\frac{kr\rho'}{z}\right)\exp\left(\frac{ik\rho'^2}{2z}\right)\mathrm{d}\rho',
\end{aligned} \tag{4.7}
$$

where μ is an integer number and δ is the Kronecker's function. The proportionality is used to simplify the equation and lose the constant term in the equation. Estimation of the leading part of the integral using the stationary phase method is done. The stationary point of the integral is at $\rho' = 2\pi z/(kr_0)$ [150]. So, approximately, Eq. (4.7) can be rewritten as

$$
\begin{aligned}
E(r,\varphi,z) \propto \sqrt{\frac{8z}{k}}\exp\left(i\frac{2z\pi^2}{kr_0^2}\right) \\
\times \sum_{\mu,n=-\infty}^{\infty}\left[2\pi\delta_{n,0} + \frac{4(-1)^\nu}{n}\delta_{n,2\nu+1}\right] \\
\times (-i)^{2\mu} J_{2\mu-n}(\pi p) J_{2\mu}\left(\frac{2\pi r}{r_0}\right)\exp(2i\mu\varphi),
\end{aligned} \tag{4.8}
$$

where a relation $\sin(n\pi/2) = (-1)^\nu\delta_{n,2\nu+1}$ $(n \neq 0)$ with ν being also an integer number, was used. Finally, rewriting Eq. (4.8) as

$$
\begin{aligned}
E(r,\varphi,z) \propto \sqrt{\frac{8z}{k}}\exp\left(i\frac{2z\pi^2}{kr_0^2}\right) \\
\times \sum_{\mu=-\infty}^{\infty}(-1)^\mu A_\mu(p) J_{2\mu}\left(\frac{2\pi r}{r_0}\right)\exp(2i\mu\varphi),
\end{aligned} \tag{4.9}
$$

where coefficients $A_\mu(p)$ are

$$A_\mu(p) = \sum_{n=-\infty}^{\infty} \left[2\pi\delta_{n,0} + \frac{4(-1)^\nu}{n}\delta_{n,2\nu+1}\right] J_{2\mu-n}\left(\pi p\right). \tag{4.10}$$

Firstly to note, the presence of only even order non-diffracting Bessel vortices in Eq. (4.9), so the beam profile has inversion symmetry and the values at azimuths ϕ and $\phi+\pi$ coincide. Second, from Eq. (4.10) comes $A_{-\mu} \neq A_\mu$ and the expansion coefficients demonstrate an oscillatory behavior as p changes. Analysis reveals that in general, the diffracted field is always a superposition of many even-order Bessel non-diffracting beams. The amplitude of the zeroth-order Bessel beam is $A_0 = 2\pi J_0(\pi p)$ and this term is always present in the expansion, except the cases when $A_0 = 0$. In the region of interest ($p \in [0, 2]$) this happens for $p \approx 0.765$ and $p \approx 1.755$ etc. As a result, no electric field is present in the center of the diffracted field in those two cases. For the first zero $p \approx 0.765$, the situation is similar to a coherent addition of two Bessel vortices with topological charges -2 and 2 (as depicted in example in Fig. 2.29).

4.1.1. Numerical modeling and experimental results

Numerical modeling and comparison of the results

The presented analytical solution is only valid for plane wave illumination, i.e., beams with infinite energy, the apodization effects of the initial beam are not accounted for. By introducing the initial Gaussian beam intensity distribution, the numerical modeling is executed, comparing the results with the experiment. The spatial displacement parameter p was changed in steps of one quarter up to $p = 2$, and profiles of transverse intensities were evaluated over the full length of the Bessel zone. The parameter r_0, which describes an effective Bessel angle, was $r_0 = 80$ µm. This is equivalent to a half-angle $\theta_c = 0.74°$ of the Bessel beam cone. Results of numerical simulations are presented in Fig. 4.2. For the comparison, the experimental data, which was obtained with the SLM, is depicted in Fig. 4.2, too. Transverse intensity distributions of resulting patterned non-diffracting beams were measured in the middle of the Bessel zone. Additionally, the far-field intensity distributions of all beams together with the used phase masks are also presented in Fig. 4.2.

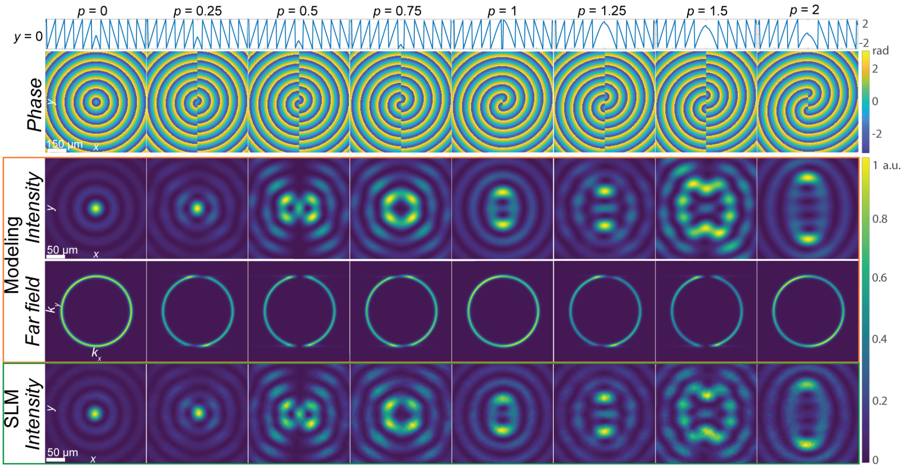

Figure 4.2: Intensity patterns of non-diffracting beams as a function of the spatial displacement between two halves of axicon masks. The displacement p is given in steps of the quarter period. The phase period $r_0 = 80$ μm is selected so, that the Bessel beam cone half-angle is $\theta_c = 0.74°$. The bottom row depicts the intensity distribution of experimentally generated by using a spatial light modulator.

As expected, the results of numerical simulations are in line with the analytical predictions. When no displacement ($p = 0$) is present, one observes a generation of a zeroth-order Bessel-Gauss beam of high quality, i.e. the transverse intensity profile consists of a central peak surrounded by concentric rings. The far-field structure is expectantly a ring-like intensity distribution. An introduction of the relatively small spatial shift $p = 0.25$ results only in a small transverse intensity modulation that is mostly visible on the outer ring. The central peak obtains slight ellipticity, i.e., elongates in the direction of the spatial shift. Modulation of the spatial spectrum is observed - the ring is separated visibly into two halves, with an intensity nearly zero on the k_y axis at $k_x \approx 0$.

The displacement between half-masks of a half period causes more radical distortions in the beam transverse intensity pattern to appear - the intensity of the central core is not highest in the profile anymore. The analytical analysis shows that the natural cause for that is the decreasing amplitude of the zeroth-order Bessel beam in the superposition Eq. (4.9), whilst amplitudes of higher-order Bessel beams increase, see Eq. (4.10). The central peak is surrounded by rings that have a strong intensity modulation and the first ring intensity peaks are higher than the central spike, see Fig. 4.2. The region of near-zero intensity at the intersection of negative and positive x half-planes is clearly visible.

As predicted in the analytical analysis section, the displacement of $p = 0.75$ causes the zeroth-order Bessel beam to disappear, therefore an intensity minimum is at the center of the beam appears and a phase singularity with the topological charge of $m = 2$ is present, see Ref. [122]. Four interconnected intensity peaks forming a ring are observed. If the displacement becomes equal to the full period ($p = 1$) - the pattern of the resulting non-diffracting beam is transformed into a double-peak structure and the two central minima are formed. An analytical investigation reveals that two adjacent vortices of opposite signs form this structure, while the total topological charge is zero.

When the value of p is further increased, two separate peaks appear in the transverse profile. This happens for $p = 1.25$, see Fig. 4.2. Moving on to the displacement $p = 1.5$, the analytical formulas predict an appearance of Bessel vortices with topological charges -4 and 4, and as it is near to the second zero of the amplitude A_0 the previously observed morphology of the resulting intensity distribution is replicated with higher variability in the azimuthal modulation. Once again, the central peak is very weak.

Analogically to the previously discussed cases with displacements $p = 1$ and $p = 1.25$, two distinct intensity extremes for $p = 2$ are observed, see Fig. 4.2. In this case, the distance between them is bigger and two pairs of single-charged vortices with opposite signs are observed. Because of that, the elliptically shaped profile of the resulting non-diffracting beam is now more expressed. A careful analysis reveals that due to the periodicity in $A_\mu(p)$ coefficients in Eq. (4.10) such double-peaked structures in the transverse profile are observed when the displacement p is nearly integer. Increasing the displacement p parameter even further, the extremes are even more separated and new pairs of single-charged vortices with opposite signs do appear. Thus, a controllable double-peaked Bessel-type beam can be created.

Beams shaped using manufactured GPEs

The most promising for specific laser micromachining applications cases are those with displacement values of $p = 0, 0.25, 1$ and 1.25. Therefore, the GPEs were designed to mimic the phase masks of DOE with the mentioned displacements. The experimentally measured distributions for the slow axis of actual manufactured GP elements are depicted in Fig. 4.3. Important note, that the geometrical phase ele-

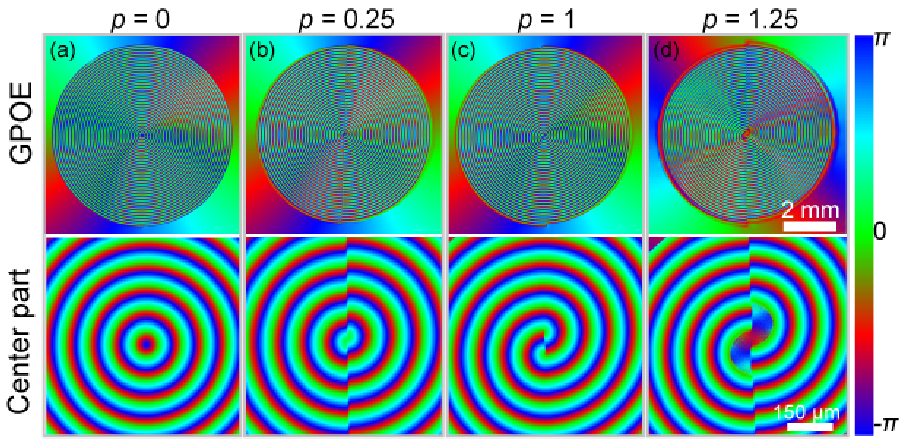

Figure 4.3: Images of slow axis distributions in fabricated GPEs for different spatial displacements p for a whole element (top row) and zoomed in centers of elements (bottom row), when (a) $p = 0$, (b) $p = 0.25$, (c) $p = 1$, (d) $p = 1.25$. Images were obtained using a birefringence microscope.

ment designed with displacement $p = 1.25$ [see Fig. 4.3(d)] is fabricated with the central part of the element being empty. No nanogratings are inscribed in its very center. This area is approximately 80 µm in radius, and the phase should change here up to π. The clear aperture of the element was 8 mm while the beam width [at the intensity of exp(-2)] was 3.5 mm, therefore the unwritten part is minuscule compared to the full element and beam diameter. Another nuance about manufacturing of such a complex pattern of concentric gratings-based slow axis is that it is difficult to accurately measure the retardance profile for final GPE, as the element would distort the measurement of birefringence data to due to initiating diffraction. Therefore, before the final inscription, a single layer of the proposed axicon pattern is made to find relevant retardance, and by extrapolating the number of writing layers to the amount of several layers, the final element is set to be manufactured.

It was noticed that a very sharp change in the orientation of the nanogratings cannot be replicated very precisely in the GPE manufacturing process, because it induces unwanted material stress and impacts the birefringence in the element. The quality of fabrication is drastically decreased in these parts and as a consequence, the accuracy and efficiency in the shaping of the incoming beam are lost. However, it was observed that the absence of the tip allows the material to relax, and material stress does not propagate far in this case. Numerical simulations have also revealed that the small empty area in the center of the GPE does not change the beam quality substantially, because the area that is empty amounts only to 1/5000 part of the whole element. Besides, simulations reveal that GPE manufacturing errors (irregularities) resulting in the phase will produce larger errors in the beam intensity than the absence of the very tip. The measured diffraction efficiencies of the uncoated GPEs are 86%, 84%, 82% and 74% for values of the displacement $p = 0$, $p = 0.25$, $p = 1$ and $p = 1.25$, respectively (taking into account of Fresnel reflections from both surfaces). The diffraction efficiency of the GPEs should reach up to 90% for simpler masks. Further iterative optimizations to the writing procedure may also increase the overall efficiency. Additionally, the anti-reflection coatings can enhance the overall performance by minimizing the losses. The efficiency slightly drops for other GPEs because of the non-concentric rings present in the design. Also, the fast changes in angles of the nanogratings (see the $x = 0$ line) together with empty areas in the centers of elements have an impact on the efficiency. The retardance of the GPE is very uniform and equal to $\lambda/2$ over the full fabricated area, which is very close to the similarly fabricated GPE with the same volume nanogratings inscription technique in Ref. [187].

Experimentally obtained intensity distributions of generated non-diffracting beams with GPEs for different values of displacements are depicted in Fig. 4.4. Pictures reveal the high quality of non-diffracting beams created using fabricated GPEs. These results are consistent with previous experiments. The zeroth-order Bessel-Gauss beam generated by GPE with $p = 0$ is of high contrast. The central peak remains of the same size in the whole focal zone and no axial intensity modulation is present. In contrast to the axicon-produced beams, no extensive beam cleaning is required [see Fig. 4.4(a)].

The second element, which has a displacement of $p = 0.25$, produces a non-diffracting beam with slightly higher modulation in the first ring when compared to the numerical simulation, but the overall pattern

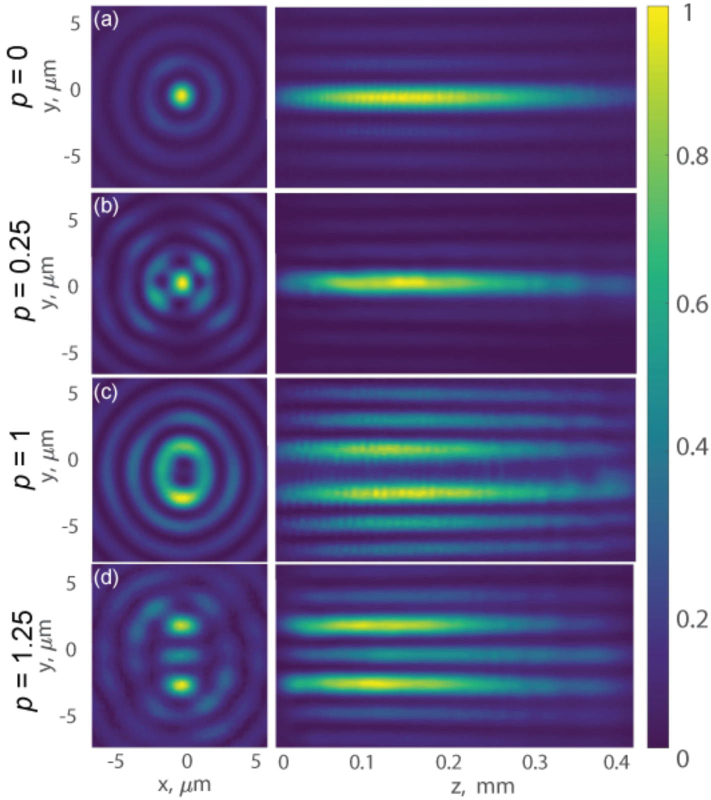

Figure 4.4: Experimentally measured intensity patterns of non-diffracting beams generated by GPEs in the xy plane (first column) and in the yz plane (second column) for different values of p: (a) $p = 0$, (b) $p = 0.25$, (c) $p = 1$, (d) $p = 1.25$. The length of the Bessel zone in the air for each beam is 332 µm.

closely resembles our expectations [see Fig. 4.4(b)]. The axial intensity has a smooth profile with no major irregularities. Non-diffracting beams generated with GPEs for values $p = 1$ and $p = 1.25$ are also of high quality and demonstrate a good agreement with previous numerical and experimental investigations [see Fig.4.4(c)-(d)].

4.1.2. Analysis of laser induced modifications in transparent media

The generated beams using GPEs were employed to induce modifications in a transparent material. Specifically, a Schott D263t glass of 0.5 mm thickness was micromachined. Pulse durations were varied from 158 fs to 5 ps FWHM (temporally stretched by phase modulation induced by a laser compressor). The energy of the pulses coming out from the laser was fixed to 120 µJ and was enough to damage not only the surface of the material but also induce volume material modification in the bulk of the transparent sample with a single pulse.

These material modifications were analyzed with an optical microscope and are displayed in Figs. 4.5-4.6. The dependence of surface modifications in Schott D263t glass on pulse duration and the spatial displacements are depicted in Fig. 4.5. For the shortest duration (158 fs)

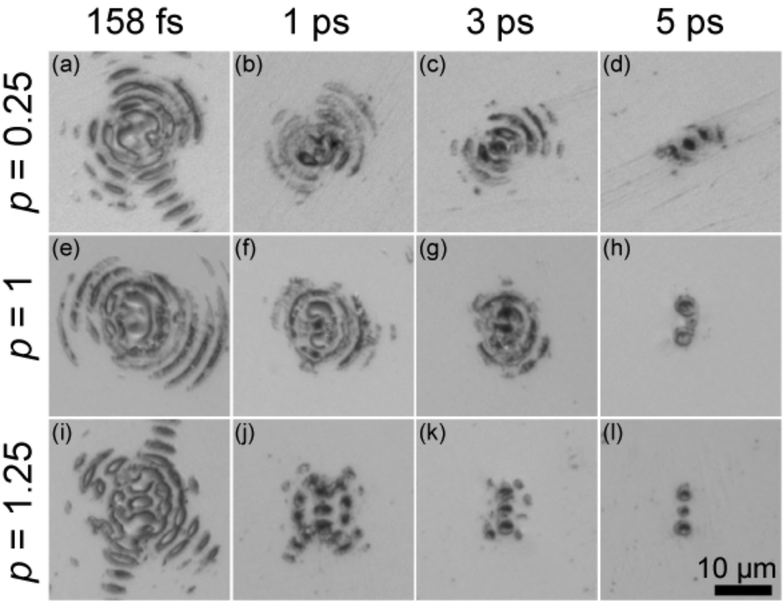

Figure 4.5: Reflection microscopy images of surface modifications on Schott D263t glass with single-shot Bessel-type beam generated by GPEs, pulse energy - 120 µJ. Rows represent axicons of different spatial displacements (a)-(d) $p = 0.25$, (e)-(h) $p = 1$, (i)-(l) $p = 1.25$, while columns represent different pulse durations: (a), (e), (i) 158 fs; (b), (f), (j) 1 ps; (c), (g), (k) 3 ps; (d), (h), (l) 5 ps.

of pulsed non-diffracting beams, the surface modification spreads over a relatively large area. Multiple rings of non-diffracting beams are clearly visible. The cause for that is the multiphoton absorption mechanism, which is observed in parts of the sample illuminated by the intensity distribution of the incident beam. The band gap of the borosilicate glass is approximately 4.2 eV, whereas the central wavelength of laser pulses is 1028 nm. This wavelength approximately translates to 1.2 eV photon energy, therefore 4 photons are involved in the multiphoton absorption process. More information on the borosilicate glass and its laser micromachining is presented in Refs. [188, 189].

An increase in the pulse duration reduces the intensity of the beam, but the fluence is unchanged, therefore the effect of impact ionization starts to have a large influence on the morphology of modifications. The reduction of surface damage by outer rings is visible. Pulses with the longest duration of 5 ps modify the sample only in the central part of the beam. For example, for an invariant beam produced by GPE with $p = 1.25$ only three spots are visible on the surface and the structure closely resembles the most intense part of the beam in Fig. 4.4(d). A non-diffracting beam with $p = 1$ modifies the surface only in two spots, compare that with Fig. 4.4(c). Surface modifications induced by the beam with $p = 0.25$ consist of a multi-peak structure.

Volume modifications were recorded by imaging the depth of the material with an optical microscope and results are depicted in Fig. 4.6. The short pulse duration has no pronounced effect on volume defect generation, much stronger volume modifications are visible when the pulse duration is longer. As expected, longer pulses induce larger material stress and microcracks inside the volume of the glass and can be produced at the cost of greatly reduced surface damage. Results reveal that the microcracks in the glass produced by non-diffracting beams do replicate a 3D profile of the beam: it remains unchanged at different depths. This suggests that the shape of the microcrack depends on the profile of the beam intensity and can be controlled. For instance, microcracks produced with a beam shaped by $p = 0.25$ displacement GPE and pulse of 5 ps duration are extended on one line. It means that the specific asymmetry of the beam causes them to favor one direction of cracking [see Fig. 4.6(d)]. This peculiar cracking case looks promising and will be investigated thoroughly in its application to the cutting of thin glasses in the next section.

The last two cases of spatial displacement ($p = 1$ and $p = 1.25$) are somewhat similar. Non-diffracting beams have also produced microcracks and their spatial distribution and direction are also influenced by the pattern of beam intensity, however, due to a more complicated dual and multi-peak structure, the cracks did not join into a single cracking line, instead, they have multiple directions of cracking or in some

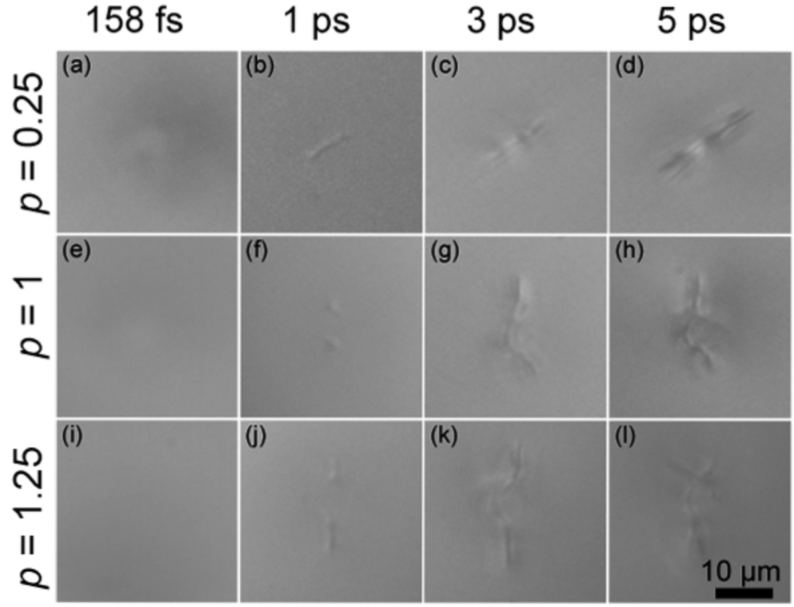

Figure 4.6: Reflection microscopy images of volume modifications in Schott D263t glass of 0.5 mm thickness at 200 µm depth with single-shot Bessel-type beam generated by GPEs, pulse energy - 120 µJ. Rows represent axicons of different spatial displacements (a)-(d) $p = 0.25$, (e)-(h) $p = 1$, (i)-(l) $p = 1.25$, while columns represent different pulse durations: (a), (e), (i) 158 fs; (b), (f), (j) 1 ps; (c), (g), (k) 3 ps; (d), (h), (l) 5 ps.

cases, the cracks are not positioned on the same line [see Figs. 4.6(d) and 4.6(h)]. The dual peak Bessel beam was also studied in Ref. [190], where it was shown that the formed microcracks do produce distinct cracking, and sometimes possible to use them in the micromachining of transparent samples. However, the beams shown in this study having $p \geqslant 1$, are more suited in creating double or multi plasma channels and could have potential use outside micro fracture assisted transparent material dicing.

Glass dicing using a non-diffracting beam produced by GPE of $p = 0.25$

As reported in the previous section, a directional cracking was observed made with the non-diffracting beam generated by GPE with the displacement of $p = 0.25$ for the energy of 120 µJ and 5 ps FWHM pulse duration. Upon a closer investigation of the beam intensity profile, a distinct asymmetry was found, see Fig. 4.7. Although the center part

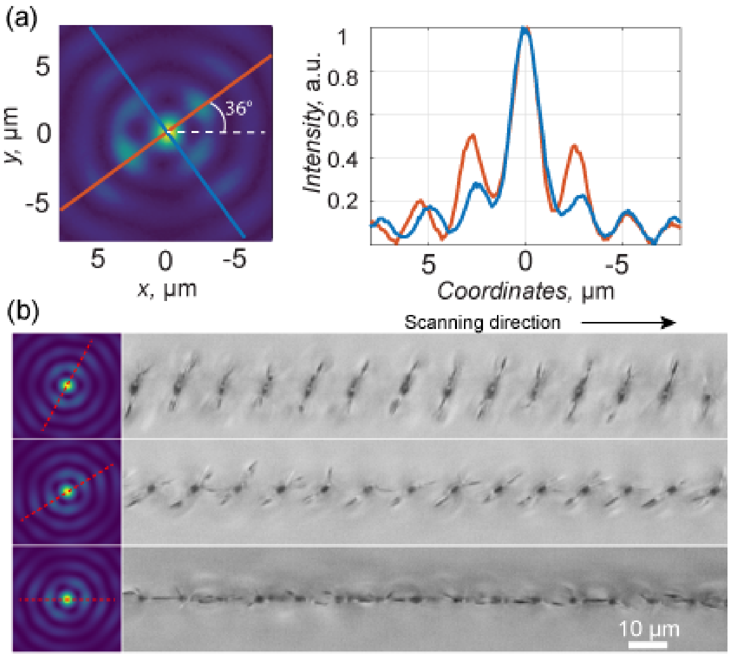

Figure 4.7: (a) Intensity distribution of the non-diffracting beam, produced by the GPE with displacement $p = 0.25$. The red line connects the most intense beam peaks. The blue line is perpendicular to the red. Intensity distributions in cross-sections at those two lines are depicted on the right using the same colors as the lines. The measured asymmetry of the central peak as ratio of red and blue lines is 1.05. (b) Images by optical microscope of dependence of volume microcrack orientation on the rotation of the intensity profile of the beam. The separation between shots in the scan line (pitch) is 10 µm. The energy of 4 ps pulse is 240 µJ.

of the beam resembles the zeroth-order Bessel beam, the first ring has a distinct modulation. The ring is split into four peaks, and two peaks have higher intensity than the other two. The line connecting the two most intense peaks and the center of the beam is tilted by 36° in respect to the x axis. The beam intensity profiles are depicted in Fig. 4.7(a). On the left-hand side, the distribution of transverse beam intensity is depicted. There are two lines connecting peaks on the ring with the same intensity. On the right, intensities of the beam in two cross-sections are depicted: on red and blue lines. The intensity in the first ring is almost two times higher for the red line than that on the blue. This implies an asymmetry in the profile of the beam, which was measured to be 1.05, meaning that the central spot along the red line was 5% wider than at the perpendicular blue line. This slight asymmetry is mainly responsible for the distinct direction of crack formation. Therefore, this asymmetry can be systematically applied to generate controllable microcracks inside the transparent materials. The control of the crack direction is of high importance in the process of glass dicing/cutting, where these cracks formed by spatially shifted beams connect, enabling the much more efficient and controllable way to separate glass samples into two pieces, than using centrosymmetric beams [191].

Elliptically asymmetric non-diffracting Bessel-like beams can achieve good efficiency, speed, and high quality in glass dicing [116, 192]. For this reason, experiments were performed on the control of the direction of microcracking. Schott D263t samples of the same thickness of 0.5 mm were used. The optical setup used for the imaging of a beam was reassembled: a $4f$ system now consists of a pair of plano-convex lenses with focal lengths 75 mm and 8 mm. Thus, a longer Bessel zone is created (1.3 mm in the air, at $\exp[-2]$ intensity). This enables illumination through the full thickness of the glass sample with a single shot. A longer Bessel zone also reduces variations in the axial intensity profile inside the sample, but requires higher pulse energy.

During the experiment, several scan lines of glass modification were produced, where consecutive laser shots were separated by 10 µm pitch, which corresponds to approximate crack length. The scanning speed was limited to 20 mm/s, to avoid position inaccuracy in transverse coordinate due to limited performance of the moving stages. Each line differs from another by the angle between the red line in the beam profile and the scan direction. A selection of three fabricated scan lines is presented in Fig. 4.7(b). The middle scan line represents the case where the direction of the translation of the beam is parallel to the x axis of the element, while the top and bottom rows represent the rotation of the GPE by 36° clockwise and counter-clockwise, respectively. The linear dependence of the formed crack direction on the angle of GPE rotation is clearly evident. As expected, the cracks are formed and connected in the last scan line, where the most intense beam intensity peak has the same direction as the scanning direction. A conclusion can be made that the rotation of the element by 36° in the counter-clockwise direction in respect to the translation direction enables laser micromachining of the continuous line of interconnecting cracks.

As the investigation has revealed in section 4.1.2, short pulses are suboptimal for this application because most of the energy is absorbed during the interaction with the front surface, consequently, no cracking was observed in the volume of the sample. While the 5 ps pulses did generate cracks, this process was not consistent over the full length of the sample. A careful choice of parameters together with numerous experiments has selected the 4 ps duration pulses as optimal for the production of cracks over the full length of the sample without induction of excessive surface damage.

Additionally, the dependence of sidewall roughness on the pulse energy was analyzed. An example is given in Fig. 4.8(a), where optical microscope images of the front surface of the separated glass pieces are presented. The pulse duration was 4 ps and the energy of the pulsed beam was changed from 240 µJ to 390 µJ. As discussed, the GPE was rotated by 36° so that interconnecting cracks were produced along the cutting line. It was found that the energy threshold for the cracks to interconnect over the full length of the sample was at around 270 µJ [see Fig. 4.8(b)]. The most consistent interconnection of cracks was achieved with 330 µJ, because higher energy pulses tended to excessively damage the surface of the sample, while lower energy pulses may have slight waviness of the crack, so the quality of the cut would decrease. The glass breaking procedure was conducted by mechanically breaking using two pairs of fingers, replicating the four point bending procedure as it was reviewed in Ref. [60]. The quality of the cut was determined by examining the surface roughness (measured as root-mean-square value of height) of the cut sidewall and peak-to-valley values as the highest and the lowest points on the surface (depicted in Fig. 4.9), measured by optical confocal profiler. It was found that the surface roughness was also optimal for the pulse energy of 330 µJ and equal to 0.52 µm. Sidewall roughness estimations of cleaved surfaces produced with remaining pulse energies are 3.31 µm (at 240 µJ), 1.77 µm (at 270 µJ), 0.79 µm (at 300 µJ), 0.68 µm (at 360 µJ) and 1.17 µm (at 390 µJ). The peak-to-valley values also correlate with roughness, as the lowest roughness

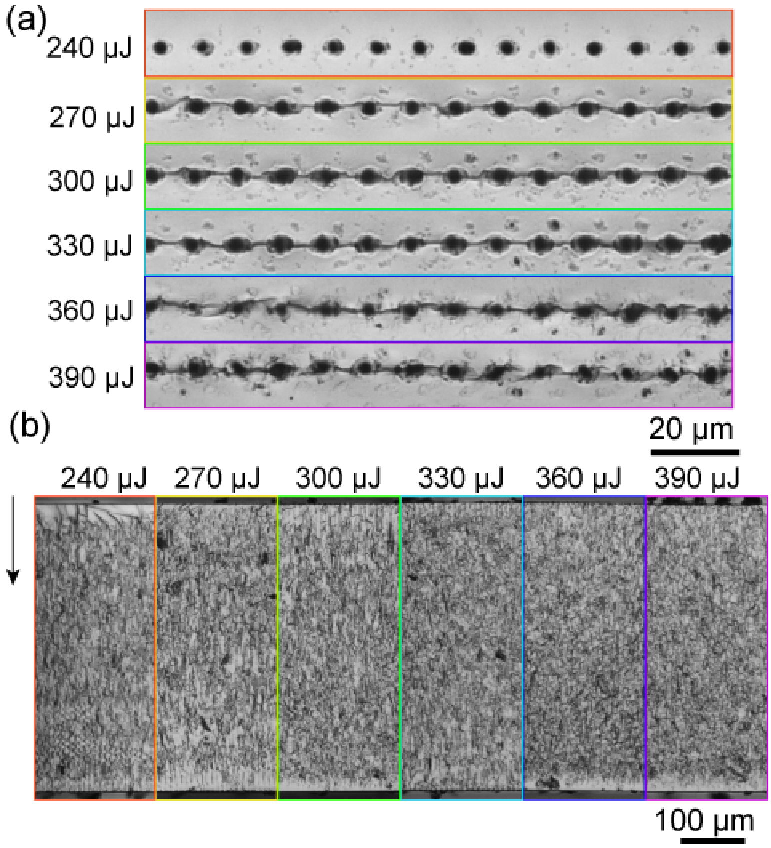

Figure 4.8: Reflection microscopy images of the glass top surface showing produced dicing lines with different pulse energies (a), side view of the cleaved sample surfaces (b). The black arrow represents the pulse propagation direction.

would also have the lowest peak-to-valley at 330–360 µJ pulse energy cuts, having 3.52 µm and -3.3 µm, and 2.94 µm and -2.89 µm, respectively. Lower energy pulses do not produce cracks over the full length of the sample, or small waviness of the crack may appear, while the high energy pulses start to deteriorate the surface of the sample, and secondary peaks of the beam intensity profile may start to modify the volume of material greatly reducing the quality of the cut. However, the presented results of stealth dicing are not defined as the ideal set of parameters. The process could be improved by adjusting the pitch, Bessel zone length versus pulse energy, or employing a laser source capable of burst regime. The burst pulse operation of the laser may enhance the

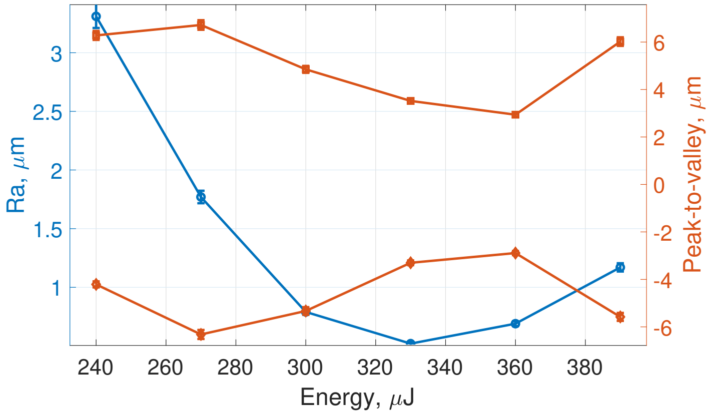

Figure 4.9: Profiler measurement data of roughness (Ra) and peak-to-valley values on the side wall surfaces of diced samples by using various pulse energies.

deposition of the energy to the material for certain parameters of the pulse train, as was demonstrated for transparent materials [55] and also metals [193]. However, even without the best energy deposition efficiencies, the additional material transformations can improve the desired effect, such as heat affected zone [194, 195], or initiate zigzagging of the crack formation [196].

4.2. Axicon phase split and optimization for controlled micro fractures

The results in previous section confirmed that the controlled directional microcrack formation in transparent material is achievable using an asymmetric Bessel-type beam, as there may be many different approaches for this technique [68]. Now let's intentionally find the optimized axicon mask with azimuthal phase modulation and test it specifically for glass stealth dicing, where directional cracking in volume of a glass along the cutting trajectory is needed. It is known that phase modulation of the beam transforms the beam's intensity distribution into a more complex pattern, for example, by superimposing multiple various order Bessel beams, as illustrated in Fig. 2.29.

For a full study of optimized dicing using a systemically found asymmetric Bessel-type beam, numerical simulation is employed to investigate the intensity distribution of the invariant beam. The axicon phase pattern is split azimuthally into uneven quarters, with induced phase shifts in opposite pairs to break the symmetry of the circular grating (phase mask pattern of an axicon), as shown in Fig. 4.10. By inves-

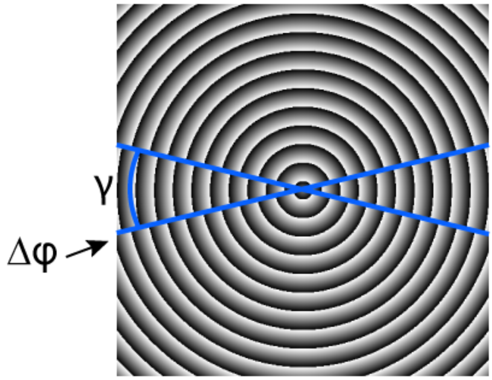

Figure 4.10: Example of axicon phase mask division into two opposite pairs having two defining parameters: opening angle γ and phase difference $\Delta\varphi$ between the zones.

tigating the parameter field of opening angle and phase difference, the aim is to find the optimal modified axicon phase pattern to generate an elliptic peak with relatively high contrast, with a following experimental verification using a manufactured GPE.

4.2.1. Numerical modeling and parameter optimization of the asymmetric spot

Analytical solution of Bessel-type beam made by azimuthally modulated axicon phase mask

To introduce azimuthal phase modulation, firstly let's take the transmission function of the axicon from Eq. (4.1), and rewrite in the form [177]:

$$T_{ax}(\rho) = \exp\left(-\mathrm{i}\beta\rho\right), \tag{4.11}$$

where $\rho = \sqrt{x^2 + y^2}$ is radial coordinate, β defines the speed of the phase change over the ρ and is determined by the cone angle of the axicon. For small axicon cone angles $\beta = 2\pi\left(n-1\right)\alpha/\lambda$, where λ is wavelength, n and α are the refractive index of the axicon and the base angle respectively.

To investigate the influence of phase distortion on the beam intensity distribution and optimize it to achieve the asymmetric Bessel-Gauss beam, numerical modeling was conducted. The petal-like phase jumps as a phase distortion are introduced, and two additional parameters are included to define those phase jumps: phase-cut angle γ and phase jump $\Delta\varphi$:

$$\varphi(\phi) = \begin{cases} 0, \text{ for } & \gamma/2 \leq \phi \leq \pi - \gamma/2, \\ & \pi + \gamma/2 < \phi \leq -\gamma/2, \\ \Delta\varphi, \text{ for } & -\gamma/2 < \phi \leq \gamma/2, \\ & \pi - \gamma/2 < \phi \leq \pi + \gamma/2, \end{cases} \tag{4.12}$$

where ϕ is azimuthal angle. The modified transmission function reads as:

$$T_{mod}(\rho, \phi) = \exp\left[-\mathrm{i}\beta\rho + \mathrm{i}\varphi(\phi)\right], \tag{4.13}$$

For analytical analysis of the generated beams, let's find solutions of the beam propagation equation that express the Fresnel integral in cylindrical coordinates [5, 150]. The solution takes the form of the following:

$$\begin{aligned} E(\rho, \phi, z) = & \frac{2\pi \exp\left[\mathrm{i}k\left(z + \rho^2/2z\right)\right]}{\mathrm{i}\lambda z} \\ & \times \sum_{n=-\infty}^{\infty} a_n(-\mathrm{i})^n \exp(\mathrm{i}n\phi) \\ & \times \int_0^{D/2} \rho' T_{ax}(\rho') J_n\left(k\rho\rho'/z\right) \exp\left(\mathrm{i}k\rho'^2/2z\right) \mathrm{d}\rho', \end{aligned} \tag{4.14}$$

where n is the order of Bessel function, $k = 2\pi/\lambda$ is wave number, $D/2$ - the radius of the aperture and a_n is:

$$a_n = \frac{1}{2\pi} \int_0^{2\pi} A\left(\phi'\right) \exp\left(-\mathrm{i}n\phi'\right) \mathrm{d}\phi'. \tag{4.15}$$

The angular function $A(\phi')$ is defined as

$$A\left(\phi'\right) = \exp\left[\mathrm{i}\varphi\left(\phi'\right)\right]. \tag{4.16}$$

Combining the expression from Eq. (4.16) with the expression (4.15) to get:

$$a_n = \frac{2\mathrm{i}\delta_{n,2\mu}\left\{(-1)^{n+1}\left[2\mathrm{i}e^{\mathrm{i}\Delta\varphi}\sin\left(\frac{1}{2}\gamma n\right) + e^{-\frac{1}{2}\mathrm{i}\gamma n}\right] + e^{\frac{1}{2}\mathrm{i}\gamma n}\right\}}{n}, \tag{4.17}$$

where μ is an integer number and δ is Kronecker's function. The leading part of the integral in Eq. (4.14) can be estimated using the stationary phase method [150]. The stationary point of the integral is at $\rho' = \beta z/k$. The expression for electric field then can be written as:

$$E(\rho, \phi, z) \propto \sqrt{\frac{8z}{k}} \exp\left(\mathrm{i}\frac{z\beta^2}{2k}\right) \times \sum_{n=-\infty}^{\infty} a_n(-\mathrm{i})^n \exp(\mathrm{i}n\phi) J_n(\beta\rho) \,. \tag{4.18}$$

Substitution of Eq. (4.17) in Eq. (4.18) results in

$$E(\rho, \phi, z) \propto -\mathrm{i}\sqrt{\frac{8z}{k}} \exp\left(\mathrm{i}\frac{z\beta^2}{2k}\right) \times \sum_{\mu=-\infty}^{\infty} \frac{\left[2\mathrm{i}e^{\mathrm{i}\Delta\varphi}\sin(\gamma\mu) + e^{-\mathrm{i}\gamma\mu}\right] - e^{\mathrm{i}\gamma\mu}}{\mu} \times (-1)^{\mu} \exp(\mathrm{i}2\mu\phi) J_{2\mu}(\beta\rho) \,, \tag{4.19}$$

Firstly, note that the sum in Eq. (4.18) will lead to the sum of only the zero-order and even-order Bessel functions. This leads to the beam profile having an inversion symmetry and, therefore, the values at azimuths ϕ and $\phi + \pi$ coincide. Second, from Eq. (4.19) follows $a_{-\mu} \neq a_{\mu}$, and the expansion coefficients demonstrate oscillatory behavior as μ changes. Analysis reveals that, in general, the diffracted field is always a superposition of zero-order and many even-order Bessel non-diffracting beams. The amplitude of the zeroth-order Bessel beam is $a_0 = 2\left\{\gamma\left[-1 + \exp(i\varphi)\right] + \pi\right\}$ and this term is always present in the expansion, except for the cases where $\gamma = \pi/2$ and $\varphi = \pi$.

Numerical modeling examples

Numerical simulations of beam propagation in free space were carried out by illuminating an ideal Gaussian beam to an axicon phase mask (equivalent to a base angle of 1.6° made out of fused silica, having refractive index $n = 1.45$). The numerically calculated Fresnel diffraction equation with the modified transmission function will be:

$$E(x,y,z) = \frac{\exp(\mathrm{i}kz)}{\mathrm{i}\lambda z} \int\int_{-D/2}^{+D/2} T_p(x',y',0) \times \exp\left[\mathrm{i}k\frac{(x-x')^2+(y-y')^2}{2z}\right] \mathrm{d}x'\mathrm{d}y', \tag{4.20}$$

where $D/2$ - the radius of the aperture, $T_p(x',y',0) = exp(-(x^2+y^2)/(w_{FWHM}/\sqrt{2ln2})^2)$ - modified axicon transmission function at the plane of incidence ($z=0$), $E(x,y,z)$ - electric field amplitude distribution at a distance z from the axicon. Several examples of simulation results are depicted in Fig. 4.11. Numerical results show that petal-like phase distortion on the axicon phase may generate an elongated central beam spot. For example, then the azimuthal phase-splitting angle is $\gamma \approx 18°$ and phase difference $\Delta\varphi = \pi$, one can obtain an elongated central beam spot depicted in Fig. 4.11(c). The increase in the mask splitting angle γ leads to a greater elongation of the central beam spot. However, the two opposite side peaks on the first surrounding distorted Bessel beam ring also increase, reducing the intensity contrast between the central and side peaks [see Fig. 4.11(d)]. With even larger angles, the side peaks become dominant, and when such beams are used in material cracking the cracking direction starts to be complicated having multiple directions [68, 190], therefore this situation should be avoided. It was observed that the intensity of the side peak can be reduced by adjusting the phase difference $\Delta\varphi$, as shown in Fig. 4.11(e)-(f). These few examples demonstrate that optimization of parameters φ and γ can lead to the optimal where elongation of the central spot is observed while the intensity of the side peak is still relatively low.

2D parameter field of elongated core variants

The optimization of the beam profile by varying the cut angle and phase shift of the phase screen was done on numerically simulated beams. Two criteria of the intensity profile were chosen for optimization: ellipticity and contrast. The ellipticity parameter $\mathcal{E}$ was evaluated by approximating the central peak of the beam as an ellipse and taking a ratio of the lengths of the major and minor axes [see Fig. 4.12 (a)]. The contrast parameter C was calculated taking a difference between the intensities of

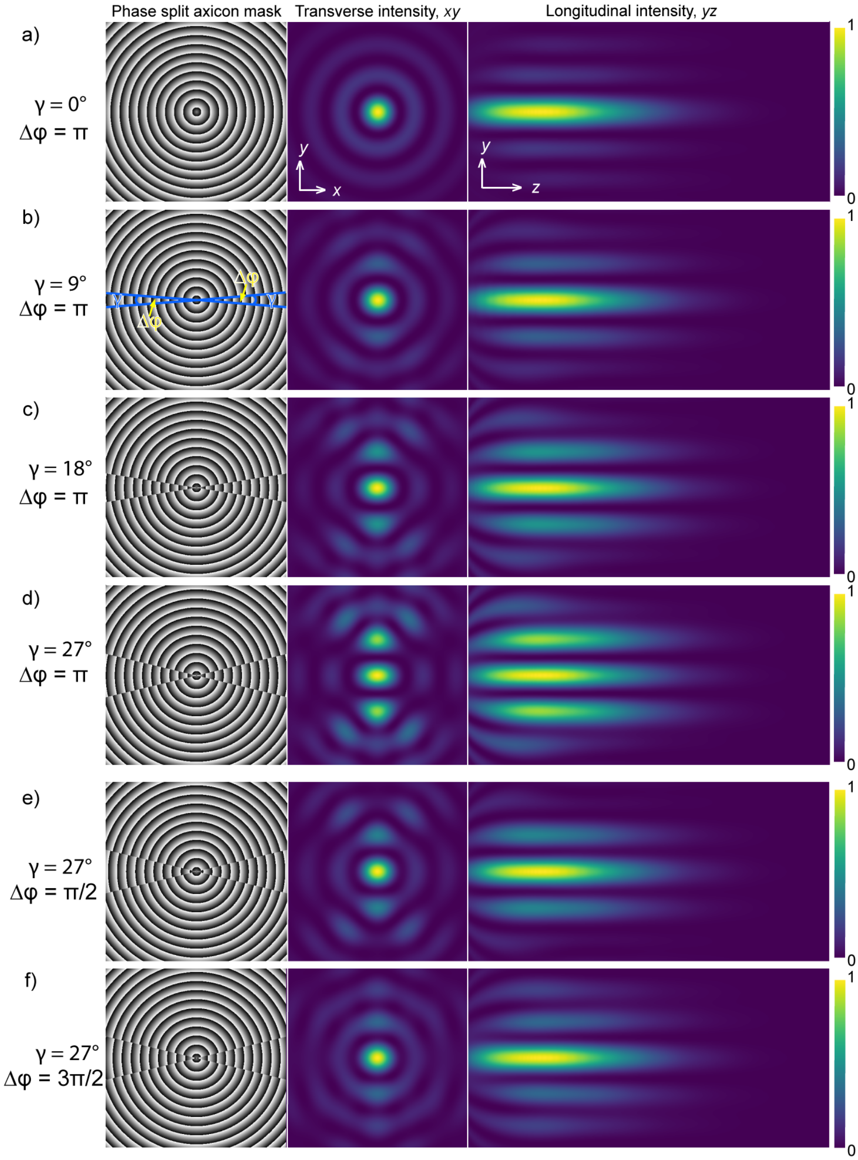

Figure 4.11: Numerical modeling of an ideal diffractive axicon with phase pattern division into two opposite areas with a phase difference of φ and splitting angle γ and the resulting simulated beam transverse and longitudinal intensity distributions in focal planes xy and yz

the central I_1 and side peak I_2, then the difference was normalized to the intensity of the central peak $C = (I_1 - I_2)/I_1$ as shown in Fig. 4.12 (b). The two-dimensional parameter field was obtained by numerical simulation of the beam propagation from Eq. (4.20) with varying parameters

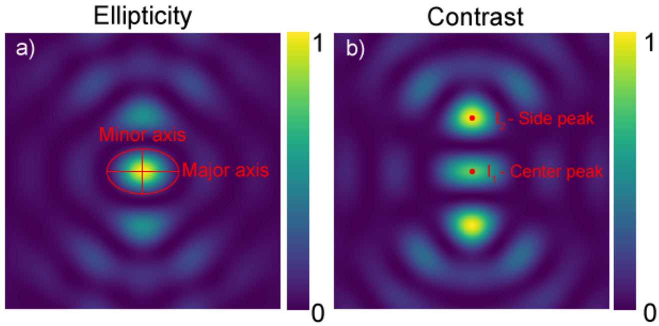

Figure 4.12: Determination of transverse beam intensity parameters: a) ellipticity parameter $\mathcal{E}$ is a ratio of the major and minor axis lengths, b) contrast parameter C is the difference between the central I_1 and side peak I_2 intensities normalized to the central peak intensity.

of γ and φ of the phase mask from Eq. (4.12), the results are depicted in Figure 4.13. Cases when the central peak intensity is equal or lower than the side lobe intensity as is shown in the Figure 4.12(b) the result was omitted in the depiction of the results in Figure 4.13, i.e. cases of $C < 0$ are removed. Nevertheless, the ellipticity of the central peak in-

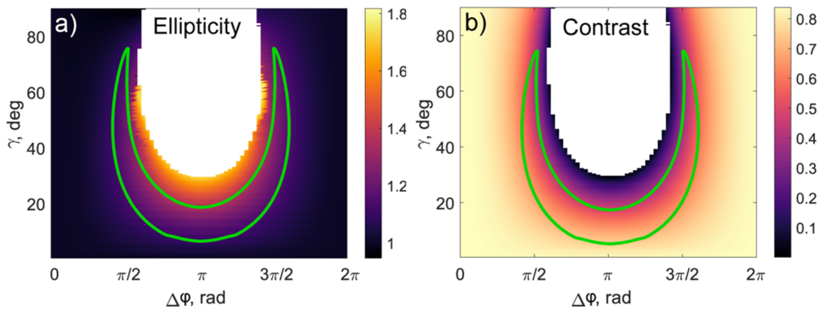

Figure 4.13: Parameter fields of modeled Bessel-type beam ellipticity (a) and contrast (b) dependencies on the axicon phase split angle γ and phase shift ϕ. The green solid line covers an area for suitable γ and φ parameters, omitting undesirable values of low contrast $C < 0.4$ and ellipticity $\mathcal{E} < 1.15$. White area corresponds to negative contrast $C < 0$, where side central peak intensity is equal or lower than the side lobe intensity, therefore this parameter field was omitted.

creases and is even higher when contrast is negative, the higher intensity of the side lobes will not produce directional controllable one-directional cracking of the material. The modeling results reveal that the contrast and ellipticity parameters are inversely proportional, meaning that the highest ellipticity is obtained with the trade-off to contrast. Therefore, another constraint was added on the beam intensity distribution. From previous experimentation experience and references from [192, 195], it is known that the contrast should not exceed $C < 0.4$ to avoid impacting the side lobe on the cracking direction and the ellipticity should be high, for example $\mathcal{E} > 1.15$, to be able to control the cracking direction. As it was presented in the first part of this section, even an approximate ellipticity of $\mathcal{E} \approx 1.05$ provided with directional cracking using the asymmetric beam. However, higher value of $\mathcal{E}$ would ensure that the direction of the cracking has stronger emphasis, possibly improving dicing quality on the side walls. Having this in mind, the acceptable parameter field becomes a narrow zone constrained by the green solid line in Fig. 4.13. In this parameter space, varying the values of the pair γ and φ is expected to give the best results, accounting for the trade-offs.

Some examples taken from the calculated parameter field are depicted in Figure 4.14. For simplicity, at a fixed value $\varphi = \pi$, only

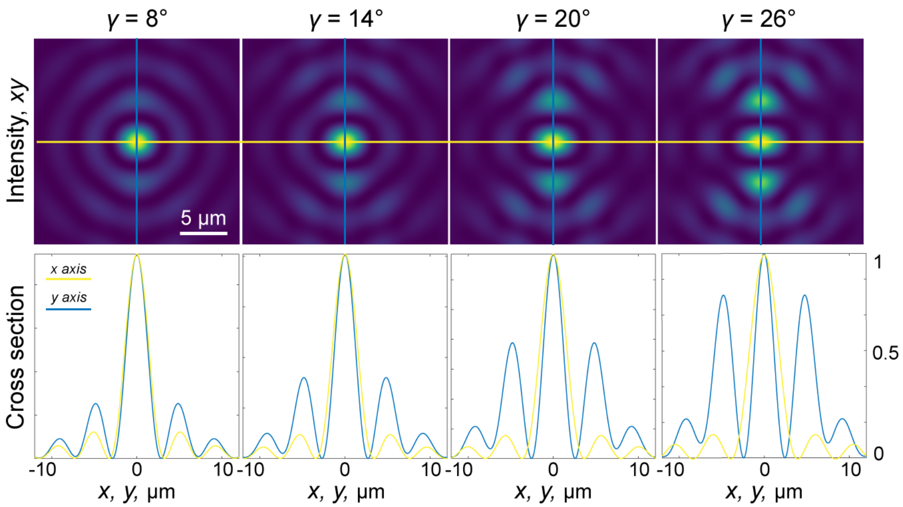

Figure 4.14: Cross-section examples with various γ at fixed $\varphi = \pi$, taken from simulation results of two-dimensional parameter field. The ellipticity parameters and the constant parameters were calculated to be $\mathcal{E}$ =[1.08, 1.15, 1.34, 1.59] and C =[0.73, 0.55, 0.38, 0.2] for γ =[8° 14° 20° 26°], respectively.

increasing the angle γ improves the elongation of the spot, where, for example, at $\gamma = 14°$, the ellipticity is $\mathcal{E} = 1.2$ and at $\gamma = 26°$ the $\mathcal{E}$ is greater than 1.4. However, in reverse, the contrast becomes too low to be successfully used in micromachining, as the side peaks would create unwanted defects outside the center spot. The best case for further experiment was selected to be in $\gamma = 17°$ and $\varphi = \frac{5}{4}\pi$ taken from inside the green solid line plot in Fig. 4.13. The particular case was chosen to increase the cut angle γ to reduce the need for higher fabrication precision of the beam shaping element. A larger angle γ reduces the relative area where the phase changes dramatically, while keeping the reduced sensitivity to the phase change.

4.2.2. Generation of controlled micro fractures for stealth dicing

Measurement of produced invariant beam using GPE

The experimentally measured focal zone of the produced beam is shown in Figure 4.15 with a comparison to numerical modeling. The

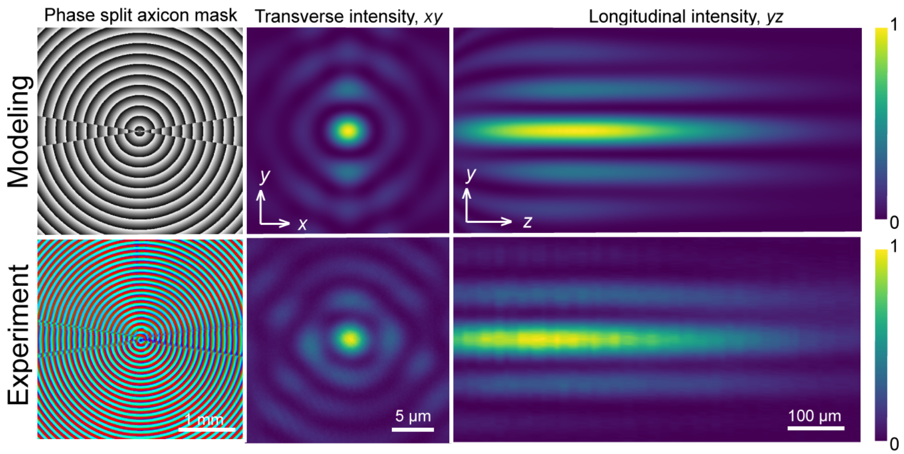

Figure 4.15: Comparison results between numerical modeling of best case phase-split axicon generated beam and experimentally measured beam intensity distribution made by GPE. The best case was selected to have $\varphi = \frac{5}{4}\pi$ and $\gamma = 17°$ values, thus producing an elongated beam spot with an ellipticity of $\mathcal{E} = 1.19$ and contrast of $C = 0.61$.

experimental data greatly match numerical modeling, as the produced Bessel-like beam has a slightly elongated transverse central intensity pattern which is translated along the focal line without any strong distortions. Only the side peaks on the surrounding rings have a higher level of disruptions, but they cannot be taken into account because of the high contrast of the central peak. The nonlinear absorption by the material also relaxes the contrast criteria for micromachining purposes, therefore the only intense central peak intensity slightly elongated distribution is most important in the stealth dicing micromachining purposes. The ellipticity and contrast of the beam generated using the GPE were measured to be $\mathcal{E} = 1.19$ and $C = 0.61$, respectively, with a focal line length of 0.7 mm (at exp[−2] intensity). The transmission efficiency of the GPE was measured to be 90% for the uncoated element. The anti-reflective coating on both surfaces could potentially minimize Fresnel reflections and increase the possible transmission to at least 97% in this case. It is worth mentioning, that the previously presented GPE axicon (without spatial shift, $p = 0$) had 86% transmission. This difference of slightly lower diffraction efficiency may be dependable on the retardance deviation from the expected $\lambda/2$ value after the inscription process.

Laser beam-matter interaction

In the laser-matter interaction experiment, a 0.5 mm thick D263T glass substrate was used. Firstly, the dependence of the induced material modification on the impulse length was investigated. Optical modifications were made to the sample with different impulse lengths using a fixed 200 µJ impulse energy. The results are shown in Fig. 4.16. Shorter impulse lengths (1 ps and less, at FWHM) produced strong surface modifications with barely any visible effect in most of the material. Significant volume modifications were observed at impulse lengths greater than 1 ps. Modifications in the sample volume were generated most effectively when using 4-6 ps impulse duration. However, the defects induced by longer pulse duration showed worse results due to decreased peak power. Consequently, a pulse duration of 6 ps was selected for further experiments.

The appropriate regime for transparent material stealth cutting was found by making modifications lines throughout the length of the sample with 8 µm pitch between shots while changing pulse energy, as this distance was the average crack length made with a single shot, and using 20 mm/s scanning speed. The smaller pitch between the shots would also be sufficient for further dicing process, but it would possibly increase the sidewall roughness and limit scanning speed, while utilization of bigger

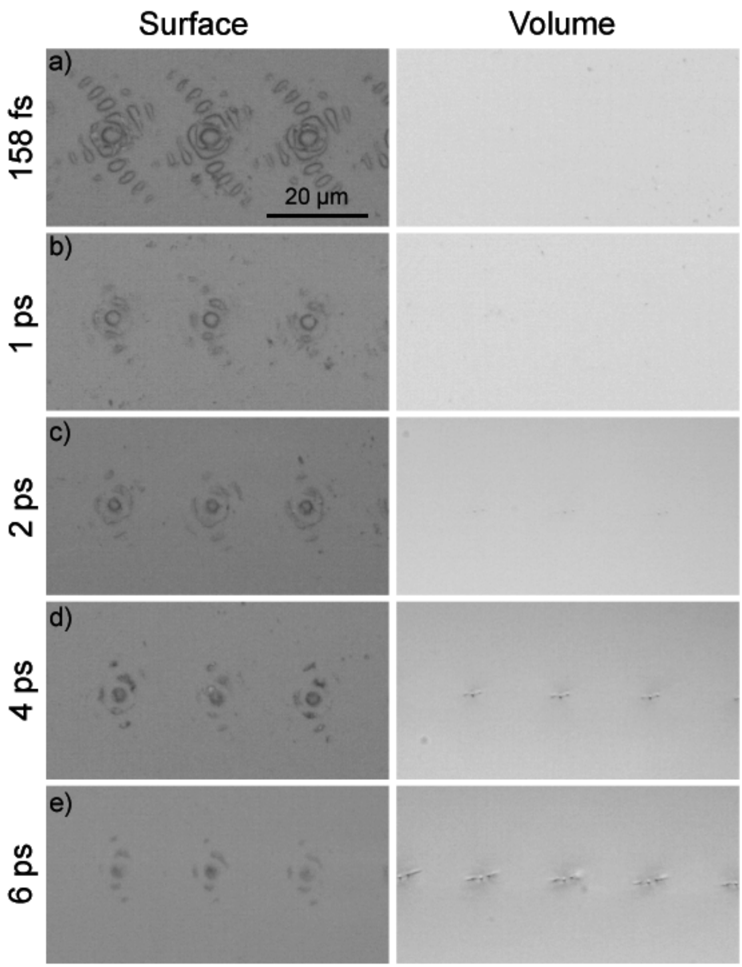

Figure 4.16: Microscope images of the glass surface and volume under different pulse durations (at FWHM): 158 fs (a), 1 ps (b), 2 ps (c), 4 ps (d), 6 ps (e). The pulse energy was fixed at 200 µJ.

pitch could be the cause of cracks not interconnecting and failure of dicing.

Attempts in stealth dicing

To proceed with the dicing process, the GPE was oriented in a way that the major axis of the elliptical peak would be in parallel to the scanning direction as shown in Fig. 4.17 and the focal line of the beam was positioned along z so that it would initiate micro-fractures along the entire thickness of the sample as expected, similarly to a previous case depicted in Fig. 2.18. At the next step, the samples were broken by two pairs of fingers, using the four point breaking procedure.

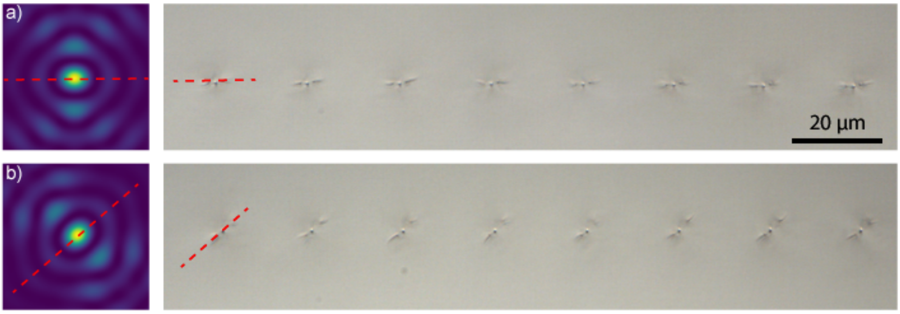

Figure 4.17: Microscope images of the glass volume when 200 µJ pulse energy and 6 ps pulse duration was used. The orientation of the crack is consistent with the major axis of the elliptical spot of the beam depicted in the dashed red line. The length of the crack is measured to be approximately 8 µm.

The optimal dicing process window was obtained by fabricating lines with different pulse energies varying from 130 µJ to 210 µJ as shown in Fig. 4.18.

With pulse energies less than 130 µJ, the inscription of orientated micro fractures did not occur on the entire thickness of the sample at a fixed pitch, therefore the separation would result in a failure leading to uncontrolled cracking when breaking or would require more breaking force. The best results were obtained when the pulse energies were selected between 150 µJ and 170 µJ [as depicted in Fig. 4.18(b)-(c)]. In this regime, the roughness of the sidewalls of the separated pieces were $R_a = 0.53$ µm and $R_a = 0.47$ µm, respectively, (as depicted in the plot in Fig 4.19).

The lowest values of peak-to-valley were measured to be 1.29 µm and -1.03 µm. By increasing pulse energy to 190 µJ, the mechanical breaking would require less force, but the quality of the cutting would also decrease significantly, due to stronger induced fractures in the material, resulting in greater roughness of the side walls. The same implies on 210 µJ case [Fig. 4.18(e)] where not only the strong modulation on the side walls is observable, but also the defects made on the glass surface are much stronger and undefined direction cracks in the bulk would appear more likely, overcoming the elongated beam effect. The breaking

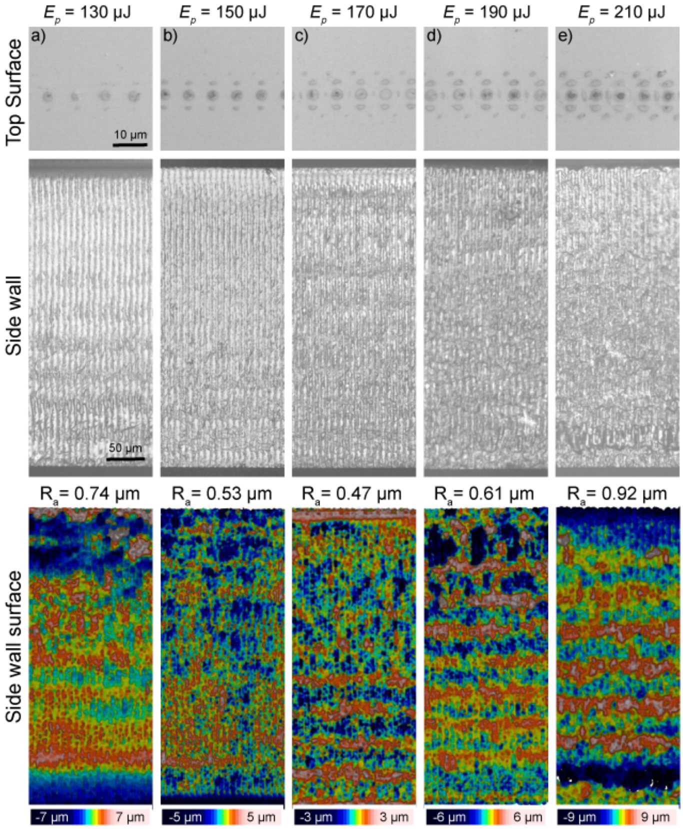

Figure 4.18: D263T (Schott) 0.5 mm thick glass cutting results. Top two rows show microscope images of the surfaces and separated sidewalls with increasing pulse energy from 130 µJ to 210 µJ at a fixed pulse duration of 6 ps (FWHM) and 8 µm pitch. The bottom row represents measured profiles for better surface morphology visualization.

forces were not measured during the experiments, but they are expected to be in similar range as presented in Ref. [60].

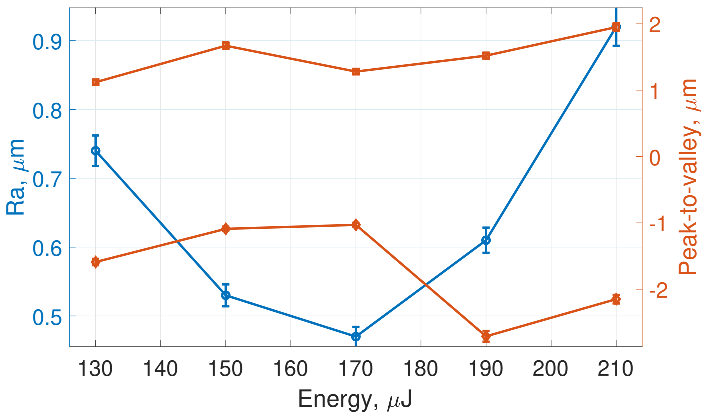

Figure 4.19: Profiler measurement data of roughness (Ra) and peak-to-valley values on the side wall surfaces of diced samples by using various pulse energies.

4.3. Summary of the results

A concept of axicon phase division into two halves and physical shifting was proposed, numerically simulated, and experimentally verified. By dividing the axicon phase masks into two halves and physically shifting them in opposite directions by the spatial displacement parameter p (measured in fractures of distance between phase values of 0 and 2π), distorted or multi-peak invariant Bessel-type beams can be generated. Numerical modeling with changeable p shifts revealed that the increasing shifting distance induces larger distortion of the central peak, splitting it into multi-peak transverse intensity distribution.

It was observed that, the broken symmetry in the phase mask produces a slightly distorted-elongated beam intensity pattern with displacement parameter $p = 0.25$. The results from the experiment reveal that this intended displacement is the key factor for inducing micro-fractures in the bulk of a glass with a 36° angle to the normal of displacement axis, with an ellipticity of $\mathcal{E} \approx 1.05$.

The further systematic analysis of introduced azimuthal phase cuts of an axicon mask was employed to find optimal beam shape with a desirable more expressed asymmetry of the central beam peak. In numerical modeling, two parameters of phase-cuts were optimized to find the best case: by altering the phase-cut angle to $\gamma = 17°$ and the extent of the phase difference $\Delta\varphi = 5\pi/4$, the elliptical beam with an ellipticity of $\mathcal{E} = 1.19$ and contrast of $C = 0.61$ was formed.

It was analytically found that for both utilized Bessel-type beam shaping cases, the resulting invariant beam is a coherent superposition of zero-order and even higher-order Bessel beams. In the first case, the amplitudes are flexibly controlled by the spatial displacement parameter p, while in the second case, the outcome is controlled by altering the phase-cut angle γ and the extent of the phase different $\Delta\varphi$.

The both obtained asymmetric beams were manufactured as GPEs and used in experiments of stealth dicing 0.5 mm thick D263t glass. For the spatially displaced axicon case ($p = 0.25$), an invariant beam of 1.3 mm Bessel zone in air (at $\exp[-2]$ intensity) was created and by using 4 ps (FWHM) pulse duration. Attempts were made to execute stealth dicing at 10 µm pitch and 20 mm/s scanning speed. With 330 µJ pulse energy, the best quality of the dicing was found. The lowest measured roughness of sidewalls was found to be approximately 0.52 µm with peak-to-valley values of 3.52 µm and -3.3 µm, respectively. In the second case of best dicing results were obtained by using azimuthally modulated axicon, an invariant beam of 0.7 mm Bessel zone in air (at $\exp[-2]$ intensity) was created and by using 6 ps (FWHM) pulse duration, 8 µm pitch with 170 µJ pulse energy, at 20 mm/s scanning speed. The obtained lowest roughness was 0.47 µm and peak-to-valley of 1.03 µm and -1.09 µm, respectively. The dicing outcome of systematically obtained beam shows better results overall: more expressed ellipticity is accountable for better alignment of fractures, along cutting trajectory, resulting in lower roughness, and especially, in peak-to-valley measurements.

Both cases confirm that the inscription of geometric phase elements proves to be reliable technology for high-power beam shaping applications, with potential uses in material micromachining tasks. Elements made with spatial shift of $p = 0$, $p = 0.25$, $p = 1$ and $p = 1.25$, had measured diffraction efficiencies of 86%, 84%, 82% and 74%, respectively. And azimuthally modulated axicon GPE was measured to have 90% transmission. The additional 7% could be added if the elements had anti-reflective coatings. The transmission losses are dependable on not only the inscribed retardance deviation but also on the complexity of the slow axis pattern. Steep slow axis changes may result in zones of correctly undefined birefringence and retardance.

5. APPLICATIONS OF VECTOR FLAT-TOP BEAMS WITH POLARIZATION SINGULARITIES IN MATERIAL PROCESSING

The transformation from a Gaussian beam to a flat-top beam in transverse coordinates is a relevant topic in laser material processing. Although there are many different methods to achieve this transformation, each method has its own drawbacks. The amplitude modulation method is straightforward and yields good results, but its efficiency is low [197]. On the other hand, phase control is complex because the formed flat-top beam does not propagate far, it diffracts and phases out, and the desired intensity structure deteriorates, making experimental implementation challenging [174, 198].

A potential solution is the superposition of vector beams, where beams with different SOPs interfere constructively. Their summation can create a more complex structured vector beam, which, for example, can have polarization singularities. In this chapter, leveraging this idea, beams with polarization singularities are used as a means to form a flat-top vector beam (Super-Gaussian) in the focal plane using inscribed birefringent nanogratings. This approach aims to create an efficient and flexible optical element that does not require a complex optical scheme compared to other methods [101, 199]. The flexibility of such an element is shown, where the transformation between Gaussian, flat-top, and doughnut-shaped beam intensity distributions is changed only by the relative variation of the incoming beam diameter to the element. The examination of the operation of the element is done both numerically and experimentally showing the propagation properties and polarization distribution of the formed beam, followed by examples of various material laser processing.

*The material related to this thesis chapter was published in paper [**A2**].*

Constructive interference of two orthogonal polarization beams

It was noticed that polarization singularities might be constructed by the interference of polarization vortices [200]. It can be achieved by modifying the vortex beam-generating element: the incoming laser beam propagates through the optical element consisting of two circular zones, one with inscribed nanogratings and one without. The central part of the element is an unmodified silica glass, whereas the outer zone is inscribed as spatially variable waveplate, known as the S-waveplate [132, 197].

The division of this element into two parts will produce two circular polarization beams rotating in opposite directions. They can be defined as two perpendicular states of light, as the interference between them is not observed. Therefore, analysis can be performed by the sum of intensity distributions, as was done similarly in [201] by decomposing into radial and azimuthal polarization states, but only for tightly focused beams.

The advantage of this proposed concept is that the superposed beam can be focused with any lens or microscope objective. The focal points of the individual parts of the beams are very close to each other and, therefore, overlap. By adjusting the unmodified center and modified zone overlap with the input Gaussian beam ratio, one can expect a change in the energy distribution between the counter-rotating circular polarization parts, which will influence the outcome.

To describe beam shaping conditions at which the transition to polarization singularity occurs, a Gaussian beam is used as an input radiation and introduces a ratio parameter σ, which defines the Gaussian beam radius and the unmodified part of the element radius ratio. Defining the Gaussian beam and ratio parameter as:

$$\mathbf{E}_{inc} = e^{-\frac{x^2+y^2}{w_0^2}} \begin{bmatrix} 1 \\ \pm i \end{bmatrix}, \qquad \sigma = \frac{w_0}{r} \tag{5.1}$$

where w_0 is the radius of the input Gaussian beam at an intensity level of e^{-2}, and r is the radius of the unmodified central zone of the shaping element. Here, x and y are the transverse coordinates.

The resulting transmission Jones matrix is described as:

$$\mathbf{M}(x,y) = \begin{cases} \begin{bmatrix} 1 & 0 \\ 0 & 1 \end{bmatrix}, & \text{for} \quad 0 \leq \rho(x,y) \leq r, \\ \begin{bmatrix} \cos N\varphi & \sin N\varphi \\ \sin N\varphi & -\cos N\varphi \end{bmatrix}, & \text{for} \quad \rho(x,y) > r. \end{cases} \tag{5.2}$$

where $\rho(x,y) = \sqrt{x^2+y^2}$ is the radial coordinate, φ is the azimuthal angle and N is the winding (slow axis modulation) number. The total field after the GPE will be:

$$\mathbf{E}_{out}(x,y) = e^{-\frac{\rho^2}{w_0^2}} \begin{cases} \begin{bmatrix} 1 \\ \pm i \end{bmatrix}, & \text{for} \quad 0 \leq \rho(x,y) \leq r, \\ e^{\pm iN\varphi} \begin{bmatrix} 1 \\ \mp i \end{bmatrix}, & \text{for} \quad \rho(x,y) > r. \end{cases} \tag{5.3}$$

A general concept of this beam shaping technique is given in Fig. 5.1. Intensity distributions of the beams are depicted in the focus of the lens. The crucial parameter σ is responsible for the transformation of the beam from Gaussian to doughnut shape. The parameter σ shows the ratio between the unmodified part of the beam that generates the bell-shaped intensity distribution and the area that generates the circular-shaped intensity distribution. If the ratio tends to zero, this means that most of the beam goes through the element unchanged and the bell-shaped intensity distribution is observed. When the ratio is very large, the element works as a vortex generator and the ring intensity distribution is observed. When the ratio is just right, a flattening of the beam intensity distribution is observed, which will be shown later that there are polarization singularities.

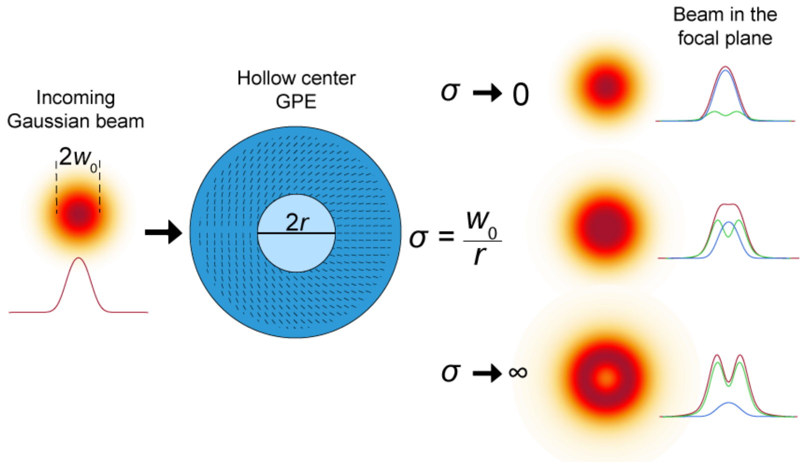

Figure 5.1: Principal sketch demonstrating the operation of the geometrical phase element. The red curves represent the total intensity cross-section consisting of constructive interference of the inner beam (blue curve) and the outer beam (green curve) parts. Black dashes represent nanogratings orientation in the element

.

Analysis of intensity and polarization distribution

To analyze the beam transformation after the focusing lens, the Debye vector approximation is employed [202], which can be summarized as follows. First, the wavefront of the beam just after the exit pupil has a spherical shape with a radius of f, which is the focal length of the lens. Second, each diffracted light ray is considered a plane wave and propagates toward the geometric focal point of the lens; thus, it is represented by a wave vector $\mathbf{k}$. Lastly, the cosine direction $\cos(\theta, \mathbf{n}) \approx 1$, where $\mathbf{n}$ is the normal vector of the diffraction aperture and θ is the angle of the propagation direction of the diffracted ray and the optical axis. The electric field distribution at an arbitrary point in the focal region is given in Cartesian coordinates by

$$\mathbf{E}(\mathbf{r}_0) = \frac{\mathrm{C}}{i\lambda} \iint_{\Omega} \mathbf{T}(s_x, s_y) \exp\left[ik\left(s_x x_0 + s_y y_0 + s_z z_0\right)\right] \mathrm{d}\Omega \tag{5.4}$$

where C is a constant, $k = 2\pi/\lambda$ is the wave number, λ is the wavelength of incident light, and Ω is a solid angle of the objective aperture. Only within this spatial angle Ω, diffracted light rays are considered to propagate towards the focal point and contribute to the formation of a focal spot. The vector $\mathbf{s} = (s_x, s_y, s_z)$ is the dimensionless direction vector along a light ray that reaches the focal point, located at $\mathbf{r}_0 - (0, 0, 0)$. The $\mathbf{T}(s_x, s_y)$ is the electric field distribution at the exit pupil (i.e. on the reference Gaussian sphere). In the case where the aperture of the optical lens is symmetric, it is convenient to recast the direction vector $\mathbf{s}$ as $\mathbf{s} = (\sin\theta\cos\varphi, \sin\theta\sin\varphi, \cos\theta)$, where the meridional angle θ is $0 < \theta < \arcsin NA$ and φ is the azimuthal angle in the focal plane. The solid angle Ω expressed in these coordinates gives $\mathrm{d}\Omega = \sin\theta \mathrm{d}\theta\mathrm{d}\varphi$.

With this in mind, the following standard expression for the electric field in the focal plane is

$$\begin{aligned} \mathbf{E}(\mathbf{r}_0) = \frac{\mathrm{C}}{i\lambda} \int_0^{\theta_{max}} \int_0^{2\pi} \sin\theta \; \mathbf{P}_{out}(\theta, \varphi) \mathrm{B}(\theta, \varphi) \\ \times \exp\left[ik\left(z_0\cos\theta + x_0\sin\theta\cos\varphi + y_0\sin\theta\sin\varphi\right)\right] \mathrm{d}\theta\mathrm{d}\varphi, \end{aligned} \tag{5.5}$$

here $\theta_{max} = \arcsin NA$, $\mathbf{P}_{out}(\theta, \varphi)$ is the polarization state of the electromagnetic vector field in the focal plane and $\mathrm{B}(\theta, \varphi) = \sqrt{\cos\theta}$ is the apodization factor. The polarization state $\mathbf{P}_{out}(\theta, \varphi)$ is related to the electric field in the input $\mathbf{E}_{out}(\theta, \varphi)$ as $\mathbf{P}_{out}(\theta, \varphi) = \mathbf{L}(\theta, \varphi)\mathbf{E}_{out}(\theta, \varphi)$, where $\mathbf{L}(\theta, \varphi)$ is a lens operator 3×3, converting the polarization state of the input plane to the proper polarization state in the focal plane. This operator can be expressed as $\mathbf{L}(\theta, \varphi) = \mathbf{R}^{-1}(\theta, \varphi)\mathbf{C}(\theta, \varphi)\mathbf{R}(\theta, \varphi)$, where $\mathbf{R}(\theta, \varphi)$ is an operator changing the coordinates from Cartesian to polar.

$$\mathbf{R}(\theta, \varphi) = \begin{pmatrix} \cos\varphi & \sin\varphi & 0 \\ -\sin\varphi & \cos\varphi & 0 \\ 0 & 0 & 1 \end{pmatrix} \tag{5.6}$$

and $\mathbf{C}(\theta, \varphi)$ is a lens operator

$$\mathbf{C}(\theta, \varphi) = \begin{pmatrix} \cos\theta & 0 & \sin\theta \\ 0 & 1 & 0 \\ -\sin\theta & 0 & \cos\theta \end{pmatrix} \tag{5.7}$$

The explicit expression for $\mathbf{L}_{out}(\theta, \varphi)$ is

$$\mathbf{L}(\theta,\varphi) = \begin{bmatrix} 1+(\cos\theta-1)\cos^2\varphi & (\cos\theta-1)\cos\varphi\sin\varphi & \sin\theta\cos\varphi \\ (\cos\theta-1)\cos\varphi\sin\varphi & 1+(\cos\theta-1)\sin^2\varphi & \sin\theta\sin\varphi \\ -\sin\theta\cos\varphi & -\sin\theta\sin\varphi & \cos\theta \end{bmatrix} \tag{5.8}$$

Lastly, since the birefringent element acts on circularly polarized vector states $\mathbf{e}_{\pm}$, introducing an operator $\mathbf{P}$

$$\mathbf{P} = \begin{pmatrix} \frac{1}{\sqrt{2}} & \frac{i}{\sqrt{2}} & 0 \\ \frac{1}{\sqrt{2}} & -\frac{i}{\sqrt{2}} & 0 \\ 0 & 0 & 1 \end{pmatrix}, \tag{5.9}$$

which converts from Cartesian basis to circular basis and express $\mathbf{L}(\theta, \varphi)$ in this basis as

$$\mathbf{L}(\theta,\varphi) = \begin{bmatrix} \cos^2\frac{\theta}{2} & -\sin^2\frac{\theta}{2}\mathrm{e}^{2i\varphi} & \sin\theta\mathrm{e}^{i\varphi}/\sqrt{2} \\ -\sin^2\frac{\theta}{2}\mathrm{e}^{-2i\varphi} & \cos^2\frac{\theta}{2} & \sin\theta\mathrm{e}^{-i\varphi}/\sqrt{2} \\ -\sin\theta\mathrm{e}^{-i\varphi}/\sqrt{2} & -\sin\theta\mathrm{e}^{i\varphi}/\sqrt{2} & \cos\theta \end{bmatrix}. \tag{5.10}$$

Knowing this expression, let's find the components $E_+(\rho, \varphi)$ and $E_-(\rho, \varphi)$ and $E_z(\rho, \varphi)$ of the electric field in the focal plane. For this task, use Eq. (5.3) and substitute it into Eq. (5.5) and use the fact that the GPE contains two zones. Multiplying Eq. (5.10) with the expression $\mathbf{E}_{out}$ and assuming $\mathbf{e}_-$ for $\rho \leq r$ and $\mathbf{e}_+$ for $\rho > r$ results in the following integral expressions for individual field components in the focal plane ($z = 0$)

$$\begin{aligned}
&E_+(\rho,\varphi) = \int_0^r \sqrt{\cos\theta}\cos^2\frac{\theta}{2} J_0\left(k_\rho\rho\sin\theta\right)\sin\theta\mathrm{d}\theta \\
&- i^N\mathrm{e}^{(N+2)i\varphi}\int_r^\infty \sqrt{\cos\theta}\sin^2\frac{\theta}{2} J_{N+2}\left(k_\rho\rho\sin\theta\right)\sin\theta\mathrm{d}\theta \\
&E_-(\rho,\varphi) = \mathrm{e}^{-2i\varphi}\int_0^r \sqrt{\cos\theta}\sin^2\frac{\theta}{2} J_2\left(k_\rho\rho\sin\theta\right)\sin\theta\mathrm{d}\theta \\
&+ i^N\mathrm{e}^{Ni\varphi}\int_r^\infty \sqrt{\cos\theta}\cos^2\frac{\theta}{2} J_N\left(k_\rho\rho\sin\theta\right)\sin\theta\mathrm{d}\theta \\
&E_z(\rho,\varphi) = 2^{-1/2} i\mathrm{e}^{-i\varphi}\int_0^r \sqrt{\cos\theta}\sin\theta J_1\left(k_\rho\rho\sin\theta\right)\sin\theta\mathrm{d}\theta \\
&- 2^{-1/2} i^{N+1}\mathrm{e}^{(N+1)i\varphi}\int_r^\infty \sqrt{\cos\theta}\sin\theta J_{N+1}\left(k_\rho\rho\sin\theta\right)\sin\theta\mathrm{d}\theta,
\end{aligned} \tag{5.11}$$

here, $r = f\sin\theta_r$.

By numerical simulation of these equations, one can accurately calculate the intensity and polarization distribution of the beam in the sharp-focusing regime. For moderate numerical apertures (in this experimental verification, it was $NA = 0.2$, thus $\sin\theta = 0.2$, leading to $\sin^2\theta/2 \approx 0.01$ and $\theta^2 \approx 0.04$ therefore) Eq. (5.11) can be approximated to:

$$\begin{aligned}
&E_+(\rho,\varphi) \approx \int_0^r \sqrt{\cos\theta}\cos^2\frac{\theta}{2} J_0\left(k_\rho\rho\sin\theta\right)\sin\theta \mathrm{d}\theta \\
&E_-(\rho,\varphi) \approx i^N \mathrm{e}^{Ni\varphi} \int_r^\infty \sqrt{\cos\theta}\cos^2\frac{\theta}{2} J_N\left(k_\rho\rho\sin\theta\right)\sin\theta \mathrm{d}\theta \\
&E_z(\rho,\varphi) \approx 0.
\end{aligned} \tag{5.12}$$

The electric field in the focal plane has a form expressed as

$$\mathbf{E}(\theta,\varphi) = \mathbf{e}_+ f_1(\rho) + i^N \mathrm{e}^{Ni\varphi}\mathbf{e}_- f_2(\rho), \tag{5.13}$$

which is a general expression of the higher-order polarization singularities [139, 203]. Equations for a reversed input polarization field (i.e.$\mathbf{e}_+$ for $\rho \le r$ and $\mathbf{e}_-$ for $\rho > r$) can be derived similarly. The derivation is omitted here for the sake of brevity.

Under a moderate focusing regime the Debye vectorial focusing analysis can be reduced to two scalar Rayleigh-Sommerfield diffraction integrals for different polarization beams [12], whilst the beam intensity is equal to the superposition of the perpendicular polarization beam intensity, and can be written in the form:

$$\begin{aligned}
&E_\pm(x,y,z) = \frac{z}{i\lambda}\iint_0^r E_\pm(x',y')\frac{\mathrm{e}^{ikr'}}{r'}\mathrm{d}x'\mathrm{d}y' \\
&I = |E_+|^2 + |E_-|^2.
\end{aligned} \tag{5.14}$$

where $r' = \sqrt{(x-x')^2 + (y-y')^2 + z^2}$ is the length from the source point (x', y') at the GPE to the observation point (x, y) at z distance from the GPE. In doing so, the polarization redistribution resulting from wavefront curvature is not accounted for, but it simplifies the analysis and explanation of the presented method. Moreover, it allows the usage of freely available diffraction codes [204].

The application of equation (5.14) for the analysis of a focused Gaussian beam after passing through the designed GPE can be performed by separating the problem into two parts. The first part is the analysis of the focused Gaussian beam with the obscured circular iris of size r, and the second part is the analysis of the outer part of the Gaussian beam altered by the vortex phase. As the polarization state coming out of the element is all circular, but the inner part and outer part rotate in different directions, one can consider them as independent, perpendicular states. This allows us to avoid interference between them. Calculations can be done by modifying the Rayleigh-Sommerfield diffraction integral from Eq. (5.14):

$$
\begin{gathered}
E_+(x,y,z) = \frac{z}{i\lambda}\int_0^{2\pi}\int_0^{r} \mathrm{e}^{-\frac{\rho'^2}{w_0^2}} L(x',y')\frac{\mathrm{e}^{ikr'}}{r'}\rho'\mathrm{d}\rho'\mathrm{d}\varphi' \\
E_-(x,y,z) = \frac{z}{i\lambda}\int_0^{2\pi}\int_r^{\infty} \mathrm{e}^{-\frac{\rho'^2}{w_0^2}-iN\varphi} L(x',y')\frac{\mathrm{e}^{ikr'}}{r'}\rho'\mathrm{d}\rho'\mathrm{d}\varphi' \\
L(x,y) = \mathrm{e}^{ik\sqrt{x^2+y^2+f^2}} \\
I(x,y,z) = |E_+(x,y,z)|^2 + |E_-(x,y,z)|^2
\end{gathered}
\tag{5.15}
$$

where L is the lens phase that focuses the beam. N is the modulation order and φ is the azimuthal angle. The total beam intensity distribution is the sum of the individual counter-rotating polarization intensity distributions.

5.2. Numerical modeling of hyper lemon polarization structures in vector flat-tops

For numerical modelling, three modulation orders $N = [1, 2, 3]$ with three σ case were investigated: from Gaussian-like beam in the focal plane to flat-top and ring-shaped distribution.

Results with modulation order $N = 1$

Numerical modeling results with birefringence axis modulation $N = 1$, depicted in Fig. 5.2. In this case, one expects to observe a polarization singularity, known as lemon [205]. This is the so-called C-point singularity. As the topological number $N = 1$, the expected topological charge of the C-point singularity is $I_c = 1/2$, see [139, 203]. For each selection of the ratio σ, the radius of the hollow center r is adjusted to obtain

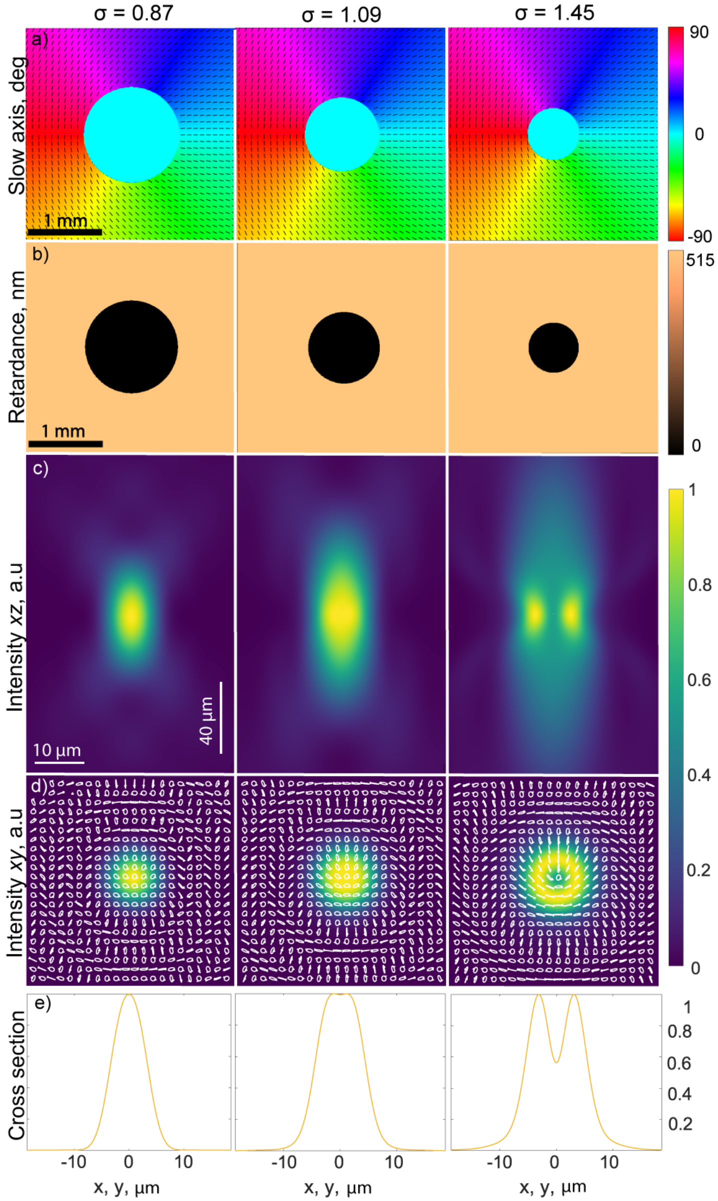

Figure 5.2: Designs of the geometrical phase elements - their birefringence axis (a) and retardation (b) for $\sigma = 0.87$ (first column), $\sigma = 1.09$ (middle column) and $\sigma = 1.45$ (third column). Numerically evaluated normalized intensity distributions in the longitudinal plane (c), the transverse plane (d), and in the cross sections x and y of the transverse plane (e). The winding number is $N = 1$. The retardance is $\tau = \lambda/2$, and GPEs are designed for wavelength $\lambda = 1030$ nm. The numerical aperture in the simulations was $NA = 0.2$.

certain beam-forming conditions. The slow axis distribution is represented by the color map in Figure 5.2(a), while the retardance is shown in Figure 5.2(b). The birefringence axis distribution clearly shows the change in the axis over the azimuthal angle that should produce the first-order vortex phase, because the retardance depicted in Figure 5.2(b) is equal to half of the wavelength in that region, see Eq. (5.3). The circle in the center shows the unaltered region of the element, where the circular polarization ($\mathbf{e}_{\pm}$) beam $\mathbf{E}_{inc}$ passes through the element without any alteration. Note the change in the diameter of the circular spot, which is responsible for the beam shape transition. The propagation in the free space is depicted as the laser beam intensity distribution in the focal region of the lens in Figure 5.2(c). Figure 5.2(d) presents the transverse intensity distribution in the focal plane, while the white ellipses represent the numerically obtained polarization states at each point. Figure 5.2(e) shows the cross-section of the intensity distribution along one transverse axis.

Different columns show different ratios σ to obtain three different distinct beam shapes. It was found that with the ratio $\sigma = 1.09$ the generated beam intensity in the focus flattens the most, while changing the ratio σ to 0.87 the bell-shaped intensity distribution is obtained. Increasing the ratio σ, the doughnut-shaped intensity distribution beam is obtained. The intensity contrast between the maximum intensity and the center of the doughnut-shaped intensity distribution can be increased by increasing the σ parameter. It is interesting to note that the ratio σ changes not only the overall intensity distribution but also the state of polarization throughout the field. The distribution of the polarization state is complex and resembles the polarization singularities examined in [139]. A clear example of a visible singularity is the beam generated in the ratio $\sigma = 1.45$. The center of the beam has a non-zero intensity, and the polarization state there is circular. The higher-intensity surrounding part has a nearly linear, constantly varying angle of polarization field. This particular distribution of the polarization state is similar to the so-called lemon-shaped polarization singularity field (C-point singularity of 1/2 index) [146, 147].

Results with modulation order $N = 2$

Next, the winding number N was increased twice by designing three geometrical phase elements, see Fig. 5.3. With a higher order of slow axis modulation $N = 2$, as depicted in Figure 5.3(a), the GPE converts the outer part of the input beam into a topological charge $m = 2$ vortex beam. The ratio σ required to generate the flat-top intensity distribution is also higher ($\sigma = 1.45$). The ratio σ increases because a higher-order vortex is created and has a larger radius in the transverse plane. This fact also results in a decrease in the maximum intensity of the vortical field when compared to the unmodified part. For this reason, the generation of a flat-top beam should require the diameter of the vortical part to increase to match the intensity of a beam passed through the central part of the GPE, see Figure 5.3(a,b).

The numerically obtained intensity distributions in the longitudinal plane are given in Figure 5.3(c). For a lower value of σ, the Gaussian beam dominates the profile of the combined beam. However, the intermediate value of σ results in a cross-like intensity distribution. A further increase in the parameter σ makes the vortical contribution more significant.

The combined beam has a larger focal spot size, maintaining a flat-top intensity distribution, while the peak-to-valley intensity variation value is less than 5%. Similarly to the previous case (from Figure 5.2), adjustment of the ratio σ provides different intensity distributions in the focal plane. In Fig. 5.3(d)-(e), the intensity distribution is shown together with the distribution of the polarization states combined. Here, at $\sigma = 1.45$, the polarization field is azimuthal at the periphery of the beam, whereas the central part is circularly polarized with elliptical states of polarization between the zones. The higher σ introduces not only an increased influence of the doughnut-shaped intensity but also the state of the polarization field for the larger area of the beam. The distribution of the polarization states also resembles the C-point singularity with index $I_C = 1$, see [206]. Therefore, as expected, an increase of 1/2 in the singularity index of C-points is observed from the previous case.

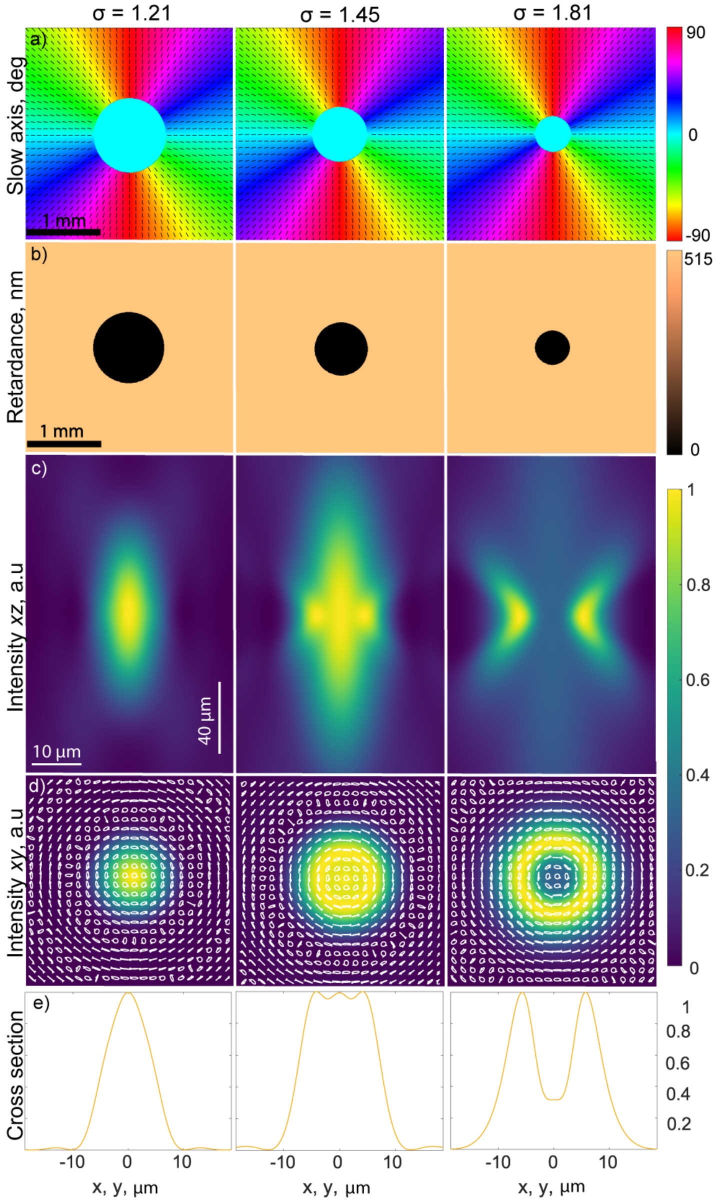

Figure 5.3: Designs of the geometrical phase elements - their birefringence axis (a) and retardation (b) for $\sigma = 1.21$ (first column), $\sigma = 1.45$ (middle column) and $\sigma = 1.81$ (third column). Numerically evaluated normalized intensity distributions in the longitudinal plane (c), transverse plane (d), and in the cross sections x and y of the transverse plane (e). The winding number is $N = 2$. The retardance is $\tau = \lambda/2$, and the GPEs are designed for the wavelength $\lambda = 1030$ nm. The numerical aperture in the simulations was $NA = 0.2$.

Results with modulation order $N = 3$

Lastly, let's further increase the winding number N, it is now $N = 3$, and design three geometrical phase elements, see Figure 5.4(a,b). Analogically to the first two cases, a part of the incoming beam will be converted to a vortex with topological charge $m = 3$ (see Fig. 5.4). The increase in topological change increases the diameter of the beam in the focal plane and reduces its maximal intensity. For this reason, three different values of the parameter σ are selected. The numerically estimated longitudinal intensity distributions are given in Fig. 5.4(c). They reveal that the selection of parameters σ for this particular case gives three different scenarios. In the first one, the Gaussian beam in the combined beam dominates over the vortical part, see the first column in Fig. 5.4(c). The next case represents well-adjusted vortical and Gaussian parts in the combined beam, whereas the last column in Fig. 5.4(c) is the case when the circularly polarized vortex dominates.

The intensity distributions in the focal plane are given in Fig. 5.4(d). Together with the intensity distributions, the polarization ellipses are plotted. The distribution of the polarization state in the combined beam becomes even more complex, as the patterns of polarization ellipses have more complicated distributions. This polarization distribution, as expected, again resembles the polarization singularity of the C-type with a topological index of $I_C = 3/2$, compared with Refs [139]. As expected from the theoretical section, the increase in the slow axis modulation order results in the polarization distribution of the beam, which resembles the C-point singularity of the topological index ($I_c = \frac{1}{2} * N$).

In Fig. 5.4(e) the transverse cross-sections in the x and y axes are shown. The best flatness of the flat-top beam is obtained for the ratio $\sigma = 1.74$. As the doughnut-shaped intensity distribution increases, while the center bell-shaped intensity does not increase so rapidly, the combined flat-top beam has at least a peak-to-valley intensity variation 10%.

From the comparison of all three examples, it can be concluded that the best case for generating flat-top intensity vector beams is achieved with the $N = 2$ order GPE with the ratio $\sigma = 1.45$. Although the flat-top beam produced has a relatively subtle increase in intensity with a small variation in intensity at the top of the profile, it is applicable for various transparent material processing tasks. This, together with other

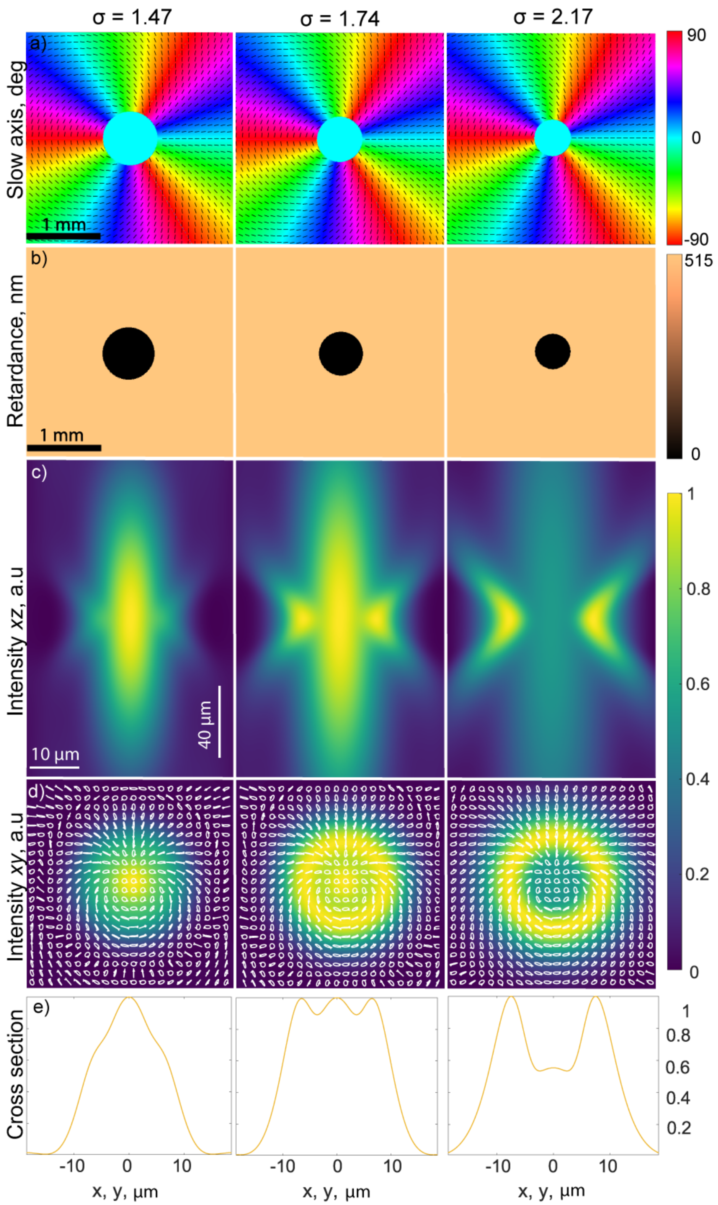

Figure 5.4: Designs of the geometrical phase elements - their birefringence axis (a) and retardation (b) for $\sigma = 1.47$ (first column), $\sigma = 1.74$ (middle column) and $\sigma = 2.17$ (third column). Numerically evaluated normalized intensity distributions in the longitudinal plane (c), the transverse plane (d), and in the cross sections x and y of the transverse plane (e). The winding number is $N = 3$. The retardance is $\tau = \lambda/2$, and GPEs are designed for wavelength $\lambda = 1030$ nm. The numerical aperture in the simulations was $NA = 0.2$.

constructed beams, do not have pre- or post-focus hot spots, which is advantageous for many transparent material processing applications.

5.3. Experimental verification of the concept

Experimental intensity measurements

For the experiments, two GPEs were manufactured from selected two particular cases, investigated in the previous section. As the main aim is the realization of vector flat-top beams, two particular numerical designs were selected: one is with winding number $N = 1$ and the second with $N = 2$, when vector flat-tops are created with tolerably small intensity oscillations in the central part of the beam. The case with the winding number $N = 3$ has oscillations in the central part that are much stronger and might not be suitable for laser micromachining purposes, therefore it was not considered for the experiment.

The experimentally measured diameter of the laser beam was $2w_o = 3.24$ mm at the intensity level $\exp(-2)$. Therefore, the hollow parts of two designed and manufactured GPEs were adjusted to this particular diameter and the ratio σ was chosen to achieve flat-top vector beam profiles. The retardance and birefringence axis measurements of the GPEs, along with the intensity distribution measured in the focal zone, are presented in Figure 5.5. The slow axis distribution clearly shows the change in angle to azimuth, while the central part is almost constant. The retardance distribution shows a constant retardance of 515 nm, which translates to $\lambda/2$ for the fundamental wavelength of the laser. Because the central part of the GPE was left unchanged, it was also observed a contrast between the part of the element with inscribed nanogratings and that which was unmodified.

The experimentally obtained beams show a close resemblance to the numerical experiment (Figs. 5.2 and 5.3). Thus, both versions of flat-top beams were successfully generated in the focal plane with some small irregularities caused by the manufacturing imperfections and other deviations in the optical setup. The laser beam phase front and intensity distribution modulation could have contributed to the observed intensity irregularities. This did not allow for recording a clear profile of the X-shaped intensity distribution in the xz plane, as seen in the numerical simulation. The measured focal spot size for the focused Gaussian beam

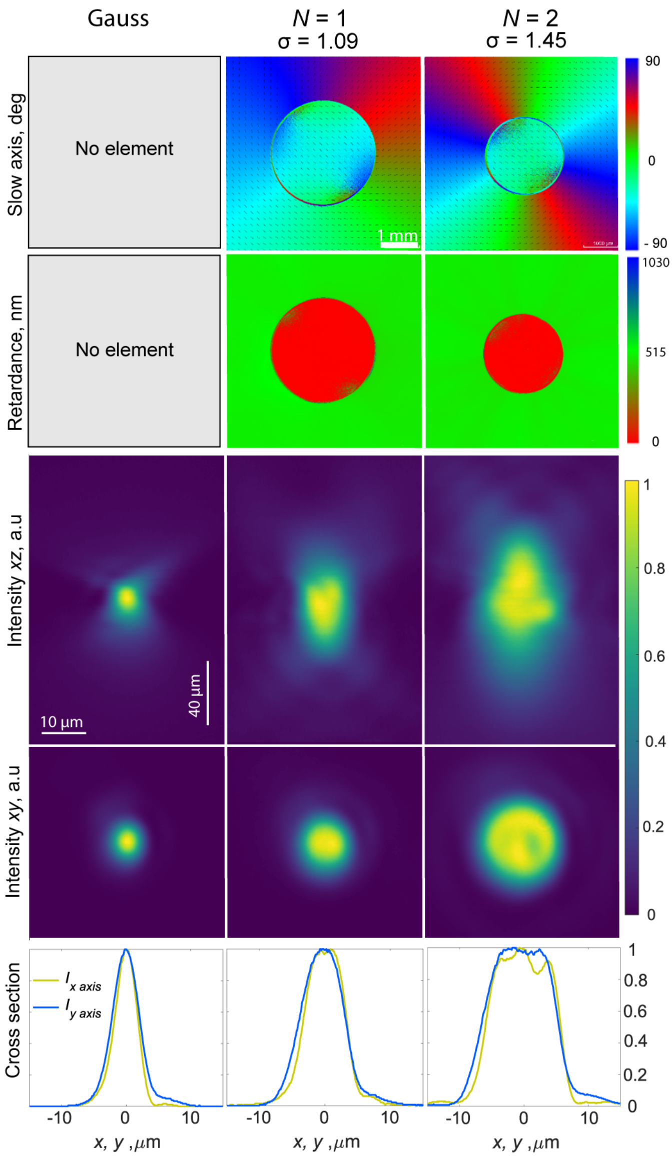

Figure 5.5: Characterization of manufactured GPEs with winding numbers $N = 1$ (second column) and $N = 2$ (third column) – the first row is the slow axis, and the second row is the retardance. Experimentally measured intensity distributions in the longitudinal plane (third row) and in the transverse focal plane (fourth row). Cross-sections in the x and y directions in the focal plane (fifth row). The first column is the Gaussian beam without a GPE. An aspherical lens of $f = 8$ mm was used to focus the beam. Intensity distributions are individually normalized

was measured to be approximately 5 µm. In the case of the combined beam with the winding number $N = 1$ beam, it is 8 µm, and for the $N = 2$ case, it is 16 µm FWHM, see the last row in Figure 5.5. Most importantly, the flattest intensity experimentally recorded is created at the focal plane having the highest intensity, without the pre- or post-focal zone intensity peaks. Although, it is obtained in a shorter focal zone range than the Rayleigh length is.

For the sake of curiosity, the performance of the two geometrical phase elements was investigated under imperfect conditions. For this purpose, the size of the incoming Gaussian beam was increased (by sliding the GPE towards the end of the fixed beam expander). As expected, this change produced a doughnut-shaped combined beam since the input beam width was slightly increased to generate the circular-shaped beam with a non-zero intensity in the center. The resulting intensity distributions for these two cases are given in Figure 5.6. They closely resemble the results predicted by numerical simulations, despite some asymmetry of the intensity patterns originating from the aberration of astigmatism, which was studied in [207]. The overall transmission efficiency for both manufactured elements was measured to be approximately 92%, with losses of 7% attributed to Fresnel reflections from the uncoated surfaces of the elements. Therefore, only the loss of 1% could be attributed to negligible transmission losses. No zeroth-order diffraction peak was observed in the focal zone of the lens. For subsequent light-matter interaction experiments, the average power for the Gaussian beam case was reduced by 8% to achieve the same irradiance level before the focus lens.

Verification of polarization singularities presence using Stokes parameters

From the experimental point of view, it is relatively problematic to measure complex polarization structures, as it is relatively easy to estimate them numerically. The complex distribution of the beam polarization depicted in Figures 5.2–5.4 could be experimentally verified using Stokes parameters or polarimetry measurements.

Therefore, the Stokes parameters were numerically estimated and visualized for the cases under investigation in Fig. 5.7. Stokes parameters S_1 and S_2 present the linear polarization distribution of the beam, while

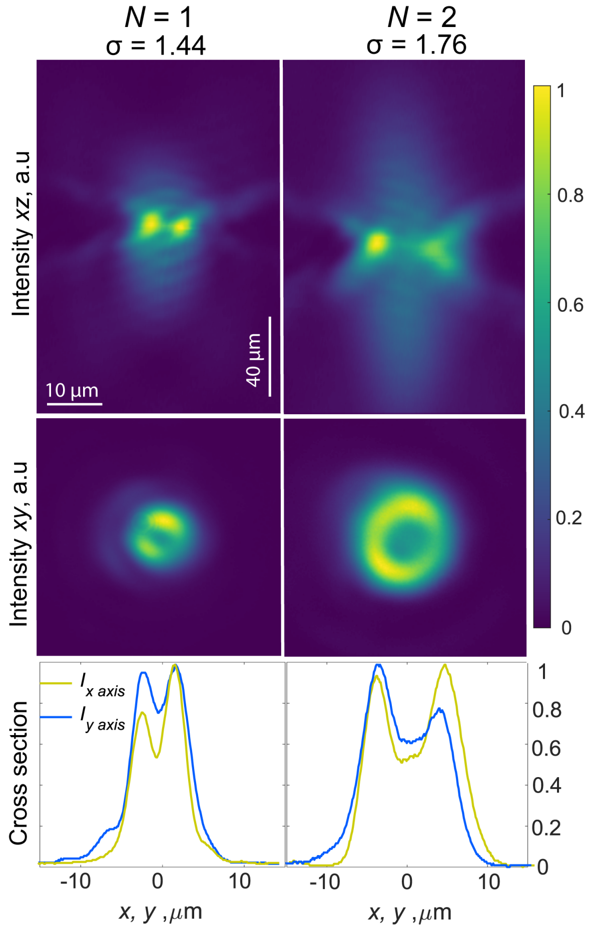

Figure 5.6: Experimentally measured intensity distributions in the longitudinal plane (first row) and the transverse focal plane (second row). Cross-sections in the x and y directions in the focal plane (third row). An aspherical lens of $f = 8$ mm was used to focus the beam. Intensity distributions are individually normalized.

S_3 present the circular polarizations of the beam. As expected from theoretical considerations, the overlap of the two circular polarization beams with opposite rotation directions generates linear polarization, which is most noticeable in the periphery of the combined beam. Note that the Stokes parameters S_1 and S_2 have opposite signs on the different sides of the combined beam. This means that the polarization rotates 90° when the azimuthal angle rotates fully. This can also be seen in Fig. 5.2, where the numerically estimated polarization distri-

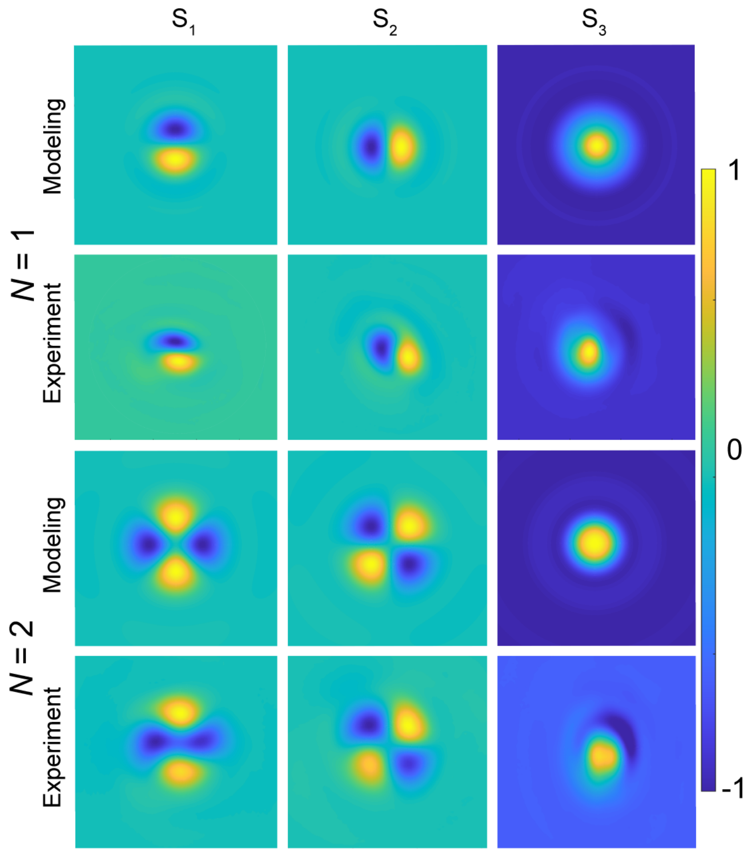

Figure 5.7: Comparison of Stokes S_1, S_2, and S_3 parameters between numerical simulation and experimental measurements of generated beams.

bution is given. The center of the beam has a pronounced circularly polarized state (S_3) in the combined beam, which is contributed by the unaltered central part of the GPE, which forms the bell-shaped intensity distribution that does not overlap with the electric field of the doughnut intensity distribution of the counter-rotating polarization beam.

A clear indication of the azimuthally polarized beam is visible in the Stokes parameters S_1 and S_2 when the second order ($N = 2$) is used to produce a flat-top beam. The distributions of the perpendicular states of linear polarization are located every quarter of the azimuthal angle, and the distributions S_1 and S_2 are rotated by 45°with respect to each other. This can also be seen in Fig. 5.3, where a flat-top beam is created. The center of the beam still has circular polarization, because of the same reasoning as in the $N = 1$ case.

The experimental findings are given in the same Figure 5.7. They verify the successful fabrication of GPEs capable of generating flat-top beams with additional vector field properties, as predicted by numerical simulations. These results validate the numeric approach and pave the way for the utilization of GPEs utilizing hyper-lemon polarization singularities in various non-linear optics and material processing applications.

5.4. Analysis of various material processing

The next part involves investigating the interaction between the materials and the combined laser beams by inducing volume modifications in transparent glass and surface ablation of silicon and thin metallic coating deposited on a glass substrate. Different materials are used in tests in order to better understand possible advantages and disadvantages of the proposed beams in material processing

Comparison in glass welding

One of the most intriguing applications of ultrashort laser irradiation is in-volume modification of transparent materials. The intensity pattern of the laser beam can significantly affect the process parameters and outcomes. Therefore, it was investigated and compared the in-volume modification process using the generated flat-top beams with the standard Gaussian beam.

Initially, two 0.7 mm thick D263T glass pieces were cleaned and placed in optical contact. The laser beams were focused near the contact plane of the glasses to generate a molten pool that propagated toward the direction of the incoming laser light (as shown in Figure 5.8). The optimal welding regime for the Gaussian beam was determined to be using a $NA = 0.2$ focus lens, a scanning velocity of $v = 10$ mm/s, the shortest pulse duration of 358 fs from the laser, and variable average power at a fixed laser repetition rate of 1 MHz. The focusing conditions and laser parameters optimal for glass welding were taken similar to the ones published in Ref. [208]. The measurements of formed molten pools were done by inspecting the cross-sections with an optical microscope with backlight illumination. The width was measured from the most left edge to the most right edge at the widest position. The heights were measured from most top positions down to the bottom edge at the focal position.

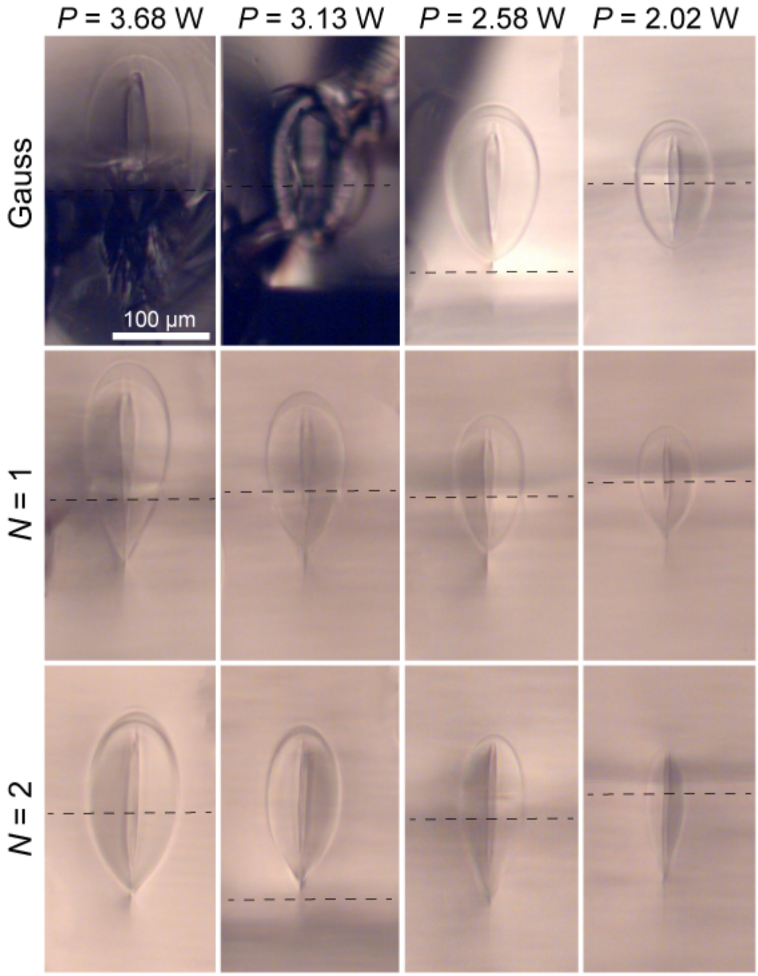

Figure 5.8: Microscope side view images of D263T glass molten pools, formed by different focusing laser beams in volume at the intersection of two samples being in optical contact. The mean power P is changed (indicated), while the constant repetition rate of 1 MHz and the scanning speed of $v = 10$ mm/s are used. Black dashed lines represent the intersection of two glass plates.

Analysis of the side-view images of the molten pools (the graph of measured dimensions is depicted in Fig. 5.9) reveals that the Gaussian beam caused severe cracking when the mean power reached $P = 3.13$ W. At lower power levels, the height and width of the molten pools were

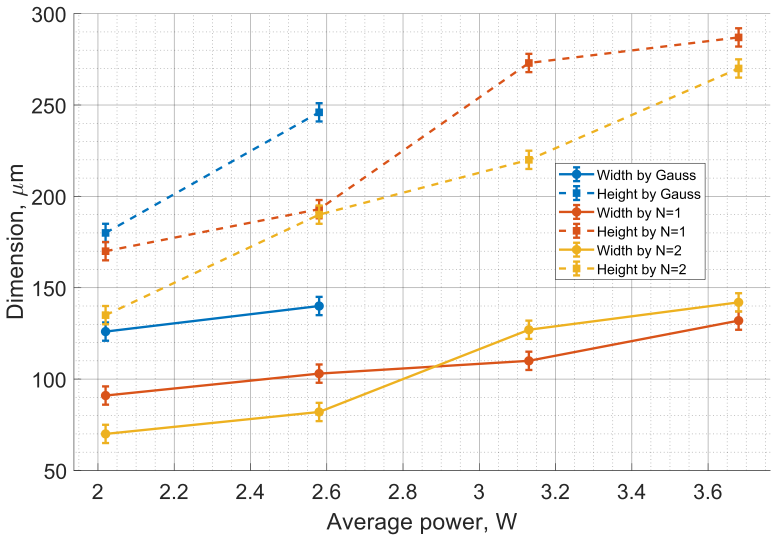

Figure 5.9: Measurement of width and height of created molten pools with different beam shapes.

245 µm and 140 µm for $P = 2.58$ W and 180 µm and 125 µm for $P = 2.02$ W, respectively. In contrast, no visible material destruction was observed when using lemon polarization singularities generated by $N = 1$ and $N = 2$ GPE, even at the highest average power of $P = 3.68$ W. The widths of the molten material formed by the lemon polarization singularity created by the GPE with $N = 1$ were 90 µm, 105 µm, 113 µm, and 132 µm, corresponding to the increase in mean power levels. For the case of hyper lemon, created with a GPE having the winding number $N = 2$, the widths are 70 µm, 82 µm, 128 µm, and 140 µm, respectively.

Despite the larger widths, the heights of the molten pools formed by GPE with $N = 1$ and $N = 2$ are comparable to those produced by the Gaussian beam. For case $N = 1$, the heights are 170 µm, 192 µm, 271 µm, and 289 µm, corresponding to the increase in the mean power levels. For case $N = 2$, the heights are 138 µm, 180 µm, 223 µm, and 267 µm, respectively.

These results indicate subtle differences in the shapes of the plasma channel and the molten pool. For the case $N = 2$, the melted material pools tend to have slightly narrower but larger height profiles, particularly at lower power levels. The most significant advantage is the avoidance of glass cracking with slightly larger dimensions of the molten pool shaped by beams generated by GPE with $N = 1$ and $N = 2$.

This conducted experiment mainly considers the properties and comparison of molten material shapes. Although, the shear tests to evaluate bonding strength were not conducted, it can be stated that the samples were successfully welded, similarly to a presented picture in Fig. 2.20.

Thin film selective ablation

In the subsequent phase of laser microprocessing experiments, the focus lens was replaced with a plano-convex lens with a focal length of $f = 50$ mm, resulting in a reduction in the numerical aperture to as low as $NA = 0.02$. The aim was to selectively remove a thin metallic chromium coating (coating thickness < 10 nm) deposited on a glass substrate. An experiment was carried out to compare the removal of the thin film using different beam shapes, the results are depicted in Figures 5.10 and 5.11. The laser repetition rate was set to 60 kHz while maintaining the shortest pulse duration of 358 fs. Optimal pulse energy values were determined, enabling a clear visualization of the properties of the removed thin film, depending on the total number of pulses applied. The number of shots varied from one to 2000 pulses in a single spot. For the Gaussian beam and the first-order GPE, the pulse energy was fixed at $E_p = 6$ µJ, while for the second-order GPE, the pulse energy increased to $E_p = 21$ µJ due to the larger spot size and reduced fluence. The laser beam and material interaction results at the light transmission regime exhibited clear distinctions for a higher number of applied pulses. When the number of consecutive shots reached at least 100, the Gaussian beam peak induced defects on the glass substrate, while the flatter beam intensity generated by the first-order GPE element effectively prevented this issue. Similar results were obtained with second-order GPE, where a large area of the metallic coating was removed without inscribing defects on the glass layer.

The use of a doughnut-shaped beam with non-zero intensity in its center for the removal of thin films shows quite similar results for high number of shots (see Figure 5.11). The single-shot ablation experiment shows uniform defect formation throughout the beam area. The two-pulse results show the ability to generate a smaller than the beam spot at the center of the cleanly ablated surface, replicating the intensity profile of the constructed beam shape. The increase in the number of

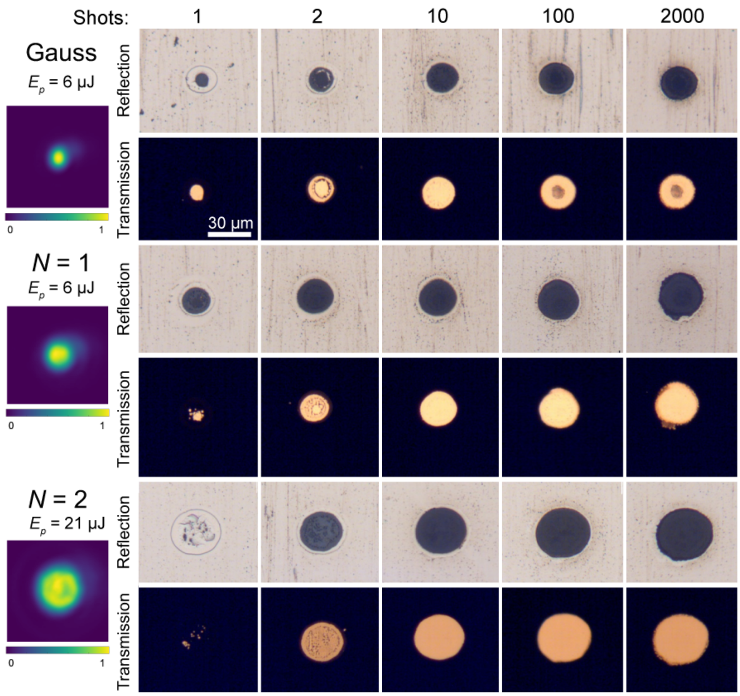

Figure 5.10: Microscope transmission and reflection images of removed thin chrome film on a glass substrate with different beam shapes in the focal plane. The focus lens of $f = 50$ mm is used. Keeping the constant pulse energy, the number of shots was changed as indicated in the pictures

laser shots (10 and more) shows a high-quality removal of the coating without damaging the glass substrate over a larger area than that of the produced Gaussian and flat-top beams.

These experimental tests demonstrate the ability of lemon-polarization singularity-generated vector flat-top beams produced by GPEs to selectively ablate thin metallic coatings in comparison to those of Gaussian beams. The uniform intensity distribution of such lemon polarization singularities reduces the risk of material damage and enables the precise removal of thin films without affecting the underlying substrate. Similarly, doughnut-shaped beams with non-zero intensity in the center can also be used for high-quality thin-film removal applications. The results obtained show the potential and advantages of using a hollow-center GPE with the ability to adjust the beam profile in the focal plane.

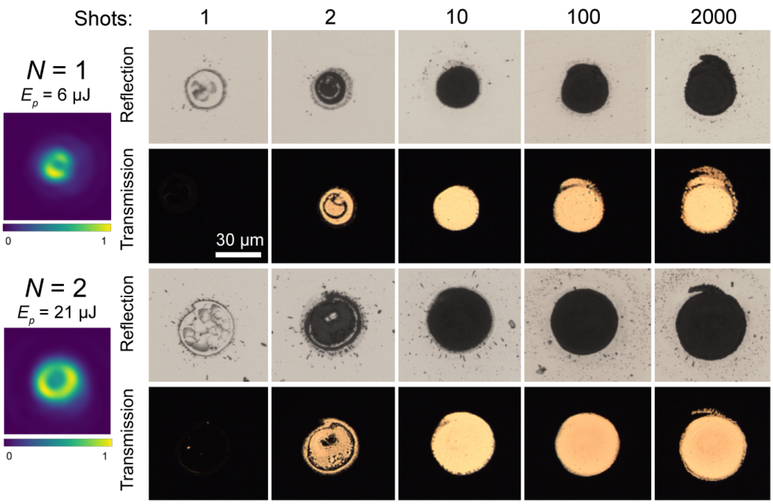

Figure 5.11: Microscope transmission and reflection images of removed thin chrome film on a glass substrate with beam shapes having reduced center part intensity in the focal plane. The focus lens of $f = 50$ mm was used. Keeping the constant pulse energy, the number of shots was changed according to the picture

Silicon surface ablation

In the last experimental part, ablation with varying consecutive shots on a pure silicon substrate was conducted (525 µm thickness, high resistivity, cut at (100) crystal plane). The same focusing conditions as for the flat beam case were used, except that the pulse energy was increased to $E_p = 46$ µJ. Scanning electron microscope images of ablated craters are depicted in Fig. 5.12. Analysis of the ablated material craters as a function of the increasing number of shots reveals distinct differences among the three beam shapes on a low number of shots. The crater generated by a single shot using the Gaussian beam exhibits a slightly different (narrower) profile than that formed by the first-order GPE, with an affected zone approximately 32 µm in width. However, second-order GPE produces a larger modified surface area, with a width of 45 µm. When increasing the number of shots from 2 to 20, noticeable differences emerge. The crater induced by the Gaussian beam tends to deepen and narrow due to tapering effect and higher fluence, whereas the bottom morphologies of craters formed by the first- and second-order GPEs remain relatively flat and uniform, with minimal irregular micro

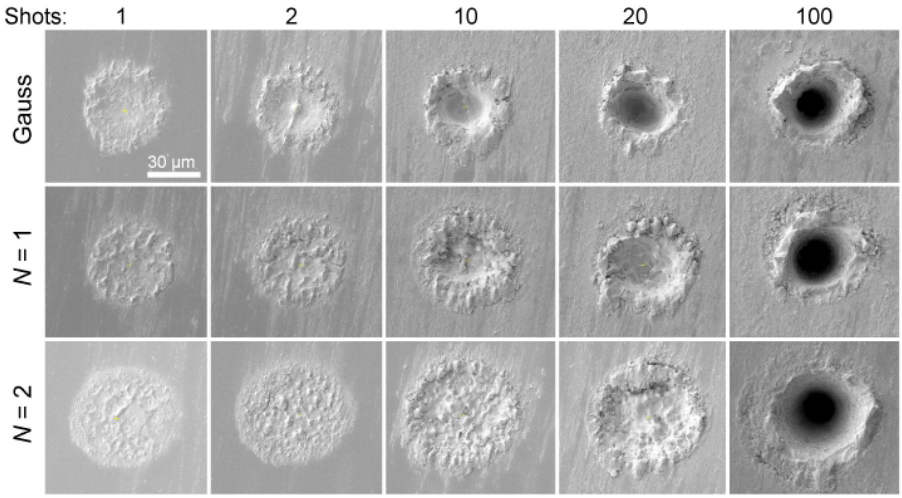

Figure 5.12: SEM images of ablated craters on silicon with different beam shapes: Gaussian and flat-tops of $N = 1$ and $N = 2$ orders. The constant pulse energy of $E_p = 46$ µJ was used for every beam case.

bumps. At higher pulse numbers, the effects of the flatter beam intensity distribution become less pronounced. The steepness of the burr and wall values are comparable for all three beam cases, indicating that the advantages of a flat-top beam are primarily evident in surface modification morphology due to the Gaussian-like side lobe intensity shape.

5.5. Summary of the results

The concept of hollow center spatially variable waveplate was proposed as a way to create vector flat-top beams having polarization singularities at the focal plane under low numerical aperture focusing conditions. Numerical modeling and experimental results verify creating vector beams with the expected presence of hyper-lemon polarization singularities having topological charges of $I_c = \frac{1}{2} * N$, where N is the winding number.

The presented vector flat-top beams are generated as the constructive superposition result of two orthogonal polarization state beams. The intensity distribution in the focal zone does not have the pre- or post-intensity peaks. The uncomplicated implementation of proposed GPEs in the optical scheme, and versatile adjustment of element center diameter versus beam diameter as ratio σ, provides the ability to dynamically change beam shape from Gaussian-like to flat-top and ring-shaped intensity distribution, without the need for additional optical elements, only using conventional focusing optics.

The flat-top forming conditions for various slow axis modulation numbers N were determined as: $\sigma = 1.09$ (for $N = 1$), $\sigma = 1.45$ (for $N = 2$), and $\sigma = 1.74$ (for $N = 3$). The increasing modulation order N at flat-top and constant focusing conditions creates larger diameter beams, but it reduces the flatness of the intensity distribution, when $N \geq 3$. The best case is obtained with the geometric phase element of $N = 2$ and $\sigma = 1.45$ providing a flat-top beam with <5% peak-to-valley intensity variation.

For the first time, distinct application of polarization singularities was experimentally demonstrated in laser microprocessing: glass welding, thin metallic film removal, and silicon ablation applications. Flat-top intensity distribution offers enhanced control over heat deposition and material modification, enabling the production of more precise and uniform structures compared to Gaussian beams. Glass welding experiment revealed the ability to create welded seams of 289 µm height without inducing fracturing of a glass at $P = 3.68$ W average power when $NA = 0.2$. Selective ablation of a thin metallic coating (< 10 nm thick) on a glass substrate demonstrated that the flat-top intensity distribution avoids creating damage by the fatigue effect to the substrate over a Gaussian beam case, even at high number (≥ 2000) of repetitive pulses in a single spot, when the spot size was 16 µm at 21 µJ pulse energy, 358 fs pulse duration. While the silicon ablation tests showed that obtained flat-top beams advantages are mainly observed at surface structuring, when repetitive pulse number is low (< 20). Higher pulse repetition number in a single spot (≥ 100) creates qualitatively deeper craters, due to the Gaussian-like intensity side lobes, the tapering effect occurs making the morphology of narrowed ablated structures similar.

Lastly, the presented geometric phase elements can be implemented as a very suitable choice for high-power and high-transmission beam shaping of flat intensity distribution at the focal plane technique, not limiting by the numerical aperture. The transmission of the uncoated manufactured elements was 92%, whereas the anti-reflective coating would increase it to up to 99% giving near-perfect performance.

6. MANUFACTURING BEAM SHAPING ELEMENTS DESIGNED FOR THZ FREQUENCIES

In previous chapters, the beam shaping technique using nanogratings inscribed by direct laser writing was examined. The knowledge and similar methods of beam modification can also be applied to significantly longer electromagnetic wave spectra, specifically in the terahertz range from 0.1 THz to 10 THz, corresponding to wavelengths from 3 mm to 30 µm. Laser ablation can remove materials with micron-level precision, which is much smaller than the wavelength used in the mentioned range [209–211]. Generally thinking, with the same 1030 nm wavelength ultrashort pulse laser, it is possible to inscribe nanogratings in fused silica and manufacture geometric phase elements for application in the VIS and NIR ranges, as well as employ ablation of various materials to create beam-shaping elements to manipulate the electromagnetic field in the terahertz frequency range [210, 212–214].

Terahertz waves are unique in that they propagate through materials without causing ionizing changes, unlike X-rays [215]. This radiation is often used in spectroscopy, imaging, and optical communication [216, 217]. In the practical implementation of THz imaging systems, special attention must be given to miniaturization and optimization, enhancing functionality, reducing power consumption, and increasing user convenience [218]. This involves overcoming several significant challenges related to the low power emitters, the reliability of sensitive detectors, and finding effective design and technological solutions for passive optical components such as mirrors, lenses, and beam splitters [219]. Typically, these elements are quite bulky, so identifying solutions based on flat optics could lay a solid foundation for developing compact imaging systems and suggest pathways for efficient, lightweight designs. This section aims for investigating beam shaping capabilities utilizing two different methods - employing production of silicon-base diffractive elements and manufacturing flexible metasurface elements (metaelements) from thin stainless steel foil, with the intended use in imaging.

The material related to this thesis chapter was published in papers ***[A3]***, ***[A4]*** *and* ***[A5]***.

Terahertz elements are made from a wide variety of materials, including plastics, metals, semiconductors, and even wax [220, 221]. One widely used material is silicon, which is readily available, extensively manufactured, and commonly used in the electronics industry. Silicon is a well-studied material in terms of light-matter interaction [222–225] and is one of the most important components in electronic devices due to its physical and mechanical properties. Additionally, silicon is transparent in the THz range and has a high refractive index ($n = 3.48$); it can be excited by visible radiation and used as an active element for THz waves [226]. Therefore, this material was chosen as the basis for further modification using laser ablation to alter the surface profile and employ it for phase control of THz waves [84, 209, 227].

6.1.1. Modeling of various flat diffractive elements

The radiation emitted from THz sources can be the same TEM_{00} mode, possessing the properties discussed earlier. To transform these waves into a more complex, structured beam, it is necessary to apply, for example, diffractive elements, similar to those used for visible or NIR light [84, 228]. Arranging elements with sub-wavelength or near-wavelength thickness in a specific spatial pattern can create phase shifts in an optical ray passing through, resulting in the desired constructive interference of transmitted waves at a particular observation point. This concept is implemented using binary or multilevel diffractive elements, where the phase delay is calculated as $(n - 1)t$ for a material with a refractive index n and a local thickness t of the substructure [227].

For this purpose, the fabrication and applicability of several different optical elements for beam shaping and imaging were examined. The production and application of Fresnel zone plates, Fibonacci, axicon, and Airy elements were selected for study at 600 GHz frequency by ablating 0.525 mm thick silicon substrates. The first designed element is a phase zone plate with the transmission function:

$$\Phi_{ZP}(r) = \frac{\pi}{f\lambda}(x^2 + y^2), \tag{6.1}$$

where $f = 10$ mm is the paraxial focal length (similar designs are investigated in Refs. [224, 227]. The quantized phase mask is depicted in Fig. 6.1(a). The generation of the Bessel THz beam was performed

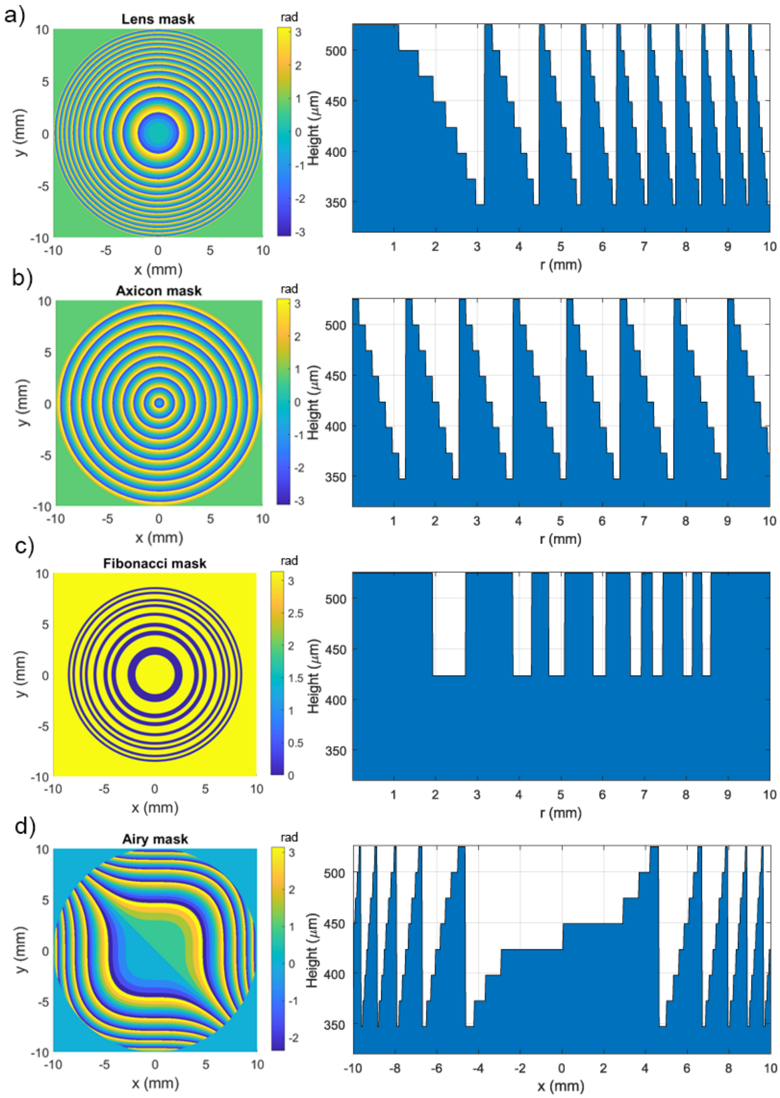

Figure 6.1: Modeling of 8-level phase masks (left) and cross-sections of quantized element profiles, where blue area resembles silicon substrate profile (right): (a) lens (zone plate) mask; (b) axicon mask having $\beta = 0.4$, (c) binary Fibonacci mask, (d) asymmetric Airy mask.

using a linear phase function:

$$\Phi_B(r) = \frac{2\pi \sin\beta}{\lambda}\sqrt{x^2+y^2}, \tag{6.2}$$

where $\beta = 0.4$ rad, see Fig. 6.1(b) for quantized phase mask.

The binary aperiodic Fibonacci lens was created by implementing a procedure described in ref. [229] using Fibonacci sequences with $n_{seq} = 7$. The element is a binary phase plate comprising parts of the surface with phases 0 and π [see Fig. 6.1(c)].

The Airy beam can be constructed with a cubic phase transmission profile:

$$\Phi_{AI}(r) = a(x^3 - y^3), \tag{6.3}$$

where $a = \pi \times 10^7$ m^{-3} [see Fig. 6.1(d)]. This design represents a phase mask plate of eight levels ($N = 8$) of diameter 20 mm, which together with a zone plate ($f = 10$ mm) is dedicated to generating an Airy beam in the range of up to 10 mm.

6.1.2. Experiments and application

Manufacturing flat DOEs by laser ablation

Following the numerical modeling, a laser ablation experiment was conducted. The laser system used in the ablation experiments is depicted in Methodology section in Fig. 3.6.

Firstly, to remove the required material according to the modeling, an experiment was performed to determine the optimal ablation parameters. The spot size of the laser system used in the experiments at focus was approximately 19 µm. Based on this, suitable ablation parameters were identified at a fixed, the shortest pulse duration available from the laser (158 fs): the optimal pulse energy, overlap density of pulses between adjacent shot positions and parallel scanning trajectories (hatching), as well as the number of repetitions required to precisely achieve desired depths were determined. An algorithm was coded for the experiment, in which square areas were ablated within a large parameter matrix: from the initial experiments, the effective spot size was determined to be 19 µm at 9 µJ energy. In the experiment, the pulse energies were varied from 9 µJ to 49 µJ, corresponding to energy densities of 5.73 J/cm^2 to 31.19 J/cm^2. The pulse density along and parallel to the scanning line was chosen to be close to the spot size: distances between adjacent shots ranged from 1 µm to 15 µm (pitch), and hatching density varied from 5 µm to 20 µm. The photographs of silicon sample containing a large array of different parameter sets is depicted in Fig. 6.2.

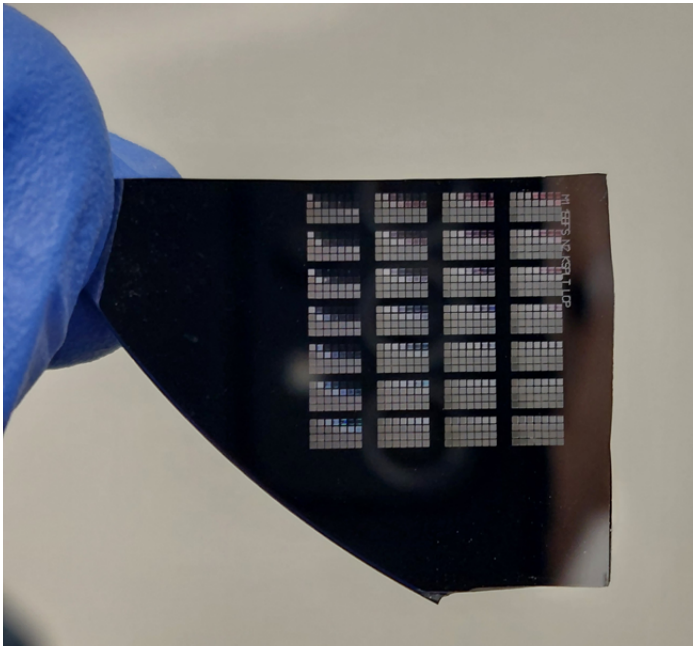

Figure 6.2: Photograph of silicon piece, used to fabricate large array of different processing parameters set. The single square size is 400 × 400 µm.

From the large parameter matrix, the most suitable variants for pulse density were selected at a fixed scanning density of 200 mm^{-1} (74% overlap), with a distance between parallel scanning lines of 10 µm (47% overlap). These parameters were chosen to avoid significant oxidation or other visibly noticeable defects on the silicon substrate while also ensuring that the ablation duration was not excessively long, aiming for a reasonable element production time. For final tests before production, only pulse energy and the number of repetitions were varied (see Fig. 6.3).

The plots show dependencies of the depth and roughness of the ablated areas as a function of the number of scans with various fluences. The plot in Figure 6.3(a) shows a linear function of the number of scans for all fluences, where higher fluence would result in a bigger amount of removed material (depth). As this is a naturally expected result, it

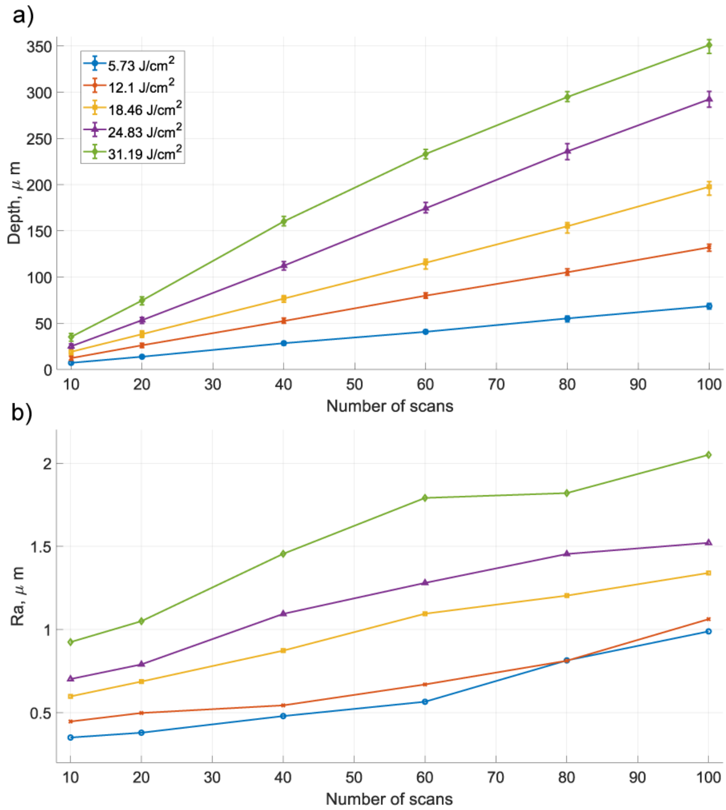

Figure 6.3: (a) Depth and (b) roughness of the bottom dependence after ablation on different numbers of scans with various fluences: 5.73 J/cm^2, 12.1 J/cm^2, 18.46 J/cm^2, 24.83 J/cm^2, 31,19 J/cm^2. The other laser parameters were fixed at 158 fs pulse duration, 74% overlap pulse density, 47% overlap between hatching lines, at 50 kHz laser repetition rate.

is further important to select the appropriate regime for the manufacturing process so it would not take extended time for fabrication. With 5.73 J/cm^2 fluence, the depth after 100 passes was 68.6 µm giving an average of 0.686 µm per pass, for 12.1 J/cm^2 the average was 1.32 µm, for 18.46 J/cm^2 the average was 1.997 µm, for 24.83 J/cm^2 the average was 2.92 µm and for 31.19 J/cm^2 the average was 3.51 µm per single pass. Increased fluence gives a higher removal rate with a trade-off to surface quality - increased roughness [see Fig. 6.3(b)]. The roughness was also measured as increasing value with the number of scans together, depending on the fluence.

It was observed that at 5.73 J/cm^2 and 12.1 J/cm^2 fluences, acceptable quality but shallow depths were achieved: Ra = 0.47 µm and Ra = 0.54 µm, respectively, at $N = 40$. Conversely, at 24.83 J/cm^2 and 31.19 J/cm^2 fluences, greater depths were obtained but with poorer edge and bottom quality resulting in higher roughness values, Ra = 1.09 µm and Ra = 1.45 µm respectively, at $N = 40$. For the final parameter choice, 18.46 J/cm^2 fluence was selected for further manufacturing. Having the final fabrication parameters, the depth of 25.25 µm of each and consecutive N-th step was achieved with repetitive scan number of $13 \times N$. With such energy density, the roughness for the deepest area of 176 µm was Ra = 1.25 µm, which is relative to $\lambda/400$ for 0.5 mm wavelength (0.6 THz). Using this parameter set, the fabrication time at 50 kHz laser repetition rate with 74% pulse overlap at 250 mm/s scanning speed would take 5–7 hours, depending on the size of ablation area.

Measurements of the intensity fields

All the manufactured silicon-based multilevel elements were experimentally tested using the THz continuous wave system: electronic multiplier chain-based emitter (*Virginia Diodes, Inc.*) to produce radiation of 0.6 THz frequency. Delivered through a converging lens of $f = 12$ cm, it was collimated to illuminate the focusing elements, and the data obtained are compared with numerical estimates in Figure 6.4.

The diffractive silicon-based multilevel lens (Fresnel zone plate) [shown in Fig. 6.4(a)] consists of concentric rings, the so-called Fresnel zones, which are spaced at such distances that light constructively interferes with the focal point located approx 8.5 mm from the element, as expected. An experimental investigation of the lens focusing performance was carried out by measuring the intensity distribution along the optical axis xz and in the focal plane xy perpendicular to the direction of THz light propagation. The zone plate functions quite well in the focal plane, the full width at half-maximum of the focused Gaussian beam is 0.27 mm, while the FWHM of the collimated beam amounts to 11.8 mm. The intensity of the focused beam increases 65 times.

In the same principle, the next element under investigation was the axicon dedicated to generating a Bessel beam. The experimentally

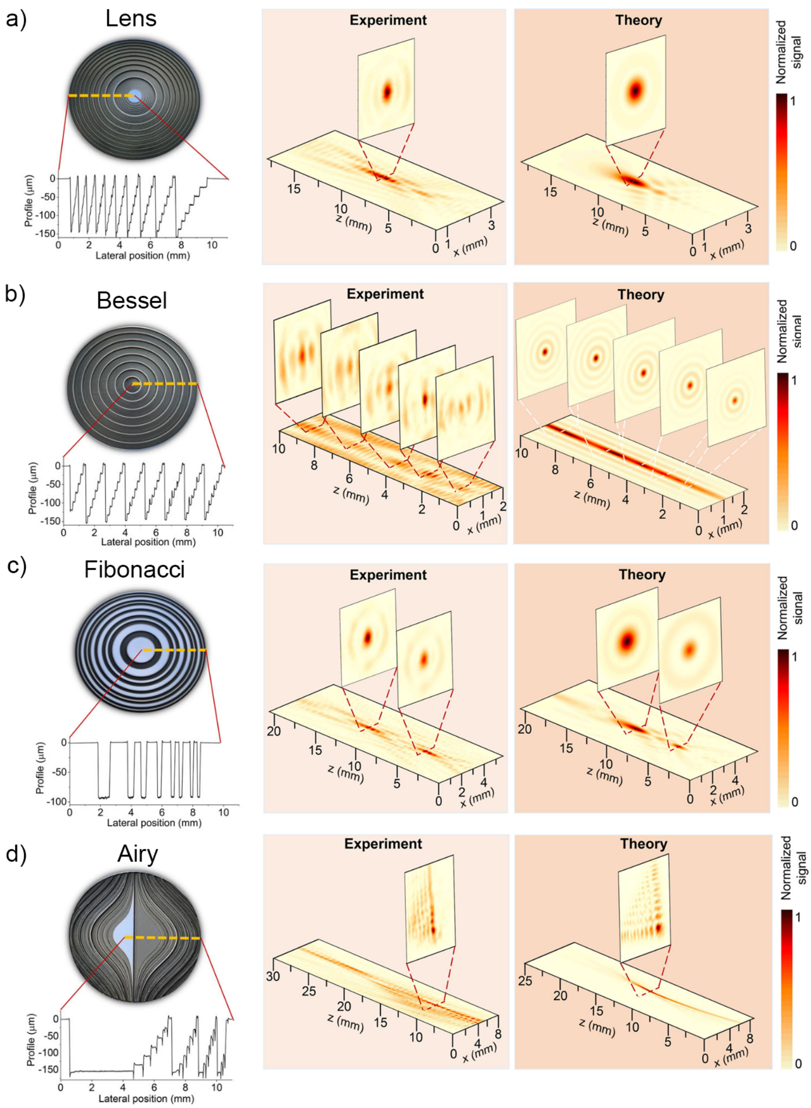

Figure 6.4: Manufactured diffractive optical elements (DOE) and their cross-sections, along with experimentally observed intensity profiles and those predicted from numerical simulations, for a) a Fresnel zone plate, showing a distinct focus in both plots, b) a Bessel axicon, generating a "needle"-shaped THz beam, c) a Fibonacci lens, demonstrating bifocal characteristics, and d) an Airy zone plate, where the beam follows a parabolic trajectory with reciprocal paths visible in the experimental plot.

obtained two-dimensional THz Bessel beam profiles are given in Figure 6.4(b). A total of five focal points are registered. The distance between focal points increases (from approx 0.2 mm to 1.5 mm) with the distance in the direction of beam propagation. Furthermore, as the beam expands, the FWHM increases with each focal point, to 1 mm, 1.1 mm, 1.9 mm, 2.2 mm, and 3.7 mm, accordingly. These experimental results are confirmed by numerical simulations, even though, the data reveals some deviations between numerical expectations and experimental observations. It might be guessed that this is caused by interference between the incident and reflected signals or by some not-perfect optical alignments in the experimental setup.

Next, the Fibonacci beam shaping element was examined. The experimental results and their comparison with the theoretical model are presented in Figure 6.4(c). As can be seen, the element forms two focal points in both cases, where the intensity in the second focus is 25% higher than in the first. Furthermore, FWHM in the first focus was found to be 0.27 mm. This could be caused by interference between the incident and reflected signals.

Finally, the performance of the Airy element was tested, see Figure 6.4(d). As depicted, the experimentally measured performance is in close line with what is expected from the numerical estimates: the Airy beam formed in the transverse and longitudinal planes displays a parabolic trajectory, which is an inherent feature of the Airy beams. The beam in the transverse plane is scanned at the point of maximal longitudinal intensity and behaves as expected, although the edges are slightly distorted as a result of some deviations from the paraxial trajectory. It can be seen that in this case, the Airy element was also combined with the zone plate. These results show that the zone plate behind the Airy zone plate slightly deflects the incident beam. Furthermore, the spatial resolution and quality of the scanned images were reported to be much better when an Airy zone plate is combined with a conventional zone plate. Therefore, verification experiments and numerical examination allowed to infer that the fabricated elements perform well and are well-suited to for precise investigation and benchmarking.

Imperfections of manufacturing

It is worth noting that manufacturing inaccuracies have minimal impact on the effective performance of the elements. When closely comparing the theoretical and experimentally obtained profiles (see Fig. 6.5), the initial (shallowest) steps closely follow the theoretical model, while the deeper steps exhibit lower manufacturing precision. This is due to

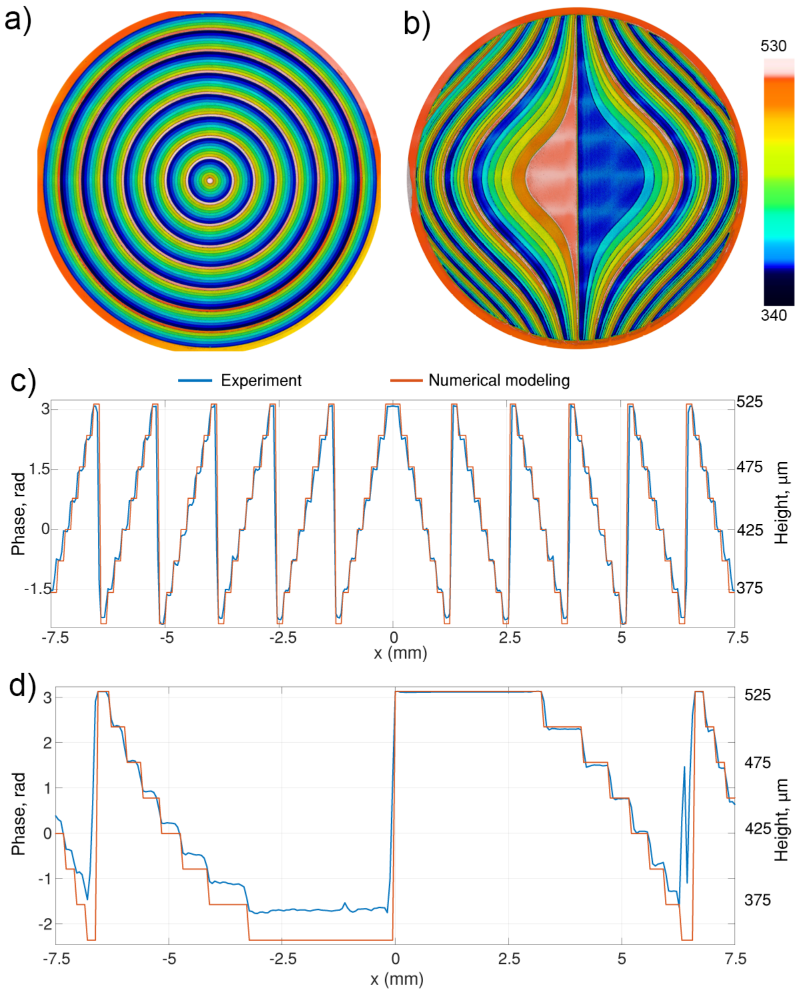

Figure 6.5: Closer comparison of manufactured (a) Axicon and (b) Airy elements to the numerical models: cross-sections of the (c) axicon and (d) Airy step profiles, measured with optical profiler.

the presence of a natural taper angle (usually between 10° and 15°) caused by ablation with a Gaussian beam, which has a bell-shaped intensity distribution. With each subsequent pulse (or repetition), the material is removed in a non-uniform manner, carving into an already-formed V-shaped groove. Due to the taper angle, part of the radiation is reflected off the walls, narrowing the ablation area. As a result, at the positions of the deepest steps, the step width becomes vanishing small, resembling more of a V-shape and failing to reach the precise intended depth [see Fig. 6.5(c)-(d)]. Another reason for the discrepancy in focal distributions is that the simulation used the Rayleigh-Sommerfeld diffraction integral with a spherical-point-source-based propagator, which is a paraxial approximation. However, due to the long wavelengths of THz radiation and the comparable size of the optics, a nonparaxial diffraction simulation method would be required for more accurate results, this issue is comprehensively covered in paper [**A3**]. Finally, a closer look at the Airy element profile reveals that seven steps were ablated instead of eight. This occurred due to an error in the manufacturing process when a software error caused the laser system to stop fabrication. Despite this, the experimental results are sufficiently high-quality to allow further testing of this element.

Imaging behind an obstacle

Distinct properties were observed when examining the Airy beam: due to its nonparaxial nature and the natural curvature of its focal zone along the z axis, an imaging experiment was conducted to compare the beam's propagation behind an obstacle, with the detector registering radiation passing through the target. Three configurations were compared: the Airy element alone, the Airy element combined with a lens, and a Bessel beam formed by an axicon. The imaging setup and results are presented in Figure 6.6. The obstacle was placed at a distance of $z = 1$ mm behind the last element in the setup before the object, with other distances selected optimally based on prior experimentation. A metal plate, impermeable to THz radiation, was used as the obstacle in all three setups. During the experiment, progressively larger areas of the optical element in front of the sample were obscured by the metal plate.

As revealed in the experimentation [see Fig. 6.6(a)], when a single Airy lens is used, the image of the target remains clear even when almost the entire optical element is blocked by the metal obstacle. The smallest resolved stripe period is 1.2 mm. These results align with the numerical estimates provided in the same figure. Minor discrepancies may be attributed to slight misalignment in the system and imperfections in position estimates. These findings confirm the self-healing properties of the Airy beam, offering the potential for THz structured light imaging even in the presence of an opaque object.

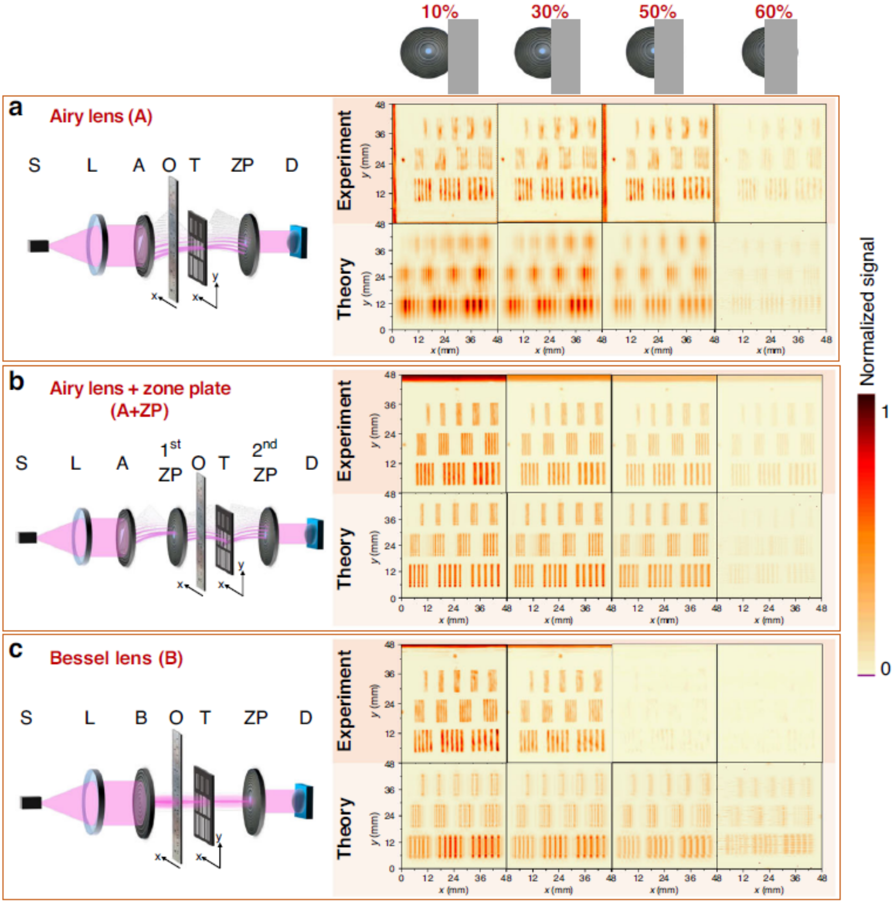

Figure 6.6: Performance of the nonparaxial Airy phase mask in THz imaging behind the obstacle in two setups: with the single nonparaxial zone plate (a) and two on paraxial zone plates (b), where O denotes an obstacle. Performance of the nonparaxial Bessel phase mask in the same THz imaging behind the obstacle setup (c). The color bar is normalized to the maximum value of the signal for each setup. The position of the obstacle is depicted on top of four columns on the right, starting from the almost uncovered object (middle, ≈ 10% is covered) and ending with the most covered object (right, ≈ 60% is covered).

Even more promising results are observed when a combination of the nonparaxial cubic phase mask and the nonparaxial zone plate is used [see Fig. 6.6(b)]. The target slits remain visible, even when more than half of the illuminating element is blocked. Surprisingly, high resolution is still achieved, with the smallest resolved stripe period being 0.7 mm.

Lastly, the performance of the Fresnel axicon was examined, as the structured THz illumination it generates is also nondiffracting and self-recovering. During experimentation with the Bessel lens [see Fig. 6.6(c)], when small portions of the generating element were blocked, the target image remained clearly visible. The smallest resolved stripe period was 0.8 mm (1.6λ). However, as larger areas of the element were blocked, the image quality deteriorated, eventually fading into noise. Numerical simulations demonstrated similar behavior, though some recognizable images remained in the background. This deviation is likely due to experimental uncertainties in the generated structured light. Overall, the cubic phase plate outperformed the Bessel-generating element in this benchmark.

To sum up, it was observed that the performance of the single Airy phase mask decreases as more of the structured illumination is blocked, with spatial resolution increasing from 2λ to 3.2λ and contrast fluctuating around 30 (a.u.). Surprisingly, in the second experiment, the combination of the Airy phase mask and the zone plate exhibited even better performance, with spatial resolution remaining constant at 1.6λ, regardless of the percentage of the element blocked. However, the contrast dropped from 30 to 20 as more of the illuminating element was covered. Lastly, the spatial resolution of the Bessel beam illumination decreased from 1.6λ to 3.2λ, and its contrast dropped sharply, with no images recorded when a large portion of the element was covered. When 30% of the element was obscured, the Bessel illumination showed a significant reduction in contrast, whereas the Airy beam and the Airy beam with the zone plate showed contrast less affected by the percentage of the block.

More extensive experimental research on THz imaging with the discussed beams is presented in publications [**A3**] and [**A5**], and is not further elaborated on in this section due to the scope of the topic.

6.2. Flexible meta optics

For the control and shaping of THz waves, metasurfaces (or meta-elements) can be used in a manner similar to that of VIS or NIR radiation. It has been demonstrated that metamaterials offer vast design flexibility for flat optical elements, allowing for the manipulation of electromagnetic wave properties, including propagation, polarization management, and control over material refractive index dispersion [230,231]. Metaelements are typically fabricated through lithography or nanoimprinting methods, and can be made from a variety of materials such as silicon, dielectrics, or metals [91,232,233]. One widely used type of metasurface is the split-ring resonator (SRR), which operates based on the electric field generated by dipoles or quadrupoles arising from charge carrier oscillations under external electromagnetic illumination [234, 235]. In the THz spectrum, SRRs are typically on the scale of several tens of micrometers and can be easily fabricated using a laser ablation process. In this subsection, the production of inverse SRRs from a thin 25 µm stainless steel foil is investigated, with the aim of demonstrating flexible and reliable THz beam profile engineering through mechanical bending of a C-shaped metasurface.

6.2.1. Design of inverse split ring resonators

The most common type of SRRs consists of a conductive periodic structure deposited on a transparent substrate, with dipole formation occurring at the gap of the ring element [236]. Alternatively, inverse SRR or complementary SRR (CSRR) structures, composed of periodic C-shaped openings in the conductive layer, can also be fabricated. In these structures, the dipole forms at the opening on the side opposite to the conductive gap [237]. It is important to note that the dipole can be generated by charge carrier interactions with either the magnetic or electric components of the external radiation, or both, depending on how the incident radiation is applied [238]. Therefore, the ability to adjust the opening angle, radius, and width of the C-shape provides three additional degrees of freedom for manipulating electromagnetic waves.

The complementary metasurface's openings were systematically arranged in a recurring design based on the Fresnel equation, functioning as a zone plate [top panel of Figure 6.7(a)], allowing for focusing and manipulation of the THz beam [239]. The gap position and cutout angle of the CSRRs (denoted by ϕ and θ, respectively) were adjusted according to their location on the metasurface to achieve the required phase shift for each CSRR. Each subzone of the zone plate was populated with identical CSRR meta-elements, ensuring a $\pi/2$ phase shift between neighboring zones. Additionally, the radius of the openings, R, and their width, c, were varied to further optimize the focusing element. It is worth noting that the detected signal is due to radiation re-emitted from the metasurface. In this case, the ratio of excitation to re-emission power depends on the metasurface's rotation angle and ranges from 6% to 10%.

Figure 6.7(b) presents a schematic representation of the THz beam engineering setup designed for investigating the metallic metasurfaces. The system utilizes an adjustable InP Gunn diode oscillator, capable of delivering tunable frequency radiation within the range of 93.8 GHz to 94.1 GHz, along with passive optical components and a bow-tie diode serving as the THz sensor. In Figure 6.7(c), the layout of the THz imaging setup is depicted, incorporating two additional paraffin lenses. These lenses are used to collimate the THz beam after it passes through the target and then focus it onto the detector.

6.2.2. Manufacturing of flexible optical elements

To fabricate C-shaped metasurfaces from stainless steel foil, an experiment similar to the previously presented silicon ablation setup was conducted. The goal was to determine the optimal laser and fabrication parameters while maintaining high shape accuracy and efficient process time. Experimental studies on the ablation of steel and other metals using ultrashort pulsed lasers is a well-researched topic, aimed at finding optimal parameters for ablation or other highly precise structures made from base materials [240–242]. Since metal reflects the majority of NIR radiation and is a good conductor with many free charge carriers, excessive heating under high fluence or repetition rate can have adverse effects on the sample, such as deformation, or oxidation, which should be avoided [243, 244].

The experiment for selecting laser parameters was also performed at a fixed, the shortest pulse duration available from the laser (158 fs), with the goal of identifying the optimal pulse overlap density, fluence, and number of repetitions. An algorithm was coded for the experiment, which involved ablation of multiple single C-shapes with varying sets of parameters on 25 µm stainless steel foil. The pulse density was varied

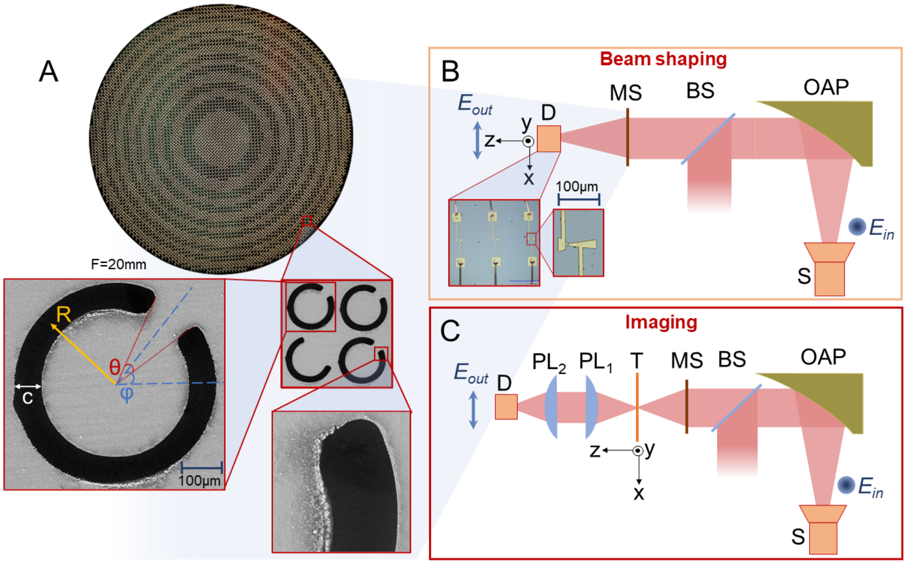

Figure 6.7: Metallic metasurface design and THz imaging setups. (a) Design of the metallic C-shaped complementary split-ring resonators metasurface, its geometry, and enlarged view of the meta element depicting the parameters to be varied: the letter c denotes the thickness of the opening, θ - the cutout angle, R is the radius, and ϕ depicts the position of the gap. (b) Schematic layout of the THz beam engineering setup dedicated to the evaluation of metallic metasurface design effect on the polarized light. The radiation of power of around 40 mW with an electric field polarized along the y axis emitted from an adjustable frequency InP Gunn diode oscillator source (GQ-440KS, *Spacek Labs*) S is collimated by $f = 10$ cm parabolic mirror (PM) as the beam diverges. The metasurface focuses the beam onto a focal point where a polarization-sensitive InGaAs-based bow-tie-shaped detector D is placed. The photo of the enlarged active part of the detector is depicted in the bottom inset. A high resistivity silicon beam splitter BS of 525 µm thickness is placed between a parabolic mirror and metallic metasurface to reduce the standing wave effects between the emitter and metallic metasurface. (c) THz imaging setup employing the THz beam engineering. The setup contains two additional paraffin lenses (PL1 and PL2) dedicated to collimating the THz beam after it passes through the target T and then focusing it into the detector.

from 100 mm^{-1} to 500 mm^{-1}, in 100 mm^{-1} steps, corresponding to a pulse step size from 10 µm to 2 µm. The pulse energy was varied from 3 µJ to 30 µJ, in 3 µJ steps, corresponding to a fluence change from 2.12 J/cm^2 to 21.16 J/cm^2. Finally, it was necessary to determine the sufficient number of repetitions required to fully ablate the desired structures through the sample. The number of repetitions was varied from 20 to 260, in steps of 20. After the first iteration of the experiment, the most suitable results were selected, and the experiment was repeated with a narrowed parameter space. The results of the second iteration are presented in Figure 6.8.

After narrowing the parameter space, a fixed pulse density of 200 mm^{-1} was chosen, while the selected fluence values were 2.12 J/cm^2, 6.35 J/cm^2, and 10.58 J/cm^2. These parameters were chosen because at higher fluence and density, significant surrounding material damage was observed, including oxidation, deformation due to excess heat, and the formation of sticky dust that could not be removed even with ultrasonic cleaning. Figure 6.8(a) shows that at low fluence, full material ablation through the sample only occurred at a high number of repetitions, around 200. At higher fluence values, clean and uniform through-cutting was achieved earlier, at around 160 [at 6.35 J/cm^2 in Fig. 6.8(b)] and 120 repetitions [at 10.58 J/cm^2 in Fig. 6.8(c)]. However, at 10.58 J/cm^2, there was a higher occurrence of burns and dust, which was more difficult to remove in an ultrasonic bath or could not be removed at all. The final selected fluence level was 6.35 J/cm^2. At this energy density, no significant deformation or oxidation of the samples was observed. It was also noted that a through-cut was achieved after 120 repetitions, but additional repetitions resulted in a more uniform cutting edge with less variation in width. When the number of repetitions exceeded 200, there was little further change, and increasing the number of scans ensured that all structures were cut, while the widening due to repeated ablation was negligible. Lower fluence values with a higher number of repetitions could also be suitable for production, but the choice of parameters was based on achieving a reasonable production time and sufficient processing quality. The duration of manufacturing a single 2 inch size element at 6.35 J/cm^2 fluence would take approximately 3 hours. Based on the selected optimal processing parameters, various meta-elements could be produced by modifying only the initial design drawing.

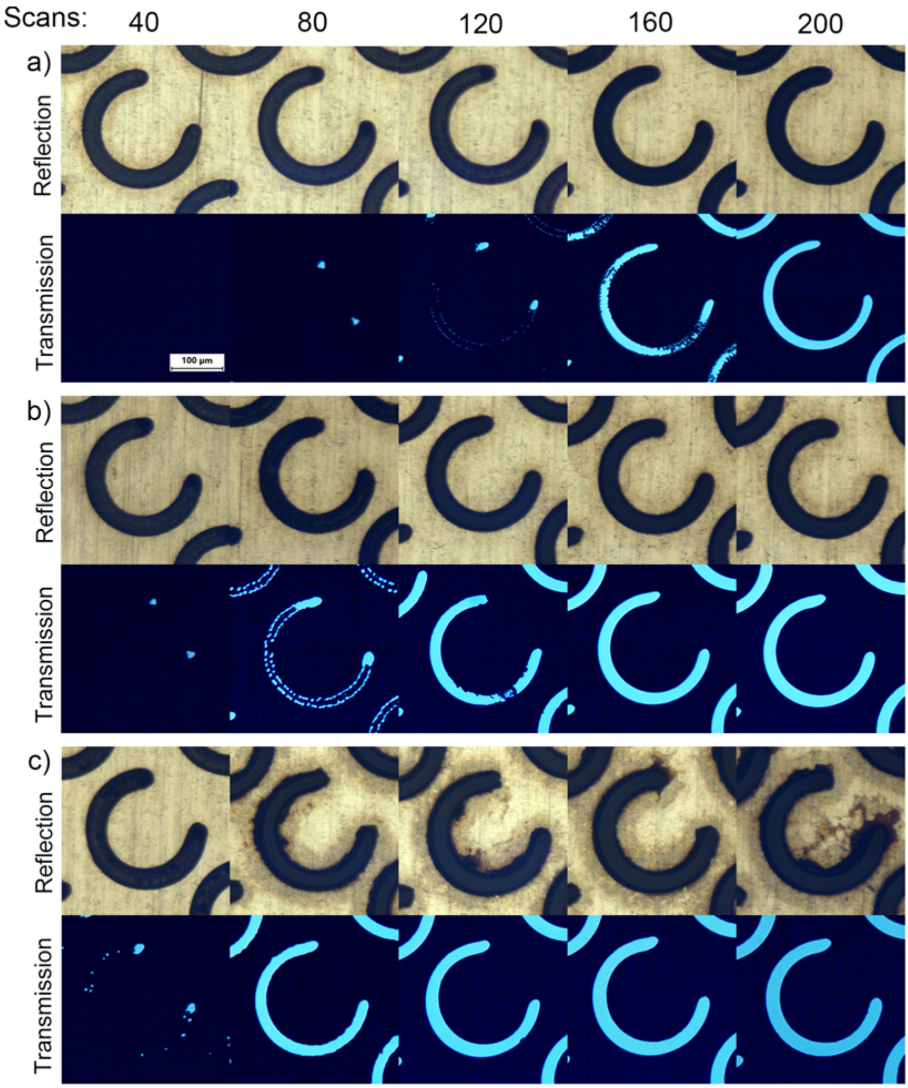

Figure 6.8: Microscope images in reflection and transmission regimes of stainless steel foil of 25 µm thickness ablation experiment. At fixed pulse density of 200 mm^{-1} and pulse duration of 158 fs, the other parameters were: (a) 2.12 J/cm^2, (b) 6.35 J/cm^2 and (c) 10.58 J/cm^2 fluences. The repetition number was changed from 40 to 200 in steps of 40.

6.2.3. Testing performance of manufactured elements

The primary aim was to assess how variations in different CSRR metaelement parameters influenced the focusing abilities of the metasurface, as shown in the center of Figure 6.9. Initial parameters, optimized for the target frequency, were derived from previous studies by another group [245]. To design the most efficient focusing metasurfaces for operation around 94 GHz, numerical simulations were conducted by varying the cutout angle, with a focal length of $f = 20$ mm, a radius of $R = 240$ µm, and an opening width of $c = 60$ µm [see Figure 6.9(a)]. The cutout angles of two distinct metaelements were varied while maintaining a constant relative phase shift of $\pi/2$. Additionally, using the optimal cutout angle determined from simulations, the effect of varying the CSRR metaelement radius R was explored [see Figure 6.9(b)]. Lastly, the CSRR opening width c was varied between 30, 60, 75, and 90 µm for the parameters of $f = 20$ mm, $R = 240$ µm, and cutout angles of $\theta_1 = 40°$ and $\theta_2 = 135°$. These metasurfaces were also experimentally tested. The results, matching the simulations and shown in Figure 6.9(c), indicate that the best focusing was achieved with an opening width of $c = 75$ µm. Metasurfaces with all three optimized parameters were subsequently used for further studies of structures with varying focal lengths and the impact of metasurface bending on focusing performance.

Four metasurfaces with focal lengths of $f = 10$, 20, 30, and 40 mm were fabricated, and their focusing performance was evaluated both experimentally and theoretically. The experimentally obtained THz beam intensity distribution along the optical axis is displayed in the main graph of Figure 6.10, represented by symbols. Theoretical modeling of the metasurface operation and THz light propagation properties, performed using the FDTD method, is depicted by solid lines. As shown, the intensity of the beam focused by the $f = 20$ mm focal length metasurface exhibits a significantly higher intensity compared to the other designs with focal lengths of $f = 10$ mm, $f = 30$ mm, and $f = 40$ mm. The performance of a single CSRR metaelement is governed by its numerical aperture (NA), where radiation is modulated by the CSRR's directrix and non-spherical wave emission. Short focal distances (large NA) result in modulated beam amplitudes due to paraxial design and aberrations, while longer focal distances reduce these effects and show conventional Gaussian beam behavior. Increased focal distances also expand beam size and Rayleigh distance, but intensity decreases, especially when constrained by the production size of the metasurfaces.

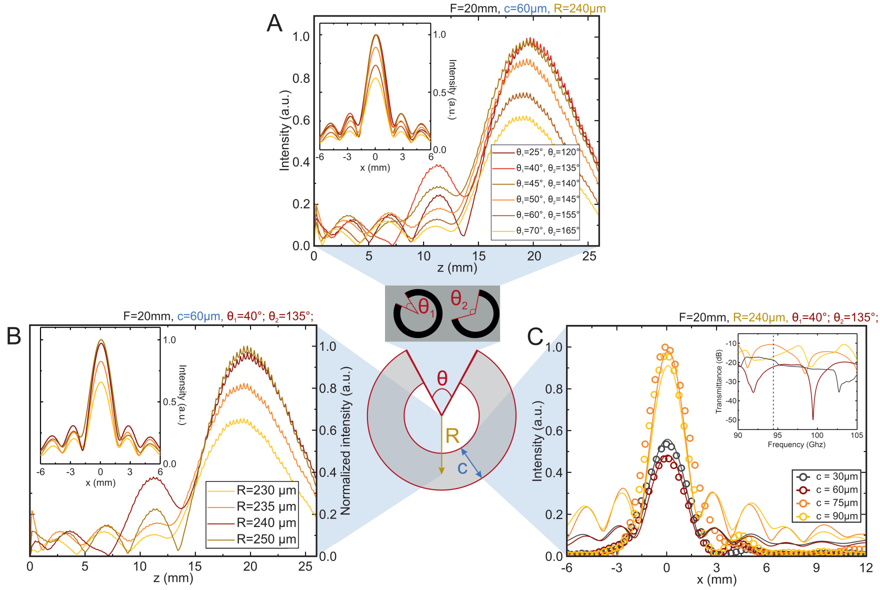

Figure 6.9: The dependence of CSRR metasurface focusing performance on different metacell geometrical parameters. (a) Simulation of the intensity distribution along the optical axis, obtained by varying cutout angles θ_1 and θ_2. Intensities along the x-axis at the focal plane are displayed in the inset. The optimal pair of angles $\theta_1 = 40°$ and $\theta_2 = 135°$ was selected for the following simulations. (b) Simulations of intensity distribution along the optical axis for the CSRRs metaelement radius R ranging from 230 µm to 250 µm. Intensities along the x axis at the focal plane are displayed in the inset. The optimal radius of $R = 240$ µm was selected for the following simulations. (c) Illustration of the experimentally measured (symbols) and simulated (solid line) intensities along x axis at the focal plane for the varying opening widths of the metaelements, noted by the letter c at the central image. The inset denotes the simulated transmission spectra of the CSRR structure at the focal point, the blue dashed line represents the frequency used during the experiments. In all cases, fixed parameters are displayed in the insets of the relevant panels.

The experimental results for metasurfaces with an optimal focal point of 20 mm (depicted in Figure 6.10) show good alignment with theoretical models, though experimental data reveals Fabry-Perot oscillations not predicted in simulations. These arise from standing waves in the experiment. The flexibility of the CSRR structure offers further tun-

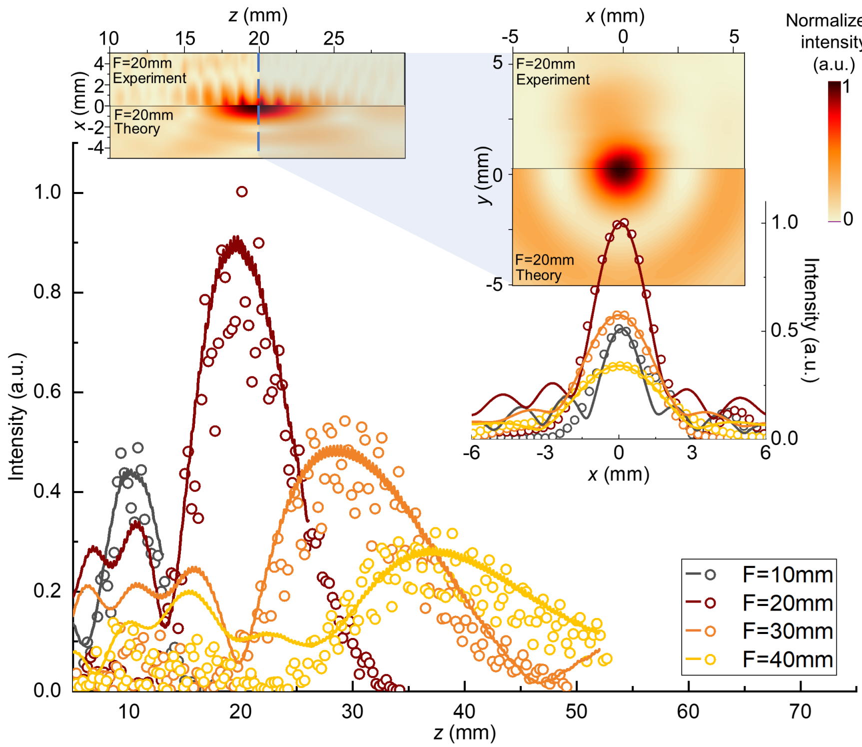

Figure 6.10: Focusing performances of the complementary C-shaped split ring resonators-based metasurface with different focal lengths (f = 10, 20, 30, and 40 mm) at 94 GHz. The main graph–experimental results (symbols) and simulation results (solid lines) of the beam profile distribution along the optical axis for metasurfaces of the different focal lengths. Top left inset–the performance of the metasurface lens with the focal length of 20 mm: top half represents experimentally obtained, and bottom half depicts simulated intensity distribution of THz beam along the optical axis. Note the standing wave effect occurring in the experimental part. The blue line indicates the focus position of the analyzed CSRR structure. The upper part of the top right inset–THz beam intensity distribution in the focal plane, corresponding to the blue dashed line of the top left inset. The top half depicts experimental results and bottom half–theoretical simulations. The bottom part corresponds to the intensity beam profile along the x-axis at the focal point of the metasurfaces with different focal lengths, where the experimental results are marked as symbols and theoretical simulations are depicted as solid lines.

ability through mechanical bending, unlike standard SRRs. As bending increases, the signal decreases but focusing is maintained, as shown for

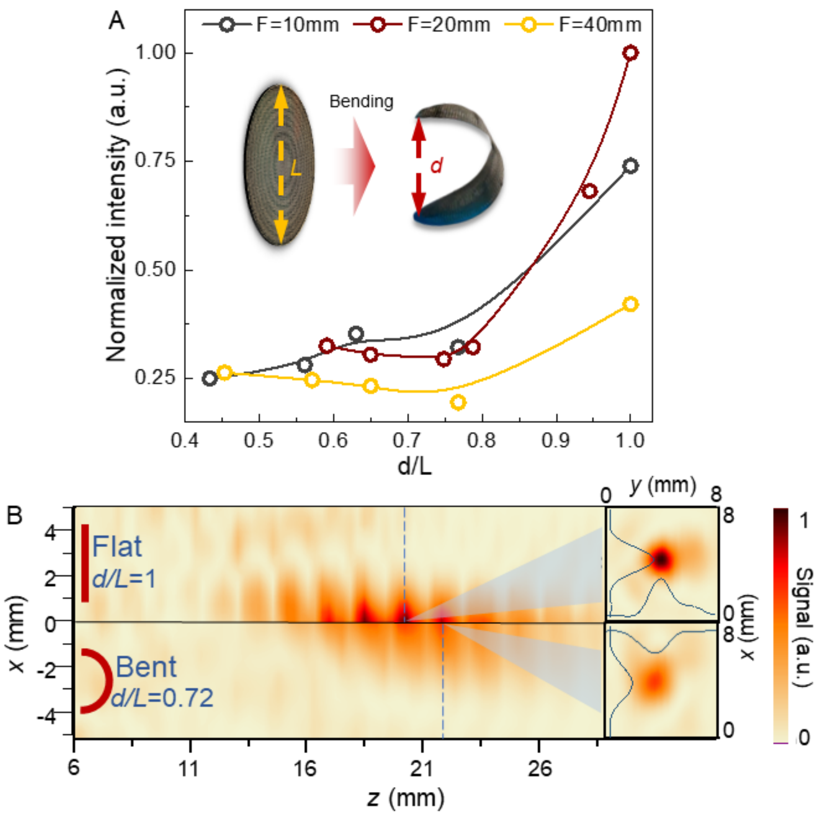

Figure 6.11: (a) Measured intensity dependence upon bending metasurfaces of different focal lengths. The inset depicts a visualization of the bent metasurface. The letter L denotes the diameter of the unbent metasurface and d is the distance between two opposite ends of the deformed plate. The bending level is represented as a ratio of d/L. (b) Intensity distribution of the THz beam along the optical axis xz: the top half represents results when the metasurface was flat and the bottom half when the metasurface was bent. The dashed blue lines indicate the focus position. Note the change of the focal distance and intensity occurring due to bending, giving additional adjustment ability. Insets on the right side represent beam intensity distribution in the focal plane xy for the cases when the metasurface is flat and bent, respectively.

metasurfaces with different focal lengths in Figure 6.11. Even at maximum bending, the signal remains functional, allowing flexible tuning of THz optics, which is beneficial for compact imaging systems. Therefore, these fabricated elements were further tested in imaging experiments; however, to avoid expanding the scope, this is further discussed in publication [**A4**].

The demonstrated manufactured meta elements can also be implemented for use in higher THz frequencies. A comparison of three meta elements made for 100 GHz, 250 GHz, and 2.5 THz resonant frequencies are depicted in Figure 6.12. The C-shaped features must have smaller

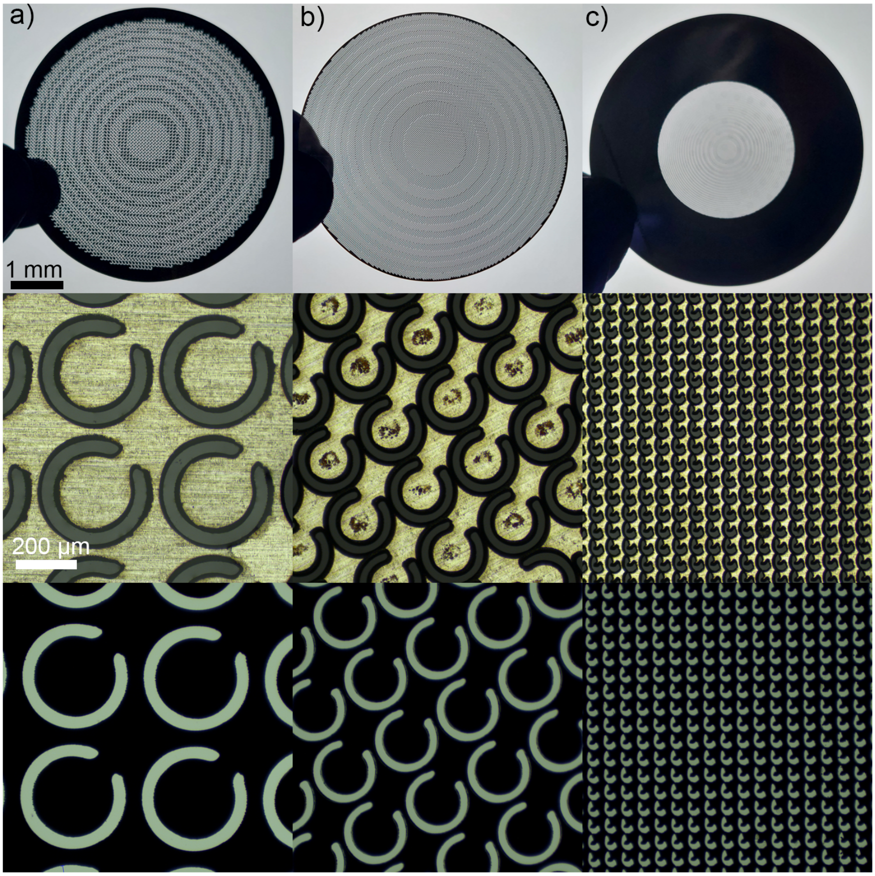

Figure 6.12: Comparison of manufactured meta elements designed for different frequencies: (a) 100 GHz, (b) 250 GHz, and (c) 2.5 THz. The top row shows images of whole manufactured elements, and the middle and bottom rows reflection and transmission microscope images under 5X magnification.

dimensions for application in the higher frequency range. For example, in Figure 6.12(a), the meta element contains C-shapes of approximately 55–60 µm widths. For efficient use in 250 GHz, the widths of the features must be as small as 30 µm [see Figure 6.12(b)]. For use in 2.5 THz, the manufactured C-shapes were in widths of 8-18 µm [see Figure 6.12(c)].

Such a higher deviation of width was due to unideal diffraction-limited spot size. The astigmatism of the focused beam makes different cutting widths in orthogonal directions. Therefore, the potential efficiency of such an element would be decreased. To overcome this issue, an ideal diffraction-limited beam should be used, i.e. having a lower M^2 factor. As well as the numerical aperture or shorter wavelength (second or third harmonics) must be used. However, due to the limitations of the existing optical system, the numerical aperture cannot be increased because of the fixed input aperture of the galvanometer scanner, as well as the fixed focal length of the F-theta lens, and the operating wavelength is only 1030 nm. Theoretically, with an upgraded fabrication system, these problems could be solved and the potential cut width of the features be as narrow as a few microns, meaning that it would be possible to manufacture elements for higher frequencies than 2.5 THz.

6.3. Summary of the results

Ultrashort pulse laser ablation using $\lambda = 1030$ nm wavelength is capable of producing diffractive beam shaping elements from silicon for terahertz frequencies with high precision. The roughness of the ablated material directly depends on both fluence and the number of repetitions, ranging from as low as < 0.5 µm (at low fluence of 5.73 J/cm^2 and 40 number of scans) to over 2 µm (at high fluence of 31.19 J/cm^2 and 100 number of scans) and lets to control the removed material depth within typical 2 µm accuracy.

The all experimentally produced silicon-based elements had the surface roughness of 1.25 µm at the deepest zones, which corresponds to a surface quality of $\lambda/400$ for a 0.6 THz wave. Theoretically extrapolating this value, it allows for the production of elements suitable for the up to 6 THz spectrum and beyond, maintaining a processed surfaces quality of no less than $\lambda/40$.

The observed differences of manufactured elements and theoretical models in terms of taper or missed single phase step, can be neglected, as the shaped beams still produce the wanted field distributions, at a lower efficiency.

In the imaging experiment, significant improvement was observed when the Airy element paired with a zone plate. Imaging through the target slits remained visible, even when more than half of the illuminating element is blocked. High resolution was still achieved, with the smallest resolved stripe period of 0.7 mm. This improvement could be subject to the accelerating (bending along focal zone) nature of the Airy beam.

Laser ablation is also a highly advantageous technology for manufacturing THz metaelements consisting of complementary split-ring resonators. By employing $\lambda = 1030$ nm wavelength USP laser source in pair with galvanometer scanner together with F-theta lens of $f = 100$ mm, several zone plates were manufactured from 25 µm thick stainless steel foil. The production from this thin material enables the making of compact and flexible alternative beam shaping elements for as low as 94 GHz frequency and up to 2.5 THz.

The limiting factors for production beyond 2.5 THz frequency is the diffraction limited spot size at the focal plane of the optical system. The possible improvement could utilization of shorter wavelength irradiation (second or third harmonic), aberration reduction or using higher numerical focusing conditions. However, the last factor is limited to the existing F-theta lens compatibility for production area over 50.8×50.8 mm field.

The quality of metasurface element production can be controlled and improved by using lower fluence levels with high repetition rates giving higher scanning speed, thus avoiding significant material deformations and oxidation while keeping reasonable production time of several hours.

7. GENERAL CONCLUSIONS

The first statement to be defended is based on these conclusions:

1. The utilization of axicon phase masks having spatially shifted halves enables to create distorted, multi-peak invariant Bessel-type beams. The increased spatial shift p in the opposite direction induces larger distortion of the central peak, splitting it into a multi-peak transverse intensity distribution with a larger physical distance between the peaks.

2. The broken symmetry in the phase mask produces a slightly distorted-elongated beam intensity pattern with displacement parameter $p = 0.25$. This intended displacement is the key factor for inducing micro-fractures in the bulk of a glass with a 36° angle to the normal of displacement axis, with an ellipticity of $\mathcal{E} \approx 1.05$. Dicing experiment revealed that it is possible to separate 0.5 mm D263t glass, with the roughness of sidewalls of approximately 0.52 µm with peak-to-valley values of 3.52 µm and -3.3 µm, by using 1.3 mm Bessel zone beam (in air, at $\exp[-2]$ intensity) at 4 ps (FWHM) pulse duration, 330 µJ pulse energy, 10 µm pitch and 20 mm/s scanning speed.

3. The optimized azimuthal phase modulation can be employed to find optimal beam shape with a desirable asymmetry of the central peak, by altering the phase-cut angle γ and the extent of the phase difference $\Delta\varphi$. Accounting for this, the elliptical Bessel-type beam with an ellipticity of $\mathcal{E} = 1.19$ and contrast of $C = 0.61$ was formed utilizing a manufactured GPE of $\gamma = 17°$ and $\varphi = 5\pi/4$ and employed in the stealth dicing experiment, by using 6 ps (FWHM) pulse duration, 8 µm pitch with 170 µJ pulse energy, at 20 mm/s scanning speed. The obtained lowest roughness was 0.47 µm and peak-to-valley of 1.03 µm and -1.09 µm, respectively. The dicing outcome of systematically obtained beam shows better results overall: more expressed ellipticity is accountable for better alignment of fractures, along cutting trajectory, resulting in comparable roughness but lower peak-to-valley values.

4. The analytic investigation manifests that for both utilized Bessel-type beam shaping cases, the resulting invariant beam is a coherent superposition of zero-order and even higher-order Bessel beams.

5. The utilization of geometric phase elements proves to be a reliable and efficient technique for high-power beam shaping, reaching for up to 74% – 90% transmission for uncoated elements at $\lambda = 1030$ nm wavelength. The transmission losses of the produced element are dependable on not only the inscribed retardance deviation but also on the complexity of the slow axis pattern. Steep slow axis changes may result in zones of correctly undefined birefringence and retardance.

The second and third statements to be defended are based on these conclusions:

6. The novel concept of hollow center spatially variable waveplate makes a way to efficiently create vector flat-top beams having hyper-lemon polarization singularities with topological charges of $I_c = \frac{1}{2} * N$, where N is the winding (modulation) number. The measured transmission can be as high as $\approx 92\%$ without anti-reflective coatings at $\lambda = 1030$ nm wavelength.

7. The presented vector flat-top beam shaping technique generates the flattest intensity distribution at the focal plane without the pre- or post-intensity peaks, independently of focusing conditions, using the constructive superposition result of two orthogonal polarization state beams.

8. The uncomplicated implementation of proposed elements in the optical scheme, and versatile adjustment of element center diameter versus beam diameter as ratio σ, provides the ability to dynamically change beam shape from Gaussian-like to flat-top and ring-shaped intensity distribution, using only a single geometric phase element.

9. The flat-top forming conditions for various slow axis modulation orders N were determined as: $\sigma = 1.09$ (for $N = 1$), $\sigma = 1.45$ (for $N = 2$), and $\sigma = 1.74$ (for $N = 3$). The increasing modulation order N at flat-top under constant focusing conditions creates larger

diameter beams, but it reduces the flatness of the intensity distribution, when $N \geq 3$. The best selected ideal case is obtained with the geometric phase element of $N = 2$ and $\sigma = 1.45$ providing a flat-top beam with <5% peak-to-valley intensity variation.

10. The experimental light-matter interaction results reveal that vector flat-top beam intensity distribution in accountable for improved selective surface ablation of thin metallic coating (< 10 nm thick) – avoiding damage to the glass substrate even at high number (≥ 2000) of repetitive pulses in a single spot, when the spot size was 16 µm at 21 µJ pulse energy, 358 fs pulse duration.

11. The silicon ablation tests showed that obtained flat-top beams advantages are mainly observed at surface structuring, when repetitive pulse number is low (< 20). Higher pulse repetition number in a single spot (≥ 100) creates qualitatively deeper craters, due to the Gaussian-like intensity side lobes, the tapering effect occurs making the morphology of narrowed ablated structures similar.

The fourth statement to be defended is based on these conclusions:

12. Ultrashort pulse laser ablation using $\lambda = 1030$ nm wavelength is capable of producing terahertz diffractive beam shaping elements from silicon and metaelements from stainless steel foil of 25 µm thickness. The possible applicable range for silicon-based manufactured diffractive elements can be up to 6 THz, maintaining a processed surfaces quality of no less than $\lambda/40$, when surface roughness is 1.25 µm, using fluence of 18.46 J/cm^2, at 358 fs pulse duration.

13. Utilization of $\lambda = 1030$ nm wavelength USP laser source in pair with galvanometer scanner together with F-theta lens of $f = 100$ mm, allows manufacturing of compact and flexible complimentary split-ring resonator-based beam shaping elements for as low as 94 GHz frequency and up to 2.5 THz.

14. The limiting factors for production beyond 2.5 THz frequency is the diffraction limited spot size at the focal plane of the optical system. The possible improvement could utilization of shorter

wavelength irradiation (second or third harmonic), aberration reduction or using higher numerical focusing conditions. However, to maintain a rapid fabrication process, the galvanometer scanner is essential. But it is limited by input aperture size and to the minimal available F-theta lens focal length with working field size, which should not be lower than the size of metaelements being 2 inches (50.8×50.8 mm).

8. SANTRAUKA

8.1. Įvadas

Su ultratrumpųjų impulsų lazerių išradimu ir pastoviu tobulinimu, bekontaktis tikslus lazerinis mikroapdirbimas tapo svarbi, sparčiai augančios fotonikos pramonės ir mokslinių tyrimų srities dalis. Lazeriai tapo nepakeičiamais įrankiais, dėl savo tikslumo ir universalumo. Tobulėjant impulsiniams lazeriams, jų vidutinė galia ir pasikartojimo dažniai vis didėja, o poreikis optimizuoti jų veikimą ir energijos perdavimą medžiagai tampa vis akivaizdesnis. Kai kuriais atvejais standartinis iš lazerio išspinduliuojamas Gauso pluoštas tampa problema įvairioms mikroapdirbimo užduotims įvykdyti: pjovimui, gręžimui ar sudėtingesnių struktūrų kūrimui iš skaidrių ar neskaidrių medžiagų. Tokio pluošto varpo intensyvumo formos pasiskirstymas erdvėje gali sukelti nepageidaujamą apdirbimo kokybės suprastėjimą dėl šilumos paveiktos zonos, ypatingai tada, kai energijos tankis yra gerokai didesnės už medžiagos pažeidimo slenkstį [1]. Relėjaus (Rayleigh) ilgis yra dar vienas ribojantis veiksnys, ypač stebimas pjaunant skaidrias medžiagas, kai reikalinga ilgesnė židinio zona. Vienas iš pagrindinių pluoštų formavimo privalumų lazeriniame mikroapdirbime yra efektyvesnis energijos perdavimas medžiagai. Pritaikant lazerio pluošto intensyvumo skirstinį pagal atliekamos užduoties reikalavimus, tampa įmanoma tiksliai koncentruoti energiją ten, kur jos reikia, taip sumažinant nuostolius ir padidinant mikroapdirbimo efektyvumą [2]. Toks tikslus energijos perskirstymas gali ne tik pagerinti apdirbimo tikslumą, bet ir prisideda prie bendro proceso ekonomiškumo, pasiekiant didesnius greičius bei išnaudojant didesnį lazerio potencialą. Židinio zonos inžinerija gali būti taikoma ne tik lazerinio apdirbimo patobulinimui, bet ir vaizdinimo užduotims, mikroskopijai bei kitoms sritims fotonikoje, neapsiribojant regimojo diapazonu, bet taip pat tinkant ir terahercų bangų spektrui. [3].

Šioje disertacijoje pagrindinis dėmesys skiriamas pluoštų formavimui, kuris gali pagerinti įvairių medžiagų mikroapdirbimo procesus bei vaizdinimą terahercinių bangų ruože. Pirmoji dalis apima geometrinės fazės elementų (GFE) naudojimą, tinkamų didelės galios lazerio spindulio formavimo taikymams, siekiant pagerinti specifinius medžiagų apdirbimo uždavinius: Beselio tipo pluoštų kūrimas greitam ir kryptingo skilimo valdymo stikle procesui; pradinio Gauso pluošto transformavimas į sudėtingesnį intensyvumo lauką su unikaliomis poliarizacijos savybėmis. Antroji darbo dalis skirta pluoštų formavimo pritaikymams terahercinių dažnių diapazone bei specialių elementų gamybai eksperimentiniam patikrinimui naudojant silicį bei plieno foliją. Šis darbas suskirstytas į pagrindinius skyrius, kuriuose aptariama pagrindinė informacija, reikalinga minėtų problemų supratimui. **Antrasis skyrius** skirtas teoriniam šviesos savybių aptarimui, būtinam lazerių optikos ir medžiagų mikroapdirbimo supratimui. Aptariami tokie reiškiniai kaip šviesos difrakcija laisvojoje erdvėje, netiesinė intensyvių pulsuojančių šviesos sąveika su medžiaga bei pluoštų formavimo svarba bei būdai. **Trečiajame skyriuje** pristatoma tyrimų metodika, kurią sudaro skaitinio modeliavimo ir eksperimentinių darbų dalys. Paaiškinami naudoti difrakcijos modeliai bei aprašomos lazerinės sistemos, su kuriomis buvo vykdyti eksperimentiniai tyrimai. **Ketvirtasis skyrius** apima nedifraguojančių Beselio tipo pluoštų ir jų variacijų taikymus unikalių židinio zonų kūrimui su potencialiu pritaikymu greitam lazeriniam skaidrių medžiagų pjovimui. **Penktasis skyrius** skirtas vektorinio pluošto formavimui, kur poliarizacijos būsena vaidina svarbų vaidmenį formavimo rezultatuose. Nagrinėjami plokščios viršūnės (dar vadinami „Flat-top“ ar „Super-Gauso“) pluoštai, turintys plokščią intensyvumo skirstinį židinyje, atvejai. Paskutinis **šestasis skyrius** nagrinėja elementų gamybą ir pritaikymą terahercinių bangų spektro diapazone, gamybai panaudojant tą patį artimosios infraredinės šviesos lazerinį šaltinį.

8.1.1. Darbo tikslas ir uždaviniai

Šiame darbe pagrindinis dėmesys skiriamas lazerinių pluoštų formavimui, sukuriant sudėtingesnės struktūros skirstinius. Šios disertacijos tikslą galima padalinti į dvi dalis.

Pirma, buvo numatyta ištirti pluoštų formavimo galimybes naudojant geometrinės fazės elementus, tai pritaikant įvairių medžiagų lazeriniame mikroapdirbime.

Antra, tyrimo tikslas buvo praplėstas pritaikant pluošto formavimo ir medžiagų mikroapdirbimo žinias struktūrizuotai terahercinei spinduliuotei formuoti, pagaminant skirtingus pluoštus formuojančius elementus iš silicio ir plieno folijos, su potencialiu pritaikomumu vaizdinime.

Siekiant įgyvendinti tikslą, buvo iškelti šie uždaviniai:

1. Naudojantis skaitiniu lazerio pluošto difrakcijos modeliavimu, atlikti sklidimo simuliacijas laisvojoje erdvėje, panaudojant tiriamus pluoštus formuojančius elementus.

2. Ištirti Beselio-tipo pluoštų formavimo techniką, naudojant pusiau padalintos aksikono fazinės kaukės ir erdviškai paslinktų jos dalių modelį. Skaitmeniškai ir eksperimentiškai ištirti gautus pluoštų intensyvumo skirstinius, kartu panaudojant erdvinį šviesos moduliatorių bei didelės galios ultratrumpųjų impulsų lazerinę sistemą. Ištirti suformuotų pluoštų ir skaidrios medžiagos sąveiką bandinio paviršiuje ir tūryje.

3. Sukurti elipsinį Beselio-tipo pluoštą, panaudojant aksikono kaukės azimutinę moduliaciją. Skaitmeniškai ištirti ir rasti optimalius fazinės kaukės zonų padalijimo parametrus, apsibrėžiant azimutinį kampą ir fazių skirtumą tarp zonų. Eksperimentiškai ištestuoti pagamintą geometrinės fazės elementą, pagal optimalius pasirinktus parametrus, sukeliant kontroliuojamus mikroįtrūkimus skaidrioje medžiagoje.

4. Ištirti statmenų poliarizacijos būsenų pluoštų superpoziciją, naudojant nemodifikuoto centro erdviškai struktūruotą banginę plokštelę, pagamintą kaip geometrinės fazės elementą. Skaitmeniškai išnagrinėti intensyvumo ir poliarizacijos būsenų pasiskirstymą pluoštuose, židinio zonos aplinkoje. Atlikti eksperimentinius pluoštų matavimus, sukelti ir ištirti suformuotas modifikacijas įvairiose medžiagose: stikle, silicio paviršiuje bei plonoje metalo dangoje.

5. Ištirti terahercinės spinduliuotės pluoštus formuojančių elementų gamybą naudojant ultratrumpųjų impulsų lazerinę abliaciją su $\lambda = 1030$ nm bangos ilgiu. Rasti optimalius mikroapdirbimo parametrus, tinkamus difrakcinių elementų iš silicio ir metaelementų iš plonos nerūdijančio plieno folijos, gaminimui.

8.1.2. Praktinė nauda ir naujumas

1. Pristatytas geometrinės fazės elementų, turinčių erdviškai praslinktos aksikono fazės pusių, dizainas, galintis suformuoti naujus Beselio-tipo pluoštus. Erdvinio praslinkimo valdymas leidžia suformuoti įvairius skersinio intensyvumo skirstinius: kelių smailių, žiedo formos arba asimetrinės centrinės smailės pluoštus. Šių skirstinių rezultatas yra nulemtas dėl Beselio nulinės ir aukštesnių lyginių eilių pluoštų superpozicijos. Asimetrinio pluošto atvejis buvo sėkmingai pritaikytas kryptingai skaldant ploną stiklą.

2. Aksikono fazinės kaukės optimizavimas dalijant ją į dvi skirtingų fazių ir azimutinių kampų poras sukuria atvejį, kai galima sugeneruoti elipsinį Beselio-tipo pluoštą. Šis optimizuotas fazinės kaukės padalijimas, realizuotas geometrinės fazės elemente, gali pakeisti įprastus aksikonus, kuriais atliekamas spartus stiklo skaldymas.

3. Pirmą kartą buvo pademonstruota erdviškai kintančių banginių plokštelių su nemodifikuotu centru kaip geometrinės fazės elemento koncepcija. Tokių elementų panaudojimas lazerinėje mikroapdirbimo sistemoje leido sukurti plokščios intensyvumo viršūnės pluoštus, sistemos optinio židinio plokštumoje, ties didžiausiu intensyvumu, naudojant standartinius fokusavimo lęšius. Pluošto intensyvumo skerspjūvio kitimas galimas keičiant įeinančio pluošto dydį, ar nemodifikuotos elemento zonos plotį, nekeičiant fokusavimo sąlygų. Tai įgalina dinamiškai keisti galutinio pluošto formą nuo Gauso iki plokščios viršūnės ar žiedo formos skirstinių.

4. Nemodifikuoto centro erdviškai struktūruotos banginės plokštelės panaudojimas leido sukurti vektorinius pluoštus, turinčius poliarizacijos singuliarumus, kurių topologiniai krūviai yra $I_c = \frac{1}{2} * N$, kur N yra lėtos ašies moduliacijos gylis. Šis naujas metodas, kuriame naudojami geometriniai fazės elementai, tinka didelės galios lazeriniui mikroapdirbimui prie įvairių skaitinės apertūros fokusavimo sąlygų.

5. Pademonstruota, kad artimosios infraraudonosios spinduliuotės pluoštų formavimo technika gali būti perkelta į terahercinės spinduliuotės bangų spektrą. Atlikti silicio mikroapdirbimo eksperi-

mentai atskleidžia galimybę pagaminti difrakcinius elementus, tinkamus iki 6 THz dažniui. Iš nerūdijančio plieno folijos gaminami lankstūs didelės apertūros (> 50 mm) pluošto formavimo elementai, panaudoti kuriant metaelementus, kurių galimas pritaikymo dažnis yra nuo 90 GHz iki 2.5 THz. Šių elementų gamyba iš silicio ir plieno folijos leidžia sukurti kompaktiškesnes vaizdinimo sistemas.

8.1.3. Ginamieji teiginiai

1. Aksikono kaukės fazinė asimetrija gali būti pritaikoma suformuojant elipsinį Beselio pluoštą, kuris yra tinkamas kryptingiems įtrūkimams formuoti skaidrioje medžiagoje. Erdviškai paslinktos aksikono fazės pusės per 0.25 fazės periodo dalį gali sukurti centrinę smailę su 1.05 elipsiškumu, kurio pakanka kryptingiems mikroįtrūkimams formuoti.

2. Atliekant parametrinę azimutinės fazės moduliacijos optimizaciją, galima rasti verčių diapazoną su tinkamais parametrais bei suformuoti asimetrinį pluoštą, tinkantį kryptingų mikroįtrūkimų formavimui stikle, o kai padalijimo kampas yra $\gamma = 17°$ ir fazių skirtumas $\Delta\varphi = 5\pi/4$, galima sukurti Beselio tipo pluoštą, kurio elipsiškumas yra 1.19.

3. Nemodifikuoto centro erdviškai kintančios banginės plokštės elementas gali būti panaudojamas efektyviai sukurti vektorinius plokščios viršūnės pluoštus, turinčius poliarizacijos singuliarumus su $I_c = \frac{1}{2} * N$ topologiniais krūviais, kur N yra lėtosios ašies moduliacijos gylis.

4. Kontroliuojant nemodifikuotos zonos ir įeinančio pluošto pločių santykį, galima dinamiškai valdyti pluošto intensyvumo skirstinį židinio plokštumoje, iš Gauso tipo į plokščios viršūnės ar žiedo formą, naudojant vieną geometrinės fazės elementą. Geriausias rezultatas pasiekiamas naudojant idealų geometrinės fazės elementą, kai lėtosios ašies moduliacijos eilė yra $N = 2$ ir santykis yra 1.45, taip suformuojant plokščios viršūnės pluoštą, kurio intensyvumo svyravimo amplitudė yra $<5\%$. Tokio elemento integracija į optinę sistema leidžia tolygiai keisti pluošto skirstinį

židinio aplinkoje.

5. Ultratrumpųjų impulsų lazerinė abliacija naudojant $\lambda = 1030$ nm bangos ilgį ir galvanometrinį skenerį gali būti naudojama tiksliai ir greitai pagaminti terahercinius difrakcinius elementus iš silicio ir metaelementus iš nerūdijančio plieno folijos, tinkančius veikimui iki 2.5 THz bei iki 6 THz silicio pagrindu pagamintiems elementams, kurių abliuoto paviršiaus kokybė gali siekti $\approx \lambda/40$.

8.1.4. Publikacijos

Pagrindiniai rezultatai buvo paskelbti 7 recenzuojamuose moksliniuose straipsniuose [A1–A7] ir 12 konferencijų pranešimų [B1–B12]. Kitos 3 nesusijusios publikacijos nebuvo įtrauktos į disertaciją [C1–C3]. Rezultatai pristatyti 12 tarptautinių ir nacionalinių konferencijų [D1–D12]. Bendraautorių pranešimai neįtraukti. Išsamūs sąrašai pateikti 1.5 poskyryje.

8.1.5. Autoriaus indėlis

Autorius atliko eksperimentinius darbus, susijusius su lazerinių sistemų projektavimu ir surinkimu, kurios buvo naudojamos lazerio pluoštų matavimams ir įvairių medžiagų mikroapdirbimui. Autorius taip pat vykdė pluoštų sklidimo simuliacijas bei vystė skaitinį sklidimo modelį. Gauti eksperimentinio darbo ir skaitinio modeliavimo rezultatai buvo analizuojami, lyginami ir apdorojami, kad būtų pristatyti galutine forma.

Straipsnyje [**A1**], autorius atliko pluošto sklidimo modeliavimą, sukūrė pradinį GFE dizainą, padėjo surinkti eksperimentinę schemą, apdorojo eksperimentinius duomenis, parašė didžiąją dalį teksto, L. Tauraitė tyrinėjo GFE modeliavimą, atliko pirminiu modeliavimo darbus ir vykdė eksperimentinį tyrimą, parašė teksto dalis, O. Ulčinas pagamino GFE, S. Orlovas parašė teorinę pluošto transformacijos analizę ir lygčių išvedimus, V. Jukna prižiūrėjo visą darbą ir redagavo tekstą.

Straipsnyje [**A2**], autorius sugalvojo pagrindinę darbo idėją, atliko pluošto sklidimo simuliacijas, surinko eksperimentinę schemą, apdorojo eksperimentinius duomenis, parašė didžiąją dalį teksto, O. Ulčinas pateikė GFE gamybos algoritmą ir pagamino keletą GFE, S. Orlovas parašė teorinę analizę ir lygčių išvedimus, pastebėjo poliarizacijos singuliarumų reiškinius, V. Jukna padėjo su skaitiniu modeliavimu, prižiūrėjo visą darbą ir redagavo tekstą.

Straipsniuose [**A3**], [**A4**] ir [**A5**], autorius buvo atsakingas už lazerinės sistemos parengimą atlikti abliacijos eksperimentus, rado optimalius mikroapdorojimo parametrus skirtingoms medžiagoms, vykdė įvairių optinių elementų gamybą, parašė tekstų dalis apie gamybos procesus. R. Ivaškevičiūtė-Povilauskienė ir likusi komanda buvo atsakingi už elementų dizainą, vaizdinimo eksperimentus, analizę ir kitas straipsnių teksto rašymo dalis.

Straipsnyje [**A6**], autorius sukūrė GFE su 6 fazių zonomis ir atliko lazerio šviesos ir medžiagos sąveikos eksperimentą, P. Šlevas sukūrė GFE su 180 fazių zonomis, atliko pluošto matavimus, analizavo duomenis ir parašė didžiąją dalį teksto, O. Ulčinas pagamino GFE. S. Orlovas parašė teorinį pagrindą, prižiūrėjo darbą ir redagavo tekstą.

Straipsnyje [**A7**], autorius sugalvojo pagrindinę darbo idėją, atliko pluošto sklidimo modeliavimą, surinko eksperimentinę schemą, apdorojo eksperimentinius duomenis, parašė didžiąją dalį teksto, P. Gotovski parašė pluošto sklidimo modelį, O. Ulčinas pagamino GFE, S. Orlovas parašė teorinę analizę ir lygčių išvedimus, A. Urbas konsultavo dėl pluošto formavimo specifikos, V. Jukna prižiūrėjo visą darbą ir redagavo tekstą.

Taip pat verti paminėjimo kolegos A. Juršėnas ir A. Gajauskaitė, kurie padėjo su skaitinio modeliavimo kodo kūrimu ir konsultacijomis. J. Berškys padėjo su Stokso parametrų analize. K. Mundrys ir P. Kizevičius padėjo analizuoti ir lyginti pagamintus THz elementus su skaitiniu modeliavimu. Autorius prižiūrėjo bakalauro studentą B. Stanionį, kuris padėjo paruošti lazerinę sistemą darbui ir gauti kai kuriuos skaitinius ir eksperimentinius rezultatus, susijusius su Beselio tipo pluoštų taikymu stiklo mikroapdirbime.

8.2. Lazerinių pluoštų formavimo svarba ir tyrimų metodika

Antrasis skyrius apžvelgia žinias iš literatūros šaltinių apie šviesos sklidimą laisvojoje erdvėje - difrakciją. Šis reiškinys, kuomet šviesai sklindant iš šaltinio, jos erdvinis skirstinys kinta, ypatingai svarbus norint geriau suprasti, kaip galima valdyti ir keisti amplitudę, fazę ar poliarizacijos būseną. Apžvelgiami difrakcijos modeliai, kuriais remiantis galima sukurti skaitinį modelį ir atlikti gana tikslias simuliacijas kompiuterio programavimo aplinkoje.

Apžvalgoje taip aptariama lazerio spinduliuotės ir medžiagos sąveika, jonizacijos procesai, lazerinės abliacijos, pjovimo ir tūrinių darinių formavimo specifikos. Skaidrių medžiagų apdirbimas ultratrumpų impulsų lazeriu skirstomas į trijų tipų optinius pažeidimus medžiagoje: I tipo modifikacijos vadinamas lūžio rodiklio pokyčiu, kada spinduliuotės poveikio taške medžiaga yra sutankinama ir suformuojama aukštesnio lūžio rodiklio sritis. Šis tipas naudingas, kada norima stiklo tūryje suformuoti šviesai laidžius kanalus, kuriais įvesta šviesa sklinda pagal lazeriu įrašytą trajektoriją. II tipo modifikacijos pasižymi dvejopalaužiškumo savybe, kuri atsiranda dėl tūryje suformuotų nanogardelių - savaime susiformavusių medžiagos sutankėjimų ir praretėjimų. Šis dvigubo lūžio rodiklio modifikacija stiklo tūryje gali keisti praeinančios šviesos poliarizaciją ar fazę ir būti panaudojamas kaip pluošto formavimo įrankis. III tipo modifikacijos pasižymi stipriu spinduliuotės poveikiu medžiagoje, kada suformuojamos mikrotuštumos ar įtrūkimai, kurie gali būti panaudoti kryptingam skaidrių terpių skaldymui. Visos šių tipų modifikacijos gali būti suformuojamos skaidriose terpėse keičiant spinduliuotės parametrus ar fokusavimo sąlygas.

Didžioji dalis šios disertacijos darbų yra paremta naudojant nanogardelių įrašymo lydyto kvarco stikle technologiją. Tiesioginio lazerinio rašymo būdu suformuotos nanogardelės turi savo orientaciją (lėtąją arba greitąją ašį) bei delsą, kurias galima keisti rašymo metu ir tuo pačiu kontroliuoti modifikacijos poziciją stiklo bandinyje. Taip pagaminami penkis laisvės laipsnius turintys optiniai elementai, kurie gali būti naudojami fazei, amplitudei ar poliarizacijai valdyti. Šie elementai dar vadinami geometrinės fazės elementais (sutrumpintai GFE, arba Pancharatnam-Berry fazės elementais), pagal aprašytą fizikinį reiškinį, kuris apibūdina šviesos fazės kitimą, kuomet ji sklinda per dvejopalaužišką terpę.

Paskutinėje apžvalgos dalyje minimi pagrindinės elektromagnetinės spinduliuotės modos - TEM modos, arba pluoštai, kuomet kalbama tik apie šviesos sklidimą. Iš standartinės Gauso pluošto (TEM_{00} modos) galimos transformacijos į kitus, sudėtingesnės sandaros pluoštus, kurie gali būti naudingai pritaikomi medžiagų apdirbime. Pavyzdžiui, nedifraguojantys Beselio tipo pluoštai, kurie suformuojami panaudojant aksikonus - kūgio formos lęšius - yra radę puikų pritaikymą skaidrių terpių mikroapdirbime. Dėl savo išilgintos židinio zonos, šie pluoštai gali suformuoti plazmos kanalą per visą bandinio storį. Kitas dėmesio vertas pluoštų tipas - Airy pluoštas, kuris taip pat turi išilgintą židinio zoną, tačiau dar papildomai ši zona turi erdvinį išlinkimą. Šių, bei kitų pluoštų tyrimai šviesos ir medžiagos sąveikose, vaizdinime ar optinėje komunikacijoje yra labai plačiai nagrinėjamos temos, tinkančios ne tik regimosios ar infraredinės spinduliuotės spektro dalyje, bet ir terahercinių bangų spektre.

8.3. Metodologija

Trečiajame disertacijos skyriuje aprašoma rezultatams gauti naudota metodika: skaitinio modeliavimo principai bei eksperimente naudotos lazerinės sistemos. Skaitinio modeliavimo rezultatai gauti naudojant paraksialinį Frenelio bei Sommerfeld-Rayleigh pluoštų sklidimo modelius, kuomet „Matlab“ (*Mathworks, Inc.*) programavimo aplinkoje naudotas laboratorijoje vystomas simuliacinis kodas. Jo veikimas pagrįstas suformuojant virtualų tinklelį, pagal kurį apibrėžiamos pradinio Gauso pluošto bei nagrinėjamo geometrinės fazės (arba difrakcinio elemento) matricos. Atlikta difrakcijos simuliacija ir pasirinktame virtualios z ašies atstume sugeneruoti pluoštų intensyvumų ir/ar poliarizacijos skirstiniai.

Eksperimentuose naudoti trys skirtingi lazeriniai stendai su trimis skirtingais lazeriniais šaltiniais, kurių pagrindinės specifikacijos pateiktos 8.1 lentelėje.

Modelis, gamintojas	MGL-III-532, *CNILaser*	Pharos SP, *Light Conversion*	Carbide, *Light Conversion*
Aktyvi terpė	Nd:YAG	Yb:KGW	Yb:KGW
Spinduliavimo tipas	nuolatinės veikos	impulsinis	impulsinis
Bangos ilgis λ, nm	532	1028	1030
Impulso trukmė FWHM τ, ps	-	0.158 – 15	0.358 – 10
Maks. vidutinė galia P, W	0.1	6	4
Pasikartojimo dažnis f, kHz	-	4–200	60–1000
Maks. impulso energija E_p, µJ	-	30 – 1500	4 - 50
Pluošto kokybės faktorius, M^2	< 1.4	< 1.3	< 1.2

Table 8.1: Pagrindiniai eksperimentuose naudotų lazerinių šaltinių parametrai.

Nuolatinės veikos šaltinis „MGL-III-532“ (*CNILaser*) buvo naudojamas apšviesti erdvinį šviesos moduliatorių „PLUTOVIS-A“ (*HOLOEYE Photonics AG*), kuris naudotas kaip dinaminis eksperimentinis pluoštų formavimo įrankis. Ketvirtajame ir šeštajame skyriuose pateikti eksperimentiškai gauti duomenys buvo naudojant lazerinį stendą su „Pharos SP“ (*Light Conversion*) šaltiniu. Šiame stende taip pat naudotos pozicionavimo ašys 50×50 mm xy eigos ašys „ANT90-XY“ (*Aerotech Inc.*), 50 mm eigos z ašis „ANT90-L-Z“ (*Aerotech Inc.*) ir 300 mm eigos papildoma x ašis „PRO165-LM“ (*Aerotech Inc.*). Greitam pluoštų skenavimui naudota galvanometrinis skeneris „IntelliScan 14“ (*ScanLab*) kartu su $f = 100$ mm židinio nuotolio telecetriniu F-theta lęšiu. Penktojo skyriaus eksperimentiniai rezultatai gauti naudojant lazerinį stendą su „Carbide“ (*Light Conversion*) šaltiniu. Šioje sistemoje naudotos xy ašys su 200×200 mm eiga „V-731“ (*Physik Instrumente*) kartu su 5 mm eigos z ašimi „ANT130V“ (*Aerotech Inc.*). Eksperimentuose pluoštų intensyvumų skirtiniams registruoti buvo naudojamos kameros „WinCamD-LCM“, (*DataRay, Inc.*) bei „UI-5240CP“ (*IDS*).

Geometrinės fazės elementų gaminimas buvo atliekamas su komercine „Workshop of Photonics“ lazerine sistema. Šioje sistemoje yra penkios sinchronizuotos ašys: trys tiesinės xyz bandinio pozicionavimo ašys bei dvi rotacinės ašys gardelių krypčiai bei delsai valdyti. Gardelių įrašymo technologija yra patentuotas procesas, išvystytas kartu su prof. P. Kazansky vadovaujama mokslininkų grupe iš Southamptono universiteto, Jungtinėje Karalystėje.

Kiti, bandinių inspekcijai naudoti prietaisai buvo: optiniai mikroskopai „Olympus BX51“ (su objektyvais nuo 5X iki 50X didinimu, skaitine apertūra nuo 0.15 iki 0.75) ir „Nikon Eclipse LV100ND“ (su objektyvais nuo 5X iki 50X didinimu, skaitine apertūra nuo 0.15 iki 0.8); dvejopalaužiškumo matuoklis „Exicor MicroImager“ (*Hinds Instruments*); optinis konfokalinis profilometras „S neox“ (*Sensorfar*); skenuojančio elektronų pluoštų mikroskopas „Axia ChemiSEM“ (*Thermo Fisher Scientific*); spinduliuotės galios matuoklis „NOVA II“ (*Ophir*).

8.4. Invariantinių Beselio-tipo pluoštų transformacijos medžiagų apdirbimui

Ketvirtajame disertacijos skyriuje buvo nagrinėjama nedifraguojančių, Beselio tipo pluoštų transformacijos ir suformuotų pluoštų poveikis sukeltas skaidrioje medžiagoje. Beselio tipo pluoštams tirti buvo atliekamas skaitinis modeliavimas, kada modifikiuota fazinė aksikono kaukė: pirmajame poskyryje iš dviejų, aksikono kaukė buvo padalinta į dvi erdvės sritis ir jos praslenkamos erdviškai į priešingas kryptis. Keičiant erdvinės dislokacijos dydį p, išreikštą fazinės moduliacijos periodo dalimi, gauti skirtingi rezultatai: nuo asimetrinės formos pluošto iki sudėtingesnės sandaros, kelių smailių intensyvumo skirstinių. Atrinkti įdomūs variantai buvo išbandyti eksperimentiškai: atliktas eksperimentas su erdviniu šviesos moduliatoriumi bei pagaminti keli geometrinės fazės elementai. Eksperimentiniai rezultatai parodė glaudų sutapimą su skaitiniu modeliu. Su pagamintais geometrinės fazės elementais suformuoti Beselio tipo nedifraguojantys pluoštai buvo panaudoti sukeliant optines pažaidas stikle. Vienas iš rezultatų, su $p = 0.25$ erdviniu poslinkiu, parodė, jog suformuotas pluošto asimetriškumas sukelia kryptingus mikroįtrūkimus per visą bandinio storį. Ši savybė buvo plačiau ištyrinėta ir rasti spinduliuotės parametrai, su kuriais pavyko atlikti tikslų stiklo pjovimą, panaudojant kryptingai suformuojamus mikroįtrūkimus dėka pluošto formos. Antrojoje šio skyriaus dalyje, buvo tikslingai siekiama suformuoti asimetrinį Beselio tipo pluoštą: atliktas skaitinis modeliavimas, kuriame aksikono fazinė kaukė padalinta į dvi skirtingų azimutinių kampų poras, turinčias fazės skirtumą tarpusavyje. Keičiant azimutinį padalijimo kampą γ bei fazės skirtumą ϕ galima gauti išilgintos - elipsinės formos Beselio tipo pluoštą, kuris, kaip jau žinoma, lemia kryptingų įtrūkių suformavimą skaidrioje medžiagoje. Tačiau vien tik elipsiškumo didinimas suformuoja ir didesnio intensyvumo antrines smailes, esančias pirmame Beselio pluošto žiede. Todėl buvo atliktas parametrų γ ir ϕ erdvės skaitinio modeliavimo tyrimas, kuris leido rasti tokias šių kintamųjų reikšmes, su kuriomis dėmės elipsiškumas bei aukštas kontrastas tarp centrinės ir antrinių smailių, buvo tinkami tolimesniam eksperimentui atlikti. Pasirinktų parametrų modifikuoto aksikono fazinė kaukė buvo pagaminta kaip geometrinės fazės elementas. Eksperimentiškai išbandytas elementas suformavo glaudžiai modelį atitinkantį pluoštą, kuris buvo sėkmingai panaudotas kontroliuojamos krypties mikroįtrūkimams stikle suformuoti ir, išstačius šių įtrūkimų ašis lygiagrečiai judėjimo krypčiai, atlikti kokybišką pjovimą, suformuojant tarpusavyje susijungiančių įtrūkimų liniją per visą bandinio storį.

Skyriuje minimi rezultatai paremti išleistomis [**A1**], [**A6**] ir [**A7**] publikacijomis.

Pagrindiniai šio skyriaus rezultatai ir išvados:

1. Aksikono fazinės kaukės, turinčios erdviškai paslinktas puses, naudojimas leidžia sukurti asimetrinius bei daug intensyvumo smailių turinčius invariantinius Beselio tipo pluoštus. Didinamas erdvinio poslinkio p žingsnis priešingomis kryptimis sukelia stipresnį centrinės smailės iškraipymą, suskaidydamas ją į sudėtingesnę daugiasmailę skersinę intensyvumo struktūrą su didesniu fiziniu atstumu tarp smailių.

2. Įvesta asimetrija fazinėje kaukėje suformuoja iškraipytą, nežymiai išilgintą spindulio intensyvumo skirstinį su elipsiškumu $\mathcal{E} \approx 1.05$, kai poslinkio parametras yra $p = 0.25$. Šis poslinkis yra pagrindinis veiksnys, dėl kurio pavyko sukurti kryptingai atsikartojančius mikroįtrūkimus stiklo tūryje 36° kampu į poslinkio krypties normalę. Paslėptojo stiklo skaldymo eksperimentas parodė, kad galima atskirti 0.5 mm storio D263t stiklą, pasiekiant geriausią šoninių sienelių šiurkštumą apie 0.52 µm bei, kai didžiausios ir mažiausios paviršiaus vertės yra 3.52 µm ir -3.3 µm, naudojant 1.3 mm Beselio zonos ilgio pluoštą (ore, ties $\exp[-2]$ intensyvumo lygiu) su 4 ps impulso trukme, 330 µJ impulso energija, 10 µm žingsniu tarp šūvių ir 20 mm/s skenavimo greičiu.

3. Optimizuota aksikono fazinės kaukės azimutinė moduliacija gali būti panaudojama norint rasti optimalią centrinės smailės formą su norima asimetrija, keičiant fazės azimutinio pjūvio kampą γ ir fazės skirtumą $\Delta\varphi$. Atsižvelgiant į tai, buvo suformuotas ir naudojamas elipsinis Beselio tipo pluoštas su elipsiškumu $\mathcal{E} = 1.19$ ir kontrastu tarp centrinės ir antrinių smailių $C = 0.61$, kai $\gamma = 17°$ ir $\varphi = 5\pi/4$. Paslėptojo skaldymo eksperimente, naudojant 6 ps impulso trukmę, 8 µm žingsnį tarp šūvių ir 170 µJ impulso energiją, su 20 mm/s skenavimo greičiu, gautas geriausias atlaužto bandinio sienelės šiurkštumas buvo 0.47 µm, kai didžiausios ir

žemiausios paviršiaus vertės buvo išmatuotos 1.03 µm ir -1.09 µm atitinkamai. Sistemiškai gauto elipsiško pluošto eksperimentiniai stiklo skaldymo duomenys parodė aukštesnės kokybės rezultatus: labiau išreikštas elipsiškumas leidžia sukurti tolygiau išdėstytus mikroįtrūkimus išilgai pjovimo trajektorijai, o tai padeda pasiekti panašų šiurkštumą kaip ir pirmuoju atveju, tačiau kur kas mažesnes didžiausios ir žemiausios paviršiaus smailių reikšmes.

4. Pluoštų analizė rodo, kad abiem pademonstruotais Beselio tipo pluoštų formavimo atvejais, galutinis invariantinis pluoštas yra koherentinė nulinės eilės ir aukštesnių eilių Beselio pluoštų superpozicija.

5. Geometrinės fazės elementų panaudojimas įrodo, kad tai yra patikimas ir efektyvus būdas didelės energijos pluoštų formavimui, pasiekiant 74% – 90% pralaidumą naudojant $\lambda = 1030$ nm bangos ilgį (be antireflektinių dangų). Pagaminto elemento pralaidumo nuostoliai gali priklausyti ne tik nuo įrašytos delsos nuokrypių, bet ir nuo lėtosios ašies skirstinio sudėtingumo. Staigūs lėtosios ašies pokyčiai nanogardelių įrašymo metu gali sukelti netiksliai suformuotas delsos ir anizotropijos ašies zonas.

8.5. Vektorinių plokščios viršūnės pluoštų formavimas

Penktajame skyriuje nagrinėtas modifikuotų erdviškai struktūruotų banginių plokštelių panaudojimas plokščios viršūnės pluoštams suformuoti. Taip vadinamos struktūruotos (S-banginės) plokštelės yra nanogardelių pagrindu suformuotos tolygiai kintančios orientacijos banginės plokštelės, kurios paprastai yra naudojamos azimutinės ar radialinės poliarizacijas būsenas turintiems pluoštams sukurti. Šiame skyriuje, šie elementai buvo modifikuoti taip, kad centrinė elemento dalis butų be suformuotų nanogardelių. Prasklidęs lazerio pluoštas pro tokį elementą pasidalina į du pluoštus: pirmoji, periferinė pluošto dalis pakeičia savo poliarizacijos būseną ir fazę, o antroji, centrinė pluošto dalis prasklinda nepakitusi. Valdant pluošto dydžio ir centrinės nemodifikuotos zonos dydžių santykį σ, galima dinamiškai gauti skirtingų intensyvumo skirstinių bei poliarizacijos būsenos superpozicinius pluošus optiniame židinyje. Pirmiausia, atliktas skaitinis modeliavimas, kurio rezultatai parodė, jog priklausomai nuo erdvinės banginės plokštelės moduliacijos gylio (eilės) N, superpozicijos rezultate galima gauti pluoštus su poliarizacijos singuliarumais, o keičiant santykį σ suformuoti Gauso, plokščios viršūnės ar žiedo formos intensyvumo skirstinius su tuo pačiu geometrinės fazės elementu, be optinės schemos koregavimo. Toliau sekė eksperimentinis tyrimas, kuriam buvo pagaminti $N = 1$ bei $N = 2$ eilės modifikuotos zonos S-banginės plokštelės. Gauti eksperimentiniai duomenys sutapo su modeliu, o poliarizacinis skirstinys patikrintas panaudojant Stokso parametrų įvertinimą. Paskutinėje eksperimentinio dalyje atliktas įvairių medžiagų modifikavimo tyrimas: lazerinis dviejų stiklų mikrosuvirinimas, selektyvi metalinės dangos bei silicio abliacija. Palyginti Gauso, plokščios viršūnės bei žiedo formos su daliniu intensyvumu centre pluoštų sukeliami poveikiai. Lazeriniame mikrosuvirinime plokščios viršūnės pluoštas suformavo suvirintą siūlę be įtrūkimų naudojant tą pačią vidutinę galią, priešingai nei Gauso pluošto atveju. Taip pat pastebėta, jog plokščios ar žiedo formos su daliniu intensyvumu centre pluoštai labiau tinka selektyviai plonos dangos abliacijai, kadangi su Gauso pluoštu pastebėtas akumuliuotų defektų susiformavimas ant padėklo. Galiausiai silicio abliacijoje, suformuotų kraterių formos labiausiai skyrėsi prie mažų šūvių skaičių į vieną tašką - atitiko pluoštų skirstinius. Tačiau prie didesnio pakartojimų skaičiaus gilesni krateriai tapo panašesni, parodydami, jog plokščios viršūnės pluoštai labiau tinka negiliai, selektyviai paviršiaus abliacijai atlikti.

Skyriuje minimi rezultatai paremti išleista [**A2**] publikacija.

Pagrindiniai šio skyriaus rezultatai ir išvados:

1. S-banginės plokštelės su nemodifikuotu centru elementai leidžia efektyviai sukurti vektorinius plokščios viršūnės pluoštus, turinčius poliarizacijos singuliarumus su topologiniais krūviais $I_c = \frac{1}{2} * N$, kur N yra lėtosios ašies moduliacijos gylis. Išmatuotas pagamintų elementų be antireflektinių dangų pralaidumas siekia 92% $\lambda = 1030$ nm bangos ilgiui.

2. Pademonstuota konstruktyvios superpozicijos iš dviejų ortogonalių poliarizacijos būsenų pluoštų formavimo technika sukuria plokščios viršūnės pluoštus židinio plokštumoje ties didžiausiu intensyvumu, nesuformuojant antrinių intensyvumo smailių prieš ar už fokusavimo plokštumos, nepriklausomai nuo skaitinės apertūros vertės.

3. Elemento centro skersmens ir įeinančio pluošto skersmens santykio σ reguliavimas suteikia galimybę dinamiškai keisti pluošto poliarizacijos būsenų ir intensyvumo skirstinį nuo Gauso pluošto iki plokščios viršūnės ar žiedo formos pluoštų, naudojant vieną geometrinės fazės elementą, kuris gali būti nesudėtingai integruojamas į lazerinę sistemą.

4. Plokščios viršūnės formavimo sąlygos prie įvairių lėtosios ašies moduliacijos gylių N yra: $\sigma = 1.09$ (kai $N = 1$), $\sigma = 1.45$ (kai $N = 2$), ir $\sigma = 1.74$ (kai $N = 3$). Didėjant moduliacijos gyliui N ir esant plokščiausio intensyvumo skirstiniui turint pastovias fokusavimo sąlygas suformuojami didesnio diametro suminiai pluoštai, tačiau prastėja plokštiškumas, kai $N \geq 3$. Geriausias rezultatas gaunamas su geometrinės fazės elementu $N = 2$ ir $\sigma = 1.45$, suformuojant plokščią profilį su <5% intensyvumo svyravimų amplitude.

5. Eksperimentiniai suformuotų pluoštų ir medžiagų sąveikos rezultatai atskleidžia, kad vektoriniai plokščios viršūnės pluoštai gali pagerinti selektyvią plonos metalinės dangos (< 10 nm storio) abliaciją. Tai padeda išvengti stiklo pagrindėlio pažeidimo, net esant dideliam pakartotinių impulsų skaičiui ($\geq$ 2000) viename taške, kai poveikio taško dydis buvo 16 µm naudojant 21 µJ impulso energiją, 358 fs impulso trukmę.

6. Silicio abliacijos testai parodė, kad gautų plokščios viršūnės pluoštų pranašumai daugiausiai pasireiškia paviršiaus struktūravime, kai pakartotinių impulsų skaičius yra mažas (< 20). Didesnis impulsų pakartojimo skaičius viename taške ($\geq$ 100) sukuria kokybiškai gilesnius kraterius, tačiau dėl į Gauso pluoštą panašaus intensyvumo skirstinio nužulnumų, vyksta išabliuotos duobės siaurėjimo efektas ir galutinis abliacijos rezultatas tampa panašus į atvejį, kuriam naudotas tik Gauso pluoštas.

8.6. THz dažniams skirtų elementų gamybos tyrimas

Ketvirtame ir penktame skyriuose buvo nagrinėjama pluoštų formavimo technika panaudojant dvejopai laužiančių nanogardelių pagrindu pagamintus geometrinės fazės elementus. Pagamintų optininių elementų veikimo bangos ilgis buvo 1030 nm (efektyvaus veikimo spektras yra tarp

200 nm ir 4000 nm). Šias pluoštų formavimo žinias galima pritaikyti ir gerokai ilgesniems bangos ilgiams terahercinių bangų ruože nuo 0.1 Thz iki 10 Thz, kas atitiktų bangos ilgius nuo 3 mm iki 30 µm. Kadangi lazerine abliacija galima pašalinti medžiagas dalis mikrometrų dalies tikslumu, o tai yra gerokai mažiau nei naudojamas bangos ilgis minėtame THz bangų diapazone. Taigi su tuo pačiu 1030 nm bangos ilgio ultratrumpu impulsų lazeriu galima pagaminti ir nanogardeles lydytame kvarce ir abliuoti įvairias medžiagas bei jas panaudoti kaip optinius elementus THz spinduliuotei manipuliuoti. Todėl šeštajame skyriuje buvo atliktas eksperimentinis tyrimas, siekiant pagaminti pluoštus transformuojančius elementus, tinkančius THz spektrui. Pirmojoje šešto skyriaus pusėje nagrinėta silicio abliacija. Sukonstruota lazerinė sistema su galvoskeneriu bei ieškoti optimalūs parametrai abliacijai. Atrinkti parametrai, su kuriais toliau buvo gaminami įvairūs elementai, buvo naudojant: 158 fs impulsų trukmę, 50 kHz lazerio pasikartojimo dažnį, 200 mm^{-1} impulsų šaudymo tankį bei 18.46 J/cm^2, energijos įtėkį. Varijuojant energijos įtėkį buvo galima pasiekti išabliuoto ploto dugno šiurkštumą nuo 0.36 µm iki kiek daugiau nei 1 µm (prie mažo pakartojimų skaičiaus), tuo pačiu pasiekiant ir skirtingą pašalintos medžiagos gylį. Eksperimente pastebėta, jog šiurkštumas priklauso ir nuo pakartotinių skenavimų skaičiaus, kuriam didėjant šiurkštumas taip pat augo, tačiau prie 350 µm gylio tesiekė apie 2 µm, kas THz bangos yra nykstamai mažas dydis. Pagaminti keturių tipų 8 lygių difrakciniai elementai skirti 0.6 THz spinduliuotei: Frenelio lęšis (zoninė plokštelė), aksikonas, Fibonacci (dvigubo židinio) lęšis bei Airy elementas. Išmatuotų elementų suformuojami pluoštų skirstiniai buvo artimi teoriniam modeliavimui, o pasitaikę nukrypimai nebuvo drastiški: pagamintame Airy elemente trūko vieno išabliuoto laiptelio, dėl gamybos klaidos. Taip pat dėl natūralaus nuožulnų formavimosi abliuojant, sienelių statumas buvo 75°–80°, todėl giliausi laipteliai gauti šiek tiek siauresni.

Antrojoje šio skyriaus dalyje, buvo nagrinėjama metaelementų gamyba iš nerūdyjančio plienio folijos. Ši 25 µm storio medžiaga buvo išabliuota kiaurai, taip išpjaunat C formos kiaurymes-rezonatorius. Šios kiaurymės veikia kaip sub-banginiai metapaviršiai THz spinduliuotei ir gali keisti fazę, poliarizaciją. Eksperimentiniu būdu buvo nustatyti optimalūs abliacijos parametrai, su kuriais išpjautos C formos: 158 fs impulsų trukmę, 200 kHz lazerio pasikartojimo dažnį, 200 mm^{-1} impulsų šaudymo tankį bei 6.35 J/cm^2 energijos įtėkį. Pastebėta, jog prie didesnių energijos įtėkių abliacija vyksta greičiau, tačiau pastebimas stipresnis šiluminis poveikis, kuris folijai buvo nenaudingas, dėl atsiradusių deformacijų ar sunkiau pašalinamų nešvarumų. Priešingai, su mažu energijos įtėkiu, pavyko išpjauti C formas švariai ir tiksliai, tačiau tai reikalavo didesnio pakartojimų skaičiaus, o tai ilgino gamybos trukmę. Su atrinktais optimaliais abliacijos parametrais pagaminti keli skirtingi metalęšiai su židinio nuotoliais f = 10, 20, 30 ir 40 mm bei skirtingais formos pločiais c = 30, 60, 75 ir 90 µm.

Visi šiame skyriuje pristatyti elementai buvo panaudoti vaizdinimo eksperimentuose, kurių rezultatai plačiau aptariami išleistose [**A3**], [**A4**] ir [**A5**] publikacijose.

Pagrindiniai šio skyriaus rezultatai ir išvados:

1. Ultratrumpųjų impulsų lazerinė abliacija naudojant $\lambda = 1030$ nm bangos ilgį gali būti pritaikyta gaminant aukštos kokybės terahercinius difrakcinius pluoštų formavimo elementus iš silicio ir metaelementus iš nerūdijančio plieno folijos, kurios storis yra 25 µm. Galimas taikymo diapazonas silicio pagrindu pagamintiems difrakciniams elementams gali siekti iki 6 THz, išlaikant apdorotų paviršių kokybę ne mažesnę nei $\lambda/40$, kai paviršiaus šiurkštumas yra 1.25 µm, naudojant 18.46 J/cm^2 energijos įtėkį, su 358 fs impulso trukme.

2. $\lambda = 1030$ nm nm bangos ilgio lazerio šaltinio naudojimas kartu su galvanometriniu skeneriu ir F-theta objektyvu su $f = 100$ mm židinio nuotoliu generuojant 19 µm diametro dėmę, leidžia greitai gaminti kompaktiškus ir lanksčius metapaviršių pagrindu sukurtus pluoštus formuojančius elementus, skirtus veikti iki 2.5 THz.

3. Apribojantys veiksniai, limituojantys elementų pritaikomumą iki 2.5 THz dažnio, yra difrakcijos ribotas pluošto dydis optiniame sistemos židinyje. Norint išabliuoti mažesnio pločio C formos rezonatorius, reikalingas trumpesnio bangos ilgio spinduliuotės naudojimas (pavyzdžiui, antrosios arba trečiosios harmonikos), pluošto aberacijų sumažinimas arba aukštesnės skaitinės apertūros vertės fokusavimas. Tačiau norint išlaikyti greitą gamybos procesą, būtinas galvanometrinis skeneris, kuris turi ribotą apertūros plotį įeinančiam pluoštui. Taip pat F-theta lęšio židinio nuotolis

yra surištas su darbiniu plotu, kuris neturėtų būti mažesnis nei metaelementų dydis, o tai yra 2 coliai (50.8×50.8 mm).

PADĖKA

Noriu padėkoti savo darbo vadovui dr. Vytautui Juknai už pagalbą ir mokymus rengiant disertaciją bei straipsnius, už suteiktą laisvę ir savarankiškumą dirbant, pasisemtą išmintį. Esu dėkingas buvusiems ir esamiems FTMC ir WOP kolegoms už galimybę suderinti studijas ir darbą, būdamas abiejose darbuose - mokslo ir privataus sektoriaus - įgijau dvigubą patirtį sprendžiant lazerinio mikroapdirbimo problemas. Ačiū savo bakalaurinio darbo vadovui dr. Sergejui Orlovui už suteiktą galimybę pradėti mokslininko darbą FTMC. Esu dėkingas Antanui Urbui už įtraukimą į WOP kolektyvą.

Taip pat ačiū kolegoms iš Optoelektronikos skyriaus FTMC, ypatingai Dr. Linui Minkevičiui, Dr. Rusnei Ivaškevičiūtei-Poviliauskienei bei kitiems už įtraukimą į THz elementų gamybą bei tyrimus, kurių rezultatai svariai papildė ir išplėtė šią disertaciją.

Ačiū žmonai Kotrynai, visiems artimiesiems ir draugams už palaikymą rengiant šį darbą.

Ir ačiū geriausiai (ne)rašymo padėjėjai Preilai :)

BIBLIOGRAPHY

[1] D. Bouilly, D. Perez, L. J. Lewis, Damage in materials following ablation by ultrashort laser pulses: A molecular-dynamics study, Physical Review B **76**(18) (2007), https://doi.org/10.1103/physrevb.76.184119.

[2] M. D. Shirk, P. A. Molian, A review of ultrashort pulsed laser ablation of materials, Journal of Laser Applications **10**(1), 18–28 (1998), https://doi.org/10.2351/1.521827.

[3] F. M. Dickey, *Laser beam shaping: theory and techniques* (CRC press, 2018).

[4] M. Born, E. Wolf, A. B. Bhatia, P. C. Clemmow, D. Gabor, A. R. Stokes, A. M. Taylor, P. A. Wayman, W. L. Wilcock, *Principles of Optics: Electromagnetic Theory of Propagation, Interference and Diffraction of Light* (Cambridge University Press, 1999).

[5] K. Iizuka, *Engineering Optics* (Springer International Publishing, 2019).

[6] C. Huygens, *Traite de la lumiere: Ou sont expliquees les causes de ce qui lui arrive dans la reflexion, dans la refraction et particulierement dans l'etrange refraction du cristal d'Islande* (Chez Pierre vander Aa, marchand libraire, 1690).

[7] J. E. Greivenkamp, *Field Guide to Geometrical Optics* (SPIE, 2004).

[8] J. Goodman, *Introduction to Fourier Optics*, McGraw-Hill physical and quantum electronics series (W. H. Freeman, 2005).

[9] R. Bracewell, *The Fourier Transform and Its Applications*, Circuits and systems (McGraw Hill, 2000).

[10] O. K. Ersoy, *Diffraction, Fourier Optics and Imaging* (Wiley, 2006).

[11] D. G. Voelz, *Computational Fourier Optics: A MATLAB Tutorial* (SPIE, 2011).

[12] J. A. Stratton, *Electromagnetic Theory* (Wiley, 2015).

[13] M. Chekhova, P. Banzer, *Polarization of Light: In Classical, Quantum, and Nonlinear Optics* (De Gruyter, 2021).

[14] A. Kumar, A. Ghatak, *Polarization of Light with Applications in Optical Fibers* (SPIE, 2011).

[15] R. C. Jones, A new calculus for the treatment of optical systemsi. description and discussion of the calculus, J. Opt. Soc. Am. **31**(7), 488–493 (1941), https://doi.org/10.1364/JOSA.31.000488.

[16] D. Goldstein, D. Goldstein, *Polarized Light, Revised and Expanded*, Optical engineering (CRC Press, 2003).

[17] S. Pancharatnam, Generalized theory of interference, and its applications: Part I. Coherent pencils, in *Proceedings of the Indian Academy of Sciences-Section A* (Springer, 1956), volume 44, 247–262.

[18] M. V. Berry, The adiabatic phase and Pancharatnam's phase for polarized light, Journal of Modern Optics **34**(11), 1401–1407 (1987), https://doi.org/10.1080/09500348714551321.

[19] E. Cohen, H. Larocque, F. Bouchard, F. Nejadsattari, Y. Gefen, E. Karimi, Geometric phase from Aharonov–Bohm to Pancharatnam–Berry and beyond, Nature Reviews Physics 1 (2019), https://doi.org/10.1038/s42254-019-0071-1.

[20] T. H. Maiman, Stimulated optical radiation in ruby, Nature **187**(4736), 493–494 (1960), https://doi.org/10.1038/187493a0.

[21] K. Sugioka, M. Meunier, A. Piqué, *Laser Precision Microfabrication* (Springer Berlin Heidelberg, 2010).

[22] R. Osellame, G. Cerullo, R. Ramponi, *Femtosecond Laser Micromachining: Photonic and Microfluidic Devices in Transparent Materials* (Springer Berlin Heidelberg, 2012).

[23] G. Zaremba, D. Paipulas, V. Vaičaitis, O. Balachninaite, Effect of femtosecond ultraviolet and infrared laser wavelength on plasma characteristics of metals, ceramics and

glass samples using femtosecond laser-induced breakdown spectroscopy, Applied Spectroscopy **78**(6), 579–590 (2024), https://doi.org/10.1177/00037028241240782.

[24] L. Sudrie, A. Couairon, M. Franco, B. Lamouroux, B. Prade, S. Tzortzakis, A. Mysyrowicz, Femtosecond laser-induced damage and filamentary propagation in fused silica, Physical Review Letters **89**(18) (2002), https://doi.org/10.1103/physrevlett.89.186601.

[25] V. Nathan, S. S. Mitra, A. H. Guenther, Review of multiphoton absorption in crystalline solids, Journal of the Optical Society of America B **2**(2), 294 (1985), https://doi.org/10.1364/josab.2.000294.

[26] L. V. Keldysh, Ionization in the field of a strong electromagnetic wave, J. Exptl. Theoret. Phys. **47**, 1945–1957 (1964).

[27] C. B. Schaffer, A. Brodeur, E. Mazur, Laser-induced breakdown and damage in bulk transparent materials induced by tightly focused femtosecond laser pulses, Measurement Science and Technology **12**(11), 1784–1794 (2001), https://doi.org/10.1088/0957-0233/12/11/305.

[28] M. Ams, G. D. Marshall, P. Dekker, M. Dubov, V. K. Mezentsev, I. Bennion, M. J. Withford, Investigation of ultrafast laser–photonic material interactions: challenges for directly written glass photonics, IEEE journal of selected topics in quantum electronics **14**(5), 1370–1381 (2008).

[29] K. Itoh, W. Watanabe, S. Nolte, C. B. Schaffer, Ultrafast processes for bulk modification of transparent materials, MRS Bulletin **31**(8), 620–625 (2006), https://doi.org/10.1557/mrs2006.159.

[30] C. Florea, K. Winick, Fabrication and characterization of photonic devices directly written in glass using femtosecond laser pulses, Journal of Lightwave Technology **21**(1), 246–253 (2003), https://doi.org/10.1109/jlt.2003.808678.

[31] K. M. Davis, K. Miura, N. Sugimoto, K. Hirao, Writing waveguides in glass with a femtosecond laser, Opt. Lett. **21**(21), 1729–1731 (1996), https://doi.org/10.1364/OL.21.001729.

[32] K. Miura, J. Qiu, H. Inouye, T. Mitsuyu, K. Hirao, Photowritten optical waveguides in various glasses with ultrashort pulse laser, Applied Physics Letters **71**(23), 3329–3331 (1997), https://doi.org/10.1063/1.120327.

[33] C. Hnatovsky, R. S. Taylor, P. P. Rajeev, E. Simova, V. R. Bhardwaj, D. M. Rayner, P. B. Corkum, Pulse duration dependence of femtosecond-laser-fabricated nanogratings in fused silica, Applied Physics Letters **87**(1) (2005), https://doi.org/10.1063/1.1991991.

[34] J. Solis, T. T. Fernandez, J. del Hoyo, J. Siegel, P. M. Zarate, Femtosecond-laser-induced compositional changes for high-performance photonics, SPIE Newsroom (2015), https://doi.org/10.1117/2.1201511.006127.

[35] C. Cai, J. Wang, Femtosecond laser-fabricated photonic chips for optical communications: A review, Micromachines **13**(4), 630 (2022), https://doi.org/10.3390/mi13040630.

[36] L. Sudrie, M. Franco, B. Prade, A. Mysyrowicz, Writing of permanent birefringent microlayers in bulk fused silica with femtosecond laser pulses, Optics Communications **171**(4–6), 279–284 (1999), https://doi.org/10.1016/s0030-4018(99)00562-3.

[37] L. Sudrie, M. Franco, B. Prade, A. Mysyrowicz, Study of damage in fused silica induced by ultra-short ir laser pulses, Optics Communications **191**(3–6), 333–339 (2001), https://doi.org/10.1016/s0030-4018(01)01152-x.

[38] Q. Xie, M. Cavillon, D. Pugliese, D. Janner, B. Poumellec, M. Lancry, On the formation of nanogratings in commercial oxide glasses by femtosecond laser direct writing, Nanomaterials **12**(17), 2986 (2022), https://doi.org/10.3390/nano12172986.

[39] Y. Lei, H. Wang, L. Skuja, B. Kühn, B. Franz, Y. Svirko, P. G. Kazansky, Ultrafast laser writing in different types of silica glass, Laser & Photonics Reviews **17**(7) (2023), https://doi.org/10.1002/lpor.202200978.

[40] Y. Shimotsuma, P. G. Kazansky, J. Qiu, K. Hirao, Self-organized nanogratings in glass irradiated by ultra-

short light pulses, Phys. Rev. Lett. **91**, 247405 (2003), https://doi.org/10.1103/PhysRevLett.91.247405.

[41] E. Bricchi, B. G. Klappauf, P. G. Kazansky, Form birefringence and negative index change created by femtosecond direct writing in transparent materials, Optics Letters **29**(1), 119 (2004), https://doi.org/10.1364/ol.29.000119.

[42] M. Beresna, M. Gecevičius, P. G. Kazansky, T. Taylor, A. V. Kavokin, Exciton mediated self-organization in glass driven by ultrashort light pulses, Applied Physics Letters **101**(5), 053120 (2012), https://doi.org/10.1063/1.4742899.

[43] N. M. Bulgakova, V. P. Zhukov, Y. P. Meshcheryakov, Theoretical treatments of ultrashort pulse laser processing of transparent materials: toward understanding the volume nanograting formation and “quill” writing effect, Applied Physics B **113**(3), 437–449 (2013), https://doi.org/10.1007/s00340-013-5488-0.

[44] M. Sakakura, Y. Lei, L. Wang, Y. Yu, P. G. Kazansky, Ultralow-loss geometric phase and polarization shaping by ultrafast laser writing in silica glass, Light: Science & Applications **9** (2020), https://doi.org/10.1038/s41377-020-0250-y.

[45] C. Hnatovsky, R. Taylor, E. Simova, P. Rajeev, D. Rayner, V. Bhardwaj, P. Corkum, Fabrication of microchannels in glass using focused femtosecond laser radiation and selective chemical etching, Applied Physics A **84**(1–2), 47–61 (2006), https://doi.org/10.1007/s00339-006-3590-4.

[46] Y. Lei, H. Wang, G. Shayeganrad, P. G. Kazansky, Ultrafast laser nanostructuring in transparent materials for beam shaping and data storage [invited], Optical Materials Express **12**(9), 3327 (2022), https://doi.org/10.1364/ome.463151.

[47] P. N. Saeta, B. I. Greene, Primary relaxation processes at the band edge of sio2, Physical Review Letters **70**(23), 3588–3591 (1993), https://doi.org/10.1103/physrevlett.70.3588.

[48] Y. Dai, J. Ye, M. Gong, X. Ye, X. Yan, G. Ma, J. Qiu, Forced rotation of nanograting in glass by pulse-front tilted femtosec-

ond laser direct writing, Optics Express **22**(23), 28500 (2014), https://doi.org/10.1364/oe.22.028500.

[49] Y.-S. Xu, Z.-Z. Li, Z.-H. Wang, H. Xia, Y.-F. Liu, S. Juodkazis, Q.-D. Chen, L. Wang, Nanoscale control of nonreciprocal ripple writing, Optics Express **31**(9), 14796 (2023), https://doi.org/10.1364/oe.487107.

[50] Y. Lei, H. Wang, G. Shayeganrad, Y. Svirko, P. G. Kazansky, Controlling ultrafast laser writing in silica glass by pulse temporal contrast, Optics Letters **49**(9), 2385 (2024), https://doi.org/10.1364/ol.522307.

[51] J. Zhang, M. Gecevičius, M. Beresna, P. G. Kazansky, Seemingly unlimited lifetime data storage in nanostructured glass, Physical Review Letters **112**(3) (2014), https://doi.org/10.1103/physrevlett.112.033901.

[52] G. Shayeganrad, X. Chang, H. Wang, C. Deng, Y. Lei, P. G. Kazansky, High damage threshold birefringent elements produced by ultrafast laser nanostructuring in silica glass, Optics Express **30**(22), 41002 (2022), https://doi.org/10.1364/oe.473469.

[53] E. N. Glezer, E. Mazur, Ultrafast-laser driven micro-explosions in transparent materials, Applied Physics Letters **71**(7), 882–884 (1997), https://doi.org/10.1063/1.119677.

[54] X. Wang, F. Chen, Q. Yang, H. Liu, H. Bian, J. Si, X. Hou, Fabrication of quasi-periodic micro-voids in fused silica by single femtosecond laser pulse, Applied Physics A **102**(1), 39–44 (2010), https://doi.org/10.1007/s00339-010-6063-8.

[55] K. Mishchik, R. Beuton, O. D. Caulier, S. Skupin, B. Chimier, G. Duchateau, B. Chassagne, R. Kling, C. Hönninger, E. Mottay, J. Lopez, Improved laser glass cutting by spatio-temporal control of energy deposition using bursts of femtosecond pulses, Opt. Express **25**(26), 33271–33282 (2017), https://doi.org/10.1364/OE.25.033271.

[56] S. Richter, M. Heinrich, S. Döring, A. Tünnermann, S. Nolte, Formation of femtosecond laser-induced nanogratings at high

repetition rates, Applied Physics A **104**(2), 503–507 (2011), https://doi.org/10.1007/s00339-011-6489-7.

[57] L. P. R. Ramirez, M. Heinrich, S. Richter, F. Dreisow, R. Keil, A. V. Korovin, U. Peschel, S. Nolte, A. Tünnermann, Tuning the structural properties of femtosecond-laser-induced nanogratings, Applied Physics A **100**(1), 1–6 (2010), https://doi.org/10.1007/s00339-010-5684-2.

[58] K. Sugioka, Y. Cheng, *Ultrafast Laser Processing: From Micro- to Nanoscale* (Pan Stanford, 2013).

[59] A. Tuennermann, S. Nolte, J. Limpert, Femtosecond vs. picosecond laser material processing: Challenges in ultrafast precision laser micromachining of metals at high repetition rates, Laser Technik Journal **7**(1), 34–38 (2010), https://doi.org/10.1002/latj.201090006.

[60] J. Dudutis, J. Pipiras, R. Stonys, E. Daknys, A. Kilikevičius, A. Kasparaitis, G. Račiukaitis, P. Gečys, In-depth comparison of conventional glass cutting technologies with laser-based methods by volumetric scribing using Bessel beam and rear-side machining, Optics Express **28**(21), 32133 (2020), https://doi.org/10.1364/oe.402567.

[61] A. Horn, I. Mingareev, A. Werth, M. Kachel, U. Brenk, Investigations on ultrafast welding of glass–glass and glass–silicon, Applied Physics A **93**(1), 171–175 (2008), https://doi.org/10.1007/s00339-008-4654-4.

[62] M. von Allmen, A. Blatter, *Laser-Beam Interactions with Materials: Physical Principles and Applications* (Springer Berlin Heidelberg, 1995).

[63] J. P. McDonald, S. Ma, T. M. Pollock, S. M. Yalisove, J. A. Nees, Femtosecond pulsed laser ablation dynamics and ablation morphology of nickel based superalloy cmsx-4, Journal of Applied Physics **103**(9) (2008), https://doi.org/10.1063/1.2917418.

[64] W. M. Steen, *Laser Material Processing* (Springer London, 1991).

[65] B. Kim, H. K. Nam, S. Watanabe, S. Park, Y. Kim, Y.-J. Kim, K. Fushinobu, S.-W. Kim, Selective laser ablation of metal thin films using ultrashort pulses, International Journal of Precision Engineering and Manufacturing-Green Technology **8**(3), 771–782 (2020), https://doi.org/10.1007/s40684-020-00272-w.

[66] B. Neuenschwander, B. Jaeggi, M. Schmid, G. Hennig, Surface structuring with ultra-short laser pulses: Basics, limitations and needs for high throughput, Physics Procedia **56**, 1047–1058 (2014), https://doi.org/10.1016/j.phpro.2014.08.017.

[67] A. Collins, D. Rostohar, C. Prieto, Y. Chan, G. M. O'Connor, Laser scribing of thin dielectrics with polarised ultrashort pulses, Optics and Lasers in Engineering **60**, 18–24 (2014), https://doi.org/10.1016/j.optlaseng.2014.03.010.

[68] J. Dudutis, M. Mackevičiūtė, J. Pipiras, R. Stonys, V. Stankevič, G. Račiukaitis, P. Gečys, Transversal and axial modulation of axicon-generated Bessel beams using amplitude and phase masks for glass processing applications, Opt. Express **30**(2), 1860–1874 (2022), https://doi.org/10.1364/OE.447035.

[69] J. Dudutis, J. Pipiras, S. Schwarz, S. Rung, R. Hellmann, G. Račiukaitis, P. Gečys, Laser-fabricated axicons challenging the conventional optics in glass processing applications, Optics Express **28**(4), 5715 (2020), https://doi.org/10.1364/oe.377108.

[70] K. Cvecek, R. Odato, S. Dehmel, I. Miyamoto, M. Schmidt, Gap bridging in joining of glass using ultra short laser pulses, Optics Express **23**(5), 5681 (2015), https://doi.org/10.1364/oe.23.005681.

[71] S. Richter, F. Zimmermann, A. Tünnermann, S. Nolte, Laser welding of glasses at high repetition rates – fundamentals and prospects, Optics & Laser Technology **83**, 59–66 (2016), https://doi.org/10.1016/j.optlastec.2016.03.022.

[72] J. Zhang, S. Chen, H. Lu, M. Huang, J. Li, L. Guo, Q. Lue, Q. Zhang, The effect of gap on the quality of glass-to-glass welding using a picosecond laser, Optics and Lasers in Engineering **134**, 106248 (2020), https://doi.org/10.1016/j.optlaseng.2020.106248.

[73] A. Butkutė, T. Jurkšas, T. Baravykas, B. Leber, G. Merkininkaitė, R. Žilėnaitė, D. Čereška, A. Gulla, M. Kvietkauskas, K. Marcinkevičiūtė, P. Schemmer, K. Strupas, Combined femtosecond laser glass microprocessing for liver-on-chip device fabrication, Materials **16**(6), 2174 (2023), https://doi.org/10.3390/ma16062174.

[74] F. Courvoisier, *Nonstandard Light for Ultrafast Laser Microstructuring and Nanostructuring* (Springer International Publishing, 2023).

[75] M. Duocastella, C. Arnold, Bessel and annular beams for materials processing, Laser & Photonics Reviews **6** (2012), https://doi.org/10.1002/lpor.201100031.

[76] R. Stoian, M. K. Bhuyan, G. Zhang, G. Cheng, R. Meyer, F. Courvoisier, Ultrafast Bessel beams: advanced tools for laser materials processing, Advanced Optical Technologies **7**(3), 165–174 (2018), https://doi.org/10.1515/aot-2019-0029.

[77] H. Rubinsztein-Dunlop, A. Forbes, M. V. Berry, M. R. Dennis, D. L. Andrews, M. Mansuripur, C. Denz, C. Alpmann, P. Banzer, T. Bauer, et al., Roadmap on structured light, Journal of Optics **19**(1), 013001 (2016), https://doi.org/10.1088/2040-8978/19/1/013001.

[78] O. V. Angelsky, A. Y. Bekshaev, S. G. Hanson, C. Y. Zenkova, I. I. Mokhun, Z. Jun, Structured light: ideas and concepts, Frontiers in Physics **8**, 114 (2020), https://doi.org/10.3389/fphy.2020.00114.

[79] A. Forbes, M. de Oliveira, M. R. Dennis, Structured light, Nature Photonics **15**(4), 253–262 (2021), https://doi.org/10.1038/s41566-021-00780-4.

[80] Y. Yuan, T. Lei, Z. Li, Y. Li, S. Gao, Z. Xie, X. Yuan, Beam wander relieved orbital angular momentum communication in turbulent atmosphere using Bessel beams, Scientific Reports **7**(1), 42276 (2017), https://doi.org/10.1038/srep42276.

[81] L. Zhu, Z. Yang, S. Fu, Z. Cao, Y. Wang, Y. Qin, A. M. J. Koonen, Airy beam for free-space photonic interconnection: Generation strategy and trajectory manipulation,

Journal of Lightwave Technology **38**(23), 6474–6480 (2020), https://doi.org/10.1109/jlt.2020.3014893.

[82] J. Geng, Structured-light 3D surface imaging: a tutorial, Advances in Optics and Photonics **3**(2), 128–160 (2011), https://doi.org/10.1364/aop.3.000128.

[83] A. Bitman, I. Moshe, Z. Zalevsky, Improving depth-of field in broadband THz beams using nondiffractive Bessel beams, Optics Letters **37**(19), 4164–4166 (2012), https://doi.org/10.1364/ol.37.004164.

[84] L. Minkevičius, D. Jokubauskis, I. Kašalynas, S. Orlov, A. Urbas, G. Valušis, Bessel terahertz imaging with enhanced contrast realized by silicon multi-phase diffractive optics, Optics Express **27**(25), 36358–36367 (2019), https://doi.org/10.1364/oe.27.036358.

[85] J. Wang, X. Hua, C. Guo, W. Liu, S. Jia, Airy-beam tomographic microscopy, Optica **7**(7), 790–793 (2020), https://doi.org/10.1364/optica.389894.

[86] T. Vettenburg, H. I. Dalgarno, J. Nylk, C. Coll-Lladó, D. E. Ferrier, T. Čižmár, F. J. Gunn-Moore, K. Dholakia, Light-sheet microscopy using an airy beam, Nature Methods **11**(5), 541–544 (2014), https://doi.org/10.1038/nmeth.2922.

[87] D. S. Simon, *A Guided Tour of Light Beams* (IOP Publishing, 2020).

[88] N. Hodgson, H. Weber, *Optical Resonators* (Springer London, 1997).

[89] L. G. Gouy, *Sur une propriété nouvelle des ondes lumineuses* (Gauthier-Villars, 1890).

[90] S. Rung, J. Barth, R. Hellmann, Characterization of laser beam shaping optics based on their ablation geometry of thin films, Micromachines **5**(4), 943–953 (2014), https://doi.org/10.3390/mi5040943.

[91] Y. Wang, Y. Chen, Y. Zhang, H. Chen, S. Yu, Generalised hermite–gaussian beams and mode transformations, Journal of Optics **18**(5), 055001 (2016), https://doi.org/10.1088/2040-8978/18/5/055001.

[92] E. G. Abramochkin, V. G. Volostnikov, Generalized gaussian beams, Journal of Optics A: Pure and Applied Optics **6**(5), S157–S161 (2004), https://doi.org/10.1088/1464-4258/6/5/001.

[93] M. A. Bandres, J. C. Gutiérrez-Vega, Ince–gaussian beams, Optics Letters **29**(2), 144 (2004), https://doi.org/10.1364/ol.29.000144.

[94] H. Yang, Y. Wu, Z. Lin, J. Jiang, H. Huang, D. Xu, Z. Mo, Z. Wang, Y. Sun, L. Shui, D. Deng, Self-accelerating and self-healing of ince-gaussian-like beams, Results in Physics **32**, 105060 (2022), https://doi.org/10.1016/j.rinp.2021.105060.

[95] S. Fu, C. Gao, *Vector Beams and Vectorial Vortex Beams* (Springer Nature Singapore, Singapore, 2023), 277–333.

[96] P. Coullet, L. Gil, F. Rocca, Optical vortices, Optics Communications **73**(5), 403–408 (1989), https://doi.org/10.1016/0030-4018(89)90180-6.

[97] L. Allen, M. W. Beijersbergen, R. J. C. Spreeuw, J. P. Woerdman, Orbital angular momentum of light and the transformation of laguerre-gaussian laser modes, Physical Review A **45**(11), 8185–8189 (1992), https://doi.org/10.1103/physreva.45.8185.

[98] H. He, N. Heckenberg, H. Rubinsztein-Dunlop, Optical particle trapping with higher-order doughnut beams produced using high efficiency computer generated holograms, Journal of Modern Optics **42**(1), 217–223 (1995), https://doi.org/10.1080/09500349514550171.

[99] D. Andrews, a. O. M. C. Safari, *Structured Light and Its Applications* (Academic Press, 2008).

[100] W. B. Veldkamp, Laser beam profile shaping with interlaced binary diffraction gratings, Applied Optics **21**(17), 3209 (1982), https://doi.org/10.1364/ao.21.003209.

[101] O. Homburg, T. Mitra, Gaussian-to-top-hat beam shaping: an overview of parameters, methods, and applications, in A. V. Kudryashov, A. H. Paxton, V. S. Ilchenko (eds.), *Laser Resonators, Microresonators, and Beam Control XIV* (SPIE, 2012).

[102] A. N. K. Reddy, V. Pal, Robust design of diffractive optical elements for forming flat-top beams with extended depth of focus, Applied Physics B **125**(12) (2019), https://doi.org/10.1007/s00340-019-7345-2.

[103] H. Le, P. Penchev, A. Henrottin, D. Bruneel, V. Nasrollahi, J. A. Ramos-de Campos, S. Dimov, Effects of top-hat laser beam processing and scanning strategies in laser micro-structuring, Micromachines **11**(2), 221 (2020), https://doi.org/10.3390/mi11020221.

[104] V. Pal, C. Tradonsky, R. Chriki, N. Kaplan, A. Brodsky, M. Attia, N. Davidson, A. A. Friesem, Generating flat-top beams with extended depth of focus, Applied Optics **57**(16), 4583 (2018), https://doi.org/10.1364/ao.57.004583.

[105] J. Durnin, J. Miceli Jr, J. H. Eberly, Diffraction-free beams, Physical review letters **58**(15), 1499 (1987), https://doi.org/10.1103/physrevlett.58.1499.

[106] J. Turunen, A. T. Friberg, *Propagation-Invariant Optical Fields* (Elsevier, 2010), 1–88.

[107] D. McGloin, K. Dholakia, Bessel beams: Diffraction in a new light, Contemporary Physics **46**(1), 15–28 (2005), https://doi.org/10.1080/0010751042000275259.

[108] J. C. Gutiérrez-Vega, M. D. Iturbe-Castillo, S. Chávez-Cerda, Alternative formulation for invariant optical fields: Mathieu beams, Optics Letters **25**(20), 1493 (2000), https://doi.org/10.1364/ol.25.001493.

[109] I. Rondón-Ojeda, F. Soto-Eguibar, Properties of the poynting vector for invariant beams: Negative propagation in weber beams, Wave Motion **78**, 176–184 (2018), https://doi.org/10.1016/j.wavemoti.2018.02.003.

[110] N. K. Efremidis, Z. Chen, M. Segev, D. N. Christodoulides, Airy beams and accelerating waves: an overview of recent advances, Optica **6**(5), 686 (2019), https://doi.org/10.1364/optica.6.000686.

[111] R. Grunwald, M. Bock, Needle beams: a review, Advances in Physics: X **5**(1), 1736950 (2020), https://doi.org/10.1080/23746149.2020.1736950.

[112] R. MacDonald, S. Boothroyd, T. Okamoto, J. Chrostowski, B. Syrett, Interboard optical data distribution by Bessel beam shadowing, Optics Communications **122**(4), 169–177 (1996), https://doi.org/https://doi.org/10.1016/0030-4018(95)00432-7.

[113] H. Nagar, E. Dekel, D. Kasimov, Y. Roichman, Non-diffracting beams for label-free imaging through turbid media, Optics Letters **43**(2), 190 (2018), https://doi.org/10.1364/ol.43.000190.

[114] T. Čižmár, V. Kollárová, X. Tsampoula, F. Gunn-Moore, W. Sibbett, Z. Bouchal, K. Dholakia, Generation of multiple Bessel beams for a biophotonics workstation, Optics Express **16**(18), 14024 (2008), https://doi.org/10.1364/oe.16.014024.

[115] I. Alexeev, K.-H. Leitz, A. Otto, M. Schmidt, Application of Bessel beams for ultrafast laser volume structuring of non-transparent media, Physics Procedia **5**, 533–540 (2010), https://doi.org/10.1016/j.phpro.2010.08.177.

[116] R. Meyer, M. Jacquot, R. Giust, J. Safioui, L. Rapp, L. Furfaro, P.-A. Lacourt, J. Dudley, F. Courvoisier, Single shot ultrafast laser processing of high-aspect ratio nanochannels using elliptical Bessel beams, Optics Letters **42** (2017), https://doi.org/10.1364/OL.42.004307.

[117] S. Li, J. Wang, Adaptive free-space optical communications through turbulence using self-healing Bessel beams, Scientific Reports **7**(1) (2017), https://doi.org/10.1038/srep43233.

[118] J. Durnin, Exact solutions for nondiffracting beams. I. The scalar theory, JOSA A **4**(4), 651–654 (1987), https://doi.org/10.1364/josaa.4.000651.

[119] J. H. McLeod, The Axicon: A new type of optical element, J. Opt. Soc. Am. **44**(8), 592–597 (1954), https://doi.org/10.1364/JOSA.44.000592.

[120] V. Jarutis, R. Paškauskas, A. Stabinis, Focusing of Laguerre–Gaussian beams by axicon, Optics communications **184**(1-4), 105–112 (2000), https://doi.org/https://doi.org/10.1016/S0030-4018(00)00961-5.

[121] Y. Shen, X. Wang, Z. Xie, C. Min, X. Fu, Q. Liu, M. Gong, X. Yuan, Optical vortices 30 years on: Oam manipulation from topological charge to multiple singularities, Light: Science & Applications **8**(1), 1–29 (2019), https://doi.org/10.1038/s41377-019-0194-2.

[122] S. Orlov, K. Regelskis, V. Smilgevičius, A. Stabinis, Propagation of Bessel beams carrying optical vortices, Optics communications **209**(1-3), 155–165 (2002), https://doi.org/https://doi.org/10.1016/S0030-4018(02)01667-X.

[123] R. Vasilyeu, A. Dudley, N. Khilo, A. Forbes, Generating superpositions of higher order Bessel beams, in *Frontiers in Optics 2009 Laser Science XXV Fall 2009 OSA Optics & Photonics Technical Digest* (OSA, 2009), FiO.

[124] A. Mathis, F. Courvoisier, L. Froehly, L. Furfaro, M. Jacquot, P. A. Lacourt, J. M. Dudley, Micromachining along a curve: Femtosecond laser micromachining of curved profiles in diamond and silicon using accelerating beams, Applied Physics Letters **101**(7), 071110 (2012), https://doi.org/10.1063/1.4745925.

[125] C. Ungaro, A. Liu, Single-pass cutting of glass with a curved edge using ultrafast curving Bessel beams and oblong airy beams, Optics & Laser Technology **144**, 107398 (2021), https://doi.org/10.1016/j.optlastec.2021.107398.

[126] Z. Zheng, B.-F. Zhang, H. Chen, J. Ding, H.-T. Wang, Optical trapping with focused airy beams, Applied Optics **50**(1), 43 (2010), https://doi.org/10.1364/ao.50.000043.

[127] S. Orlov, P. Banzer, Vectorial complex-source vortex beams, Physical Review A **90**(2) (2014), https://doi.org/10.1103/physreva.90.023832.

[128] G. Milione, T. A. Nguyen, J. Leach, D. A. Nolan, R. R. Alfano, Using the nonseparability of vector beams to encode information for optical communication, Optics Letters **40**(21), 4887 (2015), https://doi.org/10.1364/ol.40.004887.

[129] O. J. Allegre, Z. Li, L. Li, Tailored laser vector fields for high-precision micro-manufacturing, CIRP Annals **68**(1), 193–196 (2019), https://doi.org/10.1016/j.cirp.2019.04.125.

[130] A. Rubano, F. Cardano, B. Piccirillo, L. Marrucci, Q-plate technology: a progress review [invited], Journal of the Optical Society of America B **36**(5), D70 (2019), https://doi.org/10.1364/josab.36.000d70.

[131] M. M. Sánchez-López, J. A. Davis, N. Hashimoto, I. Moreno, E. Hurtado, K. Badham, A. Tanabe, S. W. Delaney, Performance of a q-plate tunable retarder in reflection for the switchable generation of both first- and second-order vector beams, Optics Letters **41**(1), 13 (2015), https://doi.org/10.1364/ol.41.000013.

[132] M. Beresna, M. Gecevičius, P. Kazansky, T. Gertus, Radially polarized converter created by femtosecond laser nanostructuring of glass, Applied Physics Letters **98**, 201101 – 201101 (2011), https://doi.org/10.1063/1.3590716.

[133] R. Chen, K. Agarwal, C. J. R. Sheppard, X. Chen, Imaging using cylindrical vector beams in a high-numerical-aperture microscopy system, Optics Letters **38**(16), 3111 (2013), https://doi.org/10.1364/ol.38.003111.

[134] R. Drevinskas, J. Zhang, M. Beresna, M. Gecevičius, A. G. Kazanskii, Y. P. Svirko, P. G. Kazansky, Laser material processing with tightly focused cylindrical vector beams, Applied Physics Letters **108**(22) (2016), https://doi.org/10.1063/1.4953455.

[135] A. M. Beckley, T. G. Brown, M. A. Alonso, Full poincaré beams, Optics Express **18**(10), 10777 (2010), https://doi.org/10.1364/oe.18.010777.

[136] J. Ferrero-Hernanz, J. C. Sande, Design of non uniformly polarized beams, in *Online Scientific Conference* (Publishing Society, 2017), scieconf 2017.

[137] M. Dennis, Polarization singularities in paraxial vector fields: morphology and statistics, Optics Communications **213**(4-6), 201–221 (2002), https://doi.org/10.1016/s0030-4018(02)02088-6.

[138] M. R. Dennis, K. O'holleran, M. J. Padgett, Singular optics: optical vortices and polarization singularities, in *Progress in optics* (Elsevier, 2009), volume 53, 293–363.

[139] Ruchi, P. Senthilkumaran, S. K. Pal, Phase singularities to polarization singularities, International Journal of Optics **2020**, 1–33 (2020), https://doi.org/10.1155/2020/2812803.

[140] O. Angelsky, A. Mokhun, I. Mokhun, M. Soskin, The relationship between topological characteristics of component vortices and polarization singularities, Optics communications **207**(1-6), 57–65 (2002), https://doi.org/10.1016/s0030-4018(02)01479-7.

[141] Q. Wang, C.-H. Tu, Y.-N. Li, H.-T. Wang, Polarization singularities: Progress, fundamental physics, and prospects, Apl Photonics **6**(4) (2021), https://doi.org/10.1063/5.0045261.

[142] W. Liu, W. Liu, L. Shi, Y. Kivshar, Topological polarization singularities in metaphotonics, Nanophotonics **10**(5), 1469–1486 (2021), https://doi.org/10.1515/nanoph-2020-0654.

[143] V. V. Kotlyar, A. A. Kovalev, V. D. Zaitsev, Topological charge of light fields with a polarization singularity, Photonics **9**(5), 298 (2022), https://doi.org/10.3390/photonics9050298.

[144] M. V. Berry, J. H. Hannay, Umbilic points on gaussian random surfaces, Journal of Physics A: Mathematical and General **10**(11), 1809–1821 (1977), https://doi.org/10.1088/0305-4470/10/11/009.

[145] V. Shvedov, P. Karpinski, Y. Sheng, X. Chen, W. Zhu, W. Krolikowski, C. Hnatovsky, Visualizing polarization singularities in Bessel-Poincaré beams, Optics Express **23**(9), 12444 (2015), https://doi.org/10.1364/oe.23.012444.

[146] S. K. Pal, P. Senthilkumaran, Cultivation of lemon fields, Opt. Express **24**(24), 28008–28013 (2016), https://doi.org/10.1364/OE.24.028008.

[147] B. S. B. Ram, Ruchi, P. Senthilkumaran, Angular momentum switching and orthogonal field construction of c-points, Opt. Lett. **43**(9), 2157–2160 (2018), https://doi.org/10.1364/OL.43.002157.

[148] J. Liang, J. Rudolph N. Kohn, M. F. Becker, D. J. Heinzen, High-precision laser beam shaping using a binary-amplitude spatial light modulator, Appl. Opt. **49**(8), 1323–1330 (2010), https://doi.org/10.1364/AO.49.001323.

[149] D. L. Shealy, J. A. Hoffnagle, Laser beam shaping profiles and propagation, Applied Optics **45**(21), 5118 (2006), https://doi.org/10.1364/ao.45.005118.

[150] A. Vasara, J. Turunen, A. T. Friberg, Realization of general nondiffracting beams with computer-generated holograms, J. Opt. Soc. Am. A **6**(11), 1748–1754 (1989), https://doi.org/10.1364/JOSAA.6.001748.

[151] P. Stanislovaitis, M. Ivanov, A. Matijošius, V. Smilgevičius, T. Gertus, Generation of radially polarized beams and higher order polarization singularities by optical parametric amplification of optical vortices, Optical Engineering **56**(09), 1 (2017), https://doi.org/10.1117/1.oe.56.9.095101.

[152] I. Golub, Fresnel axicon, Optics Letters **31**(12), 1890 (2006), https://doi.org/10.1364/ol.31.001890.

[153] Y. Kizuka, Characteristics of a laser beam spot focused by a binary diffractive axicon, Optical Engineering **47**(5), 053401 (2008), https://doi.org/10.1117/1.2919739.

[154] G. Račiukatis, Laser processing by using diffractive optical laser beam shaping technique, Journal of Laser Micro/Nanoengineering **6**(1), 37–43 (2011), https://doi.org/10.2961/jlmn.2011.01.0009.

[155] M. J. Escuti, J. Kim, M. W. Kudenov, Controlling light with geometric-phase holograms, Optics and Photonics News **27**(2), 22 (2016), https://doi.org/10.1364/opn.27.2.000022.

[156] M.-Y. Lin, C.-H. Chuang, T.-A. Chou, C.-Y. Chen, A theoretical framework for general design of two-materials composed diffractive fresnel lens, Scientific Reports **11**(1) (2021), https://doi.org/10.1038/s41598-021-94953-4.

[157] R. Bowman, N. Muller, X. Zambrana-Puyalto, O. Jedrkiewicz, P. Trapani, M. Padgett, Efficient generation of Bessel beam arrays by means of an SLM, The European Physical Journal Special Topics **199**, 159–166 (2011), https://doi.org/10.1140/epjst/e2011-01511-3.

[158] G. Dearden, Z. Kuang, D. Liu, W. Perrie, S. Edwardson, K. Watkins, Advances in ultra short pulse laser based parallel processing using a spatial light modulator, Physics Procedia **39**, 650–660 (2012), https://doi.org/10.1016/j.phpro.2012.10.085.

[159] S. Orlov, A. Juršėnas, J. Baltrukonis, V. Jukna, Controllable spatial array of Bessel-like beams with independent axial intensity distributions for laser microprocessing, Journal of Laser Micro / Nanoengineering **13**, 324 (2018), https://doi.org/10.2961/jlmn.2018.03.0030.

[160] S. Orlov, A. Juršėnas, E. Nacius, Optical Bessel-like beams with engineered axial phase and intensity distribution, Journal of Laser Micro / Nanoengineering **13**, 244–248 (2018), https://doi.org/10.2961/jlmn.2018.03.0017.

[161] P. Křížek, G. M. Hagen, Spatial light modulators in fluorescence microscopy, Microscopy: Science, Technology, Applications and Education **2**, 1366–1377 (2010).

[162] S. Reichelt, R. Häussler, G. Fütterer, N. Leister, H. Kato, N. Usukura, Y. Kanbayashi, Full-range, complex spatial light modulator for real-time holography, Optics Letters **37**(11), 1955 (2012), https://doi.org/10.1364/ol.37.001955.

[163] D. Lin, P. Fan, E. Hasman, M. Brongersma, Dielectric gradient metasurface optical elements, Science (New York, N.Y.) **345**, 298–302 (2014), https://doi.org/10.1126/science.1253213.

[164] G. Hui, P. Mingbo, L. Xiong, M. Xiaoliang, Z. Zeyu, G. Yinghui, L. Xiangang, Super-resolution imaging with a Bessel lens realized by a geometric metasurface, Opt. Express **25**(12), 13933–13943 (2017), https://doi.org/10.1364/OE.25.013933.

[165] C. Gigli, Q. Li, P. Chavel, G. Leo, M. L. Brongersma, P. Lalanne, Fundamental limitations of huygens' metasurfaces for optical beam shaping, Laser % Photonics Reviews **15**(8) (2021), https://doi.org/10.1002/lpor.202000448.

[166] O. Avayu, O. Eisenbach, R. Ditcovski, T. Ellenbogen, Optical metasurfaces for polarization-controlled beam shaping, Optics Letters **39**(13), 3892 (2014), https://doi.org/10.1364/ol.39.003892.

[167] M. Khorasaninejad, K. B. Crozier, Silicon nanofin grating as a miniature chirality-distinguishing beam-splitter, Nature Communications **5**(1) (2014), https://doi.org/10.1038/ncomms6386.

[168] X. Luo, Subwavelength artificial structures: Opening a new era for engineering optics, Advanced Materials **31**(4) (2018), https://doi.org/10.1002/adma.201804680.

[169] N. M. Litchinitser, I. R. Gabitov, A. I. Maimistov, V. M. Shalaev, *Chapter 1 Negative refractive index metamaterials in optics* (Elsevier, 2008), 1–67.

[170] E. Hasman, V. Kleiner, G. Biener, A. Niv, Polarization dependent focusing lens by use of quantized Pancharatnam–Berry phase diffractive optics, Applied Physics Letters **82**, 328–330 (2003), https://doi.org/10.1063/1.1539300.

[171] R. Drevinskas, M. Beresna, J. Zhang, P. Kazansky, Ultrafast laser-induced metasurfaces for geometric phase manipulation, Advanced Optical Materials **5**, 1600575 (2016), https://doi.org/10.1002/adom.201600575.

[172] R. Drevinskas, P. G. Kazansky, High-performance geometric phase elements in silica glass, APL Photonics **2**(6) (2017), https://doi.org/10.1063/1.4984066.

[173] Sertificate of optical damage threshold tests on spatially variable retarder optical elements manufactured by Workshop of

Photonics, https://www.wophotonics.com/wp-content/uploads/2020/03/LIDT-result-fs-regime.pdf (2020).

[174] P. Gotovski, P. Šlevas, S. Orlov, O. Ulčinas, V. Jukna, A. Urbas, Investigation of the Pancharatnam–Berry phase element for the generation of the top-hat beam, Journal of Optics **24**(3), 035607 (2022), https://doi.org/10.1088/2040-8986/ac4317.

[175] B. Schaefer, E. Collett, R. Smyth, D. Barrett, B. Fraher, Measuring the stokes polarization parameters, American Journal of Physics **75**(2), 163–168 (2007), https://doi.org/10.1119/1.2386162.

[176] P. Kazansky, M. Beresna, Space variant polarization converter (U.S. Patent 2014/0153097 A1, Jun. 5, 2014).

[177] V. Bagini, F. Frezza, M. Santarsiero, G. Schettini, G. Spagnolo, Generalized Bessel-Gauss beams, Journal of modern optics **43**(6), 1155–1166 (1996), https://doi.org/10.1080/09500349608232794.

[178] T. Čižmár, V. Kollárová, X. Tsampoula, F. Gunn-Moore, W. Sibbett, Z. Bouchal, K. Dholakia, Generation of multiple Bessel beams for a biophotonics workstation, Opt. Express **16**(18), 14024–14035 (2008), https://doi.org/10.1364/OE.16.014024.

[179] I. Mirza, N. Bulghakova, J. Tomaštik, Ultrashort pulse laser ablation of dielectrics: Thresholds, mechanisms, role of breakdown, Sci. Rep. **6**(39133) (2016), https://doi.org/10.1038/srep39133.

[180] F. Courvoisier, J. Zhang, M. Bhuyan, M. Jacquot, J. Dudley, Applications of femtosecond Bessel beams to laser ablation, Applied Physics A **112** (2013), https://doi.org/10.1007/s00339-012-7201-2.

[181] R. Stoian, M. K. Bhuyan, G. Zhang, G. Cheng, R. Meyer, F. Courvoisier, Ultrafast Bessel beams: advanced tools for laser materials processing, Advanced Optical Technologies **7**(3), 165–174 (2018), https://doi.org/10.1515/aot-2018-0009.

[182] R. Meyer, L. Froehly, R. Giust, J. Del Hoyo, L. Furfaro, C. Billet, F. Courvoisier, Extremely high-aspect-ratio ultrafast

Bessel beam generation and stealth dicing of multi-millimeter thick glass, Applied Physics Letters **114**(20), 201105 (2019), https://doi.org/10.1063/1.5096868.

[183] M. Mikutis, T. Kudrius, G. Šlekys, D. Paipulas, S. Juodkazis, High 90% efficiency bragg gratings formed in fused silica by femtosecond Gauss-Bessel laser beams, Opt. Mater. Express **3**(11), 1862–1871 (2013), https://doi.org/10.1364/OME.3.001862.

[184] J. Baltrukonis, O. Ulčinas, S. Orlov, V. Jukna, Void and micro-crack generation in transparent materials with high-energy first-order vector Bessel beam, J. Opt. Soc. Am. B **37**(7), 2121–2127 (2020), https://doi.org/10.1364/JOSAB.394820.

[185] O. Brzobohatý, T. Čižmár, P. Zemánek, High quality quasi-Bessel beam generated by round-tip axicon, Opt. Express **16**(17), 12688–12700 (2008), https://doi.org/10.1364/OE.16.012688.

[186] P. García-Martínez, M. M. Sánchez-López, J. A. Davis, D. M. Cottrell, D. Sand, I. Moreno, Generation of Bessel beam arrays through Dammann gratings, Appl. Opt. **51**(9), 1375–1381 (2012), https://doi.org/10.1364/AO.51.001375.

[187] J. Baltrukonis, O. Ulčinas, S. Orlov, V. Jukna, High-order vector Bessel-Gauss beams for laser micromachining of transparent materials, Physical Review Applied **16**(3) (2021), https://doi.org/10.1103/physrevapplied.16.034001.

[188] D. J. Little, M. Ams, M. J. Withford, Influence of bandgap and polarization on photo-ionization: guidelines for ultrafast laser inscription, Opt. Mater. Express **1**(4), 670–677 (2011), https://doi.org/10.1364/OME.1.000670.

[189] M. Lamperti, V. Jukna, O. Jedrkiewicz, P. Di Trapani, R. Stoian, T. E. Itina, C. Xie, F. Courvoisier, A. Couairon, Invited article: Filamentary deposition of laser energy in glasses with Bessel beams, APL Photonics **3**(12), 120805 (2018), https://doi.org/10.1063/1.5053085.

[190] J. Baltrukonis, O. Ulčinas, P. Gotovski, S. Orlov, V. Jukna, Realization of higher order vector Bessel beams for transparent material processing applications, in U. Klotzbach, A. Watanabe,

R. Kling (eds.), *Laser-based Micro- and Nanoprocessing XIV*, International Society for Optics and Photonics (SPIE, 2020), volume 11268, 295 – 302.

[191] J. Dudutis, R. Stonys, G. Račiukaitis, P. Gečys, Bessel beam asymmetry control for glass dicing applications, Procedia CIRP **74**, 333–338 (2018), https://doi.org/10.1016/j.procir.2018.08.127.

[192] J. Dudutis, R. Stonys, G. Račiukaitis, P. Gečys, Glass dicing with elliptical Bessel beam, Optics and Laser Technology **111**, 331 – 337 (2019), https://doi.org/https://doi.org/10.1016/j.optlastec.2018.10.007.

[193] S. Butkus, V. Jukna, D. Paipulas, M. Barkauskas, V. Sirutkaitis, Micromachining of invar foils with GHz, MHz and kHz femtosecond burst modes, Micromachines **11**(8) (2020), https://doi.org/10.3390/mi11080733.

[194] C. Javaux, K. Mishchik, O. Dematteo-Caulier, S. Skupin, B. Chimier, G. Duchateau, A. Bourgeade, C. Hönninger, E. Mottay, J. Lopez, R. Kling, Effects of burst mode on transparent materials processing, in U. Klotzbach, K. Washio, C. B. Arnold (eds.), *Laser-based Micro- and Nanoprocessing IX*, International Society for Optics and Photonics (SPIE, 2015), volume 9351, 132 – 141.

[195] K. Mishchik, C. Javaux, O. Dematteo-Caulier, S. Skupin, B. Chimier, C. Hönninger, R. Kling, G. Duchateau, J. Lopez, Ultrashort pulse laser cutting of glass by controlled fracture propagation, Journal of Laser Micro / Nanoengineering **11**(1), 66–70 (2016), https://doi.org/10.2961/jlmn.2016.01.0012.

[196] M. Gedvilas, G. Račiukaitis, Spatial zigzag evolution of cracks in moving sapphire initiated by bursts of picosecond laser pulses for ultrafast wafer dicing, RSC Adv. **10**, 33213–33220 (2020), https://doi.org/10.1039/D0RA06791A.

[197] T. Gertus, A. Michailovas, K. Michailovas, V. Petrauskienė, Laser beam shape converter using spatially variable waveplate made by nanogratings inscription in fused silica, in A. V. Kudryashov, A. H. Paxton, V. S. Ilchenko, L. Aschke, K. Washio (eds.), *Laser Resonators, Microresonators, and Beam Control XVII* (SPIE, 2015).

[198] T. Häfner, J. Strauß, C. Roider, J. Heberle, M. Schmidt, Tailored laser beam shaping for efficient and accurate microstructuring, Applied Physics A **124**(2) (2018), https://doi.org/10.1007/s00339-017-1530-0.

[199] W. Cheng, W. Han, Q. Zhan, Compact flattop laser beam shaper using vectorial vortex, Applied Optics **52**(19), 4608 (2013), https://doi.org/10.1364/ao.52.004608.

[200] P. Kurzynowski, W. A. Woźniak, M. Zdunek, M. Borwińska, Singularities of interference of three waves with different polarization states, Optics Express **20**(24), 26755 (2012), https://doi.org/10.1364/oe.20.026755.

[201] Q. Zhan, J. Leger, Focus shaping using cylindrical vector beams, Optics Express **10**(7), 324 (2002), https://doi.org/10.1364/oe.10.000324.

[202] L. Novotny, B. Hecht, *Principles of Nano-Optics* (Cambridge University Press, 2012).

[203] B. Khajavi, E. Galvez, High-order disclinations in space-variant polarization, Journal of Optics **18**(8), 084003 (2016), https://doi.org/10.1088/2040-8978/18/8/084003.

[204] D. G. Voelz, *Computational Fourier Optics: A MATLAB Tutorial* (SPIE, 2011).

[205] P. Senthilkumaran, *Singularities in Physics and Engineering* (IOP Publishing, 2024).

[206] F. Cardano, E. Karimi, L. Marrucci, C. de Lisio, E. Santamato, Generation and dynamics of optical beams with polarization singularities, Optics express **21**(7), 8815–8820 (2013), https://doi.org/10.1364/oe.21.008815.

[207] C. Zhang, W. Kaige, J. Bai, S. Wang, W. Zhao, F. Yang, C. Gu, G. Wang, Nanopillar array with a $\lambda/11$ diameter fabricated by a kind of visible cw laser direct lithography system, Nanoscale research letters **8**, 280 (2013), https://doi.org/10.1186/1556-276X-8-280.

[208] I. Miyamoto, K. Cvecek, Y. Okamoto, M. Schmidt, Internal modification of glass by ultrashort laser pulse and its application to microwelding, Applied Physics A **114**(1), 187–208 (2013), https://doi.org/10.1007/s00339-013-8115-3.

[209] D. Jokubauskis, L. Minkevičius, M. Karaliūnas, S. Indrišiūnas, I. Kašalynas, G. Račiukaitis, G. Valušis, Fibonacci terahertz imaging by silicon diffractive optics, Optics Letters **43**(12), 2795 (2018), https://doi.org/10.1364/ol.43.002795.

[210] M. Tamošiūnaitė, S. Indrišiūnas, V. Tamošiūnas, L. Minkevičius, A. Urbanowicz, G. Račiukaitis, I. Kašalynas, G. Valušis, Focusing of terahertz radiation with laser-ablated antireflective structures, IEEE Transactions on Terahertz Science and Technology **8**(5), 541–548 (2018), https://doi.org/10.1109/tthz.2018.2859619.

[211] S. Indrišiūnas, H. Richter, I. Grigelionis, V. Janonis, L. Minkevičius, G. Valušis, G. Račiukaitis, T. Hagelschuer, H.-W. Hübers, I. Kašalynas, Laser-processed diffractive lenses for the frequency range of 4.7 thz, Optics Letters **44**(5), 1210 (2019), https://doi.org/10.1364/ol.44.001210.

[212] H. Rubinsztein-Dunlop, A. Forbes, M. V. Berry, M. R. Dennis, D. L. Andrews, M. Mansuripur, C. Denz, C. Alpmann, P. Banzer, T. Bauer, E. Karimi, L. Marrucci, M. Padgett, M. Ritsch-Marte, N. M. Litchinitser, N. P. Bigelow, C. Rosales-Guzmán, A. Belmonte, J. P. Torres, T. W. Neely, M. Baker, R. Gordon, A. B. Stilgoe, J. Romero, A. G. White, R. Fickler, A. E. Willner, G. Xie, B. McMorran, A. M. Weiner, Roadmap on structured light, Journal of Optics **19**(1), 013001 (2016), https://doi.org/10.1088/2040-8978/19/1/013001.

[213] S. R. Ayyagari, S. Indrišiūnas, I. Kašalynas, Hybrid multiphase fresnel lenses on silicon wafers for terahertz frequencies, IEEE Transactions on Terahertz Science and Technology **13**(3), 231–236 (2023), https://doi.org/10.1109/tthz.2023.3263638.

[214] S. R. Ayyagari, A. K. Klein, S. Indrišiūnas, V. Janonis, D. Pashnev, A. S. Mohammed, G. Ducournau, A. Stöhr, I. Kašalynas, Broadband high-contrast-grating-type waveplates

for the terahertz range, Optics Express **32**(9), 15870 (2024), https://doi.org/10.1364/oe.521532.

[215] L.-F. Shi, A. Zahid, A. Ren, M. Z. Ali, H. Yue, M. A. Imran, Y. Shi, Q. H. Abbasi, The perspectives and trends of thz technology in material research for future communication - a comprehensive review, Physica Scripta **98**(6), 065006 (2023), https://doi.org/10.1088/1402-4896/accd9d.

[216] D. Zhang, J. Liu, J. Yao, Z. Zhang, B. Chen, Z. Lin, J. Cao, X. Wang, Enhanced sub-terahertz microscopy based on broadband airy beam, Advanced Materials Technologies **7**(5) (2021), https://doi.org/10.1002/admt.202100985.

[217] L. Wu, Y.-S. Lin, Flexible terahertz metamaterial filter with high transmission intensity and large tuning range for optical communication application, Physica E: Low-dimensional Systems and Nanostructures **146**, 115563 (2023), https://doi.org/10.1016/j.physe.2022.115563.

[218] M. Naftaly, N. Vieweg, A. Deninger, Industrial applications of terahertz sensing: State of play, Sensors **19**(19), 4203 (2019), https://doi.org/10.3390/s19194203.

[219] K. Liu, T. Liu, Z. Wang, C. Hu, J. Shi, M. Chen, M. Ye, H. Wang, C. Xie, X. Zhang, Thz beam shaping based on diffractive transformation for forming patterned simulation lightfields and wavefronts, Infrared Physics & Technology **124**, 104225 (2022), https://doi.org/10.1016/j.infrared.2022.104225.

[220] A. Siemion, The magic of optics—an overview of recent advanced terahertz diffractive optical elements, Sensors **21**(1), 100 (2020), https://doi.org/10.3390/s21010100.

[221] K. Stanaitis, K. Redeckas, A. Bielevičiūtė, M. Bernatonis, D. Jokubauskis, V. Čizas, L. Minkevičius, Study of the low-cost hips and paraffin-based terahertz optical components, Lithuanian Journal of Physics **63**(4) (2023), https://doi.org/10.3952/physics.2023.63.4.5.

[222] B. Voisiat, S. Indrišiūnas, R. Šniaukas, L. Minkevičius, I. Kašalynas, G. Račiukaitis, Laser processing for precise fabrication of the thz optics, in B. Neuenschwander, C. P. Grigoropoulos, T. Makimura, G. Račiukaitis (eds.), *Laser Applications in Microelectronic and Optoelectronic Manufacturing (LAMOM) XXII* (SPIE, 2017), volume 10091, 100910F.

[223] K. Werner, V. Gruzdev, N. Talisa, K. Kafka, D. Austin, C. M. Liebig, E. Chowdhury, Single-shot multi-stage damage and ablation of silicon by femtosecond mid-infrared laser pulses, Scientific Reports **9**(1) (2019), https://doi.org/10.1038/s41598-019-56384-0.

[224] S. Indrišiūnas, E. Svirplys, H. Richter, A. Urbanowicz, G. Račiukaitis, T. Hagelschuer, H.-W. Hubers, I. Kašalynas, Laser-ablated silicon in the frequency range from 0.1 to 4.7 thz, IEEE Transactions on Terahertz Science and Technology **9**(6), 581–586 (2019), https://doi.org/10.1109/tthz.2019.2939554.

[225] M. G. Rahimian, A. Jain, H. Larocque, P. B. Corkum, E. Karimi, V. R. Bhardwaj, Spatially controlled nano-structuring of silicon with femtosecond vortex pulses, Scientific Reports **10**(1) (2020), https://doi.org/10.1038/s41598-020-69390-4.

[226] S. Busch, B. Scherger, M. Scheller, M. Koch, Optically controlled terahertz beam steering and imaging, Optics Letters **37**(8), 1391 (2012), https://doi.org/10.1364/ol.37.001391.

[227] L. Minkevičius, S. Indrišiūnas, R. Šniaukas, B. Voisiat, V. Janonis, V. Tamošiūnas, I. Kašalynas, G. Račiukaitis, G. Valušis, Terahertz multilevel phase fresnel lenses fabricated by laser patterning of silicon, Optics Letters **42**(10), 1875 (2017), https://doi.org/10.1364/ol.42.001875.

[228] J. Engelberg, U. Levy, The advantages of metalenses over diffractive lenses, Nature Communications **11**(1) (2020), https://doi.org/10.1038/s41467-020-15972-9.

[229] J. A. Monsoriu, A. Calatayud, L. Remon, W. D. Furlan, G. Saavedra, P. Andres, Bifocal fibonacci diffractive lenses, IEEE Photonics Journal **5**(3), 3400106–3400106 (2013), https://doi.org/10.1109/jphot.2013.2248707.

[230] J. Pendry, A. Holden, D. Robbins, W. Stewart, Magnetism from conductors and enhanced nonlinear phenomena, IEEE Transactions on Microwave Theory and Techniques **47**(11), 2075–2084 (1999), https://doi.org/10.1109/22.798002.

[231] W. T. Chen, A. Y. Zhu, F. Capasso, Flat optics with dispersion-engineered metasurfaces, Nature Reviews Materials **5**(8), 604–620 (2020), https://doi.org/10.1038/s41578-020-0203-3.

[232] E. Arbabi, A. Arbabi, S. M. Kamali, Y. Horie, M. Faraji-Dana, A. Faraon, Mems-tunable dielectric metasurface lens, Nature Communications **9**(1) (2018), https://doi.org/10.1038/s41467-018-03155-6.

[233] E. Bermúdez-Ureña, U. Steiner, Self-rolled multilayer metasurfaces, ACS Photonics **6**(9), 2198–2204 (2019), https://doi.org/10.1021/acsphotonics.9b00816.

[234] S. M. Hein, H. Giessen, Tailoring magnetic dipole emission with plasmonic split-ring resonators, Physical Review Letters **111**(2) (2013), https://doi.org/10.1103/physrevlett.111.026803.

[235] D. M. Mittleman, Twenty years of terahertz imaging [invited], Optics Express **26**(8), 9417 (2018), https://doi.org/10.1364/oe.26.009417.

[236] F. Hesmer, E. Tatartschuk, O. Zhuromskyy, A. A. Radkovskaya, M. Shamonin, T. Hao, C. J. Stevens, G. Faulkner, D. J. Edwards, E. Shamonina, Coupling mechanisms for split ring resonators: Theory and experiment, physica status solidi (b) **244**(4), 1170–1175 (2007), https://doi.org/10.1002/pssb.200674501.

[237] Z. Song, Z. Zhao, H. Zhao, W. Peng, X. He, W. Shi, Teeter-totter effect of terahertz dual modes in c-shaped complementary split-ring resonators, Journal of Applied Physics **118**(4) (2015), https://doi.org/10.1063/1.4927845.

[238] P. Gay-Balmaz, O. J. F. Martin, Electromagnetic resonances in individual and coupled split-ring resonators, Journal of Applied Physics **92**(5), 2929–2936 (2002), https://doi.org/10.1063/1.1497452.

[239] H. D. Hristov, J. Rodriguez, W. Grote, The grooved-dielectric fresnel zone plate: An effective terahertz lens and antenna, Microwave and Optical Technology Letters **54**(6), 1343–1348 (2012), https://doi.org/10.1002/mop.26812.

[240] A. Di Bernando, C. Courtois, B. Cros, G. Matthieussent, D. Batani, T. Desai, F. Strati, G. Lucchini, High-intensity ultrashort laser-induced ablation of stainless steel foil targets in the presence of ambient gas, Laser and Particle Beams **21**(1), 59–64 (2003), https://doi.org/10.1017/s0263034603211125.

[241] T. Kramer, S. Remund, B. Jäggi, M. Schmid, B. Neuenschwander, Ablation dynamics – from absorption to heat accumulation/ultrafast laser matter interaction, Advanced Optical Technologies **7**(3), 129–144 (2018), https://doi.org/10.1515/aot-2018-0010.

[242] D. J. Förster, B. Jäggi, A. Michalowski, B. Neuenschwander, Review on experimental and theoretical investigations of ultra-short pulsed laser ablation of metals with burst pulses, Materials **14**(12), 3331 (2021), https://doi.org/10.3390/ma14123331.

[243] J. Lopez, Parameters of influence in surface ablation and texturing of metals using high-power, Journal of Laser Micro/Nanoengineering **10**(1), 1–10 (2015), https://doi.org/10.2961/jlmn.2015.01.0001.

[244] J. Lopez, G. Mincuzzi, R. Devillard, Y. Zaouter, C. Hönninger, E. Mottay, R. Kling, Ablation efficiency of high average power ultrafast laser, Journal of Laser Applications **27**(S2) (2015), https://doi.org/10.2351/1.4906479.

[245] J. He, J. Ye, X. Wang, Q. Kan, Y. Zhang, A broadband terahertz ultrathin multi-focus lens, Scientific Reports **6**(1) (2016), https://doi.org/10.1038/srep28800.

CURRICULUM VITAE

Name:	Ernestas
Surname:	Nacius
Date of birth:	1995-01-13
Place of birth:	Panevėžys, Lithuania
E-mail:	ernestas.nacius[eta]gmail.com

Education:

2020 – 2024	Vilnius University, Faculty of Physics, *Doctoral studies.*
2018 – 2020	Vilnius University, Faculty of Physics *Master's degree in Laser Technology, Magna Cum Laude.*
2014 – 2018	Vilnius University, Faculty of Physics *Bachelor's degree in Applied Physics.*
2010 – 2014	Panevėžys Juozas Balčikonis Gymnasium.

Work experience:

2017-10 – present	Center for Physical Sciences and Technology, Department of Fundamental Sciences, *Junior research fellow.*
2017-11– present	Workshop of Photonics, *Researcher.*
2016-02 – 2016-08	Altechna, *Intern.*

CURRICULUM VITAE

Vardas:	Ernestas
Pavardė:	Nacius
Gimimo data:	1995-01-13
Gimimo vieta:	Panevėžys, Lietuva
El. paštas:	ernestas.nacius[eta]gmail.com

Išsilavinimas:

2020 – 2024	Vilniaus universitetas ir Fizinių ir technologijos mokslų centras, *Doktorantūros studijos.*
2018 – 2020	Vilniaus universitetas, Fizikos fakultetas *Lazerinės technologijos magistro laipsnis*, *Magna Cum Laude.*
2014 – 2018	Vilniaus universitetas, Fizikos fakultetas *Taikomosios fizikos bakalauro laipsnis.*
2010 – 2014	Panevėžio Juozo Balčikonio gimnazija.

Profesinė veikla:

2017-10 – dabar	Fizinių ir technologjos mokslų centras, Fundamentinių tyrimų skyrius, *Jaun. mokslo darbuotojas.*
2017-11 – dabar	Workshop of Photonics, *Tyrėjas.*
2016-02 – 2016-08	Altechna, *Praktikantas.*

NOTES

NOTES

NOTES

Vilniaus universiteto leidykla
Saulėtekio al. 9, III rūmai, LT-10222 Vilnius
El. p. info@leidykla.vu.lt, www.leidykla.vu.lt
bookshop.vu.lt, journals.vu.lt
Tiražas 20 egz.